

# GFZ



Helmholtz-Zentrum  
**POTS DAM**

HELMHOLTZ-ZENTRUM POTSDAM

**DEUTSCHES  
GEOFORSCHUNGSZENTRUM**

Irina Rogozhina

## **Global modeling of the effect of strong lateral viscosity variations on dynamic geoid and mantle flow velocities**

Scientific Technical Report STR08/08



# **Global modeling of the effect of strong lateral viscosity variations on dynamic geoid and mantle flow velocities**

vorgelegt von  
Dipl.-Math.  
Irina Rogozhina  
aus Moskau, Russland

Von der Fakultät VI – Planen Bauen Umwelt  
der Technischen Universität Berlin  
zur Erlangung des akademischen Grades  
Doktorin der Naturwissenschaften (Dr. rer. nat.)  
genehmigte Dissertation

Berlin 2008  
D83

Promotionsausschuss:

Vorsitzender: Prof. Dr. Ugur Yaramanci  
1. Gutachter: Prof. Dr. Markus Rothacher  
2. Gutachter: Prof. Dr. Harro Schmeling

Tag der wissenschaftlichen Aussprache: 04.02.2008

Scientific Technical Report STR08/08

## Impressum

HELMHOLTZ-ZENTRUM POTSDAM  
**DEUTSCHES**  
**GEOFORSCHUNGSZENTRUM**

Telegrafenberg  
D-14473 Potsdam

e-mail: [postmaster@gfz-potsdam.de](mailto:postmaster@gfz-potsdam.de)  
www: <http://www.gfz-potsdam.de>

Gedruckt in Potsdam  
August 2008

ISSN 1610-0956

*GLOBAL MODELING OF THE EFFECT OF STRONG  
LATERAL VISCOSITY VARIATIONS ON DYNAMIC  
GEOID AND MANTLE FLOW VELOCITIES.*

*Ph.D. Thesis*

*By Irina Rogozhina*



**I. Rogozhina**

*Berlin, 2008*



*This research has been supervised by*

*Dr. M. K. Kaban*

*Prof. V. Trubytsyn*

*Prof. M. Rothacher*

*At*

*GeoForschungsZentrum Potsdam (Germany)*

*and*

*Institute of Physics of the Earth Moscow (Russia)*





## Abstract

This study is aimed at a development of numerical method to model the dynamic geoid and the surface plate velocities induced by global mantle flow with the effect of strong lateral viscosity variations (LVV) in conjunction with the effects of self-gravitation and mantle compressibility. I employ the technique, which comprises the combination of the spherical harmonic method, the direct Godunov method used for solving the Stokes and Poisson equations in spherical harmonics with arbitrary boundary conditions, functions of density and radial viscosity, and the iterative method based on the principles suggested by Zhang and Christensen (1993) used for modeling the effect of LVV.

The 3-D mantle viscosity model is based on the global seismic tomography model S20a converted to temperature variations. The maximum lateral viscosity contrast in the lithosphere-asthenosphere zone modeled reaches four orders of magnitude. It is found that the influence of LVV on the dynamic geoid is extremely significant: an alteration of the geoid figure due to LVV exceeds 45% of the maximum geoid undulations. The detailed analysis showed that the geoid is affected by both, strong LVV induced in the upper mantle and large-scale LVV induced in the lower mantle. According to the results of this study the separated effects of the upper- and lower-mantle LVV on the geoid figure are nearly additive with respect to the whole-mantle LVV and partly compensating with respect to each other. The mantle flows are strongly affected by LVV as well, especially by the long-wavelength viscosity variations in the lower mantle: global upwellings tend to intensify due to the effects of LVV, while downwellings become weaker. The alteration of the near-surface velocities reaches 30-40% in amplitude not only due to the LVV-induced toroidal flow but also due to change in the spheroidal velocity component.

I can conclude that the LVV presented in both, upper and lower mantle, play an important part in global modeling, therefore, an incorporation of 3-D viscosity structure into the next generation global dynamic models is a task of vital significance.

## Kurzfassung

Diese Arbeit befasst sich mit der Entwicklung numerischer Methoden zur dynamischen Modellierung des Geoids sowie der Bewegung der Lithosphärenplatten als Folge der Konvektionsströme im Mantel. Im Speziellen werden die Effekte der lateralen Viskositätsvariationen (LVV) in Verbindung mit der Eigengravitation sowie die Kompressibilität des Mantels näher untersucht. Es werden eine Reihe von Methoden angewandt und miteinander kombiniert, nämlich die Methode der Beschreibung durch Kugelflächenfunktionen, die direkte Godunov-Methode für die Lösung der Stokes- und Poisson-Gleichung mit beliebigen Randbedingungen sowie die iterative Methode (Zang und Christensen 1993) zur Berücksichtigung des Effekts der LVV.

Das dreidimensionale Viskositätsmodell des Mantels basiert auf dem globalen seismischen Schichtmodell S20a, aus dem Temperaturvariationen berechnet wurden. Der maximale laterale Viskositätsunterschied im Bereich der Litho- und Asthenosphäre beträgt vier Größenordnungen. Es hat sich herausgestellt, dass das dynamische Geoid signifikant von der LVV beeinflusst wird: In Folge der LVV variiert die Geoidhöhe bis zu 45% der maximalen Geoidundulationen. Die Analyse ergab einen besonderen Einfluss der LVV im oberen Mantel auf das Geoid. Die Auswirkungen der LVV im oberen und im unteren Mantel sind nahezu entgegengesetzt und heben sich teilweise auf. Die Mantelströmungen sind ebenfalls von der LVV beeinflusst, hauptsächlich von den langwelligen Viskositätsvariationen im unteren Mantel: die globale Aufströmung wird durch die LVV intensiviert, währenddessen das Absinken schwächer wird. Die Geschwindigkeitsänderung oberflächennaher Strömungen liegt bei 30-40 % und wird sowohl durch Änderungen in den toroidalen als auch den sphäroidischen Geschwindigkeitskomponenten verursacht.

Zusammenfassend lässt sich schlussfolgern, dass die LVV im oberen und unteren Mantel eine wichtige Rolle bei der globalen Modellierung spielt und dass deren Aufnahme in zukünftige globale dynamische Modelle von großer Bedeutung ist.

### ***Acknowledgments***

I thank Dr. M. K. Kaban and Prof. V. Trubitsyn for their high responsibility in the supervision of my research. I am especially grateful to Prof. V. Trubitsyn for his deepest interest in this study and decisive contributions on the derivation of the equations for the U-transform and W-transform perturbation methods (see Appendix). These formulae were independently derived by Prof. V. Trubitsyn and me, I. Rogozhina, under duplication check.

I thank Prof. M. Rothacher, Dr. P. Schwintzer † and Prof. Ch. Reigber for active support of my work at GFZ Potsdam. I am especially grateful to Prof. M. Rothacher for his concern in my study and invaluable support on the last stage of the dissertation completing.

I thank Prof. H. Schmeling and Prof. M. Rothacher for their consent to the back-breaking reviewer labour.

I am grateful to my father Prof. E. Rogozhin for awakening the keenest interest in the Earth's processes and in geophysics.

This work has been supported by GeoForschungsZentrum Potsdam (Germany) and by Institute of Physics of the Earth, Moscow (Russia).



## Table of contents

Chapter I. <i>Introduction</i> _____	13
1.1 The problem and motivation for the research _____	13
1.2 Three-dimensional modeling history and current studies ____	17
Chapter II. <i>Internal loading theory and basic equations</i> _____	27
2.1 The Navier-Stokes and Poisson equations _____	27
2.2 Equations in spherical coordinates _____	29
Chapter III. <i>Direct method for solving the Stokes</i> <i>equation in spherical harmonics</i> _____	33
3.1 Spherical harmonic method _____	33
3.2 The Stokes equation in spherical harmonics _____	36
3.3 Direct method for solving the Stokes equation _____	39
Chapter IV. <i>Mantle compressibility and self-gravitation</i> _____	43
4.1 Geoid and geoid undulations _____	43
4.2 Mantle compressibility and self-gravitation _____	47
4.3 Effects of mantle compressibility, self-gravitation and depth-dependent gravity on the mantle velocities and geoid _____	50
Chapter V. <i>The introduction of lateral viscosity variations</i> ____	69
5.1 Iterative methods for incorporating lateral viscosity variations _____	70
5.2 Iterative method U-transform _____	75
5.3 Iterative method W-transform _____	78
5.4 Application of the W- and U-transform iterative methods to some synthetic models. Domains of method applicability _____	83
Chapter VI. <i>Inverse problem</i> _____	102
6.1 Joint inversion technique _____	103
6.2 Inverse problem applied to the radial viscosity models ____	105
Chapter VII. <i>Global spherical models with lateral viscosity</i> <i>variations</i> _____	112
7.1 Three-dimensional global viscosity models _____	112
7.2 Contribution of lateral viscosity variations to mantle	

velocities _____	115
7.3 Particular contribution of lateral viscosity variations induced in the upper and lower mantle to the geoid, dynamic topography and surface velocities _____	122
Chapter VIII. <i>Conclusions</i> _____	135
Appendix. <i>Derivation of the U-transform and W-transform</i> <i>iterative methods</i> _____	141
Part U _____	141
Part W _____	154
List of abbreviations _____	168
List of notations _____	169
List of figures _____	172
References _____	176

## Chapter I *Introduction*

### 1.1 The problem and motivation for the research

Mantle convection leaves numerous traces that can be observed on the Earth's surface. Among these evidences of internal perpetual motion there are some convection-related observables that are often used as major constraints in mantle convection models. In the last decade, numerous studies of geoid, dynamic topography and surface plate velocities (convection-related observables) have been carried out in the context of tomography-based flow models. One of the main objectives of this modeling is the inference of the rheological structure of the mantle. With a few exceptions, these studies were conducted in the framework of the viscous flow theory, which assumes that the mantle rheology can be represented in terms of pure radially variable viscosity. Most of the existing studies of the 3-D Earth's structure let the effect of lateral viscosity variations (LVV) pass although its importance was demonstrated in the context of the mantle convection process in 2-D Cartesian geometry as early as two decades ago. In recent years, several attempts were made to assess the sensitivity of the geoid to LVV. However, such studies are often inconsistent and give only a rough idea of the LVV implications for the geoid figure.

According to the present conception of the Earth's structure, real Earth's viscosity distribution in the upper mantle can be correctly approached by LVV of seven orders of magnitude. Until recently, only the finite-element (FE) and finite-volume (FV) methods provided the possibility to model mantle flows with such strong LVV. Most studies based on FD (finite-difference), FE and FV methods fail to account for the effects of self-gravitation and mantle compressibility because the incorporation of these effects into spatial methods is coupled to certain complications dramatically increasing the computation time. The introduction of

the self-gravitation effect in the FE and FV methods requires an iterative process. The mantle compressibility effect significantly complicates the solution of Stokes equations in the spatial domain. The spectral method, being extremely fast, allows both effects to be incorporated directly through the Stokes equation represented in spherical harmonics. It is generally acknowledged (and, in particular, analyzed in greater detail in this study, see Chapter IV) that a distortion of the Earth's surface and core boundaries and the resulting redistribution of internal forces due to the effect of self-gravitation have a critical influence on the geoid anomaly. As shown in this and previous studies, the effect of mantle compressibility plays an important role in forming the mantle flow pattern and thereby influences the geoid figure.

In this study, we suggest a numerical method capable of handling strong LVV (up to about seven orders of magnitude) in conjunction with the effects of self-gravitation, mantle compressibility and radially varying gravity. The technique, which we employ, is a combination of the spectral method, the direct Godunov method used for solving systems of ordinary differential equations (ODE) with arbitrary boundary conditions, functions of density anomaly and radial viscosity, and the iterative method based on the principles suggested by Zhang and Christensen (1993). This combined method provides the possibility to model simultaneously spheroidal and toroidal mantle flows, mantle stresses, dynamic topography and geoid and has an evident advantage of extremely fast computations in the case of purely radial viscosity distribution regardless of the resolution of the input data. As distinct from the kernel technique generally used for solving the Stokes equation in spherical harmonics, the direct Godunov method provides a solution for any reasonable combination of arbitrary functions of radial viscosity and density heterogeneity without any requirement on their structural layering. We employ a joint inversion of seismic tomography data constrained by the geoid to find possible

disturbances of the radial viscosity profile and the depth-dependent scaling factor.

The main goal of this study is to develop a method applicable to the modeling of the dynamic geoid, topography and mantle flow velocities with due regard for the effects of self-gravitation, mantle compressibility and highly contrasting LVV that are close to the real state of the Earth. This method is intended to investigate instantaneous 3-D models of the Earth's mantle (in the future, upgraded to evolving 3-D models) that provide a good fit to the convection-related observables in compliance with the presently available resolution of input data. Our study mainly focuses on the estimation of the LVV effect. Previous studies have led to rather contradictory conclusions on the LVV implication for global modeling. The effect of the whole mantle LVV has been poorly investigated. In this work, we do not pretend to solve all problems related to the uncertainties in the viscosity structure of the Earth's mantle. We only perform a detailed analysis of the possible effects and the consequent ways to cope with global viscosity models in order to obtain the most comprehensive information concerning the general contribution of LVV to the geoid figure and the mantle flow velocities and particular contributions of LVV situated in various mantle layers. According to the widespread opinion, LVV (especially in the lower mantle) do not have a significant effect on the geoid figure and, therefore, there is no need to complicate global models by LVV incorporation. This work aims to disprove this widespread idea. Moreover, only the LVV effect is capable of generating a toroidal flow comparable in energy with a poloidal flow. Since toroidal flows are generated by LVV, any comprehensive model of the mantle should account for this effect, even if the geoid is adequately modeled by radial viscosity.

The observed geoid provides important constraints on mantle parameters in global modeling studies, including the very

indefinite value of viscosity variations. However, the determination of the Earth's mantle structure is ambiguous if only surface gravity data are used. A usual way to cope with such a problem is to combine gravity data with other geophysical data sets to obtain a solution that fits all data sets and therefore possesses fewer degrees of freedom. Seismic tomography models are commonly used for this purpose. In our study, we chose the S20a seismic tomography model (Ekstrom and Dziewonski (1998)) as one of the most used for the modeling in question. This model provides a resolution of up to the 20th spherical harmonic degree for isotropic velocity variations, which ensures a more realistic approach to temperature, density and viscosity distributions. We get density anomaly and viscosity distributions from the S20a model in order to estimate how significant the effects of LVV are. The derived knowledge may be applied then to the latest innovations in the seismic tomography data. There exist various seismic tomography models differing in resolution and properties. These models are being continuously improved and made more accurate. Although other models can differ in details from the S20a model, the general inference about the influence of LVV on the convection-related observables and mantle flow remains valid for all models possessing this or higher resolution.

The analyzed 3-D model of the Earth implies the following assumptions and data sets:

- 1) the radial density distribution inside the Earth mantle is based on the PREM model (Dziewonski and Anderson (1981));
- 2) the density anomaly distribution is obtained from the S20a seismic tomography model (Ekstrom and Dziewonski (1998));
- 3) a depth-dependent viscosity profile obtained from a joint inversion (constrained by the geoid) generally consistent with the results of existing studies;
- 4) free-slip boundary conditions at the surface-mantle and core-mantle boundaries of the Earth;
- 5) LVV model constructed on the basis of

- (a) S20a seismic tomography model converted to temperature and
- (b) assumptions on the homologous temperature in the mantle (Paulson et al. (2005)).

## 1.2 Three-dimensional modeling history and current studies.

In global studies, the joint use of gravity and geophysical data has been applied starting from the pioneer work by Hager and O'Connell (1981). Further, their study was continued and elaborated by Hager (1984), Ricard et al. (1984), Richards and Hager (1984), Hager et al. (1985), Forte and Peltier (1987, 1991), Schmeling (1989, 1991), Ricard and Vigny (1989), Maquart and Schmeling (1989), King and Masters (1992), Corrieu et al. (1994), Gurnis et al. (1998), Forte (2000), Tackley (2000), Forte and Mitrovica (2001), Niehuus and Schmeling (2003, 2004) and many others. The inversion of a long-wavelength non-hydrostatic geoid, known also as the inferences of viscosity from the geoid (in some cases, from surface flow velocities and constraints from mineral physics as well), has provided important information on mantle viscosity since mid-eighties (Ricard and Bai Wuming (1991); Forte et al. (1994); King (1995); Thoraval et al. (1995); Kido and Čadek (1997); Steinberger and O'Connell (1998); Čadek and Fleitout (1999); Forte et al. (2002); Forte and Mitrovica (2004); Steinberger and Calderwood (2006)). Despite all these efforts, the obtained results differ significantly and a generalized dynamic model of the Earth does not exist at present. Such an indefinite situation can be due to several factors. First, there still exists a trade-off between different model parameters and the same fit can be obtained within different model clusters. Second, the models analysed are still far from reality. The dynamic response of the Earth's surface to internal loading requires the solution of the Stokes equations together with the Poisson's equation for the gravity potential. In most of the existing studies, a simplified model implies only radial viscosity variations, which provides the possibility to solve the equations separately for each spherical

harmonic coefficient. Therefore, it is sufficient to estimate the response of the Earth to an internal load (density heterogeneities) at different depths, the so-called geoid kernels, and then to use the kernels in the inversion. Although the method is extremely fast and effective, the effect of LVV remains unclear. The main difficulty is that all spherical harmonic coefficients are coupled with LVV, thereby diminishing all advantages of the kernel technique. Thus, until recently, attention had been only given to the determination of radial changes in viscosity. Lateral variations were neglected because the LVV effect was assumed to be small in comparison with the effect of radial variations in viscosity. Indeed, lateral changes in viscosity were often found to affect very little the whole-mantle flow models with a free-slip or a rigid upper boundary (Richards and Hager (1989); Ritzert and Jacoby (1992); Čadek et al. (1993); Colin (1993); Martinec et al. (1993); Zhang and Christensen (1993); Forte and Peltier (1994); King and Hager (1994)). Numerous spherically symmetric models were considered in order to fit best to the observed long-wavelength geoid. Hager and Clayton (1989) predicted 90% of the geoid on the long waves using the tomographic model of Clayton and Comer (1983). Spherically symmetric models with radially stratified viscosity also predicted successfully about 60% of the poloidal component of plate motions (Forte and Peltier (1987, 1991)). However, spherically symmetric models fail to predict the toroidal component of present-day plate motions whose energy is nearly equal to that of the poloidal component (Hager and O'Connell (1978)). The toroidal motion can only be generated by LVV.

Detailed investigation of LVV was carried out almost exclusively in terms of 2-D Cartesian geometry (Gurnis and Davies (1986); Christensen (1994); Richards and Hager (1989); Moresi and Solomatov (1995); Moresi et al. (1996); Yang and Baumgardner (2000)).

Richards and Hager (1989) demonstrated for 2-D convection models that the effect of LVV on geoid anomalies could be significant for degrees  $l \geq 4$  because, at the lowest harmonic degrees, the geoid is least affected.

Olson and Bercovici (1991) showed that most of the toroidal energy is due to plate drift and strike-slip motions on faults, rather than to the plate spin. O'Connell et al. (1991) and Čadek and Ricard (1992) demonstrated that the actual motion of plates is such that it minimizes the toroidal energy if the present-day plate situation is considered. Ricard and Vigny (1989) predicted a toroidal component of the surface flow agreeing well with observations on the basis of a model in which rigid surface plates are coupled with buoyancy-driven flow in the mantle by means of a torque balance. Gable et al. (1991) presented a similar model in the Cartesian geometry, with the plate motion being coupled with time-dependent thermal convection. The model of Ribe (1992), in which the lithosphere is represented as a thin shell with LVV overlying a radially symmetric mantle, predicted a substantial part of the toroidal component of surface motion by introducing a high contrast of LVV in the shell. This model demonstrated that LVV and the thickness of the lithosphere could have a large effect on geoid anomalies if the mantle viscosity strongly increases with depth.

Yoshida (2004) considered 2-D convection models with self-consistently moving and subducting plates with LVV and found that the observed geoid anomaly on the Earth's surface is significantly affected by plate-tectonic mechanism as a first-order effect. However, 2-D Cartesian studies cannot describe the excitation of toroidal flow and its coupling with poloidal flow. Thus, the investigation of all dynamic effects arising from LVV requires the construction of mantle flow models in fully three-dimensional spherical geometry.

In the last years, various authors attempted to assess the sensitivity of the geoid to LVV (Richards and Hager (1989); Christensen and Harder (1991); Ribe (1992); Zhang and Christensen (1993); Čadek et al. (1993); Matrinec et al. (1993); King and Hager (1994); Forte and Peltier (1994); Karpychev and Fleitout (1996); Wen and Anderson (1997); Zhong and Davies (1999); Karpychev and Fleitout (2000); Zhong (2001); Čadek and Fleitout (2003, 2005); Niehuus and Schmeling (2005); Latychev et al. (2005); Kaban et al. (2007); Moucha et al. (2007)). Although the results obtained in these papers are somewhat ambiguous, there are indications that LVV may play an important role if boundary layers are taken into account (Karpychev and Fleitout (2000); Čadek and Fleitout (2003)). Most of these studies took into consideration only regional models of LVV located in the uppermost and lowermost mantle or oversimplified 3-D viscosity models of the whole mantle. The effect of the whole mantle LVV was investigated in Kaban et al. (2007) and Moucha et al. (2007). The conclusions based on the results of these two studies are somewhat controversial because Moucha et al. (2007) arrived at the conclusion that the effect of LVV on the geoid is negligible, whereas Kaban et al. (2007) demonstrated that some particular features of the geoid could be predicted only by inclusion of the LVV effect.

Ricard et al. (1988) investigated the effects of LVV in the shallow upper mantle, in which rigid plates were dynamically coupled with buoyancy-induced mantle flow. This and some other studies showed that, due to the complex rheology and boundaries of tectonic plates, large LVV in the lithosphere must be accounted for explicitly in mantle flow models (Ricard et al (1988); Ricard and Vigny (1989); Forte and Peltier (1994)) and in viscosity inversions (Forte and Mitrovica (2001); Mitrovica and Forte (2004)). These modeling studies demonstrated that the plates have a major effect on the convective flow and on the convection-related observables such as dynamic topography and non-hydrostatic geoid.

Koch and Ribe (1989) also investigated some general effects of LVV on the surface observables, analyzing various simplified models. They found that LVV have a large (up to 50%) effect if the load is relatively "hard" and shallow, whereas this effect is small (<15%) if the load is "soft" or deep. The geoid anomaly produced by a soft upwelling plume differs only slightly (by about 13%) from that generated by an isoviscous plume. By contrast, the viscosity differences associated with subducting slabs could have a larger effect on the geoid.

Christensen and Harder (1991) found only a weak toroidal component in models of thermal convection with temperature-dependent viscosity. Only in the cases of highly nonlinear rheology with a stress-exponent of harmonic degree 6 and a high-viscosity surface layer, was a moderate ratio of toroidal-to-poloidal component velocities of 0.25 obtained.

Zhang and Christensen (1993) proposed a hybrid finite-difference and spherical harmonic method that provides the possibility to estimate the effect of realistic LVV within the mantle. The nonlinear coupling of various spherical harmonic modes was calculated by an iterative method. They examined the effect for long wavelengths ( $l=1-6$ ) and found that, for such wavelengths, the effects of LVV on the geoid are smaller than those due to variations in the radial viscosity structure. However, they can also be significant for higher modes ( $l>3$ ) if the viscosity is radially stratified. On the other hand, it was found that the misfit between the observed and modelled geoids is not reduced by introducing LVV.

Forte and Peltier (1994) presented a quazi-analytical variational formulation of buoyancy-induced mantle flow in a heterogeneous spherical shell. They examined the effect of LVV on long-wavelength surface observables (geoid undulations and dynamic topography), which were expanded up to spherical harmonic degree

6, using a dynamic complete, theoretical formulation of mantle flow. They argued that the effects of LVV are likely to have been masked by the uncertainties in the tomography models available at the time.

Zhong and Davies (1999) applied spatial finite-element (FE) method combined with density anomalies derived from a subduction history model. They examined the joint effects of plate rheology and a subducting rigid lithosphere on the geoid and plate motions. They found that the plate rheology is significant and its inclusion yields a better geoid model and, moreover, reproduces the basic features of the observed field. According to their conclusions, the slab viscosity can strongly affect the geoid, depending on whether the slab is coupled with the surface. It is unclear, however, whether the change in the mean radial viscosity caused by assigning arbitrarily high viscosities to subducting slabs has a significant effect on the predicted geoid, and the most important effect on the geoid was not quantified.

Karpychev and Fleitout (2000) calculated the effects on the geoid for a model with LVV in the upper mantle. Beneath the ancient stable continental regions, the viscosity decreases monotonically from the surface to the depth of about 400-600 km. The oceanic lithosphere and tectonically active continental provinces are underlain by the low-viscosity asthenosphere. The viscosity of the lower mantle is assumed to be constant. Mantle flows are driven by preset surface velocities and density anomalies inferred from tomography models. They found that the geoid differences between the models with and without LVV reach 30%. Contrary to what was proposed in previous studies, spherical harmonics of degrees 2 and 3 are strongly affected by LVV. It is also important that shear stresses at plate bases are sensitive to LVV.

Richards et al. (2001) estimated the effect of LVV in the upper mantle on surface plate velocities. They demonstrated that the

combination of a pronounced low-viscosity zone and a plastic yield stress accounting for localized weakening of the cold thermal boundary layer results in a distinctly plate tectonic style of convection, with ~30% toroidal surface motion in the 3-D case.

Čadek and Fleitout (2003, 2005) investigated the effects of LVV in the upper 300 km of the mantle (Čadek and Fleitout (2003)) and core-mantle boundary region (Čadek and Fleitout (2006)), using the iterative technique of Zhang and Christensen (1993). In addition to the model of Karpychev and Fleitout (2000), they analysed the possible effect of partial layering of the mantle convection at the 670 km discontinuity. Considering all effects simultaneously, the authors were able to reduce significantly the misfit between the observed and modelled geoid: the partially layered model accounts for about 90% of the observed geoid at long wavelengths ( $l=2-8$ ). Čadek and Fleitout (2003) argued that LVV in the lithosphere are needed to fit the present-day geoid with a simple viscosity profile. Furthermore, they imposed prescribed plate velocities as a surface boundary condition, thereby invoking an external energy source that had to drive mantle flow independently of the buoyancy forces in the mantle. This approach lacks dynamic consistency and, therefore, it is difficult to assess the actual effect of shallow LVV. In their further investigation of the LVV in the core-mantle boundary region, Čadek and Fleitout (2006) determined large-scale features of the viscosity structure in the lowermost mantle that yielded a high density of hotspots above the regions of a higher-than-average viscosity. The global inverse search applied to models with LVV in the lowermost mantle improved the agreement between predicted and observed geoids up to about 95%, while models with only radial viscosity could account for no more than 78% of geoid. According to these studies, the consideration of LVV in the core-mantle boundary region improves the fit to the observed geoid much better than the inclusion of LVV in the lithosphere and asthenosphere. This inexplicable result can be due to a reduced (by about two orders) value of LVV that

was considered in the first models with lithosphere and asthenosphere LVV.

Moucha et al. (2007) examined the LVV implications for global convection related observables such as the horizontal surface divergence, dynamic geoid and topography, using forward modelling of buoyancy induced incompressible flow in a 3-D spherical shell (variational formulation suggested by Forte and Peltier (1994)). The 3-D viscosity distribution was derived from a rheological law expressed in terms of a homologous temperature in the mantle. The considered 3-D viscosity distribution spans about 2.5 orders of magnitude in the upper mantle (the tomography model of Grand et al. (1997)), and 3 orders of magnitude in the lower mantle (the tomography model of Su and Dziewonski (1997)). They found that the resulting dynamic topography, as well as the gravitational response of the Earth, is affected relatively weakly by the inclusion of LVV as compared with results for a purely radial viscosity model. In particular, they revealed that the effect of LVV on the global observables is significantly smaller than the variability due to uncertainties in the current seismic tomography models. They also quantified the effect of LVV in the context of the viscosity inverse problem, using radial viscosity models and a fully three-dimensional viscosity models in which the LVV contrast reaches three orders of magnitude, and found that the LVV have virtually no effect on their inversion results. Spatial FE method CITCOMs (Zhong et al. (2000)) was included into the study for benchmarking purposes. The comparison of spectral and FE methods revealed divergences of up to 8% in the calculated geoid figures and 4.5% in the surface dynamic topography.

Kaban et al. (2007) analysed the relative effect of LVV (with a maximum viscosity contrast of three orders of magnitude) in the upper and lower mantle on dynamic geoid undulations, dynamic topography and near-surface mantle velocities, using the spectral method in conjunction with the iterative method proposed by Zhang

and Christensen (1993). It was shown that the implementation of the whole-mantle 3-D viscosity variations based on the S20a seismic tomography model (Ekstrom and Dziewonski (1998)) apparently improves the model geoid, even without any additional tuning of model parameters. According to this study, geoid disturbances induced by the lower and upper mantle are of approximately the same significance (up to 40% of total geoid heights); however, the effect of the lower mantle is pronounced mainly on mid-range wavelengths. It was also found that the effects of the upper and lower mantle LVV on the geoid are nearly complementary with respect to the effect of the whole mantle LVV. In contrast to the geoid, the effects on dynamic topography induced by the upper mantle LVV were shown to be larger in amplitude than the effects due to the lower-mantle LVV. The effect of LVV on near-surface horizontal flow velocities was found to be very significant in particular with respect to the LVV-induced toroidal flow velocities.

New generation of FE and FV methods for global spherical modelling of mantle convection is a growing tendency of the present day. The heavy computational demands of the spectral approaches (required for the incorporation of the LVV effect of a high resolution) and the complications involved in the modelling of high lateral viscosity contrasts with the aid of spectral methods gave rise to the development of the powerful numerical methods based on FE and FV techniques. Therefore, numerical spectral methods are being gradually replaced by the generation of spatial methods that are mostly applied to the development of the Earth's interior on large time scales (Rykov and Trubitsyn (1996); Bunge et al. (1996, 1997); Trubitsyn and Rykov (1999, 2000, 2001); Zhong et al. (2000), Trubitsyn et al. (2007)). The latest versions of FE and FV methods provide the possibility to avoid the pole problems, which occur in latitude-longitude grids in spherical coordinates (Zhong et al. (2000); Stemmer et al. (2006)). Since the Earth's evolutionary processes are not concerned with the subject of this

work, I do not discuss in greater detail these methods. Moreover, these numerical methods can hardly produce an accurate geoid figure due to the complications associated with the introduction of mantle compressibility and self-gravitation effects; therefore, the studies based on these methods focus on mantle convection and the effects of post-glacial rebound and relative sea levels (Gasperini and Sabadini (1989, 1990); Gasperini et al. (1991); Zhong and Gurnis (1994); Bunge et al. (1996); Kaufmann and Wu (1998, 2002); Zhong et al. (2000); Letychev et al (2005); Kaufmann et al. (2005); Steffen et al. (2006); Wu et al. (2005); Paulson et al. (2005); Zhu and Feng (2005); Wu (2002, 2005, 2006); Wu and Wang (2006); Wang and Wu (2006); Stemmer et al. (2006)).

## Chapter II.

### *Internal loading theory and basic equations.*

It is generally accepted that the Earth's solid interior behaves like a fluid on geological time scales. In order to solve the problems with fluid mechanics, it is necessary to solve the applicable continuum partial differential equations (Bachelor, 1967). The distinguishing property of fluids is their ability to deform. On large time scales the solid rocks of the mantle deform as a fluid, thus, the behavior of the Earth's mantle can be described by the Navier-Stokes equations that contain the continuity equation (conservation of mass) and momentum equation (conservation of momentum). Sometimes the energy equation (conservation of energy) is also included to Navier-Stokes equation system.

The Navier-Stokes equations are the fundamental differential equations, which describe the motion of fluid substances (such as liquids and gases). These equations state that changes in momentum (acceleration) of fluid particles are only the product of changes in pressure and dissipative viscous forces acting inside the fluid. The viscous forces originate in molecular interaction and dictate how sticky a fluid is. Hence, the Navier-Stokes equations are a dynamical statement of balance of forces acting at any given region of the fluid, balance between inertial forces, pressure forces, viscous forces and the body force due to gravity.

#### **2.1 The Navier-Stokes and Poisson equations.**

The Navier-Stokes equations are derived from the basic principles of conservation of mass, momentum and energy.

1) The continuity equation for an infinitesimal volume element:

$$\frac{\partial \rho}{\partial t} + \frac{\partial(\rho u_i)}{\partial x_i} = 0 \quad (\text{E2.1a})$$

$$\frac{\partial u_i}{\partial x_i} = 0 \quad (\text{incompressible fluid}) \quad (\text{E2.1b})$$

where  $x_i$  is the position vector,  $t$  is time,  $\rho$  is the density of the fluid, and  $u_i$  is the fluid velocity.

2) The momentum equation on the elemental fluid parcel:

$$\rho \left( \frac{\partial u_i}{\partial t} + u_j \frac{\partial u_i}{\partial x_j} \right) = -\frac{\partial p}{\partial x_j} + \frac{\partial \tau_{ij}}{\partial x_j} + \rho g_i \quad (\text{E2.2})$$

where  $p$  is the fluid pressure,  $g_i$  is the acceleration of gravity,

$\tau_{ij}$  is deviator stress tensor (in terms of strain rate):

$$\tau_{ij} = 2\eta e_{ij} + \lambda e_{kk} \delta_{ij} = \eta \left( \frac{\partial u_i}{\partial x_j} + \frac{\partial u_j}{\partial x_i} \right) + \lambda e_{kk} \delta_{ij}$$

where  $e_{ij} = \frac{1}{2} \left( \frac{\partial u_i}{\partial x_j} + \frac{\partial u_j}{\partial x_i} \right)$  are the components of strain rate tensor of a

fluid (nonzero strain rates generate deviator stresses),  $\delta_{ij} = \begin{cases} 0, & i \neq j \\ 1, & i = j \end{cases}$

- Kronecker delta,  $\eta$  is the dynamic viscosity, and  $\lambda$  is the second viscosity.

In our study we neglect the bulk viscosity  $k_B = \lambda + \frac{2}{3}\eta$  (a measure of dissipation under compression) and take it to be zero. Then the The Navier-Stokes equation takes the form of:

$$\rho \left( \frac{\partial u_i}{\partial t} + u_j \frac{\partial u_i}{\partial x_j} \right) = -\frac{\partial p}{\partial x_j} + \frac{\partial}{\partial x_j} \left[ \eta \left( \frac{\partial u_i}{\partial x_j} + \frac{\partial u_j}{\partial x_i} - \frac{2}{3} \frac{\partial u_j}{\partial x_i} \delta_{ij} \right) \right] + \rho g_i \quad (\text{E2.2a})$$

$$\rho \left( \frac{\partial u_i}{\partial t} + u_j \frac{\partial u_i}{\partial x_j} \right) = -\frac{\partial p}{\partial x_j} + \frac{\partial}{\partial x_j} \left[ \eta \left( \frac{\partial u_i}{\partial x_j} + \frac{\partial u_j}{\partial x_i} \right) \right] + \rho g_i \quad (\text{incompressible flow}) \quad (\text{E2.2b})$$

3) The Poisson equation is the equation for the gravitational potential  $V$  that takes into account the changes in acceleration of gravity  $g_i$  due to the density perturbation of the flow:

$$\nabla^2 V = -4\pi G \rho \quad (\text{E2.3})$$

where  $\rho = \bar{\rho} + \delta\rho$  is the density distribution in the mantle,  $\bar{\rho}$  is the radial density profile,  $\delta\rho$  is the density anomaly,  $G$  is the universal gravitational constant.

4) The energy equation for an elemental parcel of fluid:

$$\rho T \left( \frac{\partial s}{\partial t} + u_i \frac{\partial s}{\partial x_i} \right) = \tau_{ij} \frac{\partial u_i}{\partial x_j} + \frac{\partial}{\partial x_i} \left( k \frac{\partial T}{\partial x_i} \right) + \rho H \quad (\text{E2.4})$$

where  $k$  is thermal conductivity,  $s$  is entropy per unit mass,  $H$  is the rate of internal heat production per mass unit, and  $T$  is the temperature.

For compressible and incompressible fluids the thermal energy equation can be rewritten in clearer form:

$$\rho c_p \left( \frac{\partial T}{\partial t} + u_i \frac{\partial T}{\partial x_i} \right) - \alpha T \left( \frac{\partial p}{\partial t} + u_i \frac{\partial p}{\partial x_i} \right) = \frac{\partial}{\partial x_i} \left( k \frac{\partial T}{\partial x_i} \right) + \Phi + \rho H \quad (\text{E2.4a})$$

$$\rho c_v \left( \frac{\partial T}{\partial t} + u_i \frac{\partial T}{\partial x_i} \right) = \frac{\partial}{\partial x_i} \left( k \frac{\partial T}{\partial x_i} \right) + \Phi + \rho H \quad (\text{incompressible fluid}) \quad (\text{E2.4b})$$

where  $\alpha = \frac{1}{v} \left( \frac{\partial v}{\partial T} \right)_p = -\frac{1}{\rho} \left( \frac{\partial \rho}{\partial T} \right)_p$  is the coefficient of thermal expansion

of material,  $v = \frac{1}{\rho}$  is specific volume,  $(*)_p$   $((*)_v)$  means that the

pressure (volume) is held fixed,  $c_p$  ( $c_v$ ) is the specific heat at

constant pressure (volume),  $\Phi = \tau_{ij} \frac{\partial u_i}{\partial x_j}$  is the viscous dissipation

function.

## 2.2 Equations in spherical coordinates

As the primary subject of this work is the in-depth study of the instantaneous state of the present-day Earth, the equation system describing this state may be distinctly simplified. The Navier-Stokes equations' adaptation to the specific conditions of the Earth's "fluid" mantle (very high viscosity and relatively small velocity values) results in the following changes in equations E2.1 (the continuity equation) and E2.2 (the momentum equation):

$$\frac{\partial u}{\partial t} \rightarrow 0 \quad \text{and} \quad \frac{\partial \rho}{\partial t} \rightarrow 0 \quad \Rightarrow$$

1) The continuity equation applied to the Earth's mantle:

$$\frac{\partial(\rho u_i)}{\partial x_i} = 0 \quad (\text{E2.5a})$$

$$\frac{\partial u_i}{\partial x_i} = 0 \quad (\text{incompressible fluid}) \quad (\text{E2.5b})$$

2) The momentum equation applied to the Earth's mantle:

$$\rho u_i \frac{\partial u_i}{\partial x_i} = -\frac{\partial p}{\partial x_i} + \frac{\partial}{\partial x_j} \left[ \eta \left( \frac{\partial u_i}{\partial x_j} + \frac{\partial u_j}{\partial x_i} - \frac{2}{3} \frac{\partial u_j}{\partial x_i} \delta_{ij} \right) \right] + \rho g_i \quad (\text{compressible flow}) \quad (\text{E2.6a})$$

$$\rho u_i \frac{\partial u_i}{\partial x_i} = -\frac{\partial p}{\partial x_i} + \frac{\partial}{\partial x_j} \left[ \eta \left( \frac{\partial u_i}{\partial x_j} + \frac{\partial u_j}{\partial x_i} \right) \right] + \rho g_i \quad (\text{incompressible flow}) \quad (\text{E2.6b})$$

The energy equation E2.4 makes no sense whilst studying the state of the instantaneous Earth, thus, this equation will not be included to the equation system into be discussed further.

In our study the Earth is represented as a spherical shell with some surface and core disturbances occurring due to the self-gravitational effect, which will be defined and analyzed in the following parts. For the spherically symmetric Earth of inner radius  $R_c$ , outer radius  $R_e$  with the density distribution  $\rho(r, \theta, \varphi) = \bar{\rho}(r) + \delta\rho(r, \theta, \varphi)$ , the force of gravity  $\bar{g} = \bar{g}(r)$ , stratified by radius, and the viscosity distribution  $\eta = \eta(r, \theta, \varphi)$  it is convenient to rewrite the Stokes equations E2.5 and E2.6 in spherical coordinates  $(r, \theta, \varphi)$ :

1) The continuity equation in spherical coordinates:

$$\frac{1}{r^2 \sin \theta} \left( \sin \theta \frac{\partial(r^2 \bar{\rho} u_r)}{\partial r} + r \frac{\partial(u_\theta \bar{\rho} \sin \theta)}{\partial \theta} + r \frac{\partial(\bar{\rho} u_\varphi)}{\partial \varphi} \right) = 0 \quad (\text{E2.7})$$

(for incompressible mantle  $\bar{\rho}$  is constant)

where  $u = (u_r, u_\theta, u_\varphi)$  is the mantle flow velocity.

2) The momentum equation in spherical coordinates:

$$0 = -\frac{\partial p}{\partial r} + \bar{\rho} \frac{\partial V}{\partial r} + \frac{1}{r^2} \frac{\partial(r^2 \tau_{rr})}{\partial r} + \frac{1}{r \sin \theta} \frac{\partial(\sin \theta \tau_{r\theta})}{\partial \theta} + \frac{1}{r \sin \theta} \frac{\partial \tau_{r\varphi}}{\partial \varphi} - \frac{1}{r} (\tau_{\theta\theta} + \tau_{\varphi\varphi}) - \delta \rho \bar{g} \quad (\text{E2.8a})$$

$$0 = -\frac{1}{r} \frac{\partial p}{\partial \theta} + \frac{\bar{\rho}}{r} \frac{\partial V}{\partial \theta} + \frac{1}{r^2} \frac{\partial(r^2 \tau_{r\theta})}{\partial r} + \frac{1}{r \sin \theta} \frac{\partial(\sin \theta \tau_{\theta\theta})}{\partial \theta} + \frac{1}{r \sin \theta} \frac{\partial \tau_{\theta\varphi}}{\partial \varphi} + \frac{1}{r} (\tau_{r\theta} - \tau_{\varphi\varphi} \text{ctg} \theta) \quad (\text{E2.8b})$$

$$0 = -\frac{1}{r \sin \theta} \frac{\partial p}{\partial \varphi} + \frac{\bar{\rho}}{r \sin \theta} \frac{\partial V}{\partial \varphi} + \frac{1}{r^2} \frac{\partial(r^2 \tau_{r\varphi})}{\partial r} + \frac{1}{r} \frac{\partial \tau_{\theta\varphi}}{\partial \theta} + \frac{1}{r \sin \theta} \frac{\partial \tau_{\varphi\varphi}}{\partial \varphi} + \frac{1}{r} (\tau_{r\varphi} + 2\tau_{\theta\varphi} \text{ctg} \theta) \quad (\text{E2.8c})$$

where  $\tau_{ij}$  is the viscous stress tensor concerned with  $u = (u_r, u_\theta, u_\varphi)$

and with components of the strain rate tensor  $e_{ij}$  by the following expressions:

$$\begin{aligned} \tau_{rr} &= 2\eta \frac{\partial u_r}{\partial r} - \frac{2}{3}\eta \left( \frac{1}{r^2} \frac{\partial(r^2 u_r)}{\partial r} + \frac{1}{r \sin \theta} \frac{\partial(u_\theta \sin \theta)}{\partial \theta} + \frac{1}{r \sin \theta} \frac{\partial(u_\varphi)}{\partial \varphi} \right) = 2\eta e_{rr} - \frac{2}{3}\eta (e_{rr} + e_{\theta\theta} + e_{\varphi\varphi}) \\ \tau_{\theta\theta} &= 2\eta \left( \frac{1}{r} \frac{\partial u_\theta}{\partial \theta} + \frac{u_r}{r} \right) - \frac{2}{3}\eta \left( \frac{1}{r^2} \frac{\partial(r^2 u_r)}{\partial r} + \frac{1}{r \sin \theta} \frac{\partial(u_\theta \sin \theta)}{\partial \theta} + \frac{1}{r \sin \theta} \frac{\partial(u_\varphi)}{\partial \varphi} \right) = 2\eta e_{\theta\theta} - \frac{2}{3}\eta (e_{rr} + e_{\theta\theta} + e_{\varphi\varphi}) \\ \tau_{\varphi\varphi} &= 2\eta \left( \frac{1}{r \sin \theta} \frac{\partial u_\varphi}{\partial \varphi} + \frac{u_r}{r} + \frac{u_\theta \text{ctg} \theta}{r} \right) - \frac{2}{3}\eta \left( \frac{1}{r^2} \frac{\partial(r^2 u_r)}{\partial r} + \frac{1}{r \sin \theta} \frac{\partial(u_\theta \sin \theta)}{\partial \theta} + \frac{1}{r \sin \theta} \frac{\partial(u_\varphi)}{\partial \varphi} \right) = \\ &= 2\eta e_{\varphi\varphi} - \frac{2}{3}\eta (e_{rr} + e_{\theta\theta} + e_{\varphi\varphi}) \\ \tau_{r\theta} &= \eta \left( \frac{1}{r} \frac{\partial u_r}{\partial \theta} + r \frac{\partial}{\partial r} \left( \frac{u_\theta}{r} \right) \right) = 2\eta e_{r\theta} \\ \tau_{r\varphi} &= \eta \left( \frac{1}{r \sin \theta} \frac{\partial u_r}{\partial \varphi} + r \frac{\partial}{\partial r} \left( \frac{u_\varphi}{r} \right) \right) = 2\eta e_{r\varphi} \\ \tau_{\theta\varphi} &= \eta \left( \frac{1}{r \sin \theta} \frac{\partial u_\theta}{\partial \varphi} + \frac{\sin \theta}{r} \frac{\partial}{\partial \theta} \left( \frac{u_\varphi}{\sin \theta} \right) \right) = 2\eta e_{\theta\varphi} \end{aligned} \quad (\text{E2.9})$$

The expressions of the relation between normal strains and flow velocities will be also often required in the following parts:

$$e_{rr} = \frac{\partial u_r}{\partial r}$$

$$\begin{aligned}
e_{\theta\theta} &= \frac{1}{r} \frac{\partial u_\theta}{\partial \theta} + \frac{u_r}{r} \\
e_{\varphi\varphi} &= \frac{1}{r \sin \theta} \frac{\partial u_\varphi}{\partial \varphi} + \frac{u_r}{r} + \frac{u_\theta \operatorname{ctg} \theta}{r} \\
e_{r\theta} &= \frac{1}{2} \left( \frac{1}{r} \frac{\partial u_r}{\partial \theta} + \frac{\partial u_\theta}{\partial r} - \frac{u_\theta}{r} \right) \\
e_{r\varphi} &= \frac{1}{2} \left( \frac{1}{r \sin \theta} \frac{\partial u_r}{\partial \varphi} + \frac{\partial u_\varphi}{\partial r} - \frac{u_\varphi}{r} \right) \\
e_{\theta\varphi} &= \frac{1}{2} \left( \frac{1}{r \sin \theta} \frac{\partial u_\theta}{\partial \varphi} + \frac{1}{r} \frac{\partial u_\varphi}{\partial \theta} - \frac{u_\varphi \operatorname{ctg} \theta}{r} \right)
\end{aligned} \tag{E2.10}$$

3) The Poisson equation (gravity field flux) in spherical coordinates:

$$\frac{\partial^2 V}{\partial r^2} + \frac{2}{r} \frac{\partial V}{\partial r} - \frac{L^2}{r^2} V = -4\pi G \rho \tag{E2.11}$$

$$\text{Where } L^2 = -\frac{1}{\sin \theta} \frac{\partial \left( \sin \theta \frac{\partial}{\partial \theta} \right)}{\partial \theta} - \frac{1}{\sin^2 \theta} \frac{\partial^2}{\partial \theta^2}$$

$V = V(r, \theta, \varphi)$  is the geopotential.

4) The total stress tensor:

It is convenient to turn to the other form of the viscous stress tensor  $\sigma_{ij}$  (total stress tensor):

$$\begin{aligned}
\sigma_{rr} &= -p + \tau_{rr} \\
\sigma_{\theta\theta} &= -p + \tau_{\theta\theta} \\
\sigma_{\varphi\varphi} &= -p + \tau_{\varphi\varphi}
\end{aligned} \tag{E2.12}$$

For the total stress tensor the Stokes equations take a simplified form:

$$0 = \frac{\partial \sigma_{rr}}{\partial r} + \frac{1}{r} \frac{\partial \tau_{r\theta}}{\partial \theta} + \frac{1}{r \sin \theta} \frac{\partial \tau_{r\varphi}}{\partial \varphi} + \frac{1}{r} (2\sigma_{rr} - \sigma_{\theta\theta} + \sigma_{\varphi\varphi} + \tau_{r\theta} \operatorname{ctg} \theta) + \bar{\rho} \frac{\partial V}{\partial r} - \delta \rho \bar{g} \tag{E2.13a}$$

$$0 = \frac{\partial \tau_{r\theta}}{\partial r} + \frac{1}{r} \frac{\partial \sigma_{\theta\theta}}{\partial \theta} + \frac{1}{r \sin \theta} \frac{\partial \tau_{\theta\varphi}}{\partial \varphi} + \frac{1}{r} (\sigma_{\theta\theta} \operatorname{ctg} \theta - \sigma_{\varphi\varphi} \operatorname{ctg} \theta + 3\tau_{r\theta}) + \frac{\bar{\rho}}{r} \frac{\partial V}{\partial \theta} \tag{E2.13b}$$

$$0 = \frac{\partial \tau_{r\varphi}}{\partial r} + \frac{1}{r} \frac{\partial \tau_{\theta\varphi}}{\partial \theta} + \frac{1}{r \sin \theta} \frac{\partial \sigma_{\varphi\varphi}}{\partial \varphi} + \frac{1}{r} (3\tau_{r\varphi} + 2\tau_{\theta\varphi} \operatorname{ctg} \theta) + \frac{\bar{\rho}}{r \sin \theta} \frac{\partial V}{\partial \varphi} \tag{E2.13c}$$

## Chapter III

### *Direct method for solving the Stokes equation in spherical harmonics*

Spherical geometry is of obvious relevance to our study of the mantle convection. Therefore, it is of great importance to consider the representation of the continuity, momentum and Poisson equations in spherical harmonics and the novel advantageous method of their solution.

#### 3.1 Spherical harmonic method.

The initial (solenoidal) vector field  $U$  has three components  $U = (U_r(r, \theta, \varphi), U_\theta(r, \theta, \varphi), U_\varphi(r, \theta, \varphi))$  given in spherical coordinates  $(r, \theta, \varphi)$ . The solenoidal vector field  $U = (U_r, U_\theta, U_\varphi) = U_r e_r + U_\theta e_\theta + U_\varphi e_\varphi$  can be represented as a sum of two independent vector fields: spheroidal (S) and toroidal (T)  $U = S + T$ . In this case the radial component  $U_r$  can be represented by a complete set of spherical functions  $Y_{lm}(\theta, \varphi)$ , lateral components  $U_\theta$  and  $U_\varphi$  - by a combination of spherical functions' derivatives  $Y_{lm}^\theta(\theta, \varphi)$  and  $Y_{lm}^\varphi(\theta, \varphi)$ . The radial component  $U_r$  of the spheroidal vector field S correlates with lateral components  $U_\theta$  and  $U_\varphi$  by a differential equation.

1) Spherical functions:

Spherical functions known as spherical harmonics

$$Y_{lm}(\theta, \varphi) = \begin{cases} N_{lm} P_l^m(\cos \theta) \cos m\varphi, i = 1 \\ N_{lm} P_l^m(\cos \theta) \sin m\varphi, i = 2 \end{cases} \quad (\text{E3.1})$$

Where  $l$  ( $m$ ) is the spherical harmonic degree (order):  $l \geq 0$

( $0 \leq m \leq l$ )

$$P_l^m(\cos \theta) = (\sin \theta)^m \frac{d^m P_l(\cos \theta)}{d(\cos \theta)^m} \quad (\text{E3.2})$$

are associated Legendre functions defined in terms of the Legendre

$$\text{polynomials: } P_l(\cos\theta) = P_l^0(\cos\theta) = \frac{1}{2^l l!} \frac{d^l[(\cos^2\theta - 1)^l]}{d(\cos\theta)^l}$$

$N_{lm} = \sqrt{\frac{(2 - \delta_{m0})(2l+1)(l-m)!}{(l+m)!}}$  are normalization coefficients for the associated Legendre functions.

Every function  $f(r, \theta, \varphi)$  on a sphere can be expanded into spherical functions' series according to:

$$f(r, \theta, \varphi) = \sum_{l=0}^{\infty} \sum_{m=0}^l \sum_{i=1}^2 (f_{lmi}(r) * Y_{lmi}(\theta, \varphi)) \quad (\text{E3.3a})$$

$$f_{lmi}(r) = \frac{1}{s_{m0}} \int_0^{2\pi} d\varphi \int_0^{\pi} f(r, \theta, \varphi) Y_{lmi}(\theta, \varphi) \sin\theta d\theta \quad (\text{E3.3b})$$

2) Orthonormalization law for spherical functions:

$$\int_0^{\pi} P_l(\cos\theta) P_{l'}(\cos\theta) \sin\theta d\theta = \frac{2}{2l+1} \delta_{ll'} \quad (\text{E3.4a})$$

$$\int_0^{\pi} P_l^m(\cos\theta) P_{l'}^{m'}(\cos\theta) \sin\theta d\theta = \frac{2(l+m)!}{(2l+1)(l-m)!} \delta_{ll'} \delta_{mm'} \quad (\text{E3.4b})$$

For zonal harmonics ( $m=0$ ):  $\int_0^{2\pi} d\varphi = 2\pi$  &  $2 - \delta_{m0} = 1$  & E3.4b =>

$$\int_0^{2\pi} d\varphi \int_0^{\pi} Y_{lmi}(\theta, \varphi) Y_{l'm'i'}(\theta, \varphi) \sin\theta d\theta = 4\pi \delta_{ll'} \delta_{mm'} \delta_{ii'} = s_{m0} \delta_{ll'} \delta_{mm'} \delta_{ii'} \quad (\text{E3.5a})$$

For tesseral ( $0 < m < l$ ) and sectoral ( $m=l$ ) harmonics:

$$\int_0^{2\pi} \cos^2(m\varphi) d\varphi = \int_0^{2\pi} \sin^2(m\varphi) d\varphi = \pi \quad \& \quad 2 - \delta_{m0} = 2 \quad \& \quad \text{E3.4b} \Rightarrow$$

$$\int_0^{2\pi} d\varphi \int_0^{\pi} Y_{lmi}(\theta, \varphi) Y_{l'm'i'}(\theta, \varphi) \sin\theta d\theta = 4\pi \delta_{ll'} \delta_{mm'} \delta_{ii'} = s_{m0} \delta_{ll'} \delta_{mm'} \delta_{ii'} \quad (\text{E3.5b})$$

$$\text{E3.5a} + \text{E3.5b} \Rightarrow s_{m0} = 4\pi, \quad \forall m \leq l$$

3) Spherical functions' derivatives  $Y_{lm}^{\theta}(\theta, \varphi)$  and  $Y_{lm}^{\varphi}(\theta, \varphi)$ :

$$Y_{lm}^{\theta}(\theta, \varphi) = \frac{\partial Y_{lm}(\theta, \varphi)}{\partial \theta}$$

$$Y_{lm}^{\varphi}(\theta, \varphi) = \frac{1}{\sin \theta} \frac{\partial Y_{lm}(\theta, \varphi)}{\partial \varphi}$$

Functions  $f_1(r, \theta, \varphi)$  and  $f_2(r, \theta, \varphi)$  can be expanded into series of spherical functions' derivatives according to:

$$f_1(r, \theta, \varphi) = \sum_{l=0}^{\infty} \sum_{m=0}^l \sum_{i=1}^2 (a_{lmi}(r) * Y_{lmi}^{\theta}(\theta, \varphi) + b_{lmi}(r) * Y_{lmi}^{\varphi}(\theta, \varphi)) \quad (\text{E3.6a})$$

$$f_2(r, \theta, \varphi) = \sum_{l=0}^{\infty} \sum_{m=0}^l \sum_{i=1}^2 (a_{lmi}(r) * Y_{lmi}^{\varphi}(\theta, \varphi) - b_{lmi}(r) * Y_{lmi}^{\theta}(\theta, \varphi)) \quad (\text{E3.6b})$$

$$a_{lmi}(r) = \frac{1}{s_{lm}} \int_0^{2\pi} d\varphi \int_0^{\pi} (f_1(r, \theta, \varphi) Y_{lmi}^{\theta}(\theta, \varphi) + f_2(r, \theta, \varphi) Y_{lmi}^{\varphi}(\theta, \varphi)) \sin \theta d\theta \quad (\text{E3.6c})$$

$$b_{lmi}(r) = \frac{1}{s_{lm}} \int_0^{2\pi} d\varphi \int_0^{\pi} (f_1(r, \theta, \varphi) Y_{lmi}^{\varphi}(\theta, \varphi) - f_2(r, \theta, \varphi) Y_{lmi}^{\theta}(\theta, \varphi)) \sin \theta d\theta \quad (\text{E3.6d})$$

From the point of view of physics this expansion represents a sum of two vector fields: spheroidal S (poloidal for incompressible case) and toroidal T.

In the next chapters and the Appendix, describing the derivation of the final equations, some knowledge of spherical harmonics and their properties will be demanded. Hence, it is of some use to refresh a set of expressions for spherical functions' derivatives for the sake of following the thread of further reasoning.

The spherical function  $Y_{lm}(\theta, \varphi)$  is the solution of Laplace's equation:

$$L^2 Y_{lm}(\theta, \varphi) = L Y_{lm}(\theta, \varphi) \quad (\text{E3.7})$$

$$L Y_{lm}(\theta, \varphi) = -\frac{1}{\sin \theta} \frac{\partial(\sin \theta Y^{\theta})}{\partial \theta} - \frac{1}{\sin^2 \theta} \frac{\partial^2 Y}{\partial \varphi^2} = -Y^{\theta\theta} - \text{ctg} \theta Y^{\theta} - Y^{\varphi\varphi} \Rightarrow$$

$$Y^{\theta\theta} + \text{ctg} \theta Y^{\theta} + Y^{\varphi\varphi} = -L Y \quad (\text{E3.7a})$$

$$Y^{\varphi\theta} + \text{ctg} \theta Y^{\varphi} - Y^{\theta\varphi} = 0 \quad (\text{E3.7b})$$

$$Y^{\varphi\varphi\theta} + 2 \text{ctg} \theta Y^{\varphi\varphi} - Y^{\theta\varphi\varphi} = 0 \quad (\text{E3.7c})$$

$$Y^{\theta\theta\theta} + \text{ctg} \theta Y^{\theta\theta} - Y^{\theta} - \text{ctg}^2 \theta Y^{\theta} - 2 \text{ctg} \theta Y^{\varphi\varphi} + Y^{\theta\varphi\varphi} = -L Y^{\theta} \quad (\text{E3.7d})$$

where  $L \equiv l(l+1)$ ,  $Y^\theta \equiv Y_{lm}^\theta(\theta, \varphi)$ ,  $Y^\varphi \equiv Y_{lm}^\varphi(\theta, \varphi)$ ,  $Y^{\theta\theta} = Y_{\theta\theta} = \frac{\partial^2 Y}{\partial \theta^2}$ ,  $Y^{\varphi\varphi} = \frac{1}{\sin^2 \theta} \frac{\partial^2 Y}{\partial \varphi^2}$ ,

$$Y^{\theta\varphi} = \frac{1}{\sin \theta} \frac{\partial \left( \frac{\partial Y}{\partial \theta} \right)}{\partial \varphi}, \quad Y^{\varphi\theta} = \frac{\partial \left( \frac{1}{\sin \theta} \frac{\partial Y}{\partial \varphi} \right)}{\partial \theta}$$

4) Orthonormalization law for spherical functions' derivatives:

$$\int_0^{2\pi} d\varphi \int_0^\pi Y_{l'm'i'}^\theta(\theta, \varphi) Y_{lmi}^\varphi(\theta, \varphi) \sin \theta d\theta - \int_0^{2\pi} d\varphi \int_0^\pi Y_{l'm'i'}^\varphi(\theta, \varphi) Y_{lmi}^\theta(\theta, \varphi) \sin \theta d\theta = 0 \quad (\text{E3.8a})$$

$$\int_0^{2\pi} d\varphi \int_0^\pi Y_{l'm'i'}^\theta(\theta, \varphi) Y_{lmi}^\theta(\theta, \varphi) \sin \theta d\theta - \int_0^{2\pi} d\varphi \int_0^\pi Y_{l'm'i'}^\varphi(\theta, \varphi) Y_{lmi}^\varphi(\theta, \varphi) \sin \theta d\theta = 4\pi l(l+1) \delta_{ll'} \delta_{mm'} \delta_{ii'} \quad (\text{E3.8b})$$

Integration by parts:

$$\int_0^{2\pi} d\varphi \int_0^\pi Y_{l'm'i'}^\theta(\theta, \varphi) Y_{lmi}^\theta(\theta, \varphi) \sin \theta d\theta - \int_0^{2\pi} d\varphi \int_0^\pi Y_{l'm'i'}^\varphi(\theta, \varphi) Y_{lmi}^\varphi(\theta, \varphi) \sin \theta d\theta =$$

$$\text{First integral: } \begin{cases} v = Y_{lmi}^\theta \sin \theta \\ du = Y_{l'm'i'}^\theta d\theta \end{cases} \Rightarrow \begin{cases} dv = (Y_{lmi}^{\theta\theta} \sin \theta + Y_{lmi}^\theta \cos \theta) d\theta \\ u = Y_{l'm'i'}^\theta \end{cases}$$

$$\text{Second integral: } \begin{cases} v = Y_{lmi}^\varphi \\ du = Y_{l'm'i'}^\varphi d\varphi \end{cases} \Rightarrow \begin{cases} dv = \sin \theta Y_{lmi}^{\varphi\varphi} d\varphi \\ u = \frac{1}{\sin \theta} Y_{l'm'i'}^\varphi \end{cases}$$

$$\begin{aligned} &= \int_0^{2\pi} d\varphi \left( Y_{l'm'i'}^\theta Y_{lmi}^\theta \sin \theta \Big|_0^\pi - \int_0^\pi Y_{l'm'i'}^\theta (Y_{lmi}^\theta \cos \theta + Y_{lmi}^{\theta\theta} \sin \theta) d\theta \right) + \int_0^\pi \left( \frac{1}{\sin \theta} Y_{l'm'i'}^\varphi Y_{lmi}^\varphi \Big|_0^{2\pi} - \int_0^{2\pi} Y_{l'm'i'}^\varphi Y_{lmi}^{\varphi\varphi} d\varphi \right) \sin \theta d\theta = \\ &= \int_0^{2\pi} d\varphi \left( - \int_0^\pi Y_{l'm'i'}^\theta (Y_{lmi}^\theta \cos \theta + Y_{lmi}^{\theta\theta} \sin \theta) d\theta \right) + \int_0^\pi \left( - \int_0^{2\pi} Y_{l'm'i'}^\varphi Y_{lmi}^{\varphi\varphi} d\varphi \right) \sin \theta d\theta = \\ &= - \int_0^{2\pi} d\varphi \int_0^\pi Y_{l'm'i'}^\theta (Y_{lmi}^\theta \cos \theta + Y_{lmi}^{\theta\theta} \sin \theta + Y_{lmi}^{\varphi\varphi} \sin \theta) d\theta = - \int_0^{2\pi} d\varphi \int_0^\pi Y_{l'm'i'}^\theta (Y_{lmi}^\theta \text{ctg} \theta + Y_{lmi}^{\theta\theta} + Y_{lmi}^{\varphi\varphi}) \sin \theta d\theta = \\ &= \{ \text{E3.5a} \} = - \int_0^{2\pi} d\varphi \int_0^\pi Y_{l'm'i'}^\theta (-LY_{lmi}) \sin \theta d\theta = L \int_0^{2\pi} d\varphi \int_0^\pi Y_{l'm'i'}^\theta Y_{lmi} \sin \theta d\theta = 4\pi l(l+1) \delta_{ll'} \delta_{mm'} \delta_{ii'} = \\ &= s_{m0} l(l+1) \delta_{ll'} \delta_{mm'} \delta_{ii'} \end{aligned}$$

$$s_{ml} = 4\pi l(l+1) = s_{m0} l(l+1), \quad \forall m \leq l \quad (\text{E3.8c})$$

### 3.2 The Stokes equation in spherical harmonics.

At first I will consider only the simplified case of a radial viscosity distribution  $\eta = \bar{\eta}(r)$  because an introduction of LVV leads

to some complications (see Chapter V). The Stokes equations (in a spherical shell) can be represented in spherical harmonics by expansions of velocities  $u=(u_r, u_\theta, u_\varphi)$ , total stresses  $\sigma_{ij}$ , density anomalies  $\delta\rho(r, \theta, \varphi)$ , pressure  $p(r, \theta, \varphi)$  and gravitational potential  $V(r, \theta, \varphi)$ .

Expanding the function of density anomalies into spherical harmonic series:

$$\delta\rho(r, \theta, \varphi) = \sum_{l,m} \delta\rho^{lm}(r) Y_{lm}(\theta, \varphi) \quad (\text{E3.9a})$$

We shall search for a solution of the Stokes equations E2.7 + E2.13 and the Poisson equation E2.11 for potential V, pressure p, radial components of vector field of velocities u and total stresses  $\sigma_{ij}$  also in the form of spherical harmonic expansions:

$$V(r, \theta, \varphi) = \sum_{l,m} U_5^{lm}(r) Y_{lm}(\theta, \varphi) \quad (\text{E3.9b})$$

$$p(r, \theta, \varphi) = \sum_{l,m} p_{lm}(r) Y_{lm}(\theta, \varphi) \quad (\text{E3.9c})$$

$$u_r(r, \theta, \varphi) = \sum_{l,m} U_1^{lm}(r) Y_{lm}(\theta, \varphi) \quad (\text{E3.9d})$$

$$\sigma_{rr}(r, \theta, \varphi) = \frac{1}{r} \sum_{l,m} U_3^{lm}(r) Y_{lm}(\theta, \varphi) \quad (\text{E3.9e})$$

The solutions for lateral components of velocity  $u_\theta$ ,  $u_\varphi$  and stress  $\tau_{r\theta}$ ,  $\tau_{r\varphi}$  can be found in the form of expansions into series of

spherical functions' derivatives  $Y_{lm}^\theta = \frac{\partial Y_{lm}}{\partial \theta}$  and  $Y_{lm}^\varphi = \frac{1}{\sin \theta} \frac{\partial Y_{lm}}{\partial \varphi}$  (toroidal

part appears only due to LVV):

$$u_\theta(r, \theta, \varphi) = \sum_{l,m} U_2^{lm}(r) Y_{lm}^\theta(\theta, \varphi) \quad (\text{E3.9f})$$

$$u_\varphi(r, \theta, \varphi) = \sum_{l,m} U_2^{lm}(r) Y_{lm}^\varphi(\theta, \varphi) \quad (\text{E3.9g})$$

$$\tau_{r\theta}(r, \theta, \varphi) = \frac{1}{r} \sum_{l,m} U_4^{lm}(r) Y_{lm}^\theta(\theta, \varphi) \quad (\text{E3.9h})$$

$$\tau_{r\varphi}(r, \theta, \varphi) = \frac{1}{r} \sum_{l,m} U_4^{lm}(r) Y_{lm}^\varphi(\theta, \varphi) \quad (\text{E3.9i})$$

where r is the relative radius.

Substituting expansions E3.9d, E3.9f and E3.9g of radial and lateral components of the velocity  $u_r(r,\theta,\varphi)$ ,  $u_\theta(r,\theta,\varphi)$  and  $u_\varphi(r,\theta,\varphi)$  to expressions E2.9 and E2.12 we obtain the remaining components of the total stress tensor  $\sigma_{ij}$ :

$$\sigma_{\theta\theta}(r,\theta,\varphi) = \sum_{l,m} \left( -pY_{lm} + \frac{2\eta^*}{r} (U_1(r)Y + U_2(r)Y_{lm}^{\theta\theta}) \right) \quad (\text{E3.9j})$$

$$\sigma_{\varphi\varphi}(r,\theta,\varphi) = \sum_{l,m} \left( -pY_{lm} + \frac{2\eta^*}{r} (U_1(r)Y + U_2(r)(Y_{lm}^{\varphi\varphi} + Y_{lm}^\theta \text{ctg}\theta)) \right) \quad (\text{E3.9k})$$

$$\tau_{\theta\varphi}(r,\theta,\varphi) = \frac{2\eta^*}{r} \sum_{l,m} (U_2(r)(Y_{lm}^{\theta\varphi} - Y_{lm}^\varphi \text{ctg}\theta)) \quad (\text{E3.9l})$$

where  $\eta^*(r) = \frac{\bar{\eta}(r)}{\eta_0}$  is the dimensionless radial viscosity function and

$\eta_0$  is the mean mantle viscosity.

Taking into consideration all derived expansions E3.9 and substituting them into the Stokes equations E2.7 and E2.13 and the Poisson equation E2.11 we arrive at an equation system of first-order ordinary differential equations:

$$\begin{aligned} r \frac{dU_1^{lm}}{dr} &= -(2+k)U_1^{lm} + LU_2^{lm} \\ r \frac{dU_2^{lm}}{dr} &= -U_1^{lm} + U_2^{lm} + \frac{1}{\eta^*} U_4^{lm} \\ r \frac{dU_3^{lm}}{dr} &= (12+4k)\eta^* U_1^{lm} - 6L\eta^* U_2^{lm} + U_3^{lm} + LU_4^{lm} - \rho^* U_6^{lm} + \delta\rho^{lm} g^* r^2 \\ r \frac{dU_4^{lm}}{dr} &= -(6+2k)\eta^* U_1^{lm} - 2(2L-1)\eta^* U_2^{lm} - U_3^{lm} - 2U_4^{lm} - \rho^* U_5^{lm} \\ r \frac{dU_5^{lm}}{dr} &= U_5^{lm} + U_6^{lm} \\ r \frac{dU_6^{lm}}{dr} &= LU_5^{lm} - 4\pi\gamma\delta\rho^{lm} r^3 \end{aligned} \quad (\text{E3.10})$$

where  $\rho^*(r) = \frac{\bar{\rho}(r)}{\rho_0}$   $\left( g^*(r) = \frac{\bar{g}(r)}{g_0} \right)$  is the dimensionless radial density

(acceleration of gravity) function,  $\rho_0$  ( $g_0$ ) is the mean mantle

density (acceleration of gravity on the Earth surface) and

$k(r) = \frac{d \ln \rho^*(r)}{d \ln r}$  is the mantle compressibility.

Boundary conditions:

$$U_1(r_e) = U_1(r_c) = 0$$

$$U_4(r_e) = U_4(r_c) = 0 \quad (\text{free-slip condition})$$

$$\begin{cases} U_4(r_c) = 0 \\ U_2(r_e) = U_{obs} \end{cases} \quad (\text{no-slip condition}) \quad (\text{E3.11})$$

$$U_6(r_e) = -(l+1)U_5(r_e) - \frac{4\pi\gamma_e \rho^*(r_e)}{g^*(r_e)} U_3(r_e)$$

$$U_6(r_c) = (l-3)U_5(r_c) - \frac{4\pi\gamma_c \rho^*(r_c)}{g^*(r_c)} U_3(r_c)$$

where  $r_e$  and  $r_c$  are the relative values of the radius on the surface of the Earth and the core, correspondingly.

The ODE system of the sixth order (Stokes + Poisson) must be solved for each harmonic mode ( $l$  (degree),  $m$  (order),  $i$  (qualifier of spherical function)).

### 3.3 Direct method for solving the Stokes equation.

In case of only radial viscosity variant, the Stokes equations (continuity and momentum) together with Poisson's equation (gravity field flux) including effects of compressibility, self-gravitation and depth-dependent gravity can be solved by a direct method of solving the ODE system for each spherical harmonic mode. Thus, applying the direct method of Godunov (Godunov, 1961) to the ODE system E3.10 for each couple of harmonic order  $m$  and degree

$l \leq l_{\max}$  :

$$y' = A(r)y + f(r) \quad (\text{E3.12})$$

$$\text{where } A(r) = \begin{pmatrix} -2-k & L & 0 & 0 & 0 & 0 \\ -1 & 1 & 0 & \frac{1}{\eta^*} & 0 & 0 \\ (12+4k)\eta^* & -6L\eta^* & 1 & L & 0 & -\rho^* \\ -(6+2k)\eta^* & 2(2L-1)\eta^* & -1 & -2 & -\rho^* & 0 \\ 0 & 0 & 0 & 0 & 1 & 1 \\ 0 & 0 & 0 & 0 & L & 0 \end{pmatrix} \text{ and}$$

$$f(r) = (0, 0, \delta\rho^{lm} g^* r^2, 0, 0, -4\pi\gamma\delta\rho^{lm} r^3)^T$$

with boundary conditions E3.11:

$$By(r_c) = b \quad (\text{on the boundary between core and mantle}) \quad (\text{E3.13})$$

$$Cy(r_e) = c \quad (\text{on the surface of the Earth}),$$

$$\text{where } B = \begin{pmatrix} 1 & 0 & 0 & 0 & 0 & 0 \\ 0 & 0 & 0 & 1 & 0 & 0 \\ 0 & 0 & \frac{4\pi r_c \rho^*(r_c)}{g^*(r_c)} & 0 & -(l-3) & 1 \end{pmatrix} \text{ and } b = \begin{pmatrix} 0 \\ 0 \\ 0 \end{pmatrix} \quad (\text{E3.14a})$$

$$C = \begin{pmatrix} 1 & 0 & 0 & 0 & 0 & 0 \\ 0 & 0 & 0 & 1 & 0 & 0 \\ 0 & 0 & \frac{4\pi r_e \rho^*(r_e)}{g^*(r_e)} & 0 & l+1 & 1 \end{pmatrix} \text{ and } c = \begin{pmatrix} 0 \\ 0 \\ 0 \end{pmatrix} \quad (\text{E3.14b})$$

in the range  $r_c \leq r \leq r_e$  of the relative radius values.

The main objective of the direct Godunov method is that the preceding ODE system comes down to the Cauchy problem, which can be solved by any of the well-known methods (e.g. Runge-Kutta method). For this purpose we must redefine some missing boundary conditions on one of the boundaries (on the surface or core-mantle boundary). Therefore, three boundary conditions from the core boundary  $r_c$  from the range  $[r_c, r_e]$  are imaginary shifted to the surface boundary. Hence, the missing boundary conditions get determined on the surface and, as a result, our problem turns into the ordinary Cauchy problem, which can be solved for every value of relative radius  $r \in [r_c, r_e]$ .

In the first stage the fundamental system of solutions of the homogeneous equation system  $By=0$  must be built. As can be readily

appreciated, both boundary conditions (surface and core-mantle boundary) give us homogeneous systems E3.14a and E3.14b:

$$\begin{pmatrix} 1 & 0 & 0 & 0 & 0 & 0 \\ 0 & 0 & 0 & 1 & 0 & 0 \\ 0 & 0 & \frac{4\pi\gamma r_c \rho_0}{g_c} & 0 & -(l-3) & 1 \end{pmatrix} \begin{pmatrix} y_1 \\ y_2 \\ y_3 \\ y_4 \\ y_5 \\ y_6 \end{pmatrix} = 0 \quad (\text{E3.15})$$

Obviously, all the rows of matrix  $B$  are linearly independent, therefore, the rank of the matrix  $B$  is equal to 3 ( $|B|=3$ ). Hence, the number of solutions comprehended by the fundamental system of solutions of E3.15 is equal to the number of surface boundary conditions.

The fundamental system of solutions  $y^* = (y_1^*, y_2^*, y_3^*)$  of  $By=0$  can be easily found by Jordan's method of exclusion, for example. As readily observed,  $y_0 = (0,0,0,0,0,0)$  is the particular trivial solution of the heterogeneous system  $By=b$ .

In the second stage of Godunov's method three Cauchy problems in the following form:

$$y' = A(r)y \quad (\text{E3.16})$$

$$y(r_c) = y_i^*, i = 1, 2, 3$$

and one Cauchy problem in the form:

$$y' = A(r)y + f(r) \quad (\text{E3.17})$$

$$y(r_c) = y_0$$

must be solved.

In this way we can get the set of solutions  $y_1(r), \dots, y_k(r), y_0(r)$  for each value of radius  $r \in [r_c, r_e]$ . Taking into account the obtained sets of solutions  $y_1(r), \dots, y_k(r)$  of the homogeneous Cauchy problem E3.16 and the solution  $y_0(r)$  of the heterogeneous Cauchy problem E3.17 we can find the general solution:

$$y(r) = d_1 y_1(r) + \dots + d_k y_k(r) + y_0(r) \quad (\text{E3.18})$$

From the way the selection of the vectors  $y_1, \dots, y_k, y_0$  was done, it follows that the general solution satisfies the core-mantle boundary condition for any set of  $d_1, \dots, d_k$ . Thus, it is only necessary to find the values of coefficients  $d_1, \dots, d_k$ . The required coefficients can be found from the surface boundary condition E3.14a, E3.14b:

$$Cy_1(r_e)d_1 + \dots + Cy_k(r_e)d_k = c - Cy_0(r_e) \quad (\text{E3.19})$$

The values  $d_1, \dots, d_k$  can be obtained from the solution of the linear equation system E3.19.

## Chapter IV

### *Mantle compressibility and self-gravitation*

The comprehension of the effects of mantle compressibility and self-gravitation is of special importance in my study since the particular contribution of each of these effects to the mantle flow and geoid figure has been found extremely significant. An introduction of these effects in the new generation of the FE method is accompanied by a certain number of problems. A direct incorporation of self-gravitation and mantle compressibility effects into FD (finite-difference), FE and FV methods is impossible, consequently, we would have to fall back upon an iterative approach if using one of these methods. The grounds for the complications are concealed in the nature of the effects.

#### **4.1 Geoid and geoid undulations.**

Although the Earth is not flat or egg-shaped, as previously believed, neither is it precisely a sphere or even an ellipsoid. Mountains, ocean basins and variations in the crustal thickness contribute to the observed irregular shape and gravity field of the Earth, but they cannot explain the long-wavelength departures from a hydrostatic figure.

The geoid is the equipotential surface of constant potential energy, which coincides with the mean sea level in the oceanic regions if neglecting the dynamic perturbations. The geoid anomaly is the variation of the height of the geoid with respect to a reference model. There are two principally different reference models: one is used in geodesy (a mathematical model of the world called an ellipsoid), the other is used in geodynamics (a hydrostatic spheroid).

The geoid anomaly represents the effects of lateral density variations in the Earth. With the advent of the first seismic models of seismic tomography, it was noticed that long-wavelength

geoid lows correlate with seismically fast and therefore, presumably cold and heavy regions of the lower mantle, and vice versa, the highs of long-wavelength geoid correlate with seismically slow and light regions. This is the reverse of what would be expected in an undeformable Earth, where the geoid would exhibit a positive correlation with internal density anomalies. In order to calculate correctly the geoid due to mantle heterogeneities, it is essential to consider contributions of both, the internal density anomaly and the boundary deformations associated with flow induced by the anomaly.

For the spherically symmetric rotating Earth (simplification applied for the global modeling) the geoid shape can be derived from the Bruns formula (Heiskanen and Moritz, 1967)  $\delta r = \frac{\delta V}{g}$ , where  $g$  is the theoretical gravity on the surface of the spherical Earth,  $\delta V$  is the angular-dependent component of the gravitational potential and  $\delta r$  is the departure of the geoid from a sphere. In general and in practice the geoid undulations are denoted by  $N$ . They represent the departure from an ellipsoid and can be calculated by the Stokes formula.

The most recent gravity field combination models, for example model EIGEN-GL04C (a combination from the GRACE and LAGEOS mission results plus  $0.5^\circ \times 0.5^\circ$  gravimetry and altimetry surface data) developed by GFZ Potsdam and GRGS Toulouse, possess very fine resolution (Flechhtner et al. (2007); Förste et al. (2007)). EIGEN-GL04C is complete to degree and order 360 in terms of spherical harmonic coefficients and thus, resolves geoid and gravity anomaly wavelengths of 110 km. Such a fine resolution is surely not required in the global modeling because, at present, we are not able to predict the geoid with such accuracy due to a lack of precision in seismic tomography data. Solving an inverse problem (Chapter VI) in order to obtain the best fit of the calculated geoid to the observed geoid, we use the above-mentioned

gravity field combination model only up to spherical harmonic degree 20 in the least-square adjustment.

The long-wavelength features of the dynamic geoid contain the gravitational signal from deep-seated lateral mass and density inhomogeneities sustained by dynamic Earth mantle processes. To interpret the observed geoid with respect to mantle dynamics and structures, it is essential first to remove the lithosphere-induced anomalous gravitational potential, which is generated by the topographic surface load and its isostatically compensating masses. Based upon the most recent global compilation of crustal thickness and density data and the age distribution of cooling oceanic lithosphere, residual topography and gravity are calculated by subtracting the "known" crustal and oceanic lithosphere compensating masses and gravitational effects from the surface fields (Kaban et al., 1999, 2004). The resulting isostatic model of the lithosphere is supposed to be valid for spatial wavelengths longer than 500 km. The isostatic lithosphere model field, expressed in terms of geoid heights, is subtracted from a satellite-derived long-wavelength geoid to yield the isostatic residual geoid (F4.1). Applying the isostatic correction, the overall pattern of the geoid becomes smoother and the most pronounced features, which are separated in the observed geoid, tend to get connected to larger structures.

In the active tectonic areas the isostatic geoid reduction ranges from -18 to +43 m. The maximum value is reached in Tibet, while the large negative values mostly extend over 'old' ocean areas with a deep ocean floor. The difference in an isostatic reduction of 20 m between the oceanic ridges and the old ocean purely reflects the isostatic balance of the oceanic lithosphere.

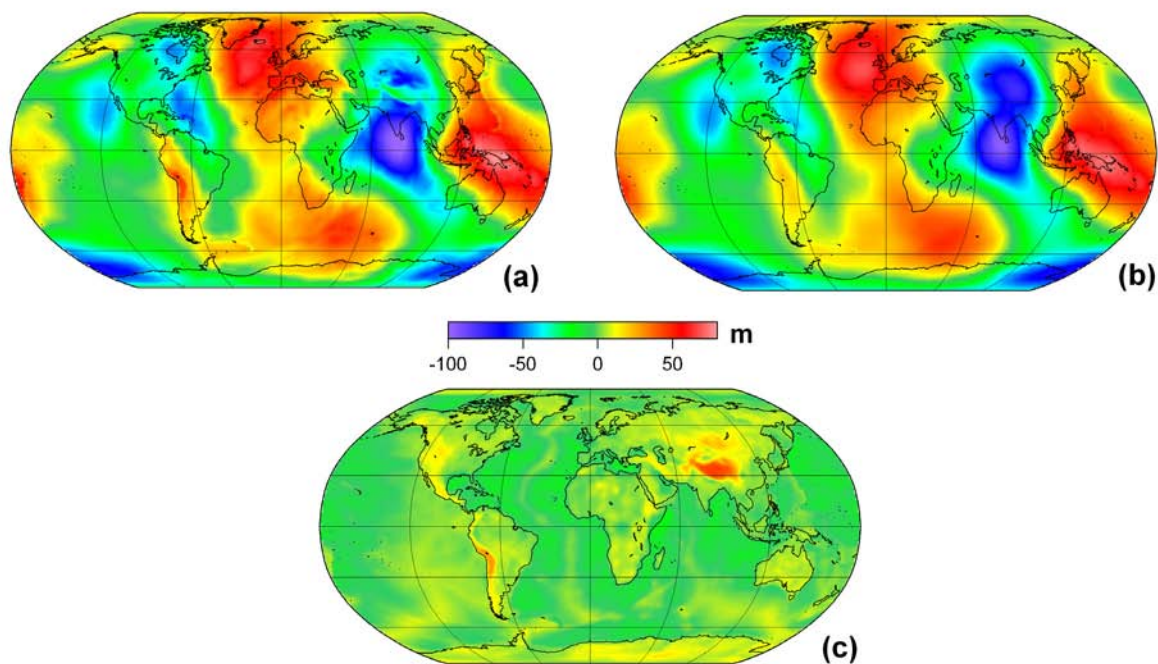


Figure (F4.1) Isostatic reduction of the geoid (Kaban et al., 2004).

- (a) Geoid (from the spherical harmonic global geopotential model to degree and order 180).
- (b) Isostatic geoid anomaly.
- (c) The geoid effect of the isostatically compensated lithospheric model.

In this study we investigate the effect of LVV on the non-isostatic geoid, which does not comprise the terms  $C_{20}$  and  $C_{40}$ . The origin of these terms in the observed geoid relative to a hydrostatic spheroid is not completely comprehended, yet (Nakiboglu, 1982; Mound et al., 2003). Furthermore, the terms  $C_{20}$  and  $C_{40}$  dominate in the observed non-hydrostatic geoid, their globally estimated root mean square (RMS) is equal to 28.5 m, which is almost identical to the RMS of the other terms (31.8 m). The modeling of the terms  $C_{20}$  and  $C_{40}$  requires precise knowledge of seismic velocity anomalies in the polar areas, which are not sufficiently resolved in the existing global tomography models, therefore, their amplitudes might be significantly reduced due to damping.

## 4.2 Mantle compressibility and self-gravitation.

Here I summarize two special physical effects (mantle compressibility and self-gravitation) that give mantle convection its unique character.

### 1) *Mantle compressibility:*

Compressibility affects convection through the complex interplay of a number of material properties and the distribution of heat sources. Compressibility enters into the flow problem directly, through the system of equations governing flow (E3.12) in three fundamentally different ways. First, through its effect on the flow field - in order to conserve flux, flow velocities decrease as the density increases with depth. Second, there is a less direct effect of compressibility on the stress due to self-gravitation. Finally, there is an indirect effect of compressibility on gravitational acceleration  $g(r)$  (Corrieu et al. (1995); Panasyuk et al. (1996)). The latter effect is very important since  $g(r)$  enters into both, the body force terms  $f(r)$  in E3.12 and the relation between stress and dynamic topography. The effect of compressibility is significant in the mantle convection because the density of the Earth's mantle increases by about 60% from the top of the mantle to the bottom (F4.2) since a parcel of mantle that flows from the uppermost mantle to the core-mantle boundary almost doubles in density.

The nature of radial density variations in the Earth has been explored with the aid of the radial profiles of compressional  $V_p$  and shear  $V_s$  wave velocities, experimental and theoretical information on chemical composition of the mantle rocks. The comprehensive analysis has concluded that the Earth's density increases with depth mostly due to mantle compressibility and phase transitions.

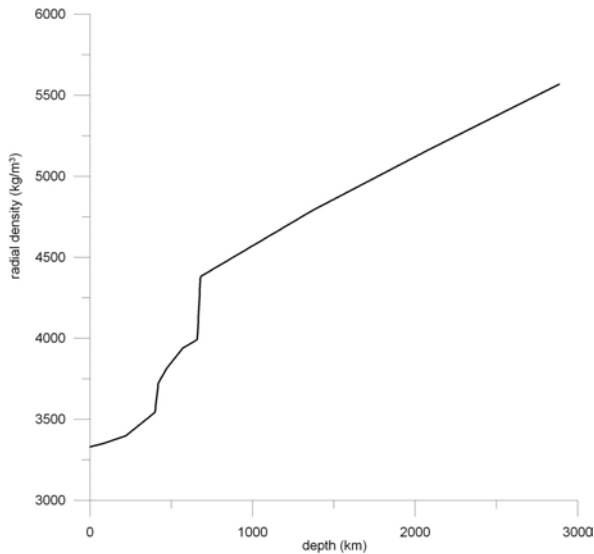


Figure (F4.2) Radial density distribution according to PREM (Dziewonski and Anderson, 1981).

The radial variations in density  $\bar{\rho}$  can be expressed in terms of the pressure  $p$  and the entropy  $s$ :

$$\frac{d\bar{\rho}}{dr} = \left( \frac{\partial \bar{\rho}}{\partial p} \right)_s \frac{dp}{dr} + \left( \frac{\partial \bar{\rho}}{\partial s} \right)_p \frac{ds}{dr} \quad (\text{E4.1})$$

where  $r$  is radial coordinate,  $(*)_s$ ,  $((*)_p)$  means isentropic (isobaric) variations - a reversible process without heat transfer (process with constant pressure).

The laboratory experiments and theoretical studies have shown that thermal expansivity in the Earth's mantle decreases with depth due to compressibility of rocks under high pressure. Although the depth dependence of thermal expansivity should be taken into account in realistic models of mantle convection, the variations of thermal expansivity with depth do not have a major influence on the style of mantle convection. Variations in viscosity with depth are much more important.

Mantle compressibility is defined by the character of radial density  $\rho^*(r)$ :

$$k(r) = \frac{d \ln \rho^*(r)}{d \ln r} = \frac{r}{\rho^*(r)} \frac{d\rho^*(r)}{dr} \quad (\text{E4.2})$$

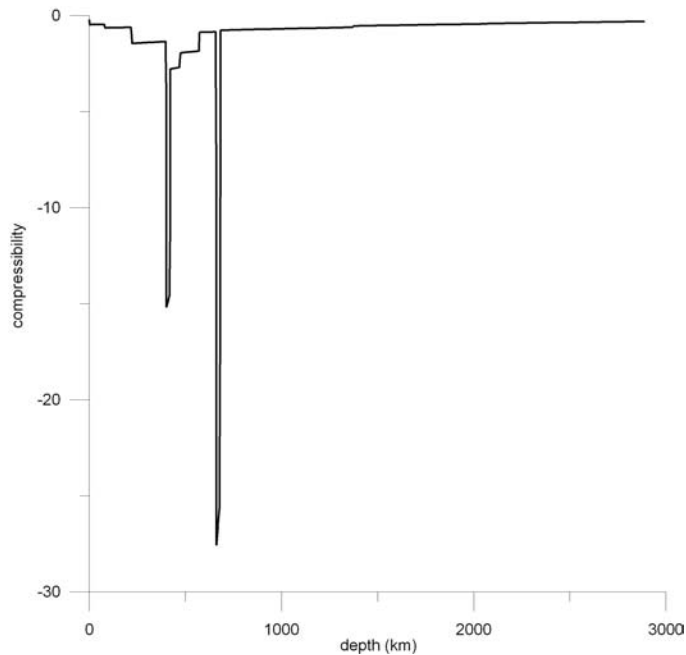


Figure (F4.3) Mantle compressibility corresponding to the radial density in figure (F4.2).

## 2) Self-gravitation:

The effect of self-gravitation is directly correlated with the lateral gravity variations in the Earth. We can schematically describe the process of appearance of lateral gravity variations as a sequence of events:

(a) A spherically symmetric field is heated from below => (b) Convection occurs => (c) Flows appear => (d) Density and temperature distribution gain lateral variations inside the sphere => (e) Surface and core boundaries are distorted.

Convection itself and consequent density redistribution lead to alterations in boundaries of surface and core. Changes in boundaries and temperature distribution react against the spherically symmetric initial state of gravity and lead to a rise of its lateral variations. The forces acting on the internal mass are to be transformed by a change of gravity. Therefore, the mantle flows are corrected by the new distribution of the forces. Due to gradual correction of the flows the boundaries are

distorted more and more, consequently gravity distribution is also changed. Thus, the process of introduction of self-gravitation effect represents a vicious circle.

### 4.3 Effects of mantle compressibility, self-gravitation and depth-dependent gravity on the mantle velocities and geoid.

The opinions differ on the importance of the effects, which I attempt to analyze in this chapter, for the global modeling of mantle convection and the most sensitive constraints. The thing is that an incorporation of the effects (compressibility and self-gravitation) into wide-spread methods, based on FE and FD, is concerned with grand problems. Thus, a presumable dramatic effect of self-gravitation on the geoid would tie up maneuverability of the mentioned methods while attempting in-depth study of the deep Earth's structure with the aid of the methods mentioned above.

In order to remove the effects of self-gravitation and mantle compressibility from our methods we need to apply some simplification to the equation system (E3.10) and the boundary conditions (E3.11):

$$\begin{aligned}
 r \frac{dU_1^{lm}}{dr} &= -(2 + k)U_1^{lm} + LU_2^{lm} \\
 r \frac{dU_2^{lm}}{dr} &= -U_1^{lm} + U_2^{lm} + \frac{1}{\eta^*}U_4^{lm} \\
 r \frac{dU_3^{lm}}{dr} &= (12 + 4k)\eta^*U_1^{lm} - 6L\eta^*U_2^{lm} + U_3^{lm} + LU_4^{lm} - \rho^*U_6^{lm} + \delta\rho^{lm}g^*r^2 \\
 r \frac{dU_4^{lm}}{dr} &= -(6 + 2k)\eta^*U_1^{lm} - 2(2L-1)\eta^*U_2^{lm} - U_3^{lm} - 2U_4^{lm} - \rho^*U_5^{lm} \\
 r \frac{dU_5^{lm}}{dr} &= U_5^{lm} + U_6^{lm} \\
 r \frac{dU_6^{lm}}{dr} &= LU_5^{lm} - 4\pi\gamma\delta\rho^{lm}r^3
 \end{aligned}$$

Figure (ES4.1) Removal of mantle compressibility and partial self-gravitation effects from the equation system.

Blue lines mark the terms in the equations responsible for the effect of mantle compressibility. These terms disappear

automatically if we assume the radial density function to be constant.

As shown in Part 4.1 the effect of self-gravitation is double-faced:

- In order to exclude partial effect of self-gravitation due to redistribution of the forces and lateral gravity variations, which is of the most interest for us, we need to disconnect the Poisson equation from the Stokes equation by the removal of geopotential-related terms (marked by red crossed lines) from our equations for mantle flows and stresses.
- The other connection between the equations comes from boundary conditions. An enormous trivial effect of boundary distortion can be excluded if we put away the influence of dynamic topography (not affected by gravity) on geopotential through the boundary conditions.

The latter effect can easily be modeled by any numerical method (spectral method, FE and FV methods) since the Poisson equation can be solved separately from the Stokes equation using the resulting topography obtained from the Stokes equation. As the main goal of this chapter is to show how important the complete effect of self-gravitation on geoid and mantle flows is, I try to analyze only the partial effect, which cannot be reproduced by FD, FE and FV methods directly. This effect can be modeled only if both Poisson and Stokes equations are being solved simultaneously. Therefore, the boundary conditions remain unchangeable (E3.11), and only the equation system is simplified by the removal of two terms (as shown in figure (ES4.1) by red lines) to uncouple the Stokes and Poisson equations.

Two models (artificial and realistic) have been considered to reveal the contribution of each effect on the mantle velocities and dynamic geoid. Within each model different combinations of effects were analyzed:

- (a) No-effect model: no mantle compressibility (radial density is constant  $\bar{\rho}(r) = \rho_0 = 4430 \left[ \frac{kg}{m^3} \right]$ ), no self-gravitation and no radial gravity change (radial acceleration of gravity is constant  $\bar{g}(r) = 10 \left[ \frac{m}{s^2} \right]$ ).
- (b) All-effect model: all three effects are included.
- (c) No-compressibility model: all effects are included except for compressibility.
- (d) No-self-gravitation model: all effects are included except for self-gravitation.
- (e) No-radial-gravity model: all effects are included except for depth-dependent gravity.

1) *Artificial model.*

The first simple set of symmetric models is aimed at isolating each particular effect from objectionable influence of other effects and some casual impacts of viscosity variations.

I have considered a set of models with the following input data:

- Radial density profile from Figure (F4.2)
- Density anomaly:  $\delta\rho = Y_{211}(\theta, \varphi) = N_{21} P_2^1(\cos\theta) \cos\varphi = \sqrt{\frac{15}{4}} \sin 2\theta * \cos\varphi$
- Viscosity  $\eta^*(r) \equiv 1$

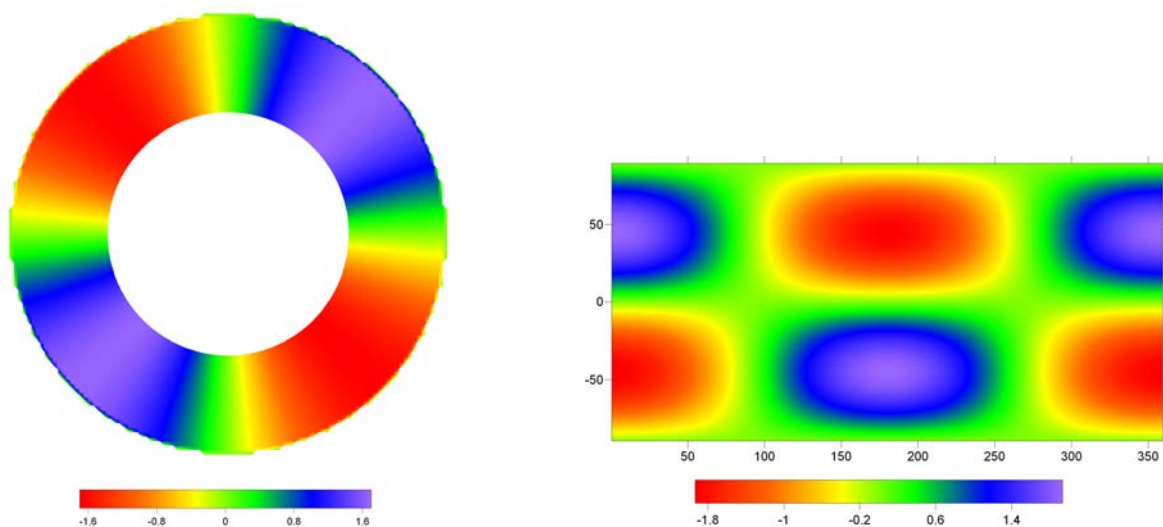


Figure (F4.4) Density anomalies:

Left: Cross-section through the longitudes 210 (left semicircle) and 30 (right semicircle).

Right: View from the surface (these density anomalies are kept at all depths).

*Mantle velocities:*

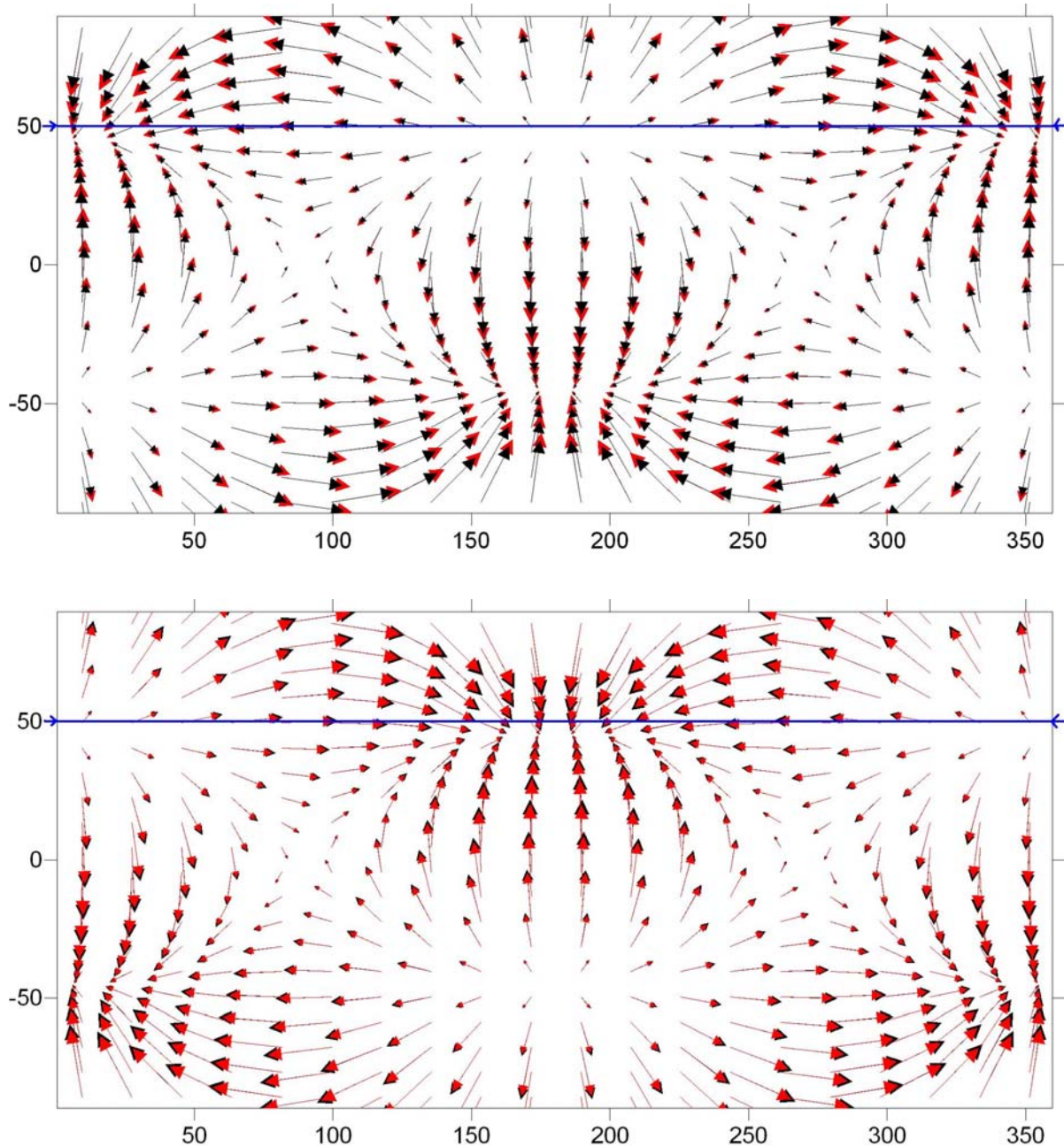


Figure (F4.5) Velocities near surface and core: black arrows - (a) no-effect model; red arrows - (b) all-effect model.

Top: Surface velocities:

- (a) no-effect model (maximal velocity value 683944 mm/year).
- (b) all-effect model (maximal velocity value 768130 mm/year).

Bottom: Velocities near core:

- (a) no-effect model (maximal velocity value 806650 mm/year).
- (b) all-effect model (maximal velocity value 749504 mm/year).

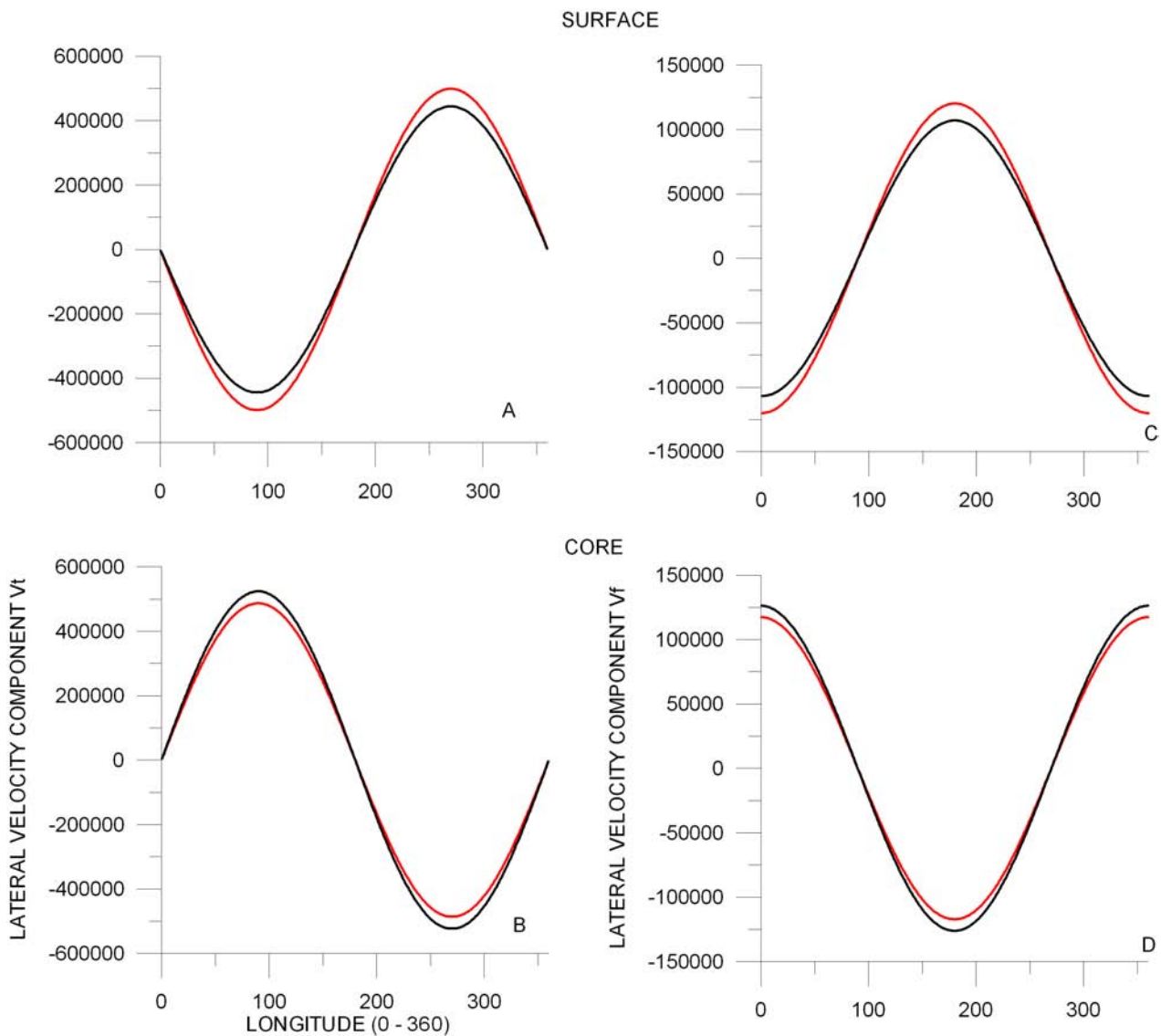


Figure (F4.6) Profiles for lateral velocity components on the surface (Figures A and C) and near the core (Figures B and D) along the blue lines in figure (F4.5).

- black curve - (a) no-effect model.
- red curve - (b) all-effect model.

The resulting values of mantle velocities [mm/year] and dynamic geoid [m] seem to be very huge since we consider an artificial model with very low constant viscosity (all through the mantle  $\bar{\eta}(r) \equiv 10^{21}$ ) and unnaturally great density anomalies (1000 times greater than in reality).

Figure (F4.5) represents the surface velocities and velocities calculated near the core for the models (a) no-effect model and (b) all-effect model. The maximal surface velocity values obtained from the model (b) near the surface of the Earth are approximately 12.3% higher than those from the model (a). Near the core the situation is quite the opposite: the no-effect model (a) gives 7.6% greater velocity values than the all-effect model (b). Thus, the no-effect model (a) produces rather significant difference between surface velocities and velocities calculated near the core (the latter ones have approximately 18% greater values). In the meanwhile the all-effect model (b) gives almost equal values for both: velocities near surface and core.

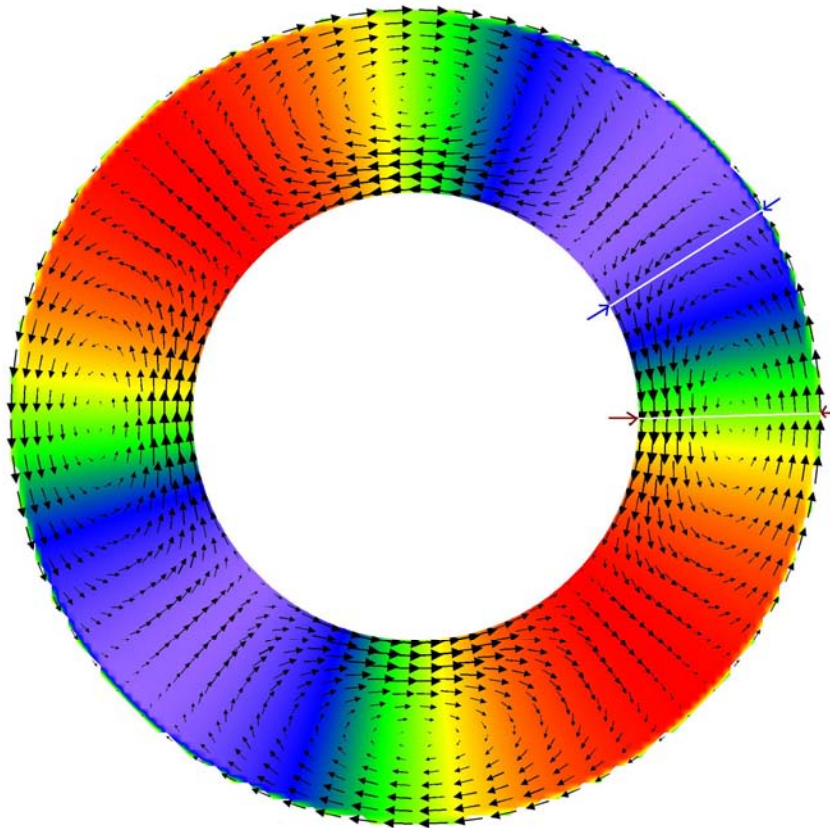


Figure (F4.7) Velocity distribution in the cross-section (F4.4 Left) for the (a) no-effect model: the following velocity profiles have been calculated in the areas marked by white lines.

- Cross-section (60): Blue arrows point at the cross-section through the latitude 60.
- Cross-section (90): Red arrows point at the cross-section through the latitude 90.

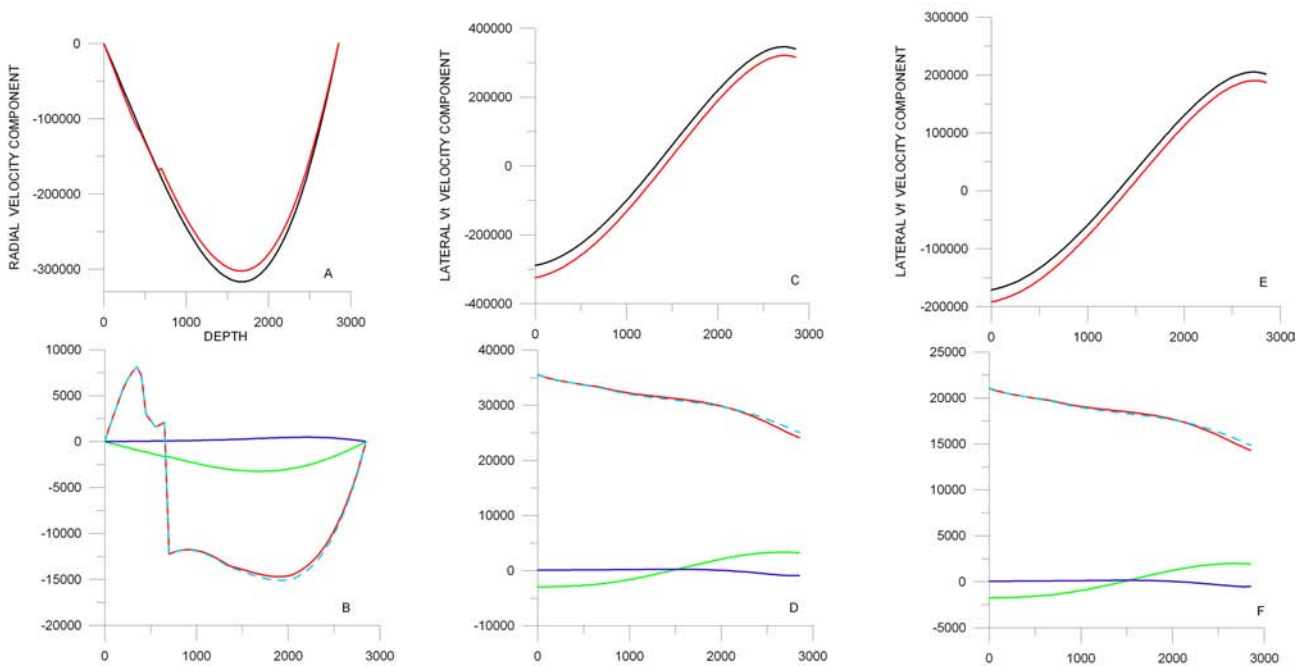


Figure (F4.8) Velocity components in the cross-section (60) and differences between models with various effect combinations:

Velocity components for models (a) and (b):

A) Radial velocity component  $V_r$ .

C) Lateral velocity component  $V_\theta$ .

E) Lateral velocity component  $V_\varphi$ .

- Black curve - (a) no-effect model
- Red curve - (b) all-effect model

Differences for models (b) and (a), (b) and (c), (b) and (d), (b) and (e) between:

B) - radial velocities  $V_r$ .

D) - lateral velocities  $V_\theta$ .

F) - lateral velocities  $V_\varphi$ .

Figures B, D and F: Impact of different effects (Red curve - contribution of all effects; Light blue curve - contribution of mantle compressibility; Green curve - contribution of self-gravitation; Dark blue curve - impact of radial gravity).

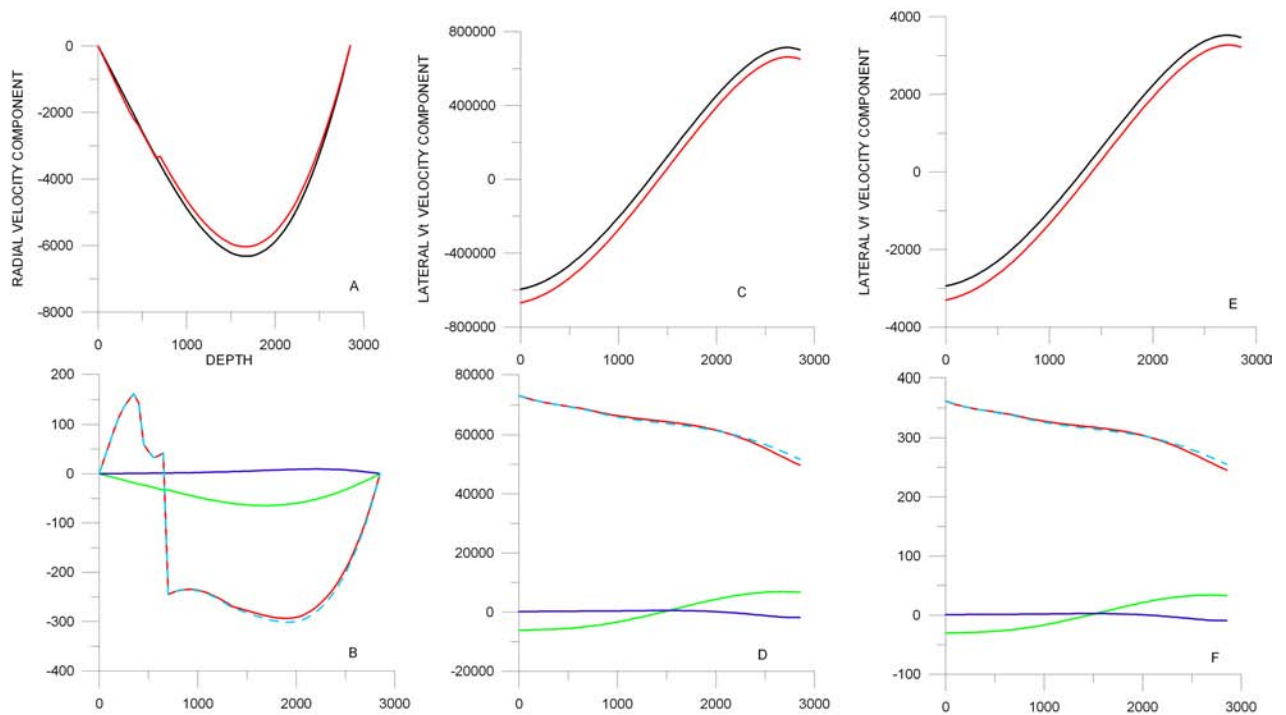


Figure (F4.9) Velocity components for cross-section (90) and differences between models with various effect combinations (analogously to (F4.8)).

Figures (F4.8) and (F4.9) represent the particular contribution of the effects of mantle compressibility, self-gravitation and depth-dependent gravity on velocity distribution. According to the figures almost all the changes in velocity distribution occur due to mantle compressibility. Contribution of depth-dependent gravity to velocity distribution is negligibly small (less than 1%) and can be taken as insignificant. Although the effect of self-gravitation on the mantle velocities is not of the major significance, it is obviously much more substantial than the effect of depth-dependent gravity: on the radial component of velocity approximately 20% (of the change due to all effects), on both lateral components - 13%.

Geoid:

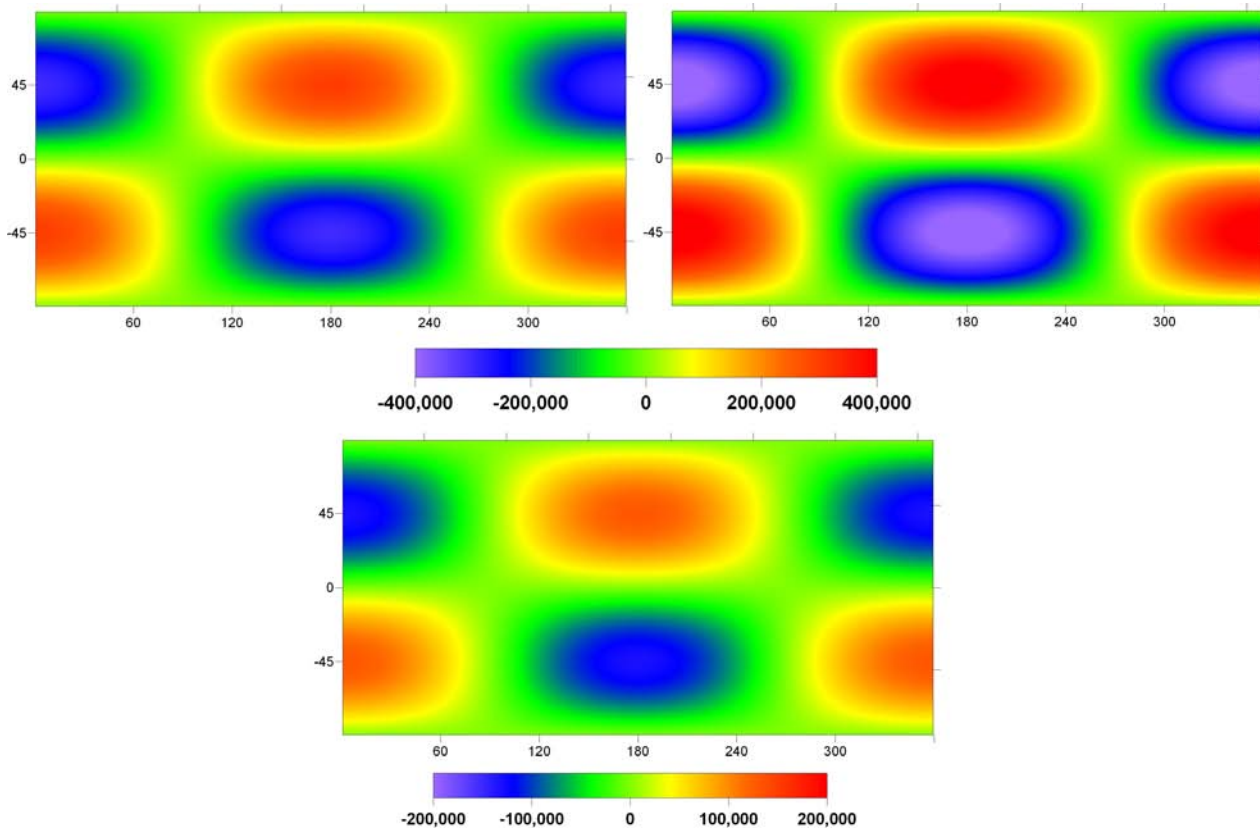


Figure (F4.10) Geoids for model (a) no-effect and (b) all-effect and difference between them.

Top left: (a) no-effect model.

Top right: (b) all-effect model.

Bottom: Difference between (b) all-effect and (a) no-effect models  $\{(b)-(a)\}$ . Impact of all effects on the geoid figure.

Figure (F4.10) represents geoids calculated for (a) no-effect and (b) all-effect models. The difference between two geoids is visible to the naked eye. Geoid highs and lows are significantly intensified by an incorporation of mantle compressibility, self-gravitation and radial gravity compared to the initial geoid figure.

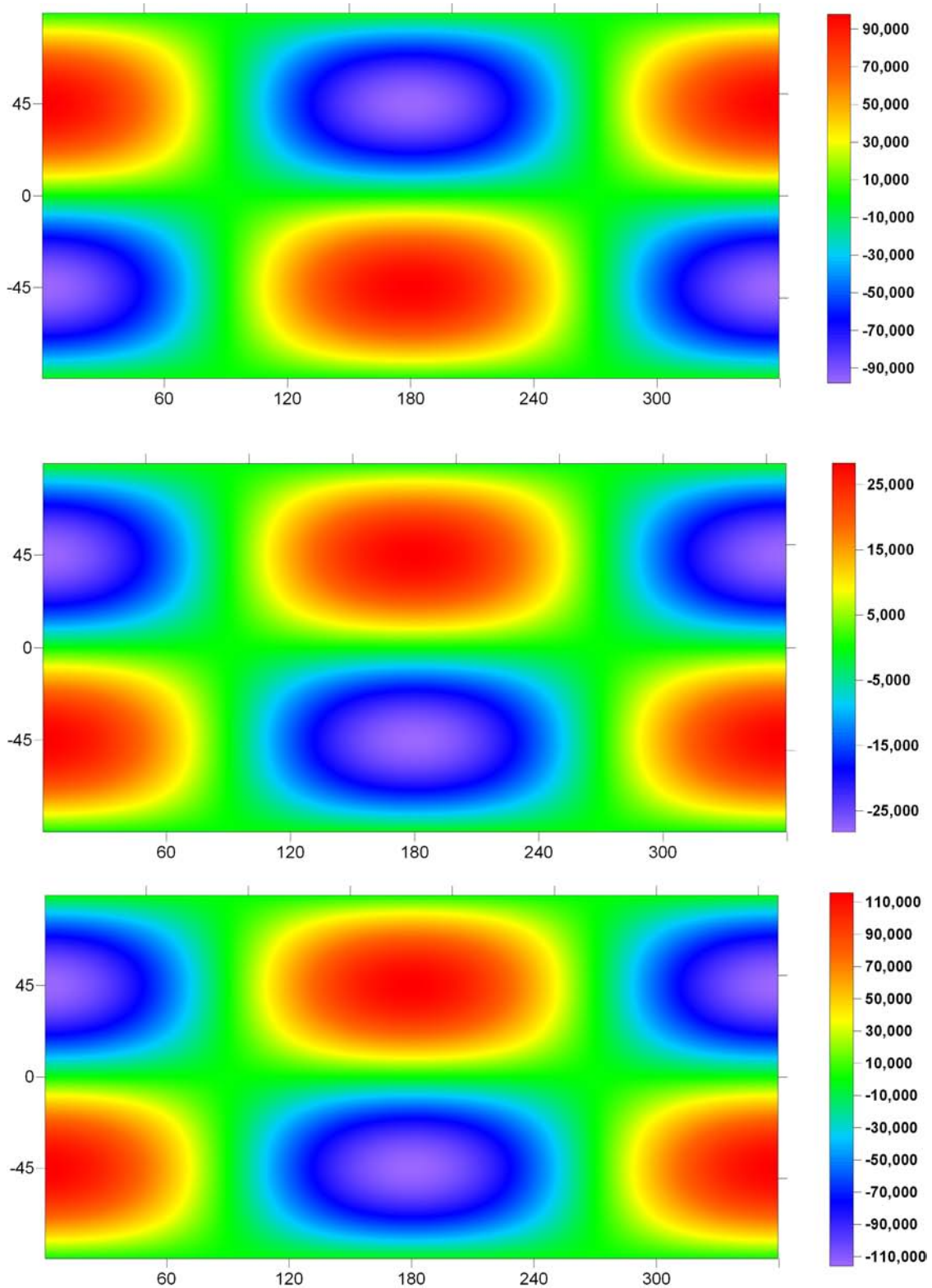


Figure (F4.11) Impact of various effects on the geoid: models (b), (c), (d) and (e) are involved [in meters]:

Top: Impact of mantle compressibility on the geoid figure.

Center: Impact of radial gravity on the geoid figure.

Bottom: Impact of partial self-gravitation effect on the geoid figure.

Figure (F4.11) demonstrates how large the contribution of each effect is. The effect of self-gravitation is obviously very high: the change of the geoid figure occurred due to only self-gravitation effect exceeds 26% of the geoid calculated with all the effects (model (b)). We can conclude that the effect of self-gravitation may not be neglected while modeling the geoid figure. The effect of compressibility on geoid is comparable with the effect of self-gravitation (22.5%) in this model. Complete neglect of depth-dependent gravity effect results in 6.5% error in the geoid figure. As is easy to see the effect of depth-dependent gravity on geoid intensifies a huge effect of self-gravitation while the effect of mantle compressibility reduces it. The rights of such a correlation between the effects can be verified by the next set of tests developed on the base of real data. We can also conclude that these effects are not additive, otherwise the resulting difference between the geoid calculated for (b) all-effect and (a) no-effect models would be much smaller.

## 2) *Realistic model.*

A set of models based on...

- Density anomalies (F4.13) from the S20 seismic velocity model
- constant scaling factor equal to 0.2
- radial density profile from figure (F4.2)
- radial viscosity profile (F4.12), which gives a rather reasonable fit to the observed geoid (approximately 78%)

...has been analyzed for the purpose of investigation of the mantle compressibility, self-gravitation and depth-dependent gravity effects on realistic models.

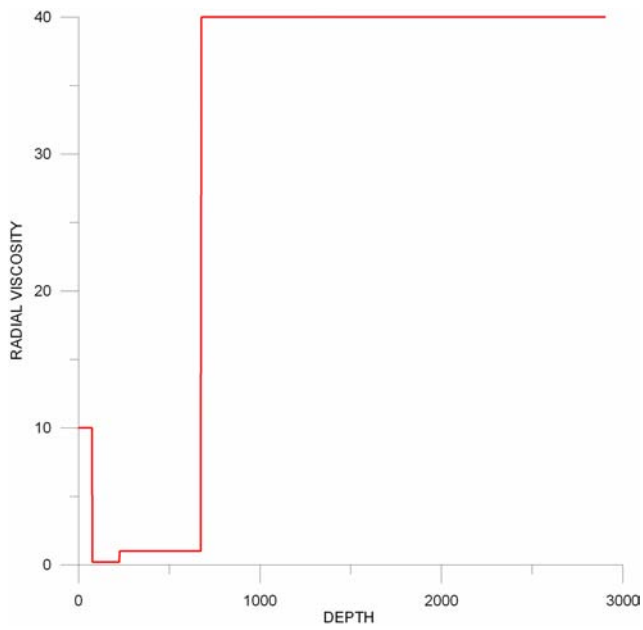


Figure (F4.12) Radial viscosity profile (relative values  $\eta^*(r)$ ).

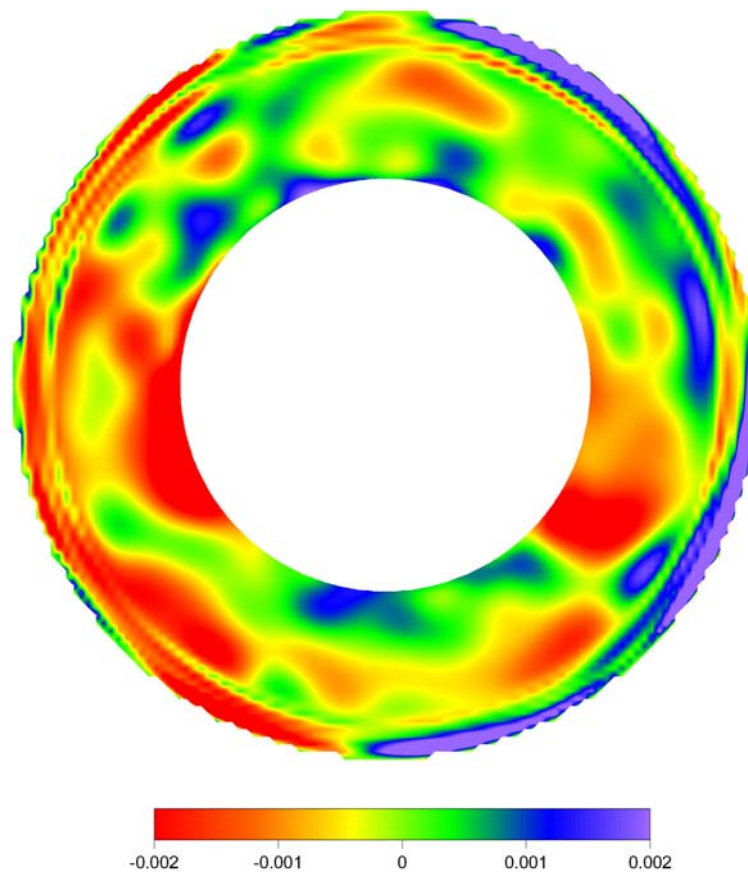


Figure (F4.13) Density anomalies: cross-section through the longitudes 210 (left semicircle) and 30 (right semicircle).

Mantle velocities:

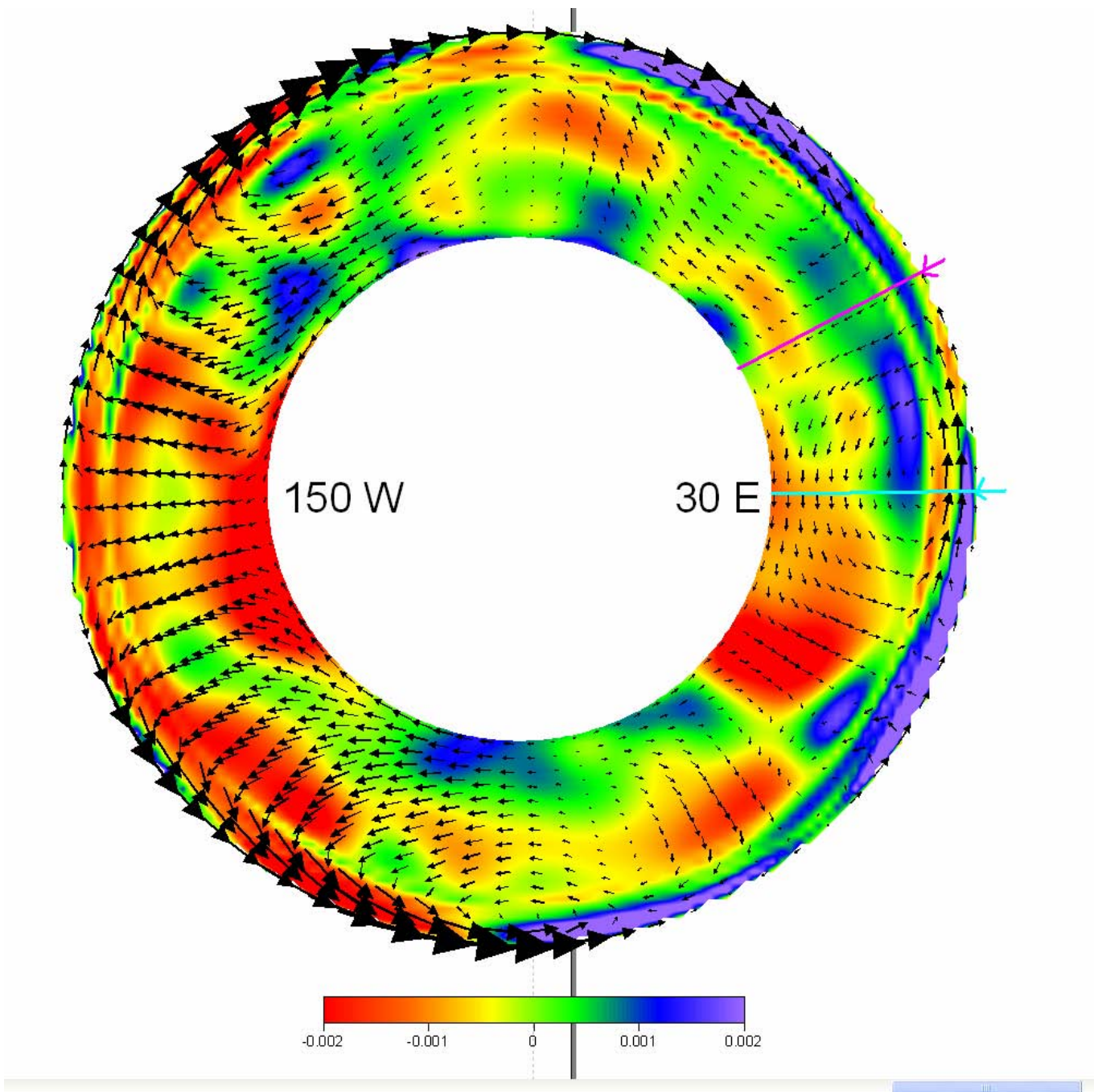


Figure (F4.14) Velocity distribution in cross-section (F4.13) for the model (a) no-effect: the following velocity profiles have been calculated in the areas marked by pink (cross-section  $\theta = 60^\circ$  &  $\varphi = 30^\circ$ ) and light blue (cross-section  $\theta = 90^\circ$  &  $\varphi = 30^\circ$ ) lines.

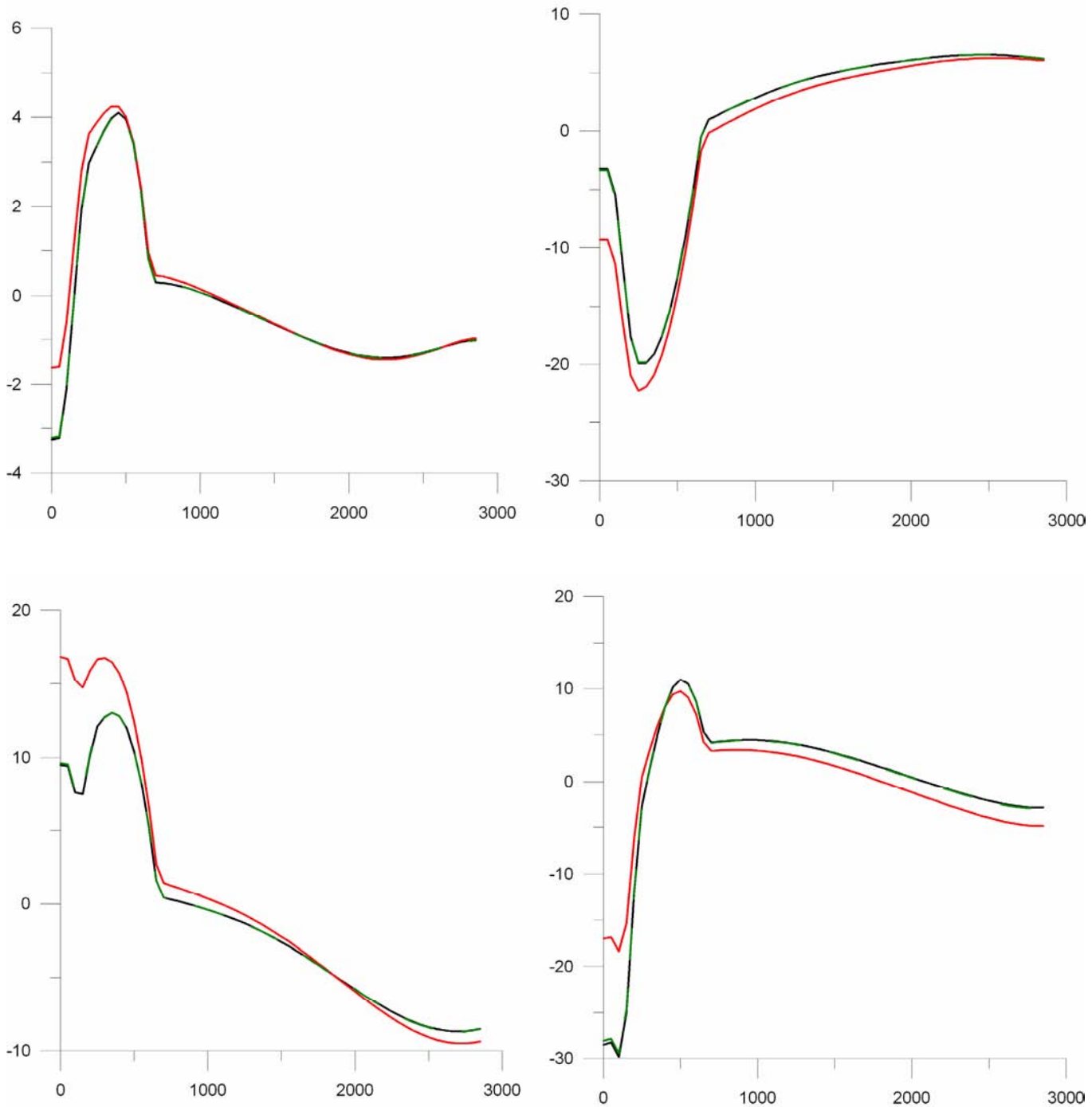


Figure (F4.15) Profiles for horizontal velocities [mm/year]  $u_\theta$  (Top) and  $u_\phi$  (Bottom) in the areas marked by lines in figure (F4.14): cross-sections  $\theta = 60^\circ$  &  $\varphi = 30^\circ$  (Left) and  $\theta = 90^\circ$  &  $\varphi = 30^\circ$  (Right).

Black curve: (a) no-effect model.

Red curve: (b) all-effect model.

Green dashed curve: (c) no-compressibility model.

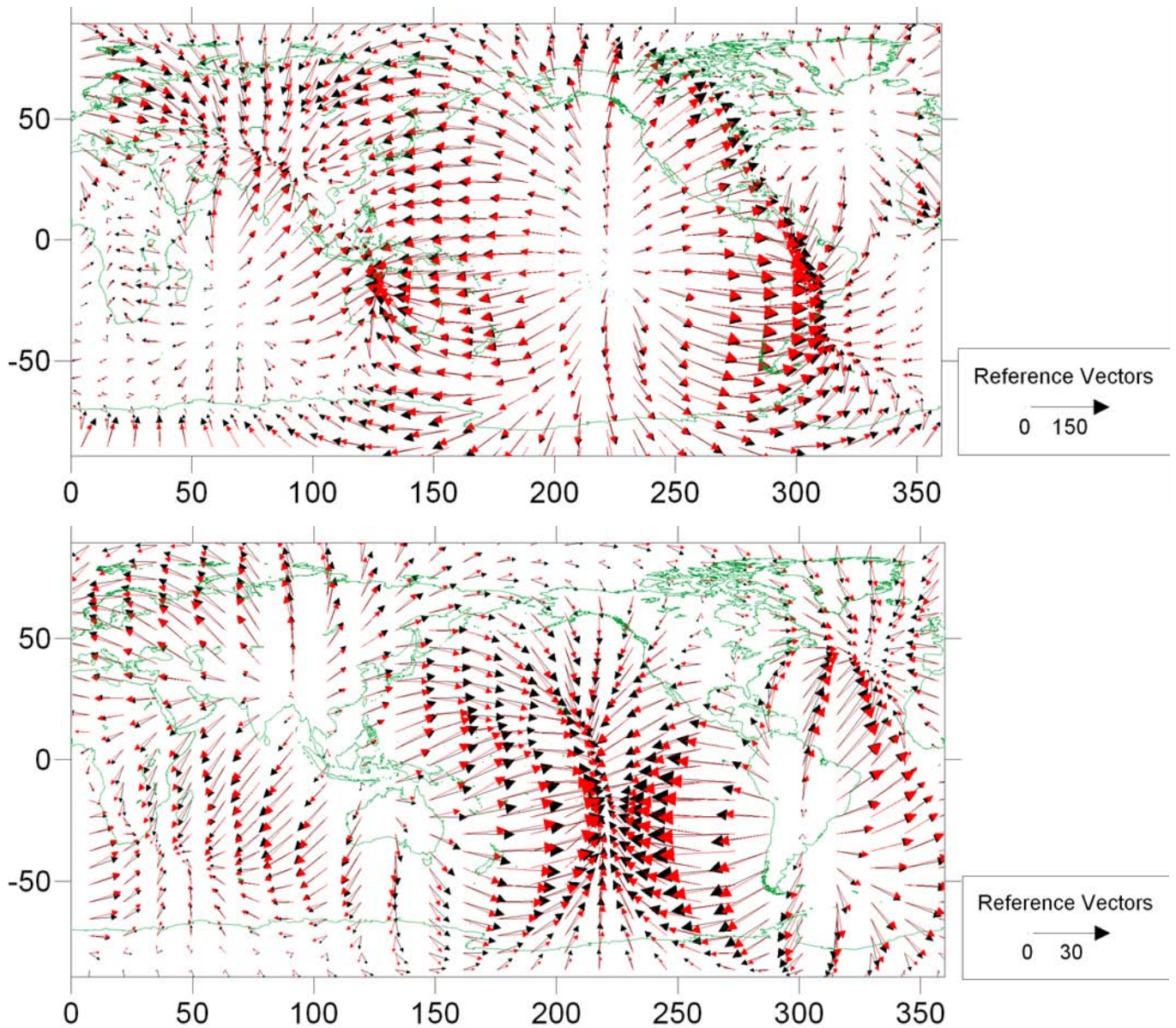


Figure (F4.16) Velocities near surface and core.

- black arrows - (a) no-effect model.
- red arrows - (b) all-effect model.

Top: Surface velocities.

- (a) no-effect model: maximum value is 102.4 mm/year
- (b) all-effect model: maximum value is 94.5 mm/year.

Bottom: Mantle velocities near core boundary.

- (a) no-effect model: maximum value is 24.25 mm/year
- (b) all-effect model: maximum value is 21.6 mm/year.

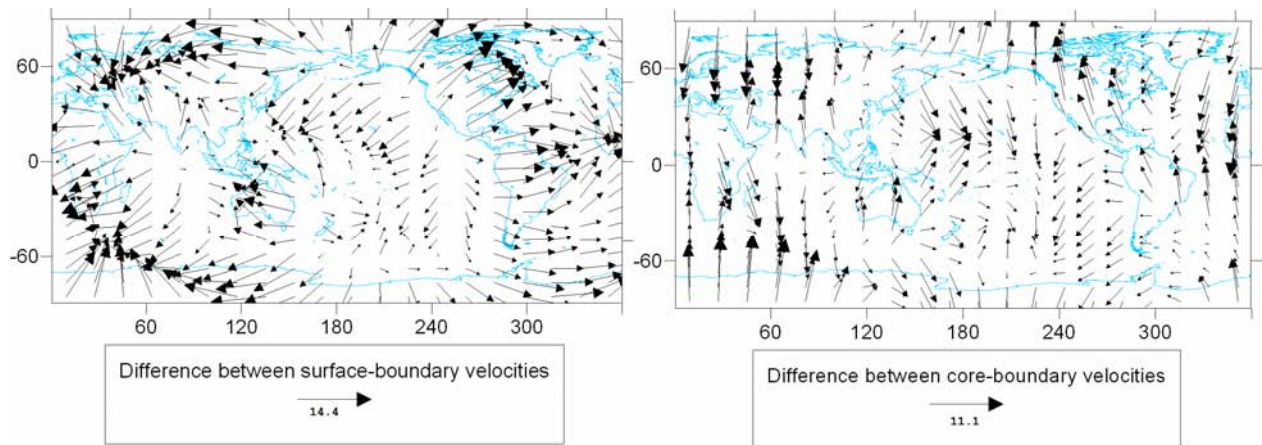


Figure (F4.17) Differences between horizontal velocities calculated for the models (a) no-effect and (b) all-effect [mm/year].

Left: near surface boundary

Right: near core boundary

Analogously to the mantle flows calculated for the artificial model 1) mantle velocities are highly affected by mantle compressibility (F4.15), the contribution of which is large in both, the uppermost and lowermost layers (F4.16 and F4.17). Since the distribution of the flows is rather intricate in the realistic models it is difficult to analyze the mean contribution percentage of the effects on it. The maximum change in horizontal mantle velocities near the core-boundary exceeds 40% of the maximum velocity value while the contribution of the effects in the uppermost layers is approximately 15% of the maximum velocity value. According to (F4.15) both components of horizontal velocity are almost doubled by the effect of mantle compressibility due to the redistribution of the global flows but the conclusions depend too much on the particular choice of the cross-sections.

Geoid:

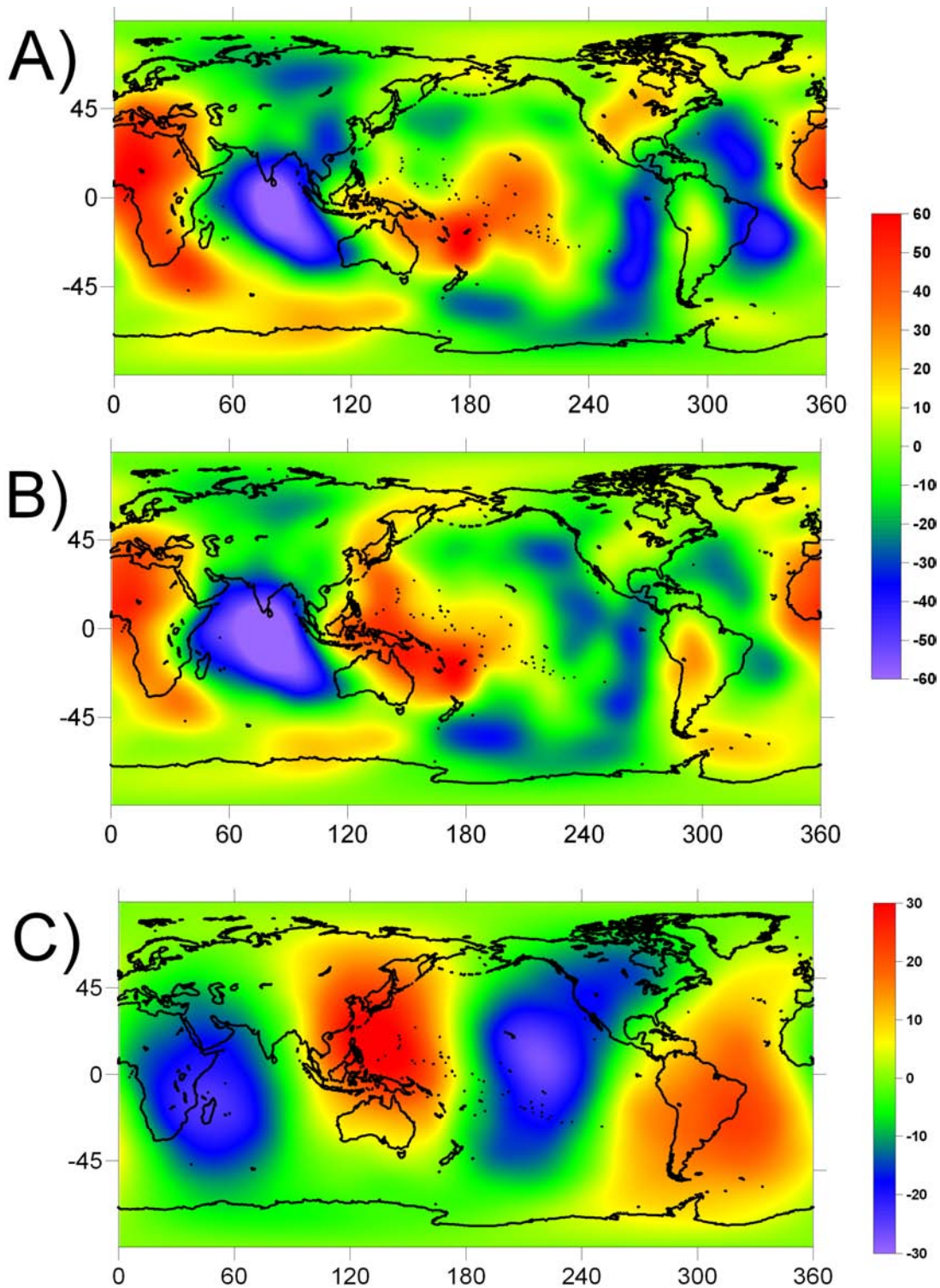


Figure (F4.18) Geoids calculated for models (a) no-effect model and (b) all-effect model and difference between them [meters].

A) (a) no-effect model.

B) (b) all-effect model.

C) difference between (b) all-effect and (a) no-effect models.

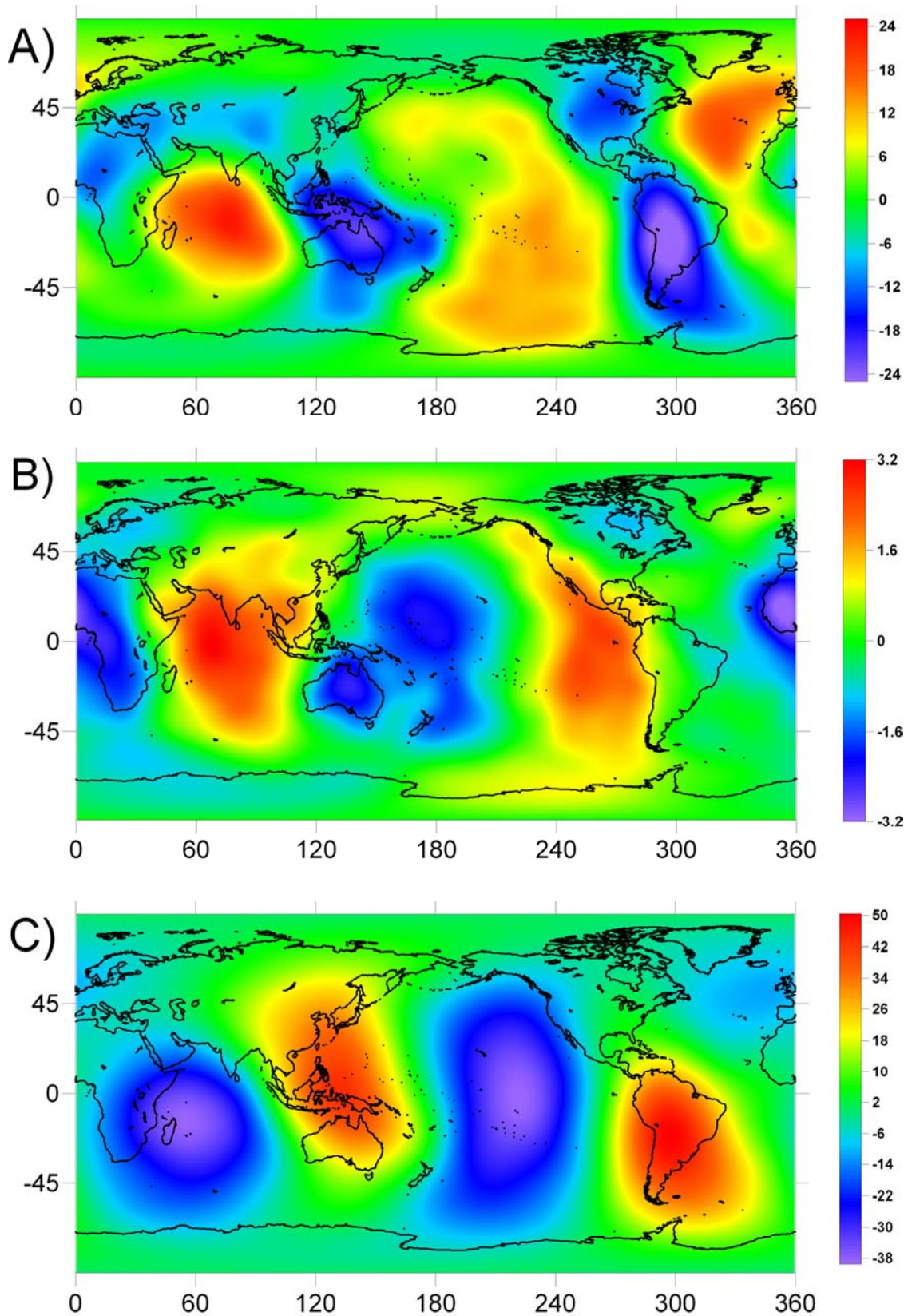


Figure (F4.19) Impact of each effect on the geoid figure [meters].

A) Impact of mantle compressibility (difference between models (b) and (c))

B) Impact of radial gravity (difference between models (b) and (e))

C) Impact of self-gravitation (difference between models (b) and (d))

The effect of self-gravitation in this model is even greater than in the artificial model considered above. The effect of self-gravitation plays an important part in the shaping of the dynamic geoid (61.6% of the resulting geoid) and by no means may be neglected. The impact of the other two effects into dynamic geoid can be estimated in terms of relative changes of the maximum geoid heights if removing separately every effect from the (b) all-effect model (F4.19). The impact of mantle compressibility to the geoid figure (F4.19A) is approximately a third part of the maximal geoid heights (approximately 38%), therefore, this effect also plays a substantial part in the total shape. The disturbance of the geoid figure due to radially variable gravity is less than 5% but even this relatively small contribution can be significant for the accurate modeling of the geoid anomalies. The correlation between the effects of self-gravitation and mantle compressibility is partially kept in the case of realistic model: mantle compressibility significantly reduces effect of self-gravitation that is why the contribution of self-gravitation into the geoid figure exceeds the contribution of all the effects.

## Chapter V.

### *The introduction of lateral viscosity variations.*

The introduction of 3-D viscosity structure is bound up with some difficulties if considering the Stokes equations in spherical harmonics. For radially symmetric viscosity the harmonic modes are decoupled, therefore, the Stokes equation can be solved directly for each harmonic mode (as it is described in Chapter III). As soon as laterally variable viscosity is involved, non-linear coupled terms appear in the basic equations because all spherical harmonics are coupled with LVV. One possible way to cope with the difficulty is to apply an iterative method in order to approximate to required equation solution by an iterative approach.

In this chapter I consider a compressible flow in a self-gravitating spherical shell with 3-D viscosity distribution  $\eta = \eta(r, \theta, \varphi)$ . Therefore, once more I have to revert to the equation system, which comprises the Stokes and Poisson equations expressed via the means of mantle flow velocity  $u = (u_r, u_\theta, u_\varphi)$ , total stress tensor  $\sigma_{ij}$  and geopotential V:

$$\frac{2u_r}{r} + \frac{\partial u_r}{\partial r} + \frac{1}{r} \left( \frac{\partial u_\theta}{\partial \theta} + \text{ctg} \theta u_\theta + \frac{1}{\sin \theta} \frac{\partial u_\varphi}{\partial \varphi} \right) = -\frac{k(r)}{r} u_r \quad (\text{E5.1a})$$

$$0 = r^2 \frac{\partial \sigma_{rr}}{\partial r} + r \frac{\partial \tau_{r\theta}}{\partial \theta} + \frac{r}{\sin \theta} \frac{\partial \tau_{r\varphi}}{\partial \varphi} + r(2\sigma_{rr} - \sigma_{\theta\theta} + \sigma_{\varphi\varphi} + \tau_{r\theta} \text{ctg} \theta) + r^2 \bar{\rho} \frac{\partial V}{\partial r} - r^2 \delta \bar{\rho} g \quad (\text{E5.1b})$$

$$0 = r^2 \frac{\partial \tau_{r\theta}}{\partial r} + r \frac{\partial \sigma_{\theta\theta}}{\partial \theta} + \frac{r}{\sin \theta} \frac{\partial \tau_{\theta\varphi}}{\partial \varphi} + r(\sigma_{\theta\theta} \text{ctg} \theta - \sigma_{\varphi\varphi} \text{ctg} \theta + 3\tau_{r\theta}) + r \bar{\rho} \frac{\partial V}{\partial \theta} \quad (\text{E5.1c})$$

$$0 = r^2 \frac{\partial \tau_{r\varphi}}{\partial r} + r \frac{\partial \tau_{\theta\varphi}}{\partial \theta} + \frac{r}{\sin \theta} \frac{\partial \sigma_{\varphi\varphi}}{\partial \varphi} + r(3\tau_{r\varphi} + 2\tau_{\theta\varphi} \text{ctg} \theta) + \frac{r \bar{\rho}}{\sin \theta} \frac{\partial V}{\partial \varphi} \quad (\text{E5.1d})$$

$$\frac{\partial^2 V}{\partial r^2} + \frac{2}{r} \frac{\partial V}{\partial r} - \frac{L^2}{r^2} V = -4\pi G \rho \quad (\text{E5.1e})$$

## 5.1 Iterative methods for incorporating lateral viscosity variations.

Two iterative methods U-transform and W-transform suggested by Zhang and Christensen (1993) for the incorporation of the LVV effect into the incompressible mantle will be completely analyzed in order to derive true formulae for non-linear coupled terms. Both methods were improved by the incorporation of the effect of mantle compressibility into them. Our detailed tests have shown a colossal difference between the results obtained from the initial methods for the same models on the contrary to the comparative analysis, which was put into practice by Zhang and Christensen (1993). As a result we had to derive all the equations and formulae from the very beginning. In both methods published by Zhang (1993) and Zhang and Christensen (1993) essential misprints were revealed that might play a crucial role in the published conclusions. First of all, a simple model with long-wavelength 3-D viscosity distributions (up to six spherical harmonics) stated by Zhang (1993) was analyzed (see Part 5.4). Using the formulae published by Zhang (1993) and Zhang and Christensen (1993) has led to the results remarkably different from those published by Zhang (1993). At the same time the results produced with the aid of each of foregoing methods also differ from the results published by Zhang (1993). This fact prevented us from determining what formulae were used by Zhang (1993) to derive the published results in reality. The new-derived formulations of U-transform and W-transform iterative methods were applied to the aforementioned simple models. Both new-derived methods produced the results though identical to one another but again dissimilar to the data published in the PhD thesis by Zhang (1993). Furthermore, a comprehensive set of different viscosity models was elaborated in order to compare the efficiency of the new realizations of U- and W-transform (see Part 5.4). The thorough analysis showed good agreement between the results produced by the new realizations of U- and W-transform methods. In a few words both new method

realizations gave almost identical results (difference less than 1%) for the models with identical input data.

Based on analyzed tests we arrive at the following conclusions:

- The new realization of the U-transform method provides the possibility to model 3-D viscosity structure with high viscosity contrasts. The convergence of the iterative method is steady even for models with a rather high resolution (up to 180 spherical harmonics) and viscosity contrast of seven orders of magnitude. The comparison of the new-derived iterative method with the FE method CITCOM (Zhong et al (2000); Tan et al (2000); Rogozhina et al. (2005, 2006); Baranov et al. (2007)) revealed good accordance between both methods.
- The new realization of the W-transform method is applicable to the 3-D long-wavelength models with input data smoothed to a certain spherical harmonic degree (for various models the limitations are different). But it fails to handle models based on the present-day seismic tomography data as well as synthetic models of rather high resolution. In this case the iterative process diverges.

The main distinction between the U-transform and W-transform methods originates from the different representation of mantle velocities and the 3-D viscosity distribution. The W-transform iterative method modifies velocity flow for account of LVV already on the first step of the iterative process. The main idea of this iterative method is to smooth the initial rough approach away and to reduce the primordial exaggerated effect of LVV on the velocity flow. On the contrary, the U-transform method as a typical iterative method implies an approach through an iterative way directly from the initial state and modifies velocity distribution obtained first for radial viscosity distribution, then changed step by step due to LVV.

The schemes used for both U- and W-transform iterative methods are ultimately rather similar. The initial solution (different for two iterative methods) for radial viscosity distribution (Chapter III) is modified to account for the effect of LVV. The non-linear coupled terms, appearing in the basic equations due to LVV, are shifted to the right-hand side and the equations are solved iteratively using the standard technique. The additions to right-hand side terms are calculated on the base of the results of the previous step. Hence, we must solve two equation systems for spheroidal and toroidal components of velocity and stress considering the appearance of a set of viscous terms. All the deductions for the new realizations of the U- and W-transform methods are stated bellow (Appendix U and W).

The equation system for the spheroidal components of mantle velocity and stress for both iterative methods:

$$\begin{aligned}
r \frac{dU_1^{lm}}{dr} &= -(2+k)U_1^{lm} + LU_2^{lm} + A_{lm}^* \\
r \frac{dU_2^{lm}}{dr} &= -U_1^{lm} + U_2^{lm} + \frac{1}{\eta^*} U_4^{lm} + B_{lm}^* \\
r \frac{dU_3^{lm}}{dr} &= (12+4k)\eta^* U_1^{lm} - 6L\eta^* U_2^{lm} + U_3^{lm} + LU_4^{lm} - \rho^* U_6^{lm} + \delta\rho^{lm} g^* r^2 + C_{lm}^* \\
r \frac{dU_4^{lm}}{dr} &= -(6+2k)\eta^* U_1^{lm} - 2(2L-1)\eta^* U_2^{lm} - U_3^{lm} - 2U_4^{lm} - \rho^* U_5^{lm} + D_{lm}^* \\
r \frac{dU_5^{lm}}{dr} &= U_5^{lm} + U_6^{lm} \\
r \frac{dU_6^{lm}}{dr} &= LU_5^{lm} - 4\pi\gamma\delta\rho^{lm} r^3
\end{aligned} \tag{E5.2}$$

Boundary conditions:

$$\begin{aligned}
U_1(r_e) &= U_1(r_c) = 0 \\
U_4(r_e) &= U_4(r_c) = 0 \quad (\text{free-slip condition}) \\
\begin{cases} U_4(r_c) = 0 \\ U_2(r_e) = U_{obs}^{sph} \end{cases} & \quad (\text{no-slip condition}) \\
U_6(r_e) &= -(l+1)U_5(r_e) - \frac{4\pi\gamma r_e \rho_0}{g_e} U_3(r_e)
\end{aligned} \tag{E5.2a}$$

$$U_6(r_c) = (l-3)U_5(r_c) - \frac{4\pi\gamma r_c \rho_0}{g_c} U_3(r_c)$$

The equation system for toroidal flow:

$$r \frac{dW_1^{lm}}{dr} = W_1^{lm} + \frac{1}{\eta^*} W_2^{lm} + E^{lm} \quad (\text{E5.3})$$

$$r \frac{dW_2^{lm}}{dr} = (L-2)\eta^* W_1^{lm} - 2W_2^{lm} + F^{lm}$$

with boundary conditions:

$$W_2(r_e) = W_2(r_c) = 0 \quad (\text{free-slip condition})$$

$$\begin{cases} W_2(r_c) = 0 \\ W_1(r_e) = U_{obs}^{tor} \end{cases} \quad (\text{no slip condition}) \quad (\text{E5.3a})$$

Applying a change of variables  $Z_1^{lm} = U_1^{lm}$ ,  $Z_2^{lm} = U_2^{lm}$ ,  $Z_3^{lm} = U_3^{lm} + \rho^* U_5^{lm}$ ,  $Z_4^{lm} = U_4^{lm}$ ,  $Z_5^{lm} = W_1^{lm}$ ,  $Z_6^{lm} = W_2^{lm}$ ,  $Z_7^{lm} = U_5^{lm}$  and  $Z_8^{lm} = U_6^{lm}$  to the equation system E5.2 we arrive at a universal system describing both spheroidal and toroidal components of mantle velocity and stress together with geopotential:

$$r \frac{dZ_1^{lm}}{dr} = -(2+k)Z_1^{lm} + LZ_2^{lm} + A^{lm} \quad (\text{E5.4a})$$

$$r \frac{dZ_2^{lm}}{dr} = -Z_1^{lm} + Z_2^{lm} + \frac{1}{\eta^*} Z_4^{lm} + B^{lm} \quad (\text{E5.4b})$$

$$r \frac{dZ_3^{lm}}{dr} = (12+4k)\eta^* Z_1^{lm} - 6L\eta^* Z_2^{lm} + Z_3^{lm} + LZ_4^{lm} - k\rho^* Z_5^{lm} + \delta\rho^{lm} g^* r^2 + C^{lm} \quad (\text{E5.4c})$$

$$r \frac{dZ_4^{lm}}{dr} = -(6+2k)\eta^* Z_1^{lm} - 2(2L-1)\eta^* Z_2^{lm} - Z_3^{lm} - 2Z_4^{lm} + D^{lm} \quad (\text{E5.4d})$$

$$r \frac{dZ_5^{lm}}{dr} = Z_5^{lm} + \frac{1}{\eta^*} Z_6^{lm} + E^{lm} \quad (\text{E5.4e})$$

$$r \frac{dZ_6^{lm}}{dr} = (L-2)\eta^* Z_5^{lm} - 2Z_6^{lm} + F^{lm} \quad (\text{E5.4f})$$

$$r \frac{dZ_7^{lm}}{dr} = Z_7^{lm} + Z_8^{lm} \quad (\text{E5.4g})$$

$$r \frac{dZ_8^{lm}}{dr} = LZ_7^{lm} - 4\pi\gamma\delta\rho^{lm} r^3 \quad (\text{E5.4h})$$

With boundary conditions modified by change of variables:

$$Z_1(r_e) = Z_1(r_c) = 0$$

$$Z_4(r_e) = Z_4(r_c) = 0 \quad (\text{free-slip condition})$$

$$Z_6(r_e) = Z_6(r_c) = 0$$

$$\begin{cases} Z_4(r_c) = 0 \\ Z_2(r_e) = U_{obs}^{sph} \end{cases} \quad (\text{no-slip condition}) \quad (\text{E5.5})$$

$$\begin{cases} Z_6(r_c) = 0 \\ Z_5(r_e) = U_{obs}^{tor} \end{cases}$$

$$Z_8(r_c) = (l-3)Z_7(r_c) - \frac{4\pi\gamma_c \rho^*(r_c)}{g^*(r_c)} (Z_3(r_c) - \rho^* Z_7(r_c))$$

$$Z_8(r_e) = -(l+1)Z_7(r_e) - \frac{4\pi\gamma_e \rho^*(r_e)}{g^*(r_e)} (Z_3(r_e) - \rho^* Z_7(r_e))$$

The equation system E5.4 for spheroidal and toroidal flows in matrix form:

$$z' = A_z(r)z + f_z(r) + F_z(r) \quad (\text{E5.6})$$

$$\text{where } A_z(r) = \begin{pmatrix} -2-k & L & 0 & 0 & 0 & 0 & 0 & 0 \\ -1 & 1 & 0 & \frac{1}{\eta^*} & 0 & 0 & 0 & 0 \\ (12+4k)\eta^* & -6L\eta^* & 1 & L & 0 & 0 & \rho^*k & 0 \\ -(6+2k)\eta^* & 2(2L-1)\eta^* & -1 & -2 & 0 & 0 & 0 & 0 \\ 0 & 0 & 0 & 0 & 1 & \frac{1}{\eta^*} & 0 & 0 \\ 0 & 0 & 0 & 0 & (L-2)\eta^* & -2 & 0 & 0 \\ 0 & 0 & 0 & 0 & 0 & 0 & 1 & 1 \\ 0 & 0 & 0 & 0 & 0 & 0 & L & 0 \end{pmatrix}$$

$$f_z(r) = (0, 0, \delta\rho^{lm} g^* r^2, 0, 0, 0, 0, -4\pi\gamma\delta\rho^{lm} g^* r^3)^T$$

$$F_z(r) = (A^{lm}, B^{lm}, C^{lm}, D^{lm}, E^{lm}, F^{lm}, 0, 0)^T$$

with boundary conditions:

$$B_z z(r_c) = b_z \quad (\text{on the boundary core-mantle}) \quad (\text{E5.7})$$

$$C_z z(r_e) = c_z \quad (\text{on the surface of the Earth}),$$

$$\text{where } B_z = \begin{pmatrix} 1 & 0 & 0 & 0 & 0 & 0 & 0 & 0 \\ 0 & 0 & 0 & 1 & 0 & 0 & 0 & 0 \\ 0 & 0 & 0 & 0 & 0 & 1 & 0 & 0 \\ 0 & 0 & \frac{4\pi\gamma_c \rho^*(r_c)}{g^*(r_c)} & 0 & 0 & 0 & -(l-3) - \frac{4\pi\gamma_c (\rho^*(r_c))^2}{g^*(r_c)} & 1 \end{pmatrix} \quad \text{and } b_z = \begin{pmatrix} 0 \\ 0 \\ 0 \\ 0 \end{pmatrix}$$

$$C_z = \begin{pmatrix} 1 & 0 & 0 & 0 & 0 & 0 & 0 \\ 0 & 0 & 0 & 1 & 0 & 0 & 0 \\ 0 & 0 & 0 & 0 & 0 & 1 & 0 \\ 0 & 0 & \frac{4\pi\gamma_e \rho^*(r_e)}{g^*(r_e)} & 0 & 0 & 0 & (l+1) - \frac{4\pi\gamma_e (\rho^*(r_e))^2}{g^*(r_e)} \\ & & & & & & 1 \end{pmatrix} \text{ and } c_z = \begin{pmatrix} 0 \\ 0 \\ 0 \\ 0 \end{pmatrix}$$

The ODE system E5.6 with boundary conditions E5.7 must be solved for each harmonic mode ( $l$  (degree),  $m$  (order),  $i$ ) and each iterative step. To solve this equation system we apply the same technique as for radial viscosity models (direct Godunov method, see Chapter III).

## 5.2 Iterative method U-transform.

The 3-D viscosity function is represented as a sum of radial and lateral viscosity components:

$$\eta(r, \theta, \varphi) = \bar{\eta}(r) + \eta_0 \tilde{\eta}(r, \theta, \varphi) \quad (\text{E5.8})$$

The nature of this representation may be actually various: the radial component  $\bar{\eta}(r)$  can be chosen in different ways but we exerted ourselves to analyze the influence of such a choice on convergence of U-transform method. According to our research a choice of a radial component itself does not play any role in the resulting solution but it can accelerate the method convergence.

On the base of velocity distribution (stress distribution) obtained from the initial stage we calculate the values of the viscous terms preceded in the Appendix U.

$$A^{lm} = 0$$

$$B^{lm} = -\frac{2r}{s_{lm}\eta^*} \int_0^{2\pi} d\varphi \int_0^\pi \tilde{\eta} (e_{r\theta} Y_{lm}^\theta + e_{r\varphi} Y_{lm}^\varphi) \sin \theta d\theta$$

$$C^{lm} = -\frac{6r}{s_{m0}} \int_0^{2\pi} d\varphi \int_0^\pi \tilde{\eta} \left( e_{rr} + \frac{k(r)}{3} u_r \right) Y_{lm} \sin \theta d\theta \quad (\text{E5.9})$$

$$D^{lm} = -\frac{2r^2}{s_{lm}} \int_0^{2\pi} d\varphi \int_0^\pi (D_\theta Y_{lm}^\theta + D_\varphi Y_{lm}^\varphi) \sin \theta d\theta - \frac{1}{3} C^{lm}$$

$$E^{lm} = -\frac{2r}{s_{lm}\eta^*} \int_0^{2\pi} d\varphi \int_0^\pi \tilde{\eta} (e_{r\theta} Y_{lm}^\varphi - e_{r\varphi} Y_{lm}^\theta) \sin \theta d\theta$$

$$F^{lm} = -\frac{2r^2}{s_{lm}} \int_0^{2\pi} d\varphi \int_0^\pi (D_\theta Y_{lm}^\varphi - D_\varphi Y_{lm}^\theta) \sin \theta d\theta$$

$$D_\theta = \frac{1}{r^2} \left[ \frac{\partial \left( r\tilde{\eta}e_{\theta\theta} + \frac{k(r)}{3}\tilde{\eta}u_r \right)}{\partial \theta} + r \operatorname{ctg} \theta \tilde{\eta} (e_{\theta\theta} - e_{\varphi\varphi}) + \frac{r}{\sin \theta} \frac{\partial (\tilde{\eta}e_{\theta\varphi})}{\partial \varphi} \right]$$

$$D_\varphi = \frac{1}{r^2} \left[ \frac{1}{\sin \theta} \frac{\partial \left( r\tilde{\eta}e_{\varphi\varphi} + \frac{k(r)}{3}\tilde{\eta}u_r \right)}{\partial \varphi} + 2r \operatorname{ctg} \theta \tilde{\eta} e_{\theta\varphi} + r \frac{\partial (\tilde{\eta}e_{\theta\varphi})}{\partial \theta} \right]$$

$$s_{m0} = 4\pi$$

$$s_{lm} = s_{m0}l(l+1) = 4\pi l(l+1) \quad (s_{m0} \text{ and } s_{lm} \text{ have been derived in Part 3.1})$$

where  $e_{ij}$  are normal strains (E2.10).

On each iterative step the velocity distribution generated on the previous step is used for determination of new viscous terms.

Just for comparison here I quote the formulae published by Zhang and Christensen (1993) and Zhang (1993):

$$A^{lm} = 0$$

$$B^{lm} = \frac{r}{s_{lm}^{ZC} \eta^*} \int_0^{2\pi} d\varphi \int_0^\pi \tilde{\eta} (e_{r\theta} Y_{lm}^\theta + e_{r\varphi} Y_{lm}^\varphi) \sin \theta d\theta$$

$$C^{lm} = \frac{3r}{s_{m0}^{ZC}} \int_0^{2\pi} d\varphi \int_0^\pi \tilde{\eta} e_{rr} Y_{lm} \sin \theta d\theta$$

$$D^{lm} = \frac{r^2}{s_{lm}^{ZC}} \int_0^{2\pi} d\varphi \int_0^\pi (D_\theta^{ZC} Y_{lm}^\theta + D_\varphi^{ZC} Y_{lm}^\varphi) \sin \theta d\theta$$

(E5.10)

$$E^{lm} = \frac{r}{s_{lm}^{ZC} \eta^*} \int_0^{2\pi} d\varphi \int_0^\pi \tilde{\eta} (e_{r\theta} Y_{lm}^\varphi - e_{r\varphi} Y_{lm}^\theta) \sin \theta d\theta$$

$$F^{lm} = \frac{r^2}{s_{lm}^{ZC}} \int_0^{2\pi} d\varphi \int_0^\pi (D_\theta^{ZC} Y_{lm}^\varphi - D_\varphi^{ZC} Y_{lm}^\theta) \sin \theta d\theta$$

$$D_\theta^{ZC} = \frac{2\tilde{\eta}}{r^2} \left[ \sum_{l=0}^{l_{\max}} \sum_{m=0}^l \left( (3Z_1^{lm} - (2L-1)Z_2^{lm}) Y_{lm}^\theta + 0.5(2-L)Z_5^{lm} Y_{lm}^\varphi \right) \right] + \frac{2}{r} \frac{\partial \tilde{\eta}}{\partial \theta} (e_{\theta\theta} - e_{rr}) + \frac{2}{r \sin \theta} \frac{\partial \tilde{\eta}}{\partial \varphi} e_{\theta\varphi}$$

$$D_\varphi^{ZC} = \frac{2\tilde{\eta}}{r^2} \left[ \sum_{l=0}^{l_{\max}} \sum_{m=0}^l \left( (3Z_1^{lm} - (2L-1)Z_2^{lm}) Y_{lm}^\varphi - 0.5(2-L)Z_5^{lm} Y_{lm}^\theta \right) \right] + \frac{2}{r \sin \theta} \frac{\partial \tilde{\eta}}{\partial \varphi} (e_{\varphi\varphi} - e_{rr}) + \frac{2}{r} \frac{\partial \tilde{\eta}}{\partial \theta} e_{\theta\varphi}$$

$$s_{m0}^{ZC} = 4\pi(2 - \delta_{m0}) = s_{m0}(2 - \delta_{m0})$$

$$s_{lm}^{ZC} = s_{m0}^{ZC}l(l+1) = 4\pi(2 - \delta_{m0})l(l+1) = s_{lm}(2 - \delta_{m0})$$

$$A^{lm} = 0$$

$$B^{lm} = \frac{2r}{s_{lm}\eta} \int_0^{2\pi} d\varphi \int_0^\pi \tilde{\eta} (e_{r\theta} Y_{lm}^\theta + e_{r\varphi} Y_{lm}^\varphi) \sin \theta d\theta$$

$$C^{lm} = \frac{6r}{s_{m0}} \int_0^{2\pi} d\varphi \int_0^\pi \tilde{\eta} \left( e_{rr} + \frac{k(r)}{3} u_r \right) Y_{lm} \sin \theta d\theta$$

$$D^{lm} = \frac{2r^2}{s_{lm}} \int_0^{2\pi} d\varphi \int_0^\pi (D_\theta Y_{lm}^\theta + D_\varphi Y_{lm}^\varphi) \sin \theta d\theta - \frac{1}{3} C^{lm}$$

$$E^{lm} = \frac{2r}{s_{lm}\eta} \int_0^{2\pi} d\varphi \int_0^\pi \tilde{\eta} (e_{r\theta} Y_{lm}^\varphi - e_{r\varphi} Y_{lm}^\theta) \sin \theta d\theta$$

$$F^{lm} = \frac{2r^2}{s_{lm}} \int_0^{2\pi} d\varphi \int_0^\pi (D_\theta Y_{lm}^\varphi - D_\varphi Y_{lm}^\theta) \sin \theta d\theta$$

$$D_\theta = \frac{1}{r^2} \left[ \frac{\partial}{\partial \theta} \left( r\tilde{\eta} e_{\theta\theta} + \frac{k(r)}{3} \tilde{\eta} u_r \right) + r \operatorname{ctg} \theta \tilde{\eta} (e_{\theta\theta} - e_{\varphi\varphi}) + \frac{r}{\sin \theta} \frac{\partial (\tilde{\eta} e_{\theta\varphi})}{\partial \varphi} \right]$$

$$D_\varphi = \frac{1}{r^2} \left[ \frac{1}{\sin \theta} \frac{\partial}{\partial \varphi} \left( r\tilde{\eta} e_{\theta\varphi} + \frac{k(r)}{3} \tilde{\eta} u_r \right) + 2r \operatorname{ctg} \theta \tilde{\eta} e_{\theta\varphi} + r \frac{\partial (\tilde{\eta} e_{\theta\varphi})}{\partial \theta} \right]$$

Figure (VT5.1) Misprints in U-transform method by Zhang and Christensen (1993) and Zhang (1993). The principal misprints (missing terms or incorrect expressions) in viscous terms are marked by red circles. The terms appearing due to the effect of mantle compressibility are marked by green circles.

$$s_{m0}^{ZC} = 4\pi(2 - \delta_{m0}) = s_{m0}(2 - \delta_{m0})$$

$$s_{lm}^{ZC} = s_{m0}^{ZC}l(l+1) = 4\pi(2 - \delta_{m0})l(l+1) = s_{lm}(2 - \delta_{m0})$$

Figure (NC5.1) Misprints in normalization coefficients in U-transform method by Zhang and Christensen (1993) and Zhang (1993).

Based on the deductions produced in Appendix U we are proceeding to the the main conclusions about the nature of distinctions between the method stated by Zhang and Christensen (1993) (Zhang (1993)) and method recently derived:

- Misprint in orthonormalization laws for the spherical functions and their derivatives result in reduction of all viscous corrections for the tesseral ( $0 < m < l$ ) and sectoral ( $m=l$ ) harmonics by appearing of surplus normalization coefficient  $2 - \delta_{m0}$  in  $s_{m0}^{zC} = 4\pi(2 - \delta_{m0})$  and  $s_{lm}^{zC} = 4\pi(2 - \delta_{m0})l(l+1)$ .
- The published viscous terms have the opposite sign compared to the recently derived. In the general case the values of mantle velocities must be reduced by the incorporation of the high-viscous areas  $\tilde{\eta}(r, \theta, \varphi) > 0$ , consequently, the signs of viscous corrections must be opposite to the signs of mantle velocities.
- The loss of the coefficient=2 in all the published viscous terms results in further reduction of viscous terms. This coefficient appears due to the nature of the relation between viscous stress tensor and mantle velocities.
- False understanding of the role of dynamic pressure (spherical harmonic coefficients for the dynamic pressure were recognized by Zhang and Christensen (1993) as the spherical functions and expanded into spherical harmonics once more) results in the wrong contribution of the spheroidal and toroidal components.

These are principal misprints, which appeared in the description of the U-transform iterative method stated by Zhang (1993), Zhang and Christensen (1993). The particular contribution of these misprints will be analyzed in details in Part 5.4 based on several models.

### 5.3 Iterative method W-transform.

As said above, the most principal distinction between the W-transform and U-transform methods originates from different ways to represent mantle velocities and 3-D viscosity. In general, the W-transform technique pursues an idea of reduction of viscous corrections appearing due to LVV and, consequently, a better

convergence of the method. Under the theoretical and numerical conclusions of this study in case of mobile small-scale viscous rocks the effect of the first approach seems to be opposite to the forethought advanced effect. In this case the first exaggerated approach eventuates colossal correction values; therefore, the method either does not converge or gives a false result. And in general, the W-transform method offers a very scanty domain of applicability according to our analysis. In Part 5.4 I consider different models aimed at estimating the efficiency of each iterative method.

The 3-D viscosity function is represented as a product of radial and lateral components:

$$\eta(r, \theta, \varphi) = \bar{\eta}(r) * \hat{\eta}(r, \theta, \varphi) \quad (\text{E5.11})$$

where choice of  $\bar{\eta}(r)$  can be various as well as in U-transform.

Thus, the initial velocities and a consequent approach of velocities appear to be imaginary approximated by the viscosity essence  $\hat{\eta}(r, \theta, \varphi)$ :

$$\begin{aligned} v_r &= \hat{\eta}(r, \theta, \varphi) * u_r = \sum_{l=0}^{l_{\max}} \sum_{m=0}^l Z_1^{lm} Y_{lm}(\theta, \varphi) \\ v_\theta &= \hat{\eta}(r, \theta, \varphi) * u_\theta = \sum_{l=0}^{l_{\max}} \sum_{m=0}^l [Z_2^{lm} Y_{lm}^\theta(\theta, \varphi) + Z_5^{lm} Y_{lm}^\varphi(\theta, \varphi)] \\ v_\varphi &= \hat{\eta}(r, \theta, \varphi) * u_\varphi = \sum_{l=0}^{l_{\max}} \sum_{m=0}^l [Z_2^{lm} Y_{lm}^\varphi(\theta, \varphi) - Z_5^{lm} Y_{lm}^\theta(\theta, \varphi)] \end{aligned} \quad (\text{E5.12})$$

The viscous terms appearing due to LVV can be calculated with the aid of mantle velocity distribution obtained from the previous iterative step:

$$\begin{aligned} A^{lm} &= \frac{1}{s_{m0}} \int_0^{2\pi} d\varphi \int_0^\pi [\eta_r v_r + r \eta_\theta v_\theta + r \eta_\varphi v_\varphi] Y_{lm} \sin \theta d\theta \\ B^{lm} &= \frac{1}{s_{lm}} \int_0^{2\pi} d\varphi \int_0^\pi [(\eta_r v_\theta + \eta_\theta v_r) Y_{lm}^\theta + (\eta_r v_\varphi + \eta_\varphi v_r) Y_{lm}^\varphi] \sin \theta d\theta \\ C^{lm} &= \frac{6\eta^*}{s_{m0}} \int_0^{2\pi} d\varphi \int_0^\pi \eta_r v_r Y_{lm} \sin \theta d\theta - 6\eta^* A^{lm} = -\frac{6\eta^* r}{s_{m0}} \int_0^{2\pi} d\varphi \int_0^\pi (\eta_\theta v_\theta + \eta_\varphi v_\varphi) Y_{lm} \sin \theta d\theta \end{aligned}$$

$$D^{lm} = \frac{\eta^*}{s_{lm}} \int_0^{2\pi} d\varphi \int_0^\pi [D_\theta Y_{lm}^\theta + D_\varphi Y_{lm}^\varphi] \sin \theta d\theta - \frac{1}{3} C^{lm} \quad (\text{E5.13})$$

$$E^{lm} = \frac{1}{s_{lm}} \int_0^{2\pi} d\varphi \int_0^\pi [(\eta_r v_\theta + \eta_\theta v_r) Y_{lm}^\varphi - (\eta_r v_\varphi + \eta_\varphi v_r) Y_{lm}^\theta] \sin \theta d\theta$$

$$F^{lm} = \frac{\eta^*}{s_{lm}} \int_0^{2\pi} d\varphi \int_0^\pi [D_\theta Y_{lm}^\varphi - D_\varphi Y_{lm}^\theta] \sin \theta d\theta$$

where  $\eta_r = \frac{\partial \ln \hat{\eta}(r, \theta, \varphi)}{\partial \ln r}$ ,  $\eta_\theta = \frac{\partial \ln \hat{\eta}(r, \theta, \varphi)}{\partial \theta}$ ,  $\eta_\varphi = \frac{1}{\sin \theta} \frac{\partial \ln \hat{\eta}(r, \theta, \varphi)}{\partial \varphi}$

$$D_\theta = 2 \frac{\partial(\eta_\theta v_\theta)}{\partial \theta} + 2 \text{ctg} \theta (\eta_\theta v_\theta - \eta_\varphi v_\varphi) + \frac{1}{\sin \theta} \frac{\partial(\eta_\varphi v_\theta + \eta_\theta v_\varphi)}{\partial \varphi}$$

$$D_\varphi = \frac{2}{\sin \theta} \frac{\partial(\eta_\varphi v_\varphi)}{\partial \varphi} + 2 \text{ctg} \theta (\eta_\varphi v_\theta + \eta_\theta v_\varphi) + \frac{\partial(\eta_\varphi v_\theta + \eta_\theta v_\varphi)}{\partial \theta}$$

Appendix W gives thorough comprehension of the deductions concerned to the W-transform iterative method.

For comparison here I cite the formulae published by Zhang (1993), Zhang and Christensen (1993):

$$A^{lm} = \frac{r}{s_{m0}^{ZC}} \int_0^{2\pi} d\varphi \int_0^\pi [v \cdot \nabla \ln \hat{\eta}] Y_{lm} \sin \theta d\theta = \frac{r}{s_{m0}^{ZC}} \int_0^{2\pi} d\varphi \int_0^\pi \left[ \frac{\partial \ln \hat{\eta}}{\partial r} v_r + \frac{\partial \ln \hat{\eta}}{\partial \theta} v_\theta + \frac{\partial \ln \hat{\eta}}{\partial \varphi} v_\varphi \right] Y_{lm} \sin \theta d\theta$$

$$B^{lm} = \frac{1}{s_{lm}^{ZC}} \int_0^{2\pi} d\varphi \int_0^\pi \left[ \left( \frac{\partial \ln \hat{\eta}}{\partial \ln r} v_\theta + \frac{\partial \ln \hat{\eta}}{\partial \theta} v_r \right) Y_{lm}^\theta + \left( \frac{\partial \ln \hat{\eta}}{\partial \ln r} v_\varphi + \frac{\partial \ln \hat{\eta}}{\partial \varphi} v_r \right) Y_{lm}^\varphi \right] Y_{lm} \sin \theta d\theta$$

$$C^{lm} = \frac{6\eta^* r}{s_{m0}^{ZC}} \int_0^{2\pi} d\varphi \int_0^\pi \frac{\partial \ln \hat{\eta}}{\partial r} v_r Y_{lm} \sin \theta d\theta - 6\eta^* A^{lm}$$

$$D^{lm} = \frac{\eta^*}{s_{lm}^{ZC}} \int_0^{2\pi} d\varphi \int_0^\pi [D_\theta^{ZC} Y_{lm}^\theta + D_\varphi^{ZC} Y_{lm}^\varphi] \sin \theta d\theta + 2\eta^* A^{lm} \quad (\text{E5.14})$$

$$E^{lm} = \frac{1}{s_{lm}^{ZC}} \int_0^{2\pi} d\varphi \int_0^\pi \left[ \left( \frac{\partial \ln \hat{\eta}}{\partial \ln r} v_\theta + \frac{\partial \ln \hat{\eta}}{\partial \theta} v_r \right) Y_{lm}^\varphi - \left( \frac{\partial \ln \hat{\eta}}{\partial \ln r} v_\varphi + \frac{\partial \ln \hat{\eta}}{\partial \varphi} v_r \right) Y_{lm}^\theta \right] Y_{lm} \sin \theta d\theta$$

$$F^{lm} = \frac{\eta^*}{s_{lm}^{ZC}} \int_0^{2\pi} d\varphi \int_0^\pi [D_\theta^{ZC} Y_{lm}^\varphi - D_\varphi^{ZC} Y_{lm}^\theta] \sin \theta d\theta Y_{lm}^\theta$$

$$D_\theta^{ZC} = 2 \frac{\partial \left( \frac{\partial \ln \hat{\eta}}{\partial \theta} v_\theta - \frac{\partial \ln \hat{\eta}}{\partial r} v_r \right)}{\partial \theta} + 2 \text{ctg} \theta \left( \frac{\partial \ln \hat{\eta}}{\partial \theta} v_\theta - \frac{1}{\sin \theta} \frac{\partial \ln \hat{\eta}}{\partial \varphi} v_\varphi \right) + \frac{1}{\sin \theta} \frac{\partial \left( \frac{1}{\sin \theta} \frac{\partial \ln \hat{\eta}}{\partial \varphi} v_\theta + \frac{\partial \ln \hat{\eta}}{\partial \theta} v_\varphi \right)}{\partial \varphi}$$

$$D_\varphi^{ZC} = \frac{2}{\sin \theta} \frac{\partial \left( \frac{1}{\sin \theta} \frac{\partial \ln \hat{\eta}}{\partial \varphi} v_\varphi - \frac{\partial \ln \hat{\eta}}{\partial r} v_r \right)}{\partial \varphi} + 2ctg\theta \left( \frac{1}{\sin \theta} \frac{\partial \ln \hat{\eta}}{\partial \varphi} v_\theta + \frac{\partial \ln \hat{\eta}}{\partial \theta} v_\varphi \right) + \frac{\partial \left( \frac{1}{\sin \theta} \frac{\partial \ln \hat{\eta}}{\partial \varphi} v_\theta + \frac{\partial \ln \hat{\eta}}{\partial \theta} v_\varphi \right)}{\partial \theta}$$

$$s_{m0}^{ZC} = 4\pi(2 - \delta_{m0}) = s_{m0}(2 - \delta_{m0})$$

$$s_{lm}^{ZC} = s_{m0}^{ZC}l(l+1) = 4\pi(2 - \delta_{m0})l(l+1) = s_{lm}(2 - \delta_{m0})$$

$$A^{lm} = \frac{1}{s_{m0}} \int_0^{2\pi} d\varphi \int_0^\pi [\eta_r v_r + r\eta_\theta v_\theta + r\eta_\varphi v_\varphi] Y_{lm} \sin \theta d\theta$$

$$B^{lm} = \frac{1}{s_{lm}} \int_0^{2\pi} d\varphi \int_0^\pi [(\eta_r v_\theta + \eta_\theta v_r) Y_{lm}^\theta + (\eta_r v_\varphi + \eta_\varphi v_r) Y_{lm}^\varphi] \sin \theta d\theta$$

$$C^{lm} = \frac{6\eta^*}{s_{m0}} \int_0^{2\pi} d\varphi \int_0^\pi \eta_r v_r Y_{lm} \sin \theta d\theta - 6\eta^* A^{lm} = -\frac{6\eta^* r}{s_{m0}} \int_0^{2\pi} d\varphi \int_0^\pi (\eta_\theta v_\theta + \eta_\varphi v_\varphi) Y_{lm} \sin \theta d\theta$$

$$D^{lm} = \frac{\eta^*}{s_{lm}} \int_0^{2\pi} d\varphi \int_0^\pi [D_\theta Y_{lm}^\theta + D_\varphi Y_{lm}^\varphi] \sin \theta d\theta - \frac{1}{3} C^{lm}$$

$$E^{lm} = \frac{1}{s_{lm}} \int_0^{2\pi} d\varphi \int_0^\pi [(\eta_r v_\theta + \eta_\theta v_r) Y_{lm}^\varphi - (\eta_r v_\varphi + \eta_\varphi v_r) Y_{lm}^\theta] \sin \theta d\theta$$

$$F^{lm} = \frac{\eta^*}{s_{lm}} \int_0^{2\pi} d\varphi \int_0^\pi [D_\theta Y_{lm}^\varphi - D_\varphi Y_{lm}^\theta] \sin \theta d\theta$$

$$D_\theta = 2 \frac{\partial(\eta_\theta v_\theta)}{\partial \theta} + 2ctg\theta(\eta_\theta v_\theta - \eta_\varphi v_\varphi) + \frac{1}{\sin \theta} \frac{\partial(\eta_\varphi v_\theta + \eta_\theta v_\varphi)}{\partial \varphi}$$

$$D_\varphi = \frac{2}{\sin \theta} \frac{\partial(\eta_\varphi v_\varphi)}{\partial \varphi} + 2ctg\theta(\eta_\varphi v_\theta + \eta_\theta v_\varphi) + \frac{\partial(\eta_\varphi v_\theta + \eta_\theta v_\varphi)}{\partial \theta}$$

Figure (VT5.2) Misprints in W-transform method by Zhang and Christensen (1993) and Zhang (1993). The principal misprints (missing terms or incorrect expressions) in viscous terms are marked by red circles.

$$s_{m0}^{ZC} = 4\pi(2 - \delta_{m0}) = s_{m0}(2 - \delta_{m0})$$

$$s_{lm}^{ZC} = s_{m0}^{ZC}l(l+1) = 4\pi(2 - \delta_{m0})l(l+1) = s_{lm}(2 - \delta_{m0})$$

Figure (NC5.2) Misprints in normalization coefficients in W-transform method by Zhang and Christensen (1993) and Zhang (1993).

The first and most obvious difference, which may attract an attention, is the difference in coefficients  $s_{m0}$  and  $s_{lm}$  stated by Zhang and Christensen (1993) (Zhang (1993)) in both iterative methods and recently derived coefficients (NC5.2). According to the formulae published by Zhang (1993), Zhang and Christensen (1993)  $s_{m0}^{ZC} = 4\pi(2 - \delta_{m0})$  and  $s_{lm}^{ZC} = 4\pi(2 - \delta_{m0})l(l+1)$  are orthonormalization coefficients for the spherical functions and their derivatives. In Chapter III, Part 3.1 orthonormalization coefficients  $s_{m0}$  and  $s_{lm}$  have been derived once more from the orthonormalization laws. They appear to differ from those stated by Zhang (1993), Zhang and Christensen (1993) for all harmonic modes except for the zonal harmonics:  $s_{m0} = 4\pi$  and  $s_{lm} = 4\pi l(l+1)$  (see Part 3.1).

The viscous terms  $D^{lm}$  and  $F^{lm}$  (VT5.2) in the equations for spheroidal and toroidal horizontal stress for the W-transform method differ from those stated by Zhang (1993), Zhang and Christensen (1993) in the same manner as  $D^{lm}$  and  $F^{lm}$  (VT5.1) derived for the U-transform method. The reason of this distinction is also the same: false understanding of the particular role of dynamic pressure. The rest of viscous terms appearing in the W-transform method due to LVV was published by Zhang and Christensen (1993) without misprints, except for the surplus normalization coefficient  $2 - \delta_{m0}$  in  $s_{m0}^{ZC} = 4\pi(2 - \delta_{m0})$  and  $s_{lm}^{ZC} = 4\pi(2 - \delta_{m0})l(l+1)$  (analogously for both methods U-transform and W-transform). An appearance of this normalization coefficient in the W-transform method results in insufficient correction of the "imaginary" mantle velocity flows. But as soon as we try to revert back to the required velocities by inverse change of variables, the effect appears to be two times exaggerated, therefore, the changes in the resulting mantle flows are to be monstrous. The misprints in the published viscous terms for spheroidal and toroidal stresses affect not only stress distribution but also the figure of the geoid (through boundary conditions) and velocity flows.

#### 5.4 Application of the W- and U-transform iterative methods to some synthetic models. Domains of method applicability.

**Model 5.4a:** The first model is aimed at comparison of mantle velocities and the geoid obtained from the U-transform and W-transform methods. As shown below the W-transform method may not be applied to the viscosity models with the high contrast, it was, therefore, decided to consider the first models with rather low viscosity contrast (approximately 1.35 orders of magnitude). In this case we can expect that both iterative methods provide a perfect convergence.

The description of the model parameters:

- Radial density profile  $\bar{\rho}(r)$  from Figure (F4.2),  $\rho^*(r) = \frac{\bar{\rho}(r)}{\rho_0}$ ,

$$\text{where } \rho_0 = 4430 \left[ \frac{\text{kg}}{\text{m}^3} \right].$$

- Density anomaly:  $\delta\rho = Y_{211}(\theta, \varphi) = N_{21} P_2^1(\cos\theta) \cos\varphi = \sqrt{\frac{15}{4}} \sin 2\theta \cos\varphi$  for all depths.

- Radial viscosity  $\eta^*(r) = 1$ ,  $\bar{\eta}(r) = \eta_0 = 10^{21} [\text{Pa}\cdot\text{s}]$

- 3-D viscosity distribution:

$$\eta(r, \theta, \varphi) = \eta_0 \cdot \begin{cases} e^{-\frac{\ln(10) \cdot (1 + \cos 4\theta)(1 + \cos 4\varphi)}{4}}, & \frac{\pi}{4} \leq \varphi \leq \frac{3\pi}{4} \\ 2 - e^{-\frac{\ln(10) \cdot (1 + \cos 4\theta)(1 + \cos 4\varphi)}{4}}, & \frac{5\pi}{4} \leq \varphi \leq \frac{7\pi}{4} \end{cases}, \frac{\pi}{4} \leq \theta \leq \frac{3\pi}{4}$$

$$\eta(r, \theta, \varphi) = \eta_0, \text{ otherwise}$$

Mantle velocities:

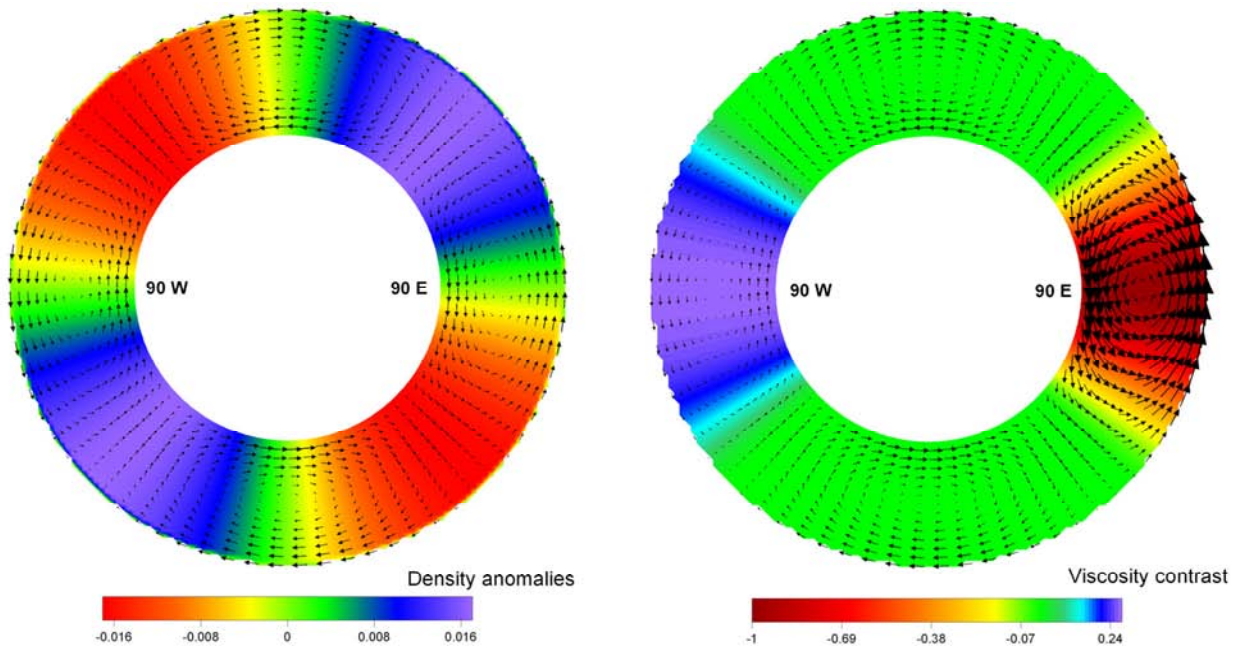


Figure (F5.1) Density anomalies and LVV [dimensionless].

Left: Density anomalies and velocities corresponding to the constant viscosity model.

Right: LVV and response of velocity flow shown in (F5.1 Left) on appearance of the LVV.

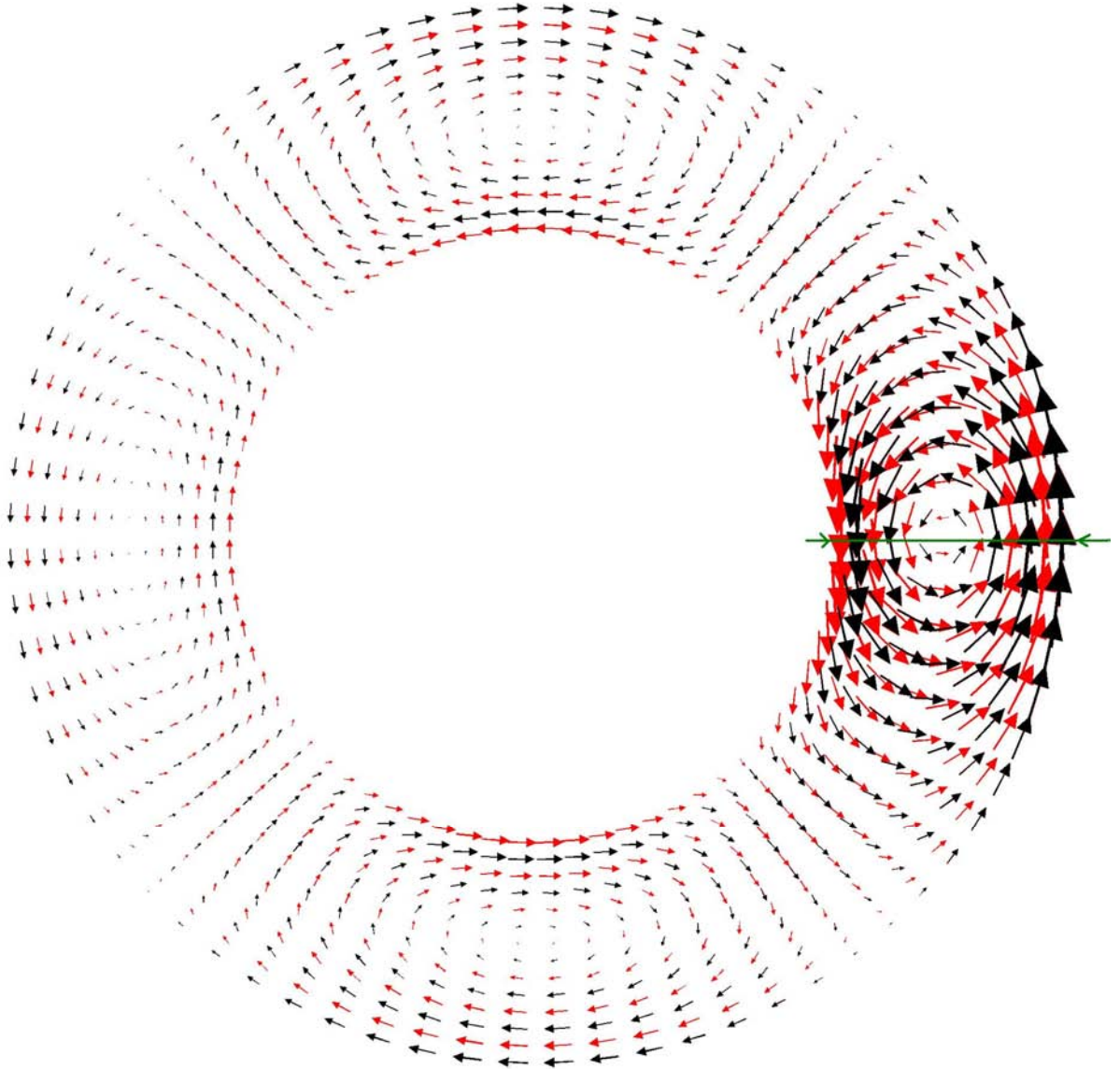


Figure (F5.2) Comparison of velocity flows calculated by U-transform (black arrows) and W-transform (red arrows) iterative methods for the model with density anomalies and LVV shown in figure (F5.1). Green pointers mark the cross-section for the velocity components, which are analysed in the following figure (F5.3).

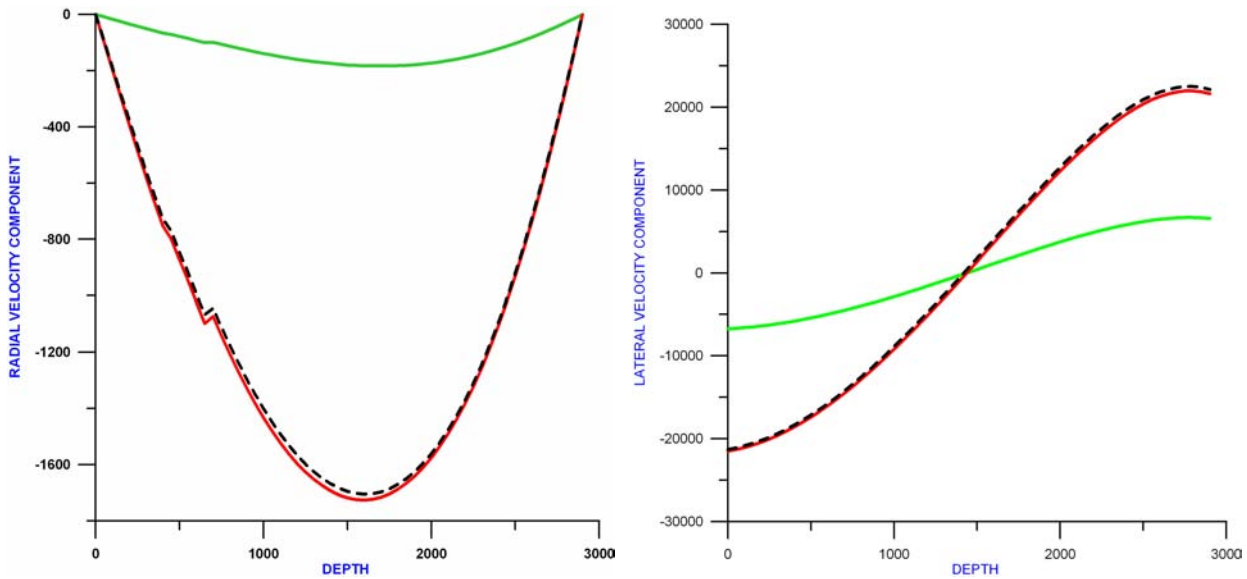


Figure (F5.3) Cross-section marked in figure (F5.2) by green line [mm/year]:

- Green curve: velocity profile calculated for the constant viscosity model.
- Black dashed curve: velocity profile calculated with effect of LVV by U-transform method.
- Red curve: velocity profile calculated with effect of LVV by W-transform method.

Left: Radial velocity component  $u_r$ .

Right: Lateral velocity component  $u_\theta$ .

Cross-sections of the velocity flows represented in figures (F5.2) and (F5.3) show good agreement between velocity distribution calculated by the U-transform and W-transform method. The difference between velocity distributions obtained with the aid of two iterative methods does not exceed 1% of the velocity values in the area with the highest contrast but still there exists some distinction, which is in general greater than the difference between the calculated geoids.

Dynamic geoid:

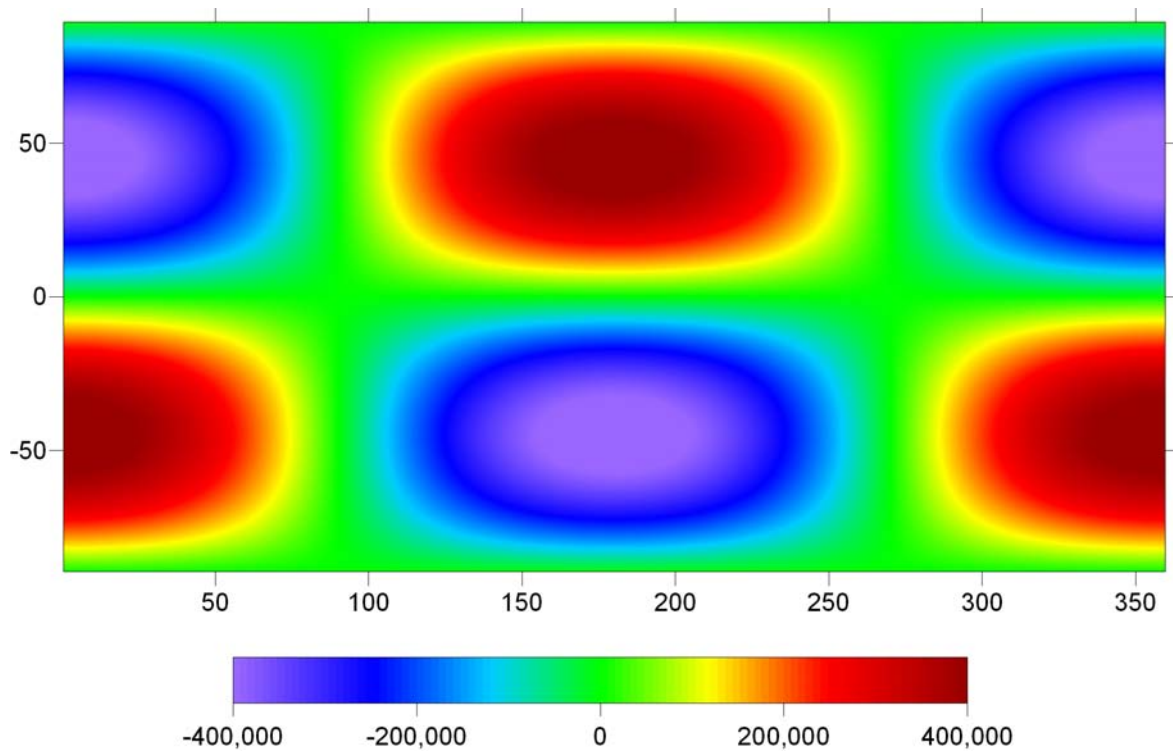


Figure (F5.4) Dynamic geoid calculated for the constant viscosity model [m].

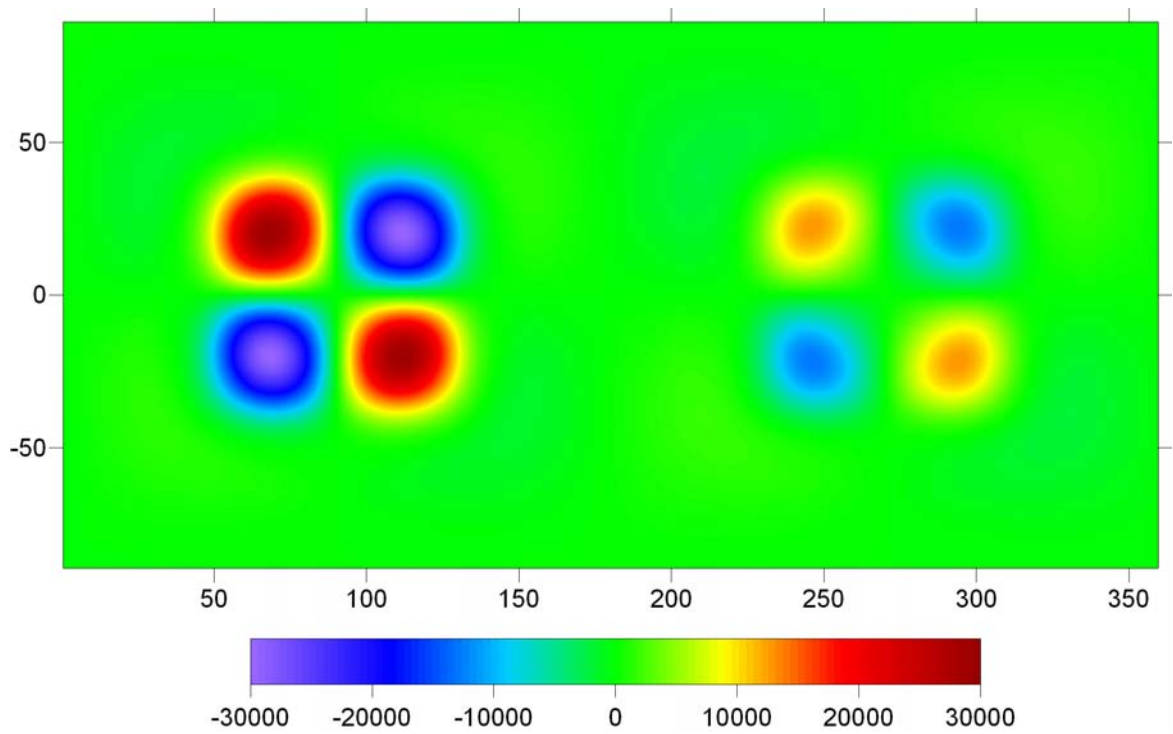


Figure (F5.5) Difference between geoid calculated with effect of LVV by U-transform method and geoid calculated for the constant viscosity model [m].

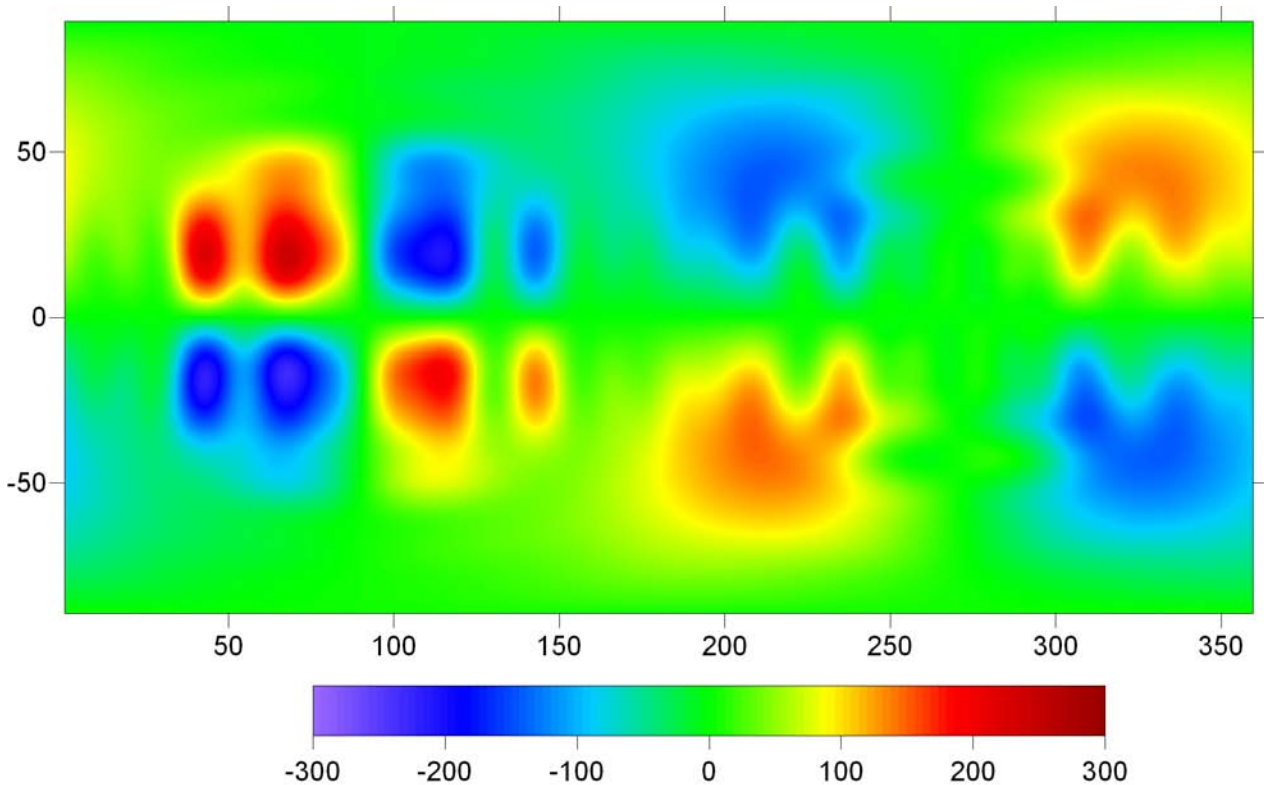


Figure (F5.6) Difference between geoids calculated with effect of LVV by U-transform and W-transform iterative methods [m].

The difference between the geoids calculated by the U-transform and W-transform methods is rather insignificant (less than 1% of the total change) as it is easy to see in figure (F5.6), especially, compared to the initial geoid calculated for the constant viscosity model (F5.4) and the contribution of LVV to the shape of the geoid according to the resulting difference shown in figure (F5.5).

**Model 5.4b:** Now let us look at the response of velocity flow on LVV simulated by the initial iterative methods stated by Zhang and Christensen (1993). This model has the same input data except for some simplification applied to LVV: the high-viscous area (on the right side of figure F5.1 right) is excluded from the test.

3-D viscosity distribution:

$$\eta(r, \theta, \varphi) = \eta_0 \cdot e^{-\ln(10) \frac{(1+\cos 4\theta)(1+\cos 4\varphi)}{4}}, \frac{\pi}{4} \leq \varphi \leq \frac{3\pi}{4} \ \& \ \frac{\pi}{4} \leq \theta \leq \frac{3\pi}{4}$$

$$\eta(r, \theta, \varphi) = \eta_0, \text{ otherwise.}$$

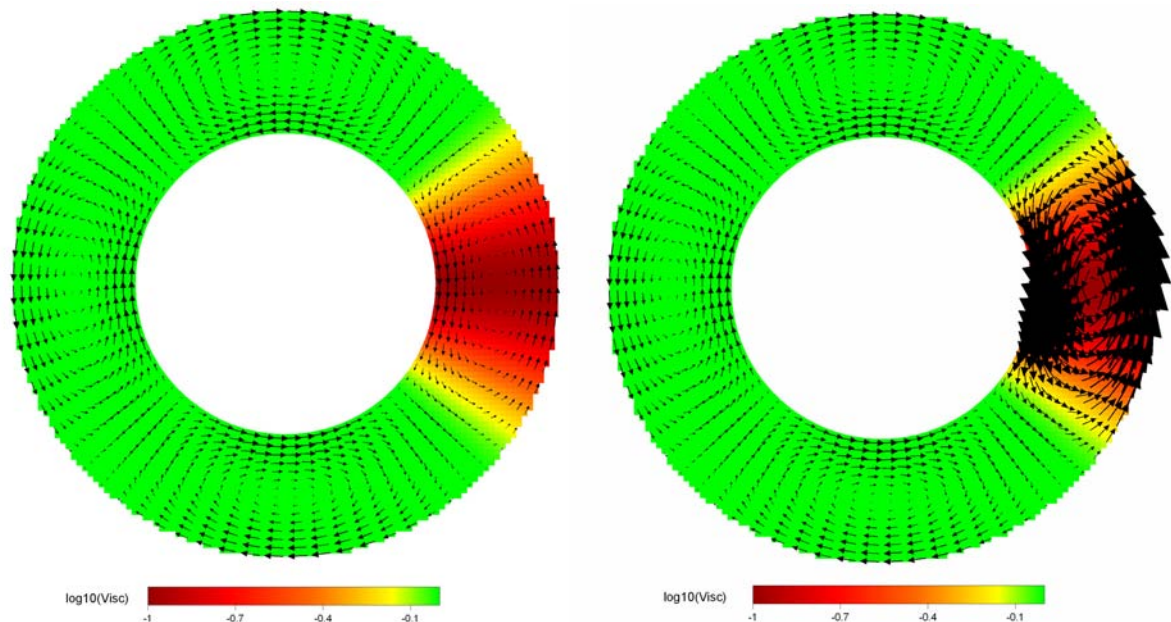


Figure (F5.7) LVV [dimensionless] and velocity distribution calculated by iterative methods with the initial formulae stated by Zhang and Christensen (1993).

Left: U-transform method by Zhang and Christensen (1993) and Zhang (1993)

Right: W-transform method by Zhang and Christensen (1993) and Zhang (1993)

As explained in Part 5.2 the viscous corrections for the U-transform method produced by Zhang and Christensen (1993) have the opposite sign, which is clearly seen in figure (F5.7 left). The velocity values have diminished in the low-viscosity area; that is quite the opposite of what we can expect. In general, the corrections occurring due to LVV are rather insignificant since two coefficients in the viscous terms were lost while publishing the methods in the works by Zhang (1993) and Zhang and Christensen (1993) (see Part 5.2). At the same time an application of the initial W-transform method stated by Zhang (1993), Zhang and Christensen (1993) to the same LVV model produced far too exaggerated changes in velocity flows (F5.7 right), that also result from the loss of coefficients in the viscous terms (see Part 5.3).

**Model 5.4c:** The next set of models is aimed at the definition of limitations for the U-transform and W-transform methods. The viscosity contrast has been gradually increased from  $10^0$  till  $10^7$ . The parameters (density anomalies, radial viscosity and density profiles) of the analyzed models are absolutely the same as for model 5.4a. The viscosity distribution is described by:

$$\eta(r, \theta, \varphi) = \eta_0 \cdot \begin{cases} e^{-\frac{\ln(\text{VC})(1+\cos 4\theta)(1+\cos 4\varphi)}{4}}, & \frac{\pi}{4} \leq \varphi \leq \frac{3\pi}{4} \\ 2 - e^{-\frac{\ln(\text{VC})(1+\cos 4\theta)(1+\cos 4\varphi)}{4}}, & \frac{5\pi}{4} \leq \varphi \leq \frac{7\pi}{4} \end{cases}, \frac{\pi}{4} \leq \theta \leq \frac{3\pi}{4}$$

$$\eta(r, \theta, \varphi) = \eta_0, \text{ otherwise}$$

where VC is the viscosity contrast [ $10^0, 10^7$ ].

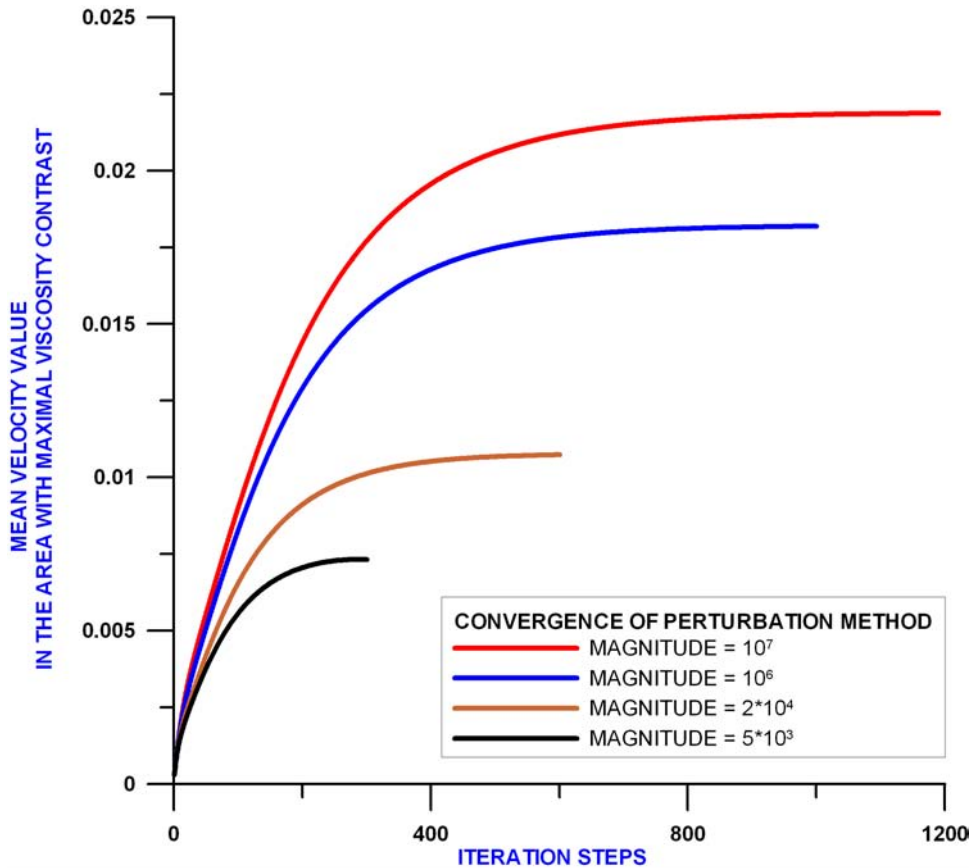


Figure (F5.8) Convergence of U-transform method applied to the strong LVV (3.5, 4.2, 6 and 7 orders of magnitude) [dimensionless velocity].

The set of the profiles shown in figure (F5.8) demonstrates stable convergence of the U-transform method under the conditions of extremely high viscosity contrast. In case of a viscosity contrast

lower than 3 orders of magnitude the number of iterative steps required for convergence achievement is rather acceptable. But in case of stronger LVV it goes up just like geometrical progression:

- Convergence of the U-transform method applied to the models with LVV of 2 orders of magnitude is already achieved after 60 iterative steps;
- LVV of 3 orders of magnitude require approximately 150-200 steps;
- In case of 7 orders of magnitude an iterative process comprises nearly 1200 iterative steps.

The adaptation of iterative methods to the models with strong LVV is, therefore, disadvantaged by the enormous number of iterative steps required for the complete convergence achievement. But this conclusion is only correct for the models with an analytical LVV specification. An iterative process converges rather fast even in case of very strong LVV if the real data used is smoothed to some harmonic degree.

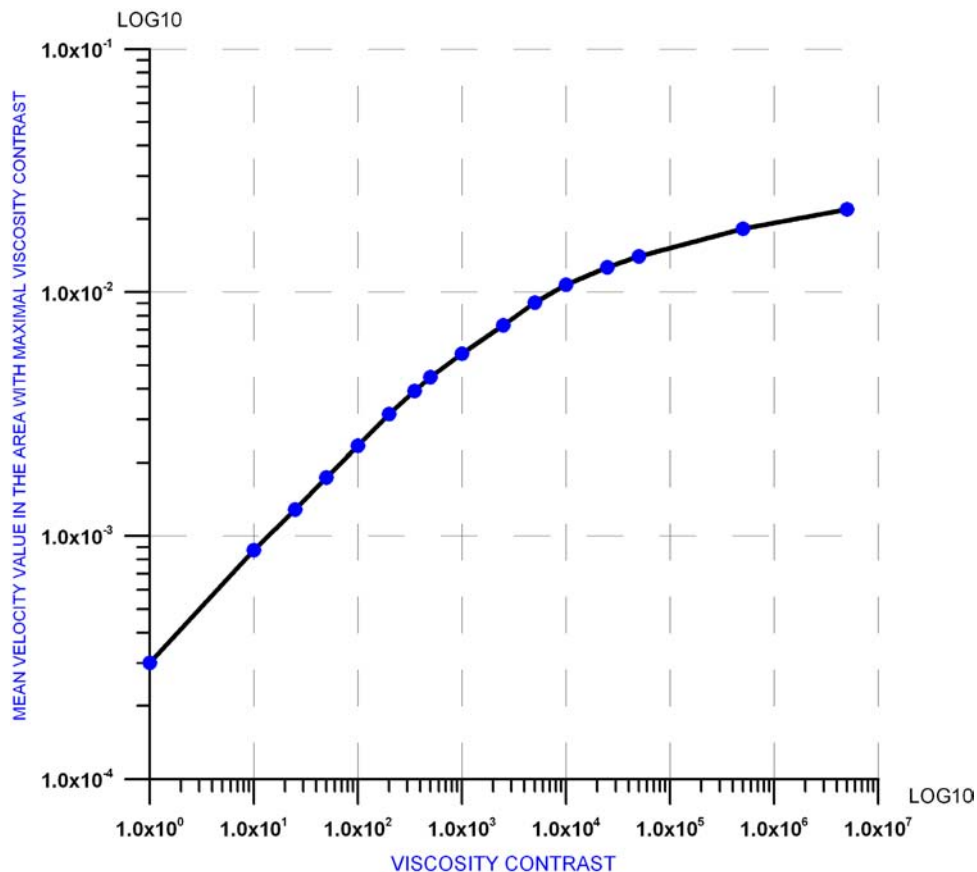


Figure (F5.9) Response of mantle flow on LVV (logarithmic scales) in the area with low viscosity [dimensionless velocity].

Figure (F5.9) shows the changes occurring due to the incorporation of the low viscosity areas with different viscosity contrasts. Up to 4 orders of magnitude the profile is almost linear (in logarithmic scales), consequently, we should not expect any significant lowering of precision, but for magnitudes larger than 4 orders the linearity of functional dependence is gradually distorted. The lack of method precision can explain this disturbance of the profile shape as well as the change of mantle flow behavior. According to the analysis provided by the help of CITCOM (Moresi et al. (2005); Rogozhina et al. (2005, 2006); Baranov et al. (2007)) the convective cells located in the low-viscosity areas with a viscosity contrast of more than 4 orders of magnitude start to behave independently of the rest of the mantle flows.

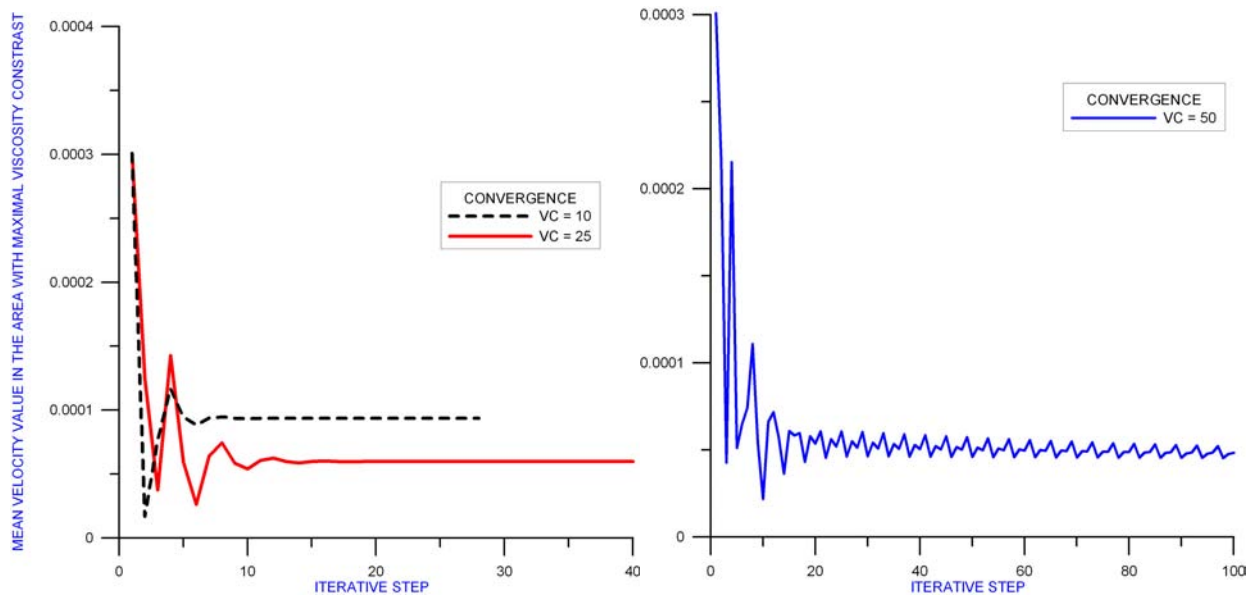


Figure (F5.10) Convergence of W-transform method. W-transform iterative method does not converge for the viscosity contrast greater than 50 [dimensionless velocity  $V$  corresponding to velocities described in Zhang and Christensen, 1993].

Figure (F5.10) shows convergence of the W-transform method under the same conditions as the U-transform method, however, for a lower viscosity contrast in the area with low viscosity. Based on this figure we can conclude that at least, for some models the W-transform method has a very scanty domain of applicability, consequently, we cannot consider this iterative method as a high-capacity technique.

**Model 5.4d:** This model has been developed to study different behaviors of small-scale high-viscous fragments in the mantle. It will be demonstrated by this set of models that the small-scale fragments of high-viscous material behave in absolutely different way under diverse conditions. Such parameters as density anomalies and density radial profile remain customary for all the models including this one.

- The radial viscosity profile is shown in figure (F5.11).



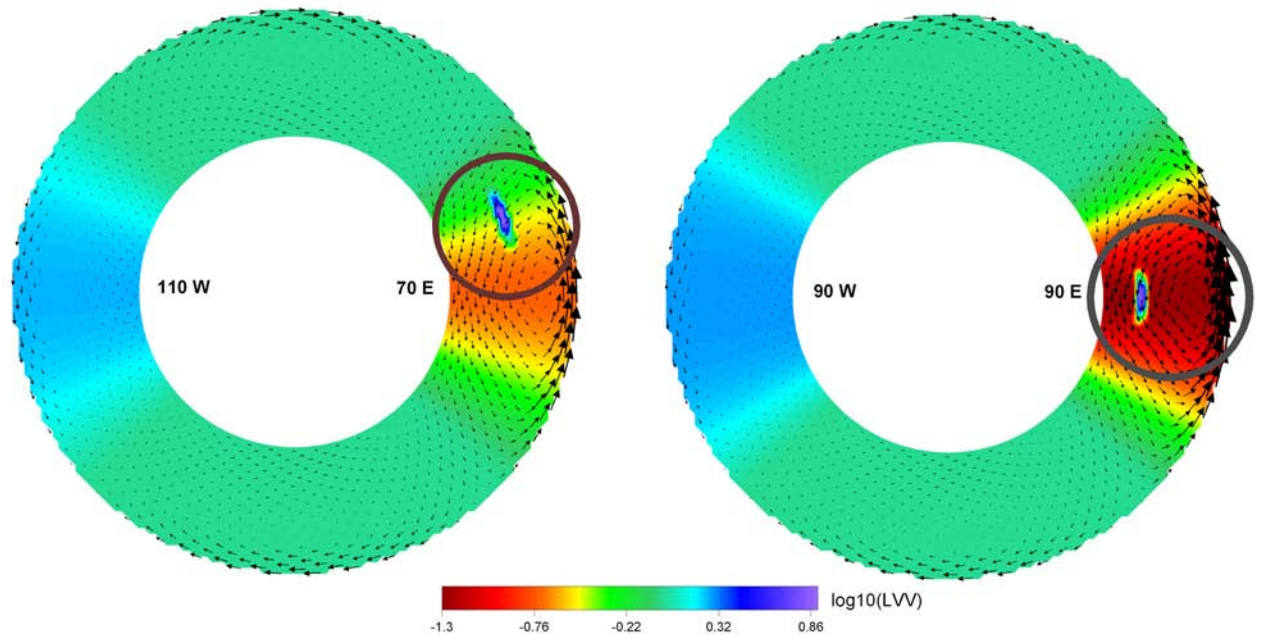


Figure (F5.12) Small-scale high-viscous fragments are located inside the low viscosity area. Shown velocities correspond to the Model 5.4b with VC = 20.

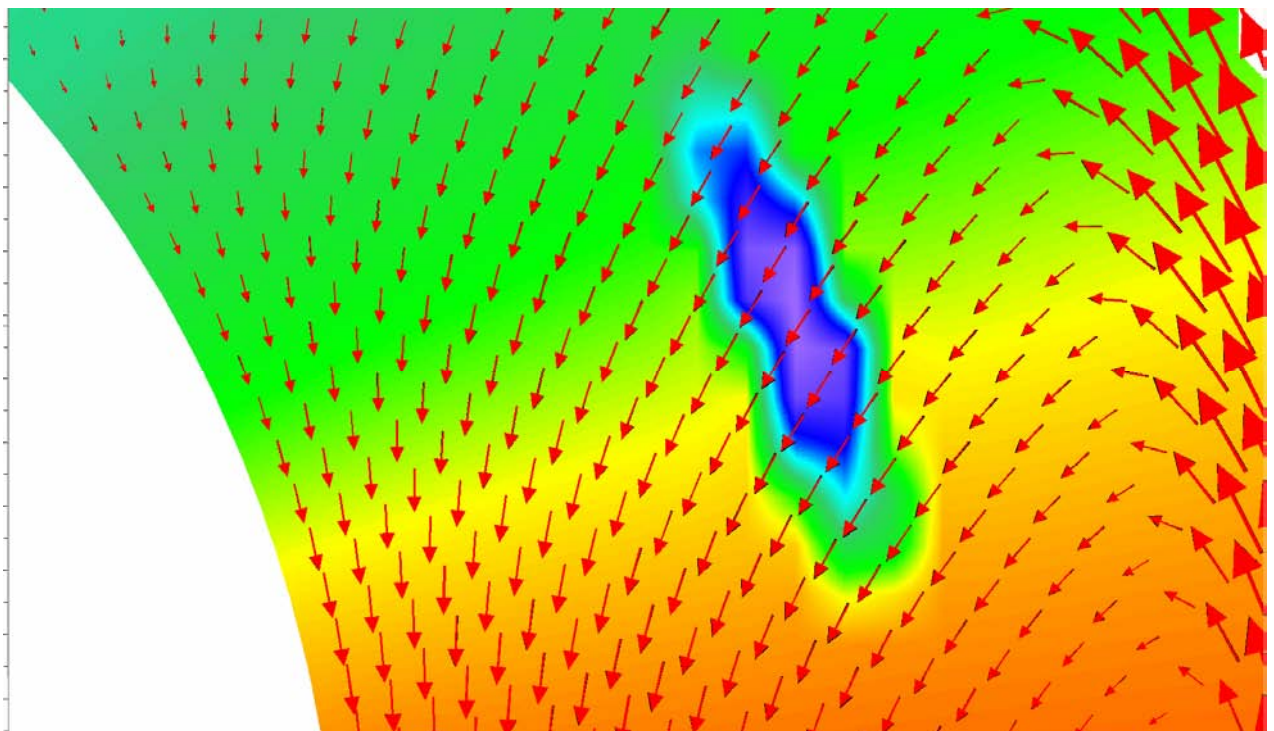


Figure (F5.13) Zoomed small-scale high-viscous fragment shown in figure (F5.12 left). The high-viscous fragment (with VC=170) is situated on the way of descending flow.

Black arrows: initial velocity distribution shown in figure (F5.12 Left)

Red arrows: velocity distribution changed by appearance of viscous fragment.

The viscous fragment located on the way of the descending flow appears to play a very small part in forming the global flow. It seems to be pulled by surrounding mass without any significant influence on its velocities.

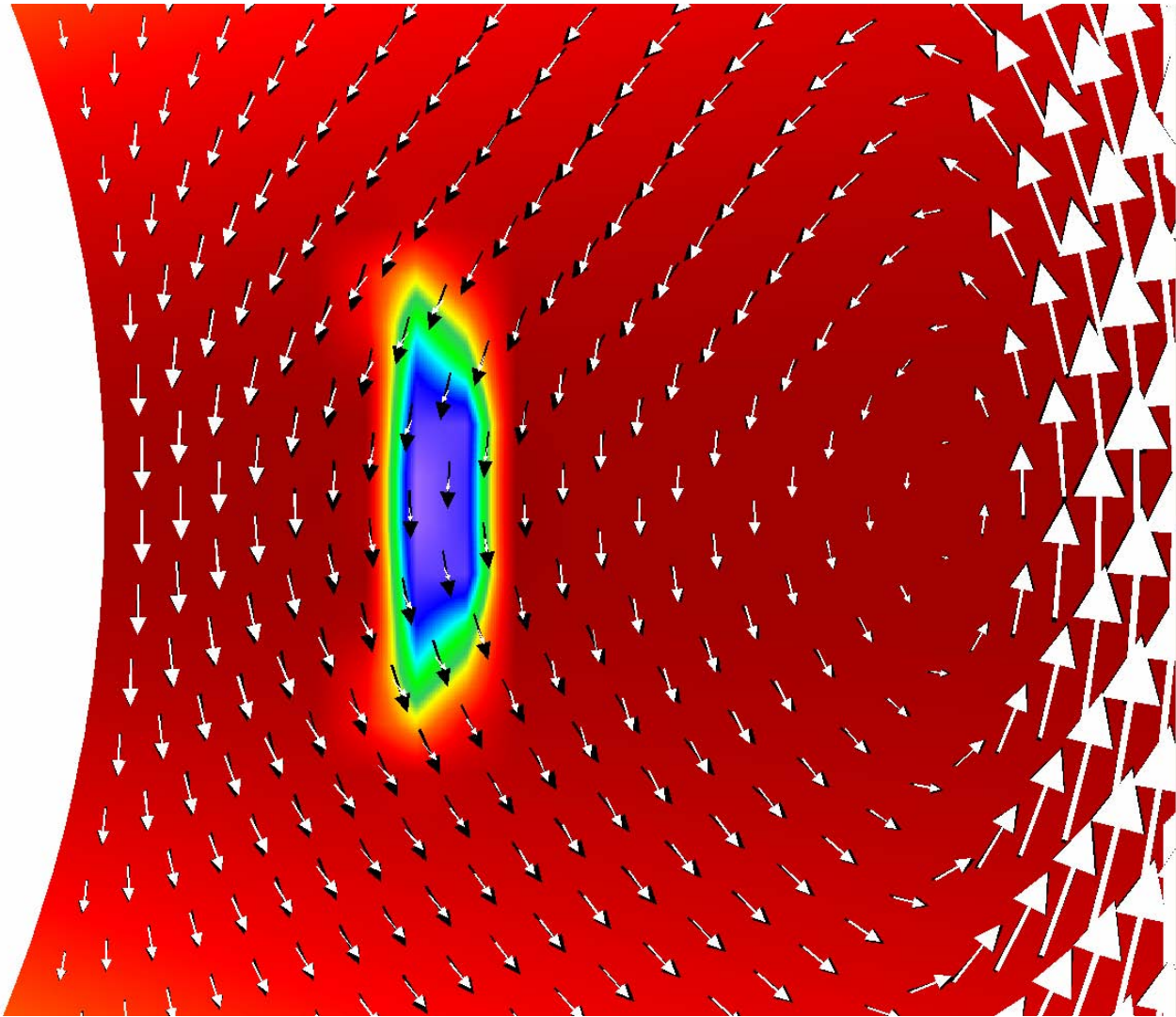


Figure (F5.14) Zoomed small-scale high-viscous fragment shown in figure (F5.12 Right). High-viscous fragment (with VC=80) is situated in the area where the global motion changes its direction and velocity.

Black arrows: initial velocity distribution shown in figure (F5.12 Left)

White arrows: velocity distribution changed by appearance of viscous fragment.

The conclusions based on the behavior of this fragment are quite the opposite. As easy to see, the initial flow starts to change the direction of its motion in the face of high-viscous small-scale fragment. The change in motion occurs in advance, that is

quite consistent with the physical laws. Thus, the high-viscous fragment remains relatively motionless in comparison with the surrounding mass.

**Model 5.4e:** Model suggested by Zhang (1993).

There arose some problems in comparing our results with the results published by Zhang (1993) on the base of those published models since no test was set irrefragably. In the PhD thesis by Zhang (1993) there are 4 tests aimed at comparison of the U-transform and W-transform methods:

- The first two tests are missing the radial viscosity profile, which is not stated, therefore, the comparison would be possible only if we guessed, which profile was meant.
- The description of the other two tests does not contain a correct statement of density anomaly and viscosity distributions.

Finally, we chose one of those tests (the third in the PhD thesis of Zhang (1993), p. 32) with given spherical harmonic coefficients for the resulting surface divergence, radial vorticity and the geoid. There still remain some degrees of freedom in the choice of the input data since they are not set correctly. Therefore, we cannot be absolutely sure if we have got the identical conditions to those models considered by Zhang (1993) since the results differ from the results obtained by Zhang.

The description of the model given in Zhang (1993):

1) Density anomaly:  $\delta\rho = \sin \pi z \cdot Y_{11} + Y_{20}$

2) Viscosity distribution:  $\frac{\eta}{\eta_0} = \exp(C_1 \cdot \delta\rho)$  with  $C_1 = 0.2$

where  $z = 1 - \frac{r_e - r}{r_e - r_c}$

Since the density anomaly is stated incorrectly with respect to

$Y_{11}$ , which can be  $Y_{1i}(\theta, \varphi) = \begin{cases} \sqrt{3}P_1^1(\cos \theta) \cos \varphi, i = 1 \\ \sqrt{3}P_1^1(\cos \theta) \sin \varphi, i = 2 \end{cases}$ , we considered both

cases but the results obtained from both models were remarkably different from those stated by Zhang (1993).

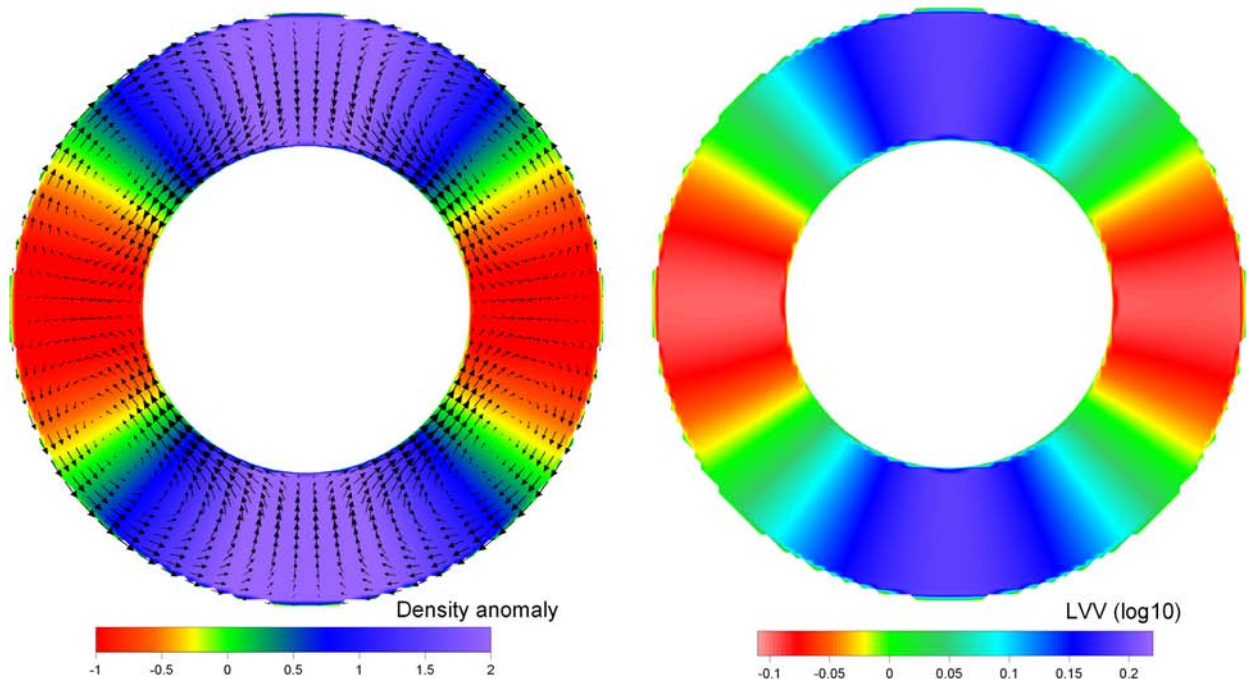


Figure (F5.15) Density anomalies and LVV in cross-section  $\varphi = 90^\circ$ .

Left: Density anomalies and velocities corresponding to the constant viscosity model (maximal velocity value is 686353 mm/year).

Right: LVV cross-section.

This model is rather similar to the artificial model considered in Part 4.3. The reason for the resulting values of mantle velocities [mm/year] and dynamic geoid [m] being so huge is also the same as in Part 4.3.

In the PhD thesis by Zhang (1993) spherical harmonic coefficients for the geoid, surface divergence and radial vorticity are stated. These coefficients were used to compare the results stated by Zhang (1993) and the results obtained with the aid of the new formulations of the U- and W-transform methods. Both methods in the new realizations gave very similar geoid figures, surface divergence and radial vorticity (distinction is less than 1%), therefore, the figures shown below demonstrate the results obtained from only U-transform method.

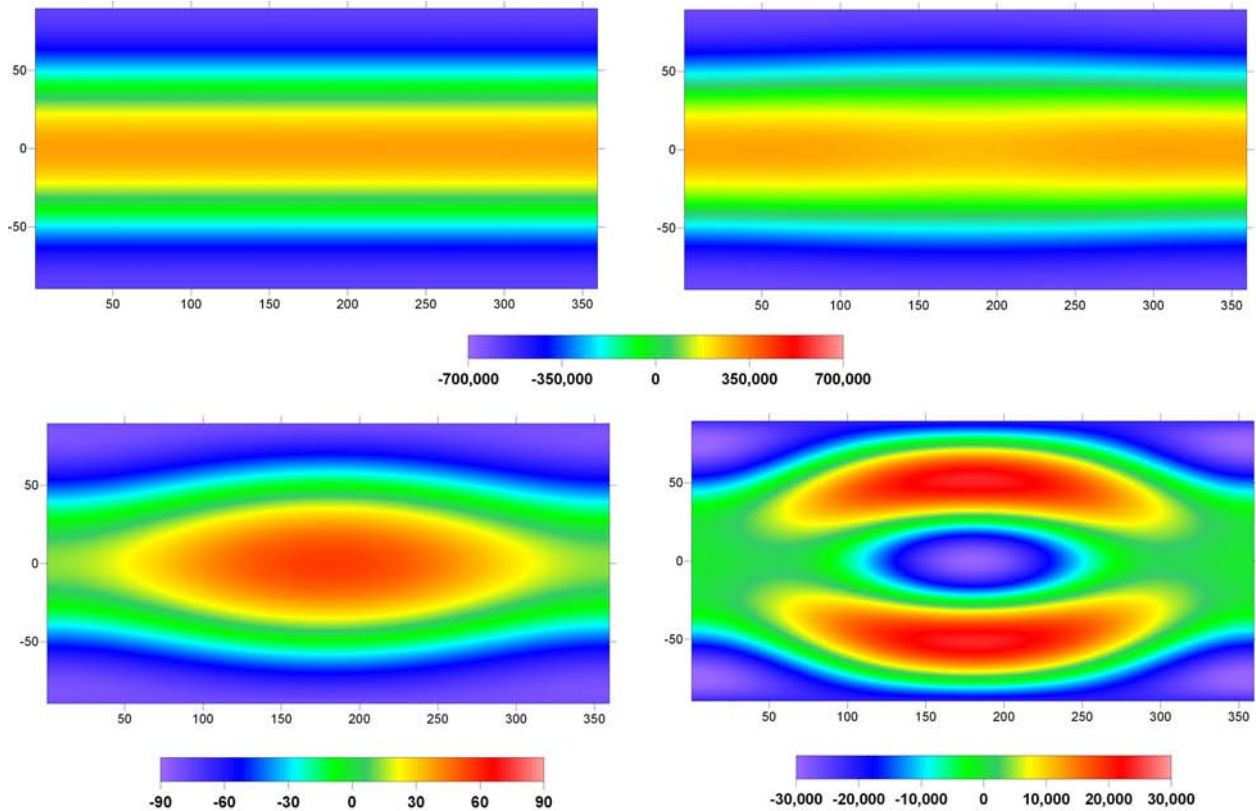


Figure (F5.16) Calculated geoid (new realizations of U- and W-transform method) and geoid stated by Zhang (1993) [m].

Left Top: Geoid calculated with the constant viscosity model

Right Top: Geoid calculated with the LVV by U- and W-transform with new formulae

Left Bottom: Dynamic geoid stated by Zhang (1993).

Right Bottom: Difference between geoid calculated with the LVV (new formulae) and geoid calculated with the constant viscosity.

The spherical harmonic coefficients for the geoid stated by Zhang (1993) are rather shady especially compared to the coefficients stated for the surface divergence and radial vorticity. First, the maximal value of spherical harmonic coefficients for the calculated geoid is  $-0.8268\text{E-}12$ , while the surface divergence is described by values of an absolutely different order of magnitude:  $-0.2166\text{E+}00$  (Zhang (1993), p.32). Thus, the distinction between two stated quantities exceeds 11 orders. According to the present study the spherical harmonic coefficients for the surface divergence and the geoid are comparable in values. We can assume that some normalization coefficient was used for the purpose of getting reasonable geoid heights in the study of Zhang (1993). If

so, a simple comparison of the geoid calculated without LVV and stated by Zhang (1993) astonishes to the most abysmal depth: taking into account that the viscosity contrast considered in this model scarcely exceeds 0.3 (less than 2 times) orders of magnitude, we could not expect such significant alteration in the geoid figure due to LVV. An obvious disagreement in changes occurring in the geoid figure and the surface divergence due to LVV sets a trap as well.

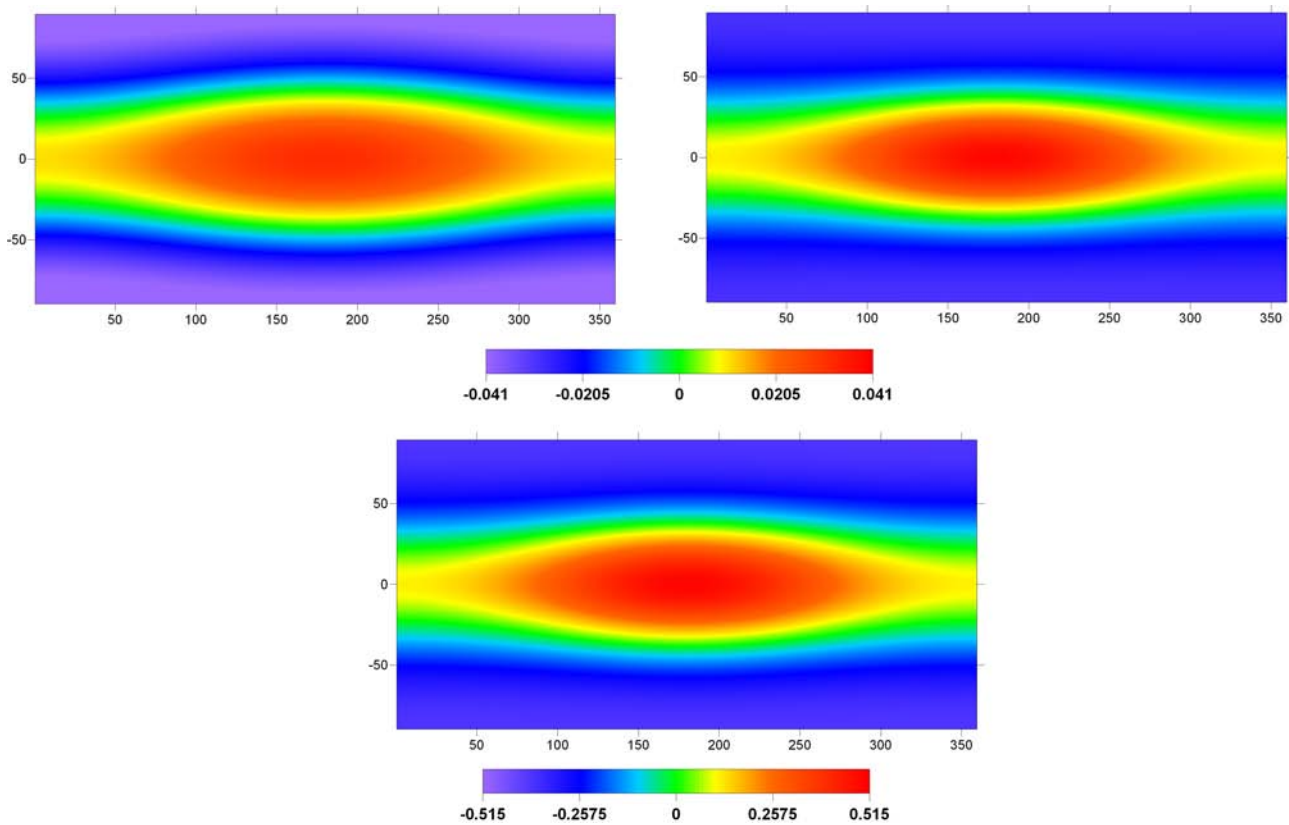


Figure (F5.17) Surface divergence calculated for the constant viscosity model and with LVV by U- and W-transform with new formulae. Surface divergence stated by Zhang (1993).

Figures (F5.17) and (F5.18) produce a better fit between the quantities stated by Zhang (1993) and the results of our calculations. Surface divergence seems to be affected by LVV in the same way in both studies. Maximal values of the surface divergence stated by Zhang (1993) and calculated by the new formulation of the U-transform method differ by a factor  $4\pi$ . This

difference can arise, for example, from the loss of the normalization coefficient  $4\pi$  appearing while spherical functions are decomposed into spherical harmonics. Similarity in the surface divergence calculated by the U-transform method in the new formulation and surface divergence stated by Zhang (1993) suggests that identical models were considered in our study and in the study of Zhang (1993). In this case the displacement of the major negative and positive anomalies of radial vorticity may not be explained simply by different input data.

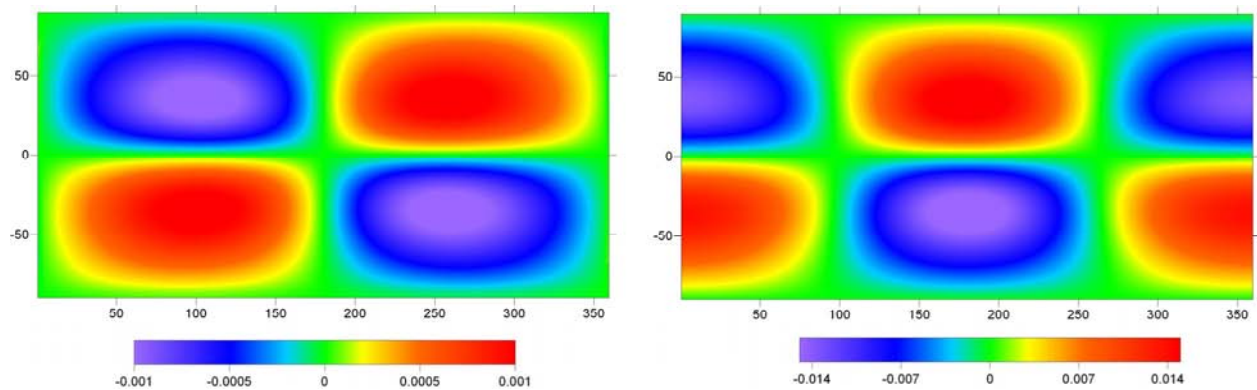


Figure (F5.18) Radial vorticity calculated by U- and W-transform with new formulae. Radial vorticity stated by Zhang (1993).

Distinction between recently derived radial vorticity and the previously published one (Zhang (1993)) can be easily observed. It is difficult to draw any conclusion based on this brief analysis, for the quantities stated by Zhang (1993) and derived in this study are too different to be compared.

## Chapter VI.

### *Inverse problem.*

To construct a global model, which can describe most comprehensively the current structure of the Earth's mantle, we need first to determine velocity-to-density scaling factor using which we are able to obtain density and temperature anomaly distribution in the Earth, and radial viscosity profile most consistent with the results of the previous studies, since this problem has been already investigated in a number of works in detail. There are basically two ways for determining a velocity-to-density scaling factor: in the first approach the scaling factor is estimated using a joint inversion of seismic tomography data and surface observables (Corrieu et al., 1994), the other way is to use mineral physics equations and experimental data (Karato, 1993). For the upper mantle we have used the results of a joint inversion of the residual mantle anomalies and  $V_s$  perturbations (Kaban and Schwintwer, 2001). Since it is not quite clear, how various factors influence velocity, density and temperature in the transition zones and in the lower mantle, we use initially the value of a velocity-to-density scaling factor at the bottom of the upper mantle also for the transition zone and the lower mantle (0.24), which is consistent with the mineral physics studies (Karato, 1993). Then the values are rescaled in a least-squares adjustment limiting a deviation from the initial scaling factor profile in the lower mantle while giving carte blanche to scaling parameters in the transition zone. The radial viscosity, which gives the most reasonable fit to the observed geoid, is to be determined from a large number of different profiles varying in several layers with respect to each other (7 layers in this study).

## 6.1 Joint inversion technique.

An initial density model is produced by a simple linear conversion of the seismic tomography velocity disturbances into density variations  $\delta\rho = a_j^0 \frac{\delta V_s}{V_s}$  using initial scaling factors  $Sc(r) = a_j^0$ . The dynamic geoid is then calculated for separate mantle layers assuming a constant velocity-to-density scaling factor for the given viscosity model. In this study, we chose the initial scaling factor constant and equal to 0.24, which is rather consistent with the assumptions of mineral physics (Karato, 1993). The initial scaling factors are rescaled in a least-squares adjustment to get the best fit to the observed geoid with a prospect not to wander away too far from the initially chosen scaling factors. The inversion to solve for unknown scaling factors is performed in the spectral domain by spherical harmonics coefficients. The computational tests have proved that, if the area is large enough, an inversion in the spectral domain, namely in the terms of spherical harmonic coefficients, which are appropriately filtered by a convolution with an area function, gives essentially the same result as working directly in the spatial domain (Kaban and Schwintzer, 2001). The scaling coefficients  $a_j$  (to rescale the initially adopted values of  $a_j^0$ ) are estimated in a least-squares adjustment starting with the linear observation equations

$$N_{obs}^{l,m} = \sum_j a_j N_j^{l,m} + \varepsilon^{l,m} \quad (\text{E6.1})$$

supplemented by the pseudo-observation equations with respect to the unknowns  $a_j$

$$0_{jj} = a_j - a_j^0 + \varepsilon_{jj} \quad (\text{E6.2})$$

where  $N_{obs}^{l,m}$  is an observed geoid for degree  $l$  and order  $m$ ;  $N_j^{l,m}$  are geoid variations induced by a layer  $j$ .

The least-squares principle implies minimization of the function:

$$\chi^2 = \sum_{l,m} \left( N_{obs}^{l,m} - \sum_j a_j N_j^{l,m} \right)^2 + \sum_j \beta_j (a_j - a_j^0)^2 \quad (\text{E6.3})$$

where  $a_j$  are unknown scaling factors and  $\beta_j$  are damping factors introduced to stabilize a solution.

The principle leads to a normal equation system:

$$Ba = c \quad (\text{E6.4})$$

where the elements of normal matrix  $B^{n \times n}$  are

$$b_{jk} = \sum_{l,m} N_j^{l,m} \cdot N_k^{l,m} + s_{jk}, \text{ where } s_{jk} = \begin{cases} 0, k \neq j \\ \beta_j (a_j - a_j^0), k = j \end{cases}$$

and the components of a right-hand-side vector  $\bar{c}$  are

$$c_k = \sum_{l,m} N_{obs}^{l,m} \cdot N_k^{l,m}$$

where  $n$  is the number of layers.

The system is solved for the vector  $\bar{a}$  by inversion of the normal matrix  $B^{n \times n}$ . The parameters  $a_j$  are a posteriori transformed to the convenient dimensionless ratio

$$\left( \frac{d \ln \rho}{d \ln V_s} \right)_j = \frac{d\rho}{\rho^*} * \left( \frac{dV_s}{V_s} \right)^{-1} = a_j^0 \frac{a_j}{\rho_j^*} = c_j \quad (\text{E6.5})$$

by computing an average density  $\rho_j^*$  for each layer from PREM (Dziewonski and Anderson, 1981). The density-velocity scaling coefficient standard deviations  $Sc_j$  resulting from the fit in the least-squares adjustment E6.3 are then

$$Sc_j = \frac{a_j^0}{\rho_j^*} Sa_j, \quad Sa_j = \sqrt{\frac{1}{f} \chi^2 q_{jj}} \quad (\text{E6.6})$$

where  $q_{jj}$  is a diagonal element of inverse matrix  $B^{-1}$ , and  $f$  denotes the degree of freedom (the number of equations E6.1 and E6.2 minus the number of the unknowns).

The pseudo-observation equation E6.2 constrains variations of the scaling factors from the initial coefficients  $a_j^0$ .

## 6.2 Inverse problem applied to the radial viscosity models.

Since we investigate principal importance of LVV in the next generation of global dynamic models, an inverse problem is not the main subject of the study but only an instrument to derive the model of density distribution, which provides a reasonable fit to the observables. It has been decided not to overload the initial model by additional details, which are ill-founded. We have emphasized 8 radial layers (upper mantle (1 layer), transition zones (2 layers), lower mantle (5 layers)) keeping scaling factor  $Sc(r)$  constant in each of layers  $j=1,\dots,8$  and varying values in respect to each other. As the initial parameters for an inverse problem we have chosen constant scaling factor equal to 0.24. For the transition zone layers a damping factor  $\beta_j$  has been taken equal to zero, therefore, the scaling factors in the layers can vary without any restrictions since our knowledge of these areas is very scanty. We have applied a least-square adjustment to the calculated geoid up to spherical degree and order 10 because the geoid has a maximum energy on the long waves. The radial viscosity profile  $\bar{\eta}(r)$  varied in 7 separated layers (the lithosphere (1 layer), the asthenosphere (1 layer), the rest of the upper mantle (1 layer), the transition zones (2 layers) and the lower mantle (2 layers)) has been sorted out from a set of 720 different combinations. The results of the inverse problem previously applied to several thousands of different radial viscosity profiles  $\bar{\eta}(r)$ , varied in the lower mantle, have revealed that the best fit to the observed geoid is reached at the averaged values of viscosity between 30 and 40 (averaged by  $\eta_0=10^{21}$ ) in the whole lower mantle.

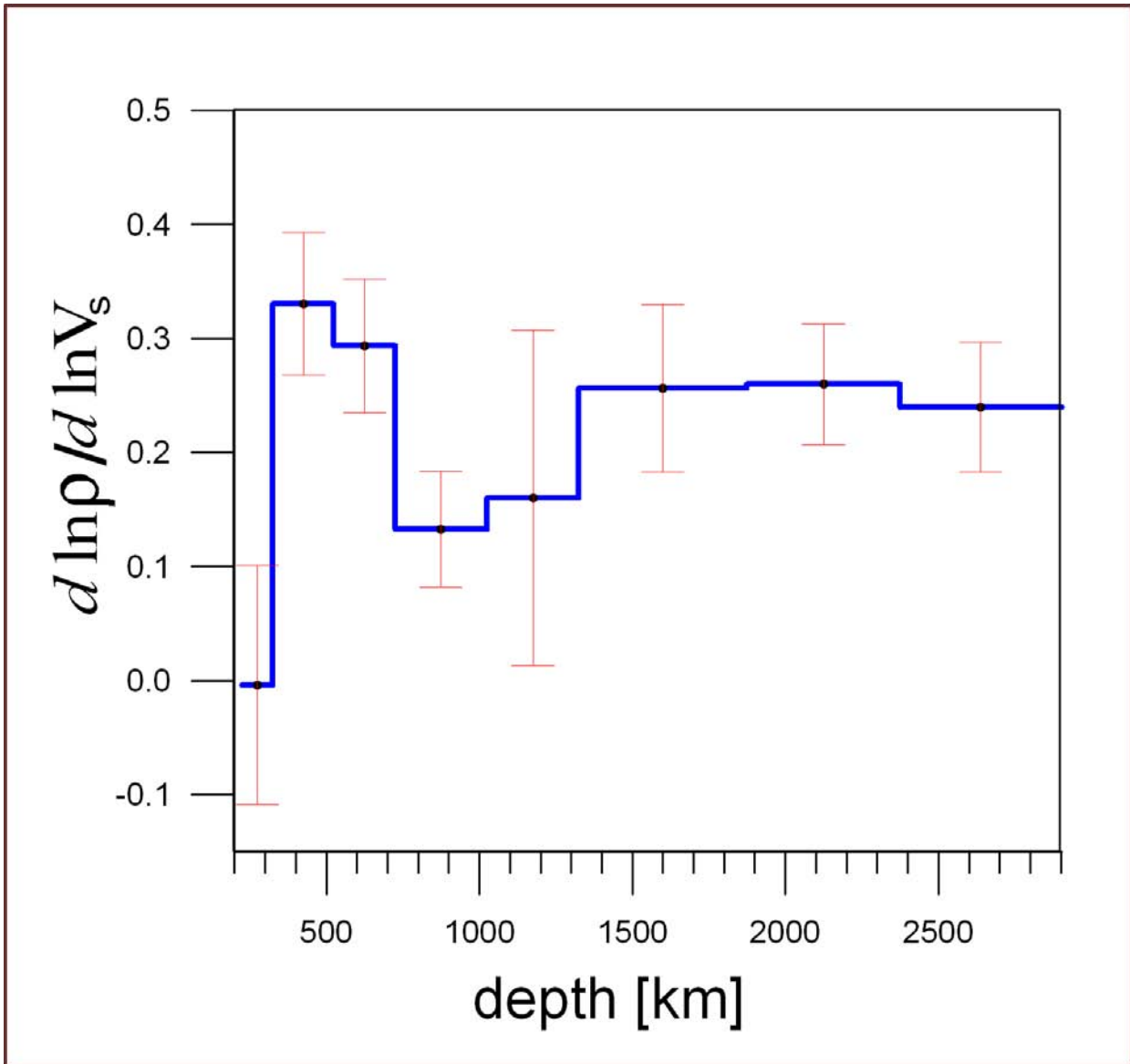


Figure (F6.1) Scaling factors (from joint inversion), which correspond to the radial viscosity profile in (F6.2). Red lines show scaling coefficient standard deviations  $Sc_j$  (E6.6).

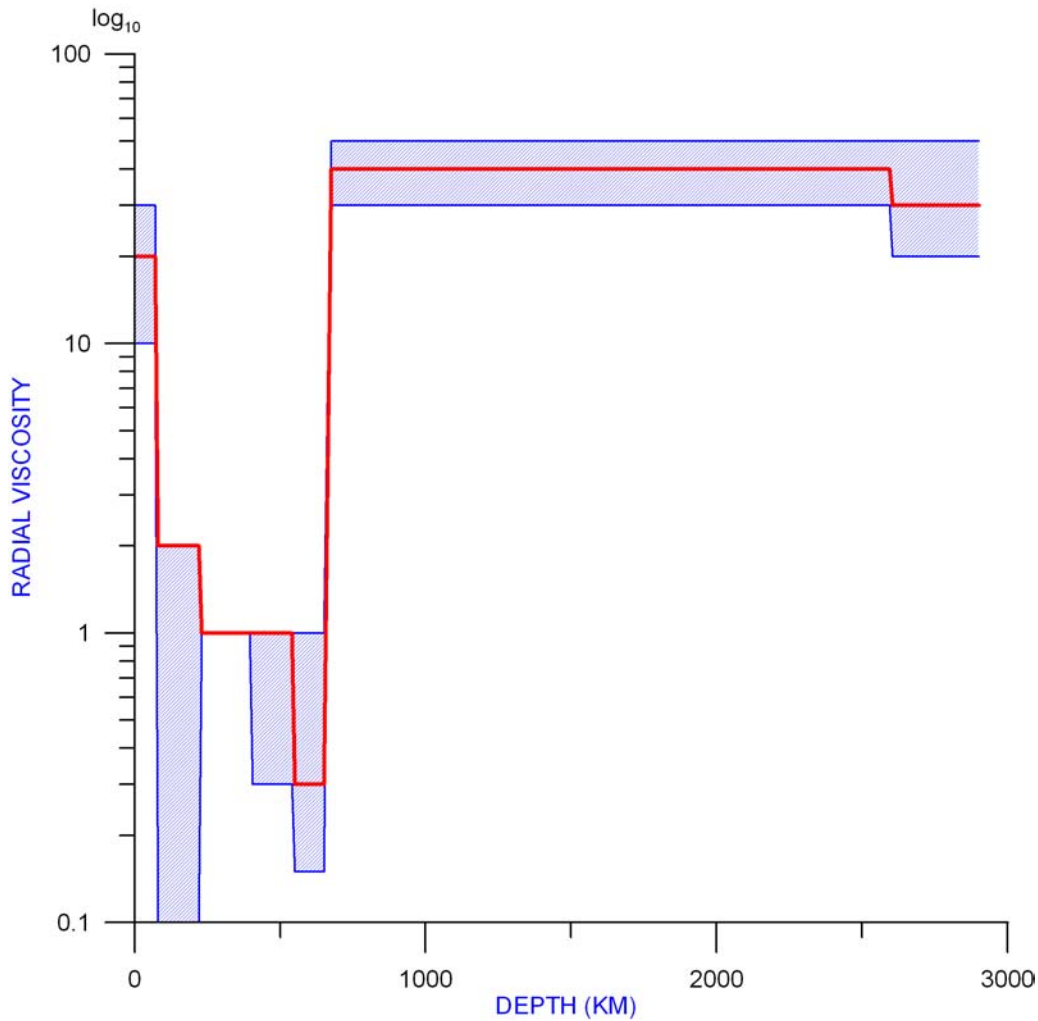


Figure (F6.2) Radial viscosity profile (red line), which corresponds to the model with the best fit to both the observed geoid (78.2%) and initial scaling factors in the lower mantle. Hatched zone shows the chosen search area.

The best combination of the radial viscosity profile and scaling factors was chosen based not only on the best fit to the observed geoid but also on the minimal deviation of the resulting scaling factors obtained for the lower mantle from the initial ones. In our study we disregard an influence of the uppermost 250 km.

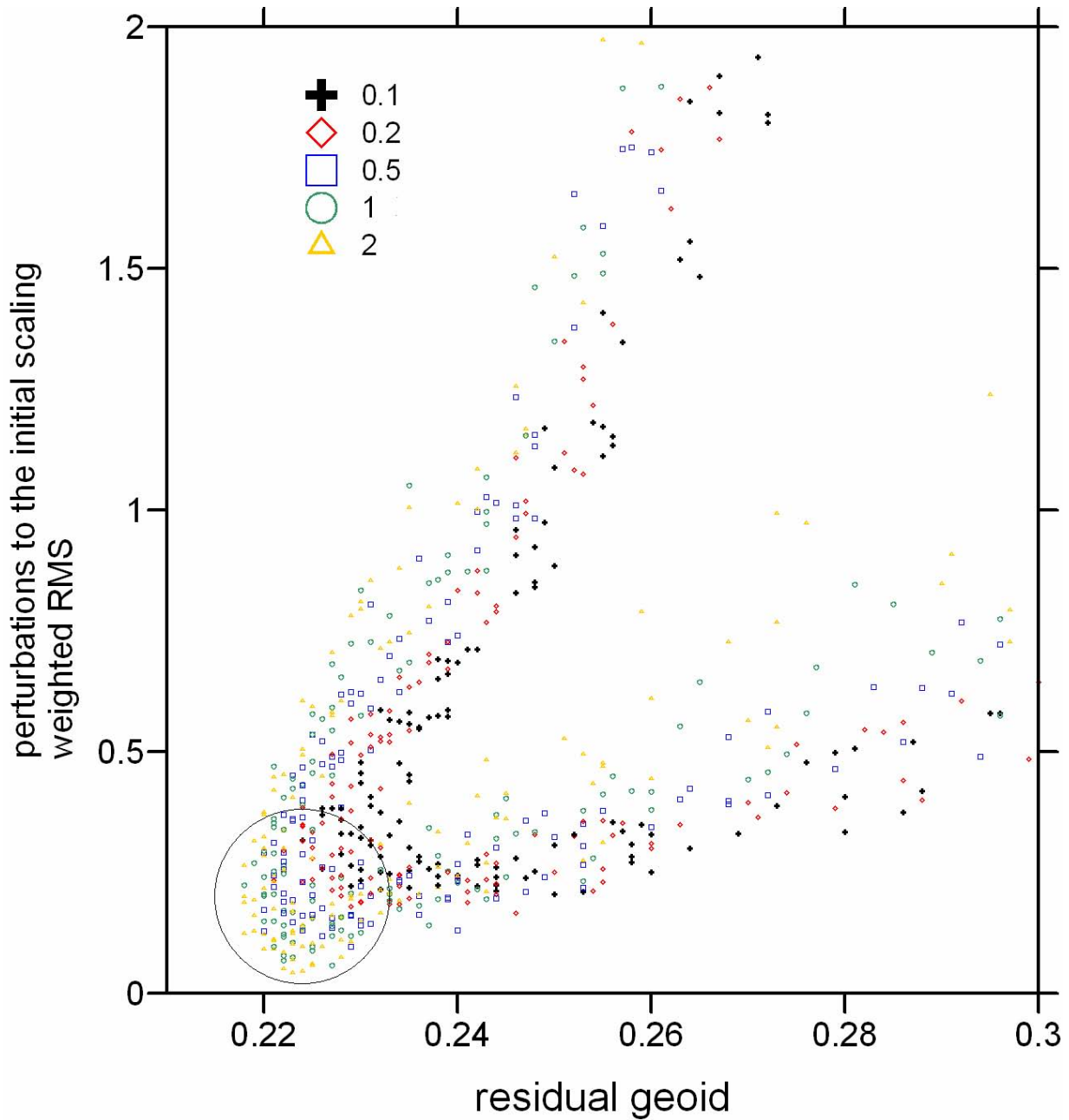


Figure (F6.3) Residual geoid versus perturbations to the initial scaling factor in different radial viscosity models. Model cluster for viscosity value in asthenosphere. Black circle marks the area with the best solutions.

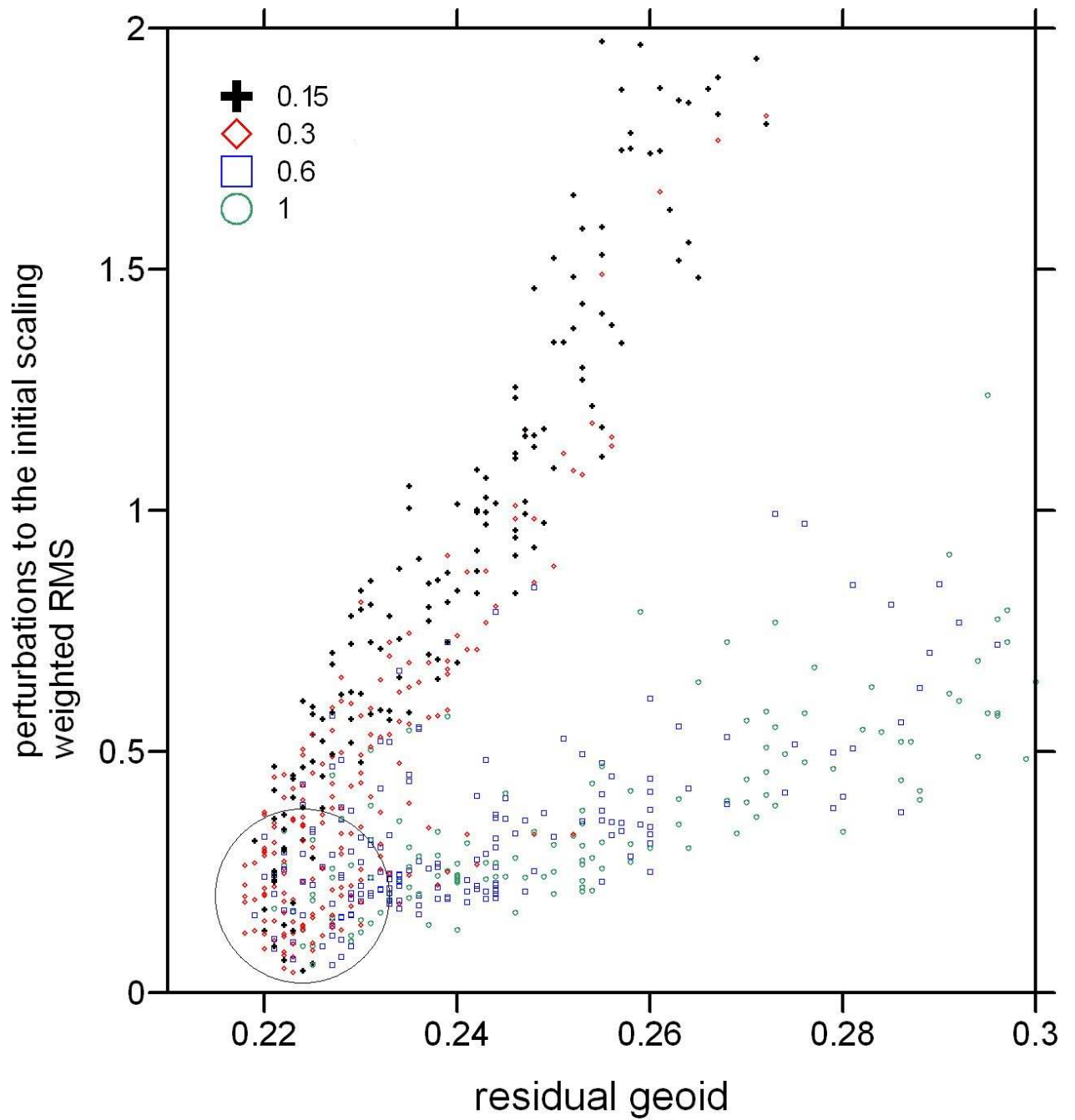
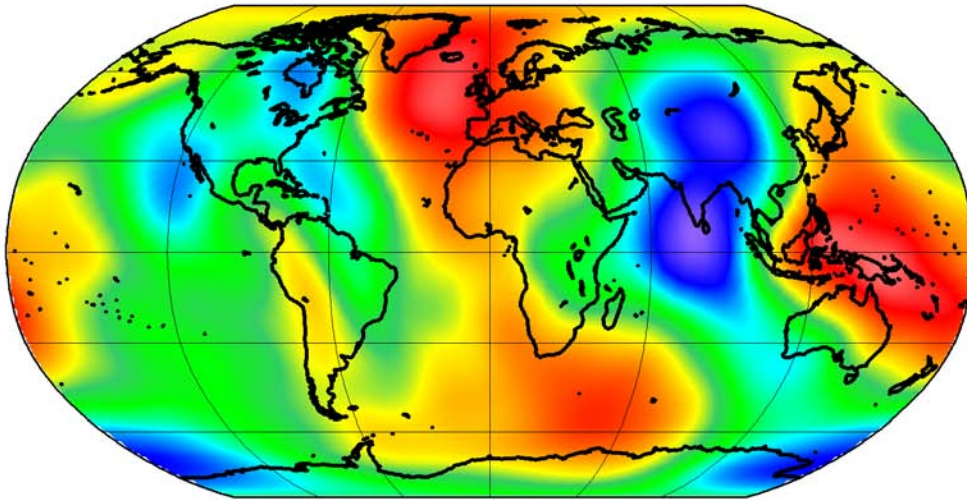


Figure (F6.4) Residual geoid versus perturbations to the initial scaling factor in different radial viscosity models. Model cluster for viscosity value in the upper part of the transition zone (above 670 km). Black circle marks the area with the best solutions.

## Observed Geoid (Isostatic Anomalies), no C20, C40



## Calculated Geoid

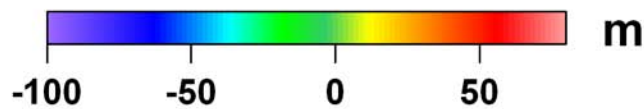
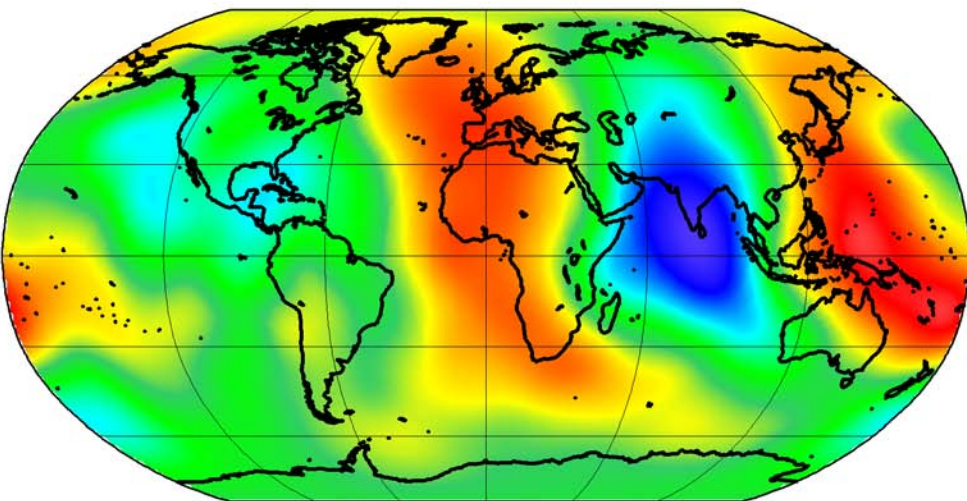


Figure (F6.5) Isostatic anomalies of the observed geoid and geoid calculated with radial viscosity shown in (F6.2) and scaling factor shown in (F6.1).

The clusters shown in figures (F6.3) and (F6.4) reveal the regularities in the model classes with the various values of effective viscosity in the asthenosphere and upper part of the transition zone (above 670 km) correspondingly. It is clearly seen in (F6.3) that the best solutions are produced by the radial viscosity models with the higher viscosity values (1, 2) in the

asthenosphere contrary to what could be expected. Figure (F6.4) also reveals very interesting regularity: the model classes with the lower viscosity values (0.15, 0.3) in the upper part of the transition zone give better solutions for the geoid while the models with the higher viscosity values (0.6, 1) produce more reasonable fit to the initial scaling factors in the lower mantle. In general the best solutions are obtained for the viscosity values 0.3 in the upper part of the transition zone. Such an analysis, if applied to an exhaustive set of models with various viscosity values, produces very important information since any clusterization of the models with specific parameters delimits the further search for the best solutions.

## Chapter VII.

### ***Global spherical models with lateral viscosity variations.***

The strong dependence of mantle viscosity on temperature exerts controlling influence on the evolution of the mantle. The temperature dependence of mantle viscosity acts as a thermostat regulating the average mantle temperature. Initially, when the Earth is hot, mantle viscosity is low, and extremely vigorous convection rapidly cools the Earth. Later in its evolution, when the Earth is relatively cold, its mantle viscosity is higher that results in more modest convection. Self-regulation tends to bring the viscosity of the mantle to a value that facilitates an efficient removal of the heat generated in the mantle.

#### **7.1 Three-dimensional global viscosity models.**

In our study 3-D global viscosity model is constructed using:

- The S20a seismic tomography model by Ekstrom and Dziewonski (1998) converted to temperature
- Assumptions about homologous temperature in the mantle (Paulson et al. (2005))

This model is one of the most commonly used in such a type of modeling. It provides resolution up to the 20<sup>th</sup> spherical harmonic degree for isotropic velocity variations. The last aspect is especially important in our study. Despite other models could differ from the S20a model in detail, the general conclusions about importance of taking into account LVV are valid also for all models with this and higher resolution. We use the procedure proposed by Paulson et al. (2005). The  $V_s$  perturbations have been initially converted into density variations. Based on the density variations we have estimated temperature distribution in the mantle  $T=T(r,\theta,\varphi)$  and determined a homologous temperature. It is consistent with the approximate nature of parameterized convection modeling to assume a Newtonian rheology with kinematic viscosity  $\eta=\eta(r,\theta,\varphi)$  related to mantle temperature by (Paulson et al., 2005):

$$\eta(r, \theta, \varphi) = \bar{\eta}_0(r) e^{\left( \gamma(r) \frac{T_m(r)}{T(r, \theta, \varphi)} \right)} \quad (\text{E7.1})$$

where  $T_m(r)$  is a solidus temperature,  $\bar{\eta}_0(r)$  are the initial coefficients,  $\gamma(r)$  are the activation parameters related to the activation energy  $E^*$  of subsolidus creep deformation by:

$$\gamma = \frac{E^*}{R} \quad (\text{E7.2})$$

where  $R$  is the universal gas constant.

The parameters  $T_m(r)$ ,  $\bar{\eta}_0(r)$  and  $\gamma(r)$  should be chosen separately for different mantle layers depending on P-T conditions and on a phase state of the material, primarily for the upper and lower mantle. So we can also adjust a vertical viscosity profile, which should be assumable close to the results of the previous studies. Thus, LVV are then produced self-consistently within this approach.

The velocity-to-density scaling factor has been estimated using joint inversion of seismic tomography data and surface observables (Corrieu et al. (1994)). This technique is described in Chapter VII. It is clear that not all velocity variations presented in the S20s model are induced by temperature effect. Compositional variations can substantially alter velocity-temperature relationship or simply mask the temperature effect. However, we assume that in spite of possible alterations of the computed fields in specific places, general conclusions about importance of incorporating LVV in global dynamic models will be convincing.

The derived density variations have been converted into temperatures applying the depth-dependent thermal expansion coefficient (Paulson et al., 2005):

$$\alpha = \left( 3 - \frac{2h}{h_c} \right) \cdot 10^{-5} \quad (\text{E7.3})$$

where  $h$  is the depth,  $h_c$  is the depth of the core-mantle boundary.

To calculate LVW with the aid of E7.1 we need radial profiles of the horizontally averaged temperature in the mantle and the solidus temperature. Since our model is instantaneous we cannot estimate the temperature distribution self-consistently and just take it from literature. The depth-dependent temperature distribution is based on Schubert et al. (2001); the temperature of solidus is taken from Yamazaki and Karato (2001). Both temperature curves are shown in figure (F7.1). The solidus temperature at the bottom of the mantle is slightly increased following Schubert et al. (2001).

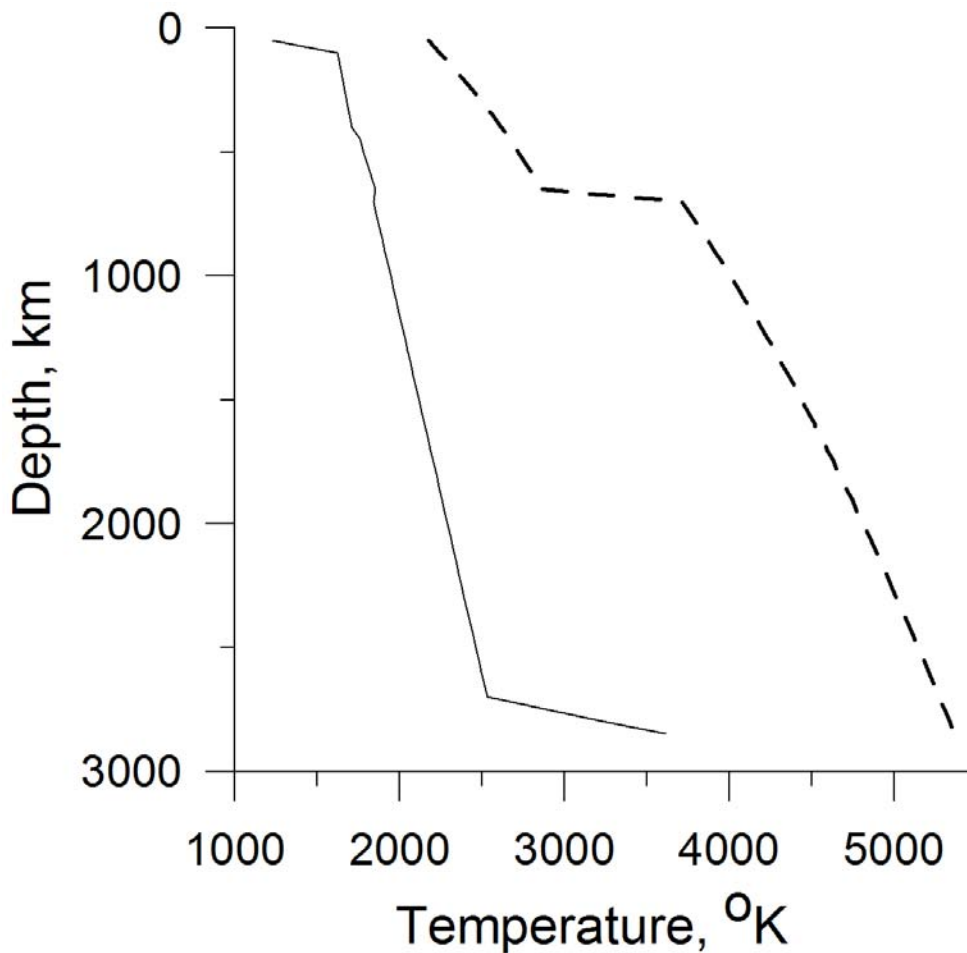


Figure (F7.1) Temperature profiles.

Small dash: radial mantle temperature (Schubert et al. (2001))

Bold dash: solidus temperature in the mantle (Yamazaki and Karato (2001))

The only activation parameters  $\gamma(r)$  are required to determine relative variations of viscosity based on temperature anomalies

(E7.1). Following Paulson et al., 2005 we take  $\gamma=10$  in the upper mantle and  $\gamma=17$  in the lower mantle (Yamazaki and Karato, 2001).

The maximum LVV in the lower mantle are about two orders of magnitude and are represented at the whole length scale: from very broad anomalies to small-scale variations. These relative variations are multiplied by the radial viscosity distribution that finally gives the 3-D viscosity model. The upper mantle viscosity variations in most of our models are likely to be less than in reality. Although we are not limited by calculation technique and can take into account the variations up to approximately 7 orders of magnitude, we have ventured on the models with LVV magnitude not higher than 4 orders as yet.

Radial viscosity profiles required in the final viscosity distribution have been chosen on the base of conclusions from the joint inversion. Thousands of different combinations for 7-layer viscosity profiles were considered to obtain the best fit to the observed dynamic geoid (also with effect of LVV). This problem is discussed in Chapter VII in detail.

## **7.2 Contribution of lateral viscosity variations to mantle velocities.**

This simple model based on the S20a tomography model is aimed at demonstrating the effect of LVV on the mantle flows and especially near-surface velocities.

The parameters of the models are following:

- Radial density distribution  $\bar{\rho}(r)$  is based on PREM (figure F4.1)
- Density anomalies are obtained from  $V_s$  using S20a tomography model with the constant scaling factor  $Sc(r)=0.2$  applying following relationship:  $\delta\rho = 0.01(\%)*Sc(r)*\rho^*(r)*\frac{\delta V_s}{V_s}$

- The radial viscosity profile is shown in figure (F7.2). The average viscosity in the upper mantle below 200 km to the depth of 670 km is equal to  $10^{21} [Pa \cdot s]$ . The average viscosity in the lower mantle is 40 times greater than the former one. Low-viscous asthenosphere and high-viscous continental keels are modulated mostly by LVV.
- The technique described above (Part 6.1) is used to derive LVV. This model corresponds to the leading coefficients:  $\bar{\eta}_0 = 5 \times 10^9 [Pa \cdot s]$  in the upper mantle and  $\bar{\eta}_0 = 5 \times 10^{13} [Pa \cdot s]$  in the lower mantle.

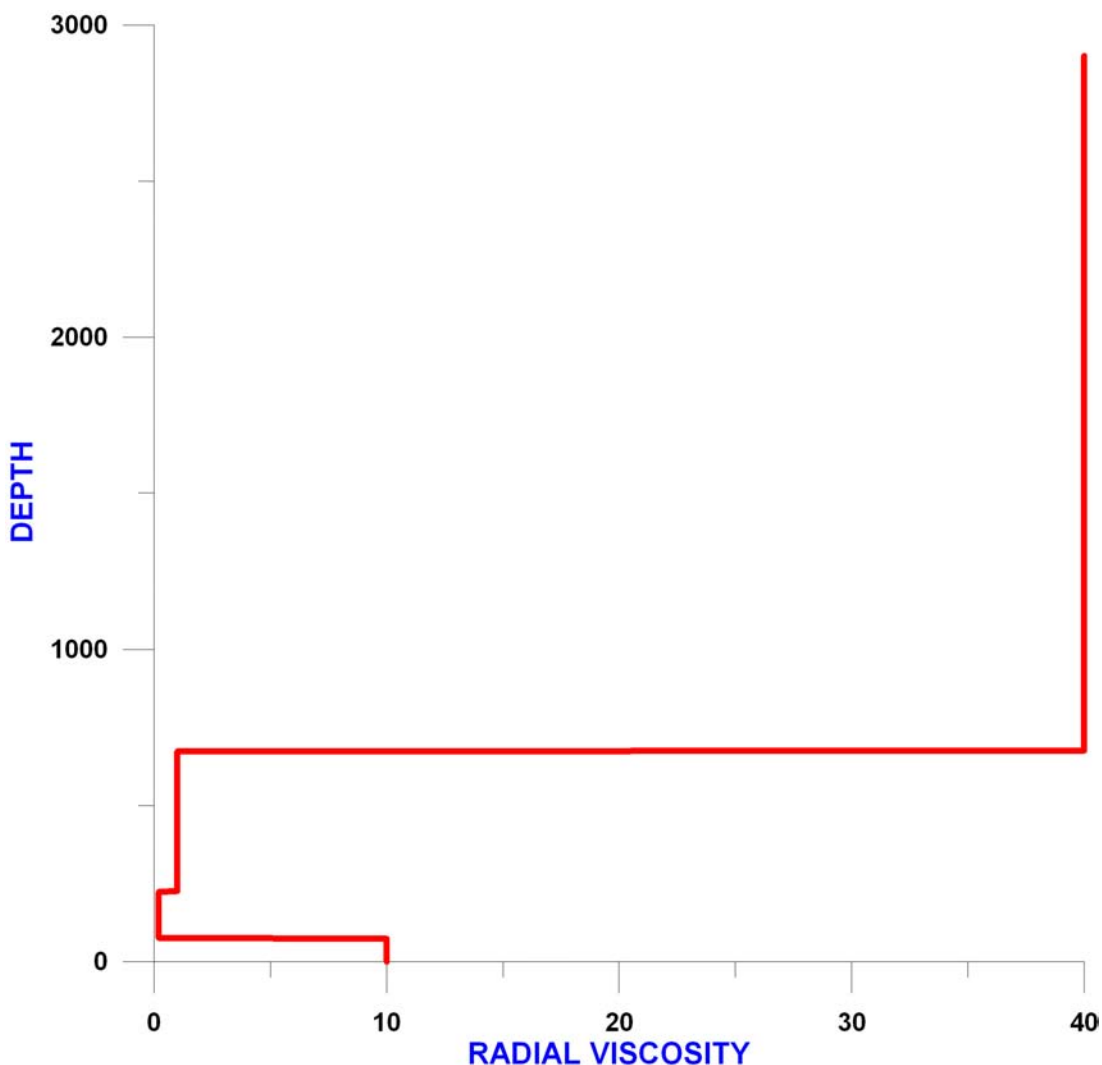


Figure (F7.2) Relative radial viscosity  $\eta^*(r)$ .

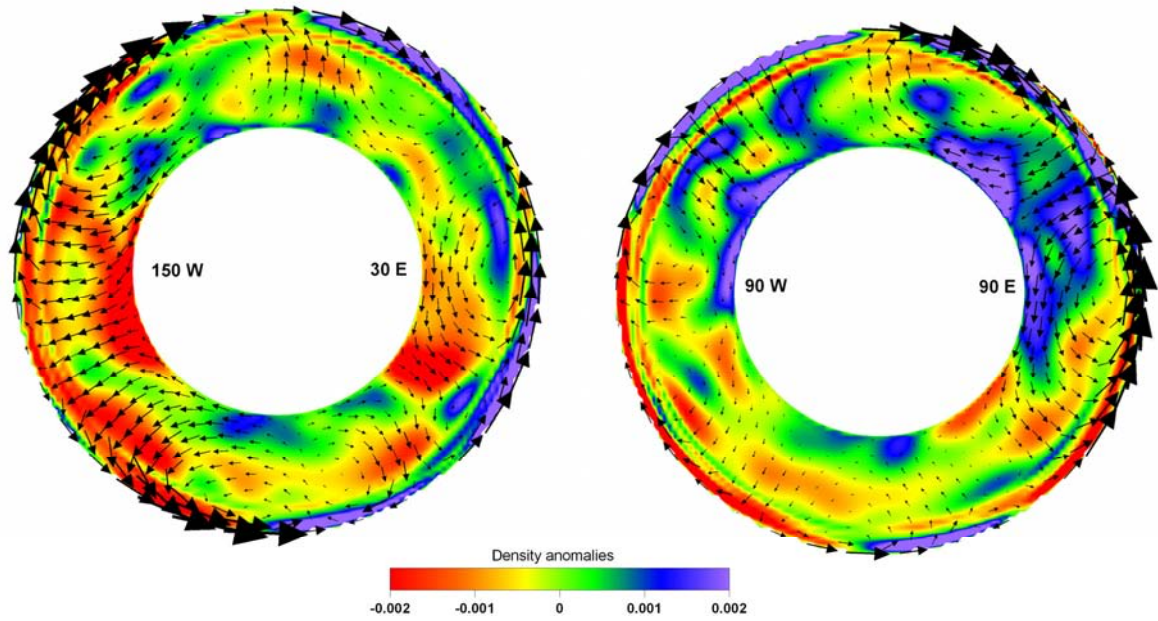


Figure (F7.3) Density anomaly distribution. Velocities are calculated for radial viscosity model.

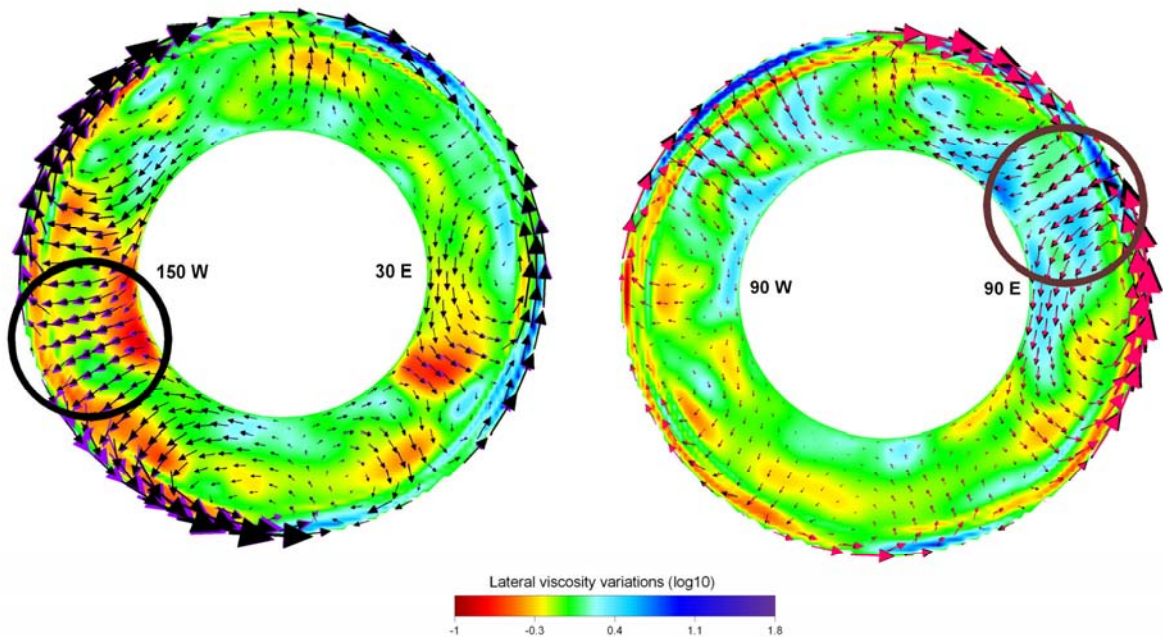


Figure (F7.4) LVV and velocity redistribution due to LVV.  
 Black arrows: Mantle velocities corresponding to the radial viscosity model.  
 Violet and red arrows: Mantle velocities corresponding to the LVV model calculated by the U-transform iterative method.  
 Black and brown circles mark zoomed areas shown in figures (F7.5) and (F7.6).

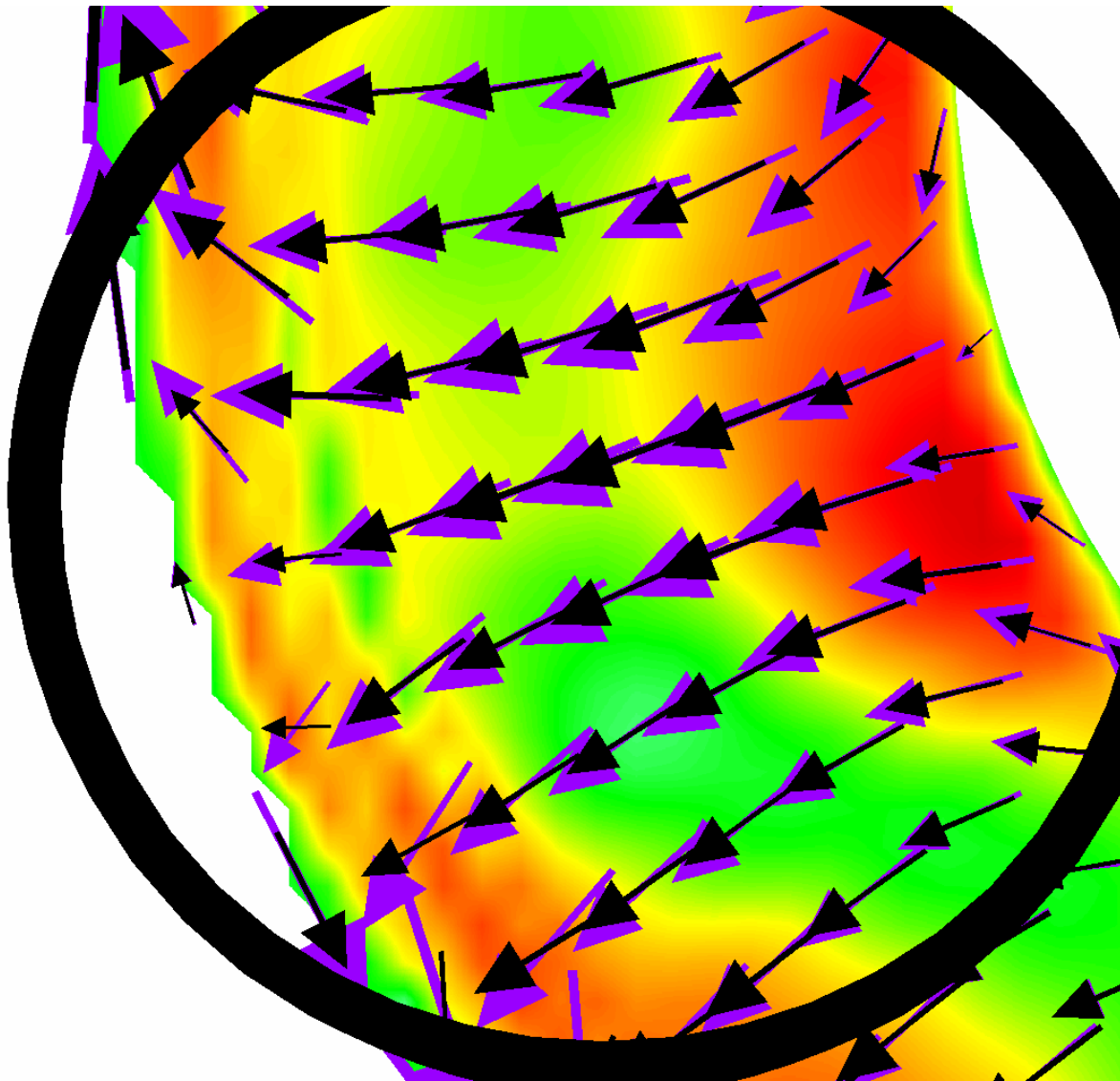


Figure (F7.5) Zoomed area with low viscosity (F7.4 Left).

Black arrows: Mantle velocities corresponding to the radial viscosity model.

Violet arrows: Mantle velocities corresponding to the LVV model.

In the area of low viscosity the mean values of the flow velocities significantly increased (>50% of the velocities calculated for radial viscosity model) therefore the upwelling global flow widens due to the viscosity heterogeneities.

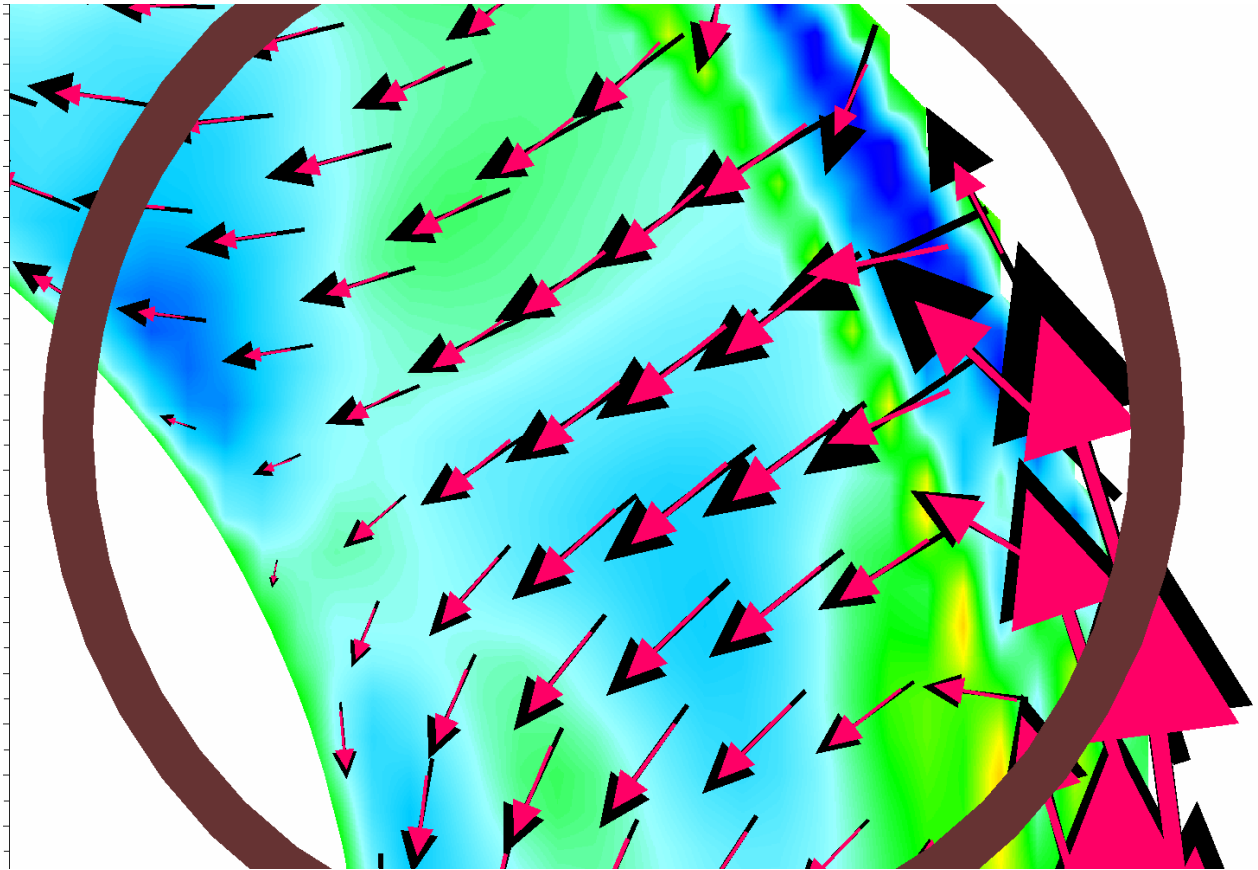


Figure (F7.6) Zoomed area with high viscosity (F7.4 Right).  
 Black arrows: Mantle velocities corresponding to the radial viscosity model.  
 Red arrows: Mantle velocities corresponding to the LVV model.

Contrary to (F7.5) the high viscosity slackens the global flow's pace and constricts the downwelling flow. Viscosity contrasts in the zone of low viscosity shown in (F7.5) and zone of high viscosity demonstrated in (F7.6) are approximately the same. The changes in mantle velocities due to LVV are of the same order in both cases, albeit the corrections have the opposite tendency.

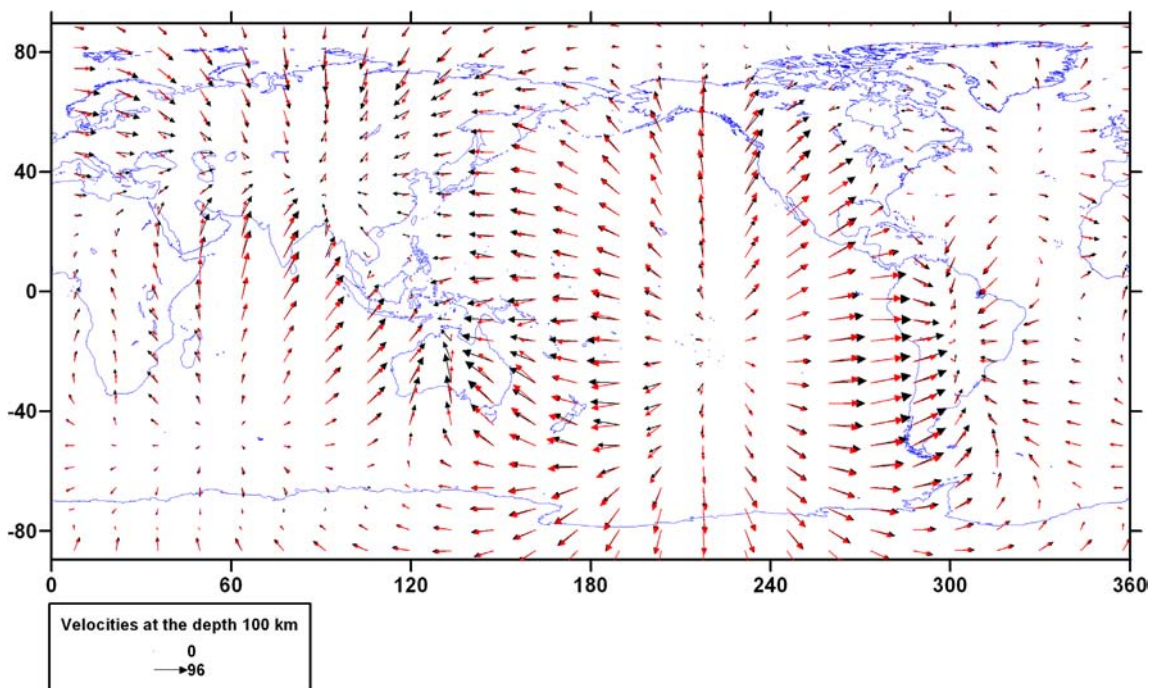


Figure (F7.7) Near-surface velocities at the depth 100 km. Maximum value of near-surface velocities is approximately 96 mm/year. Black arrows: Radial viscosity model. Red arrows: LVV model.

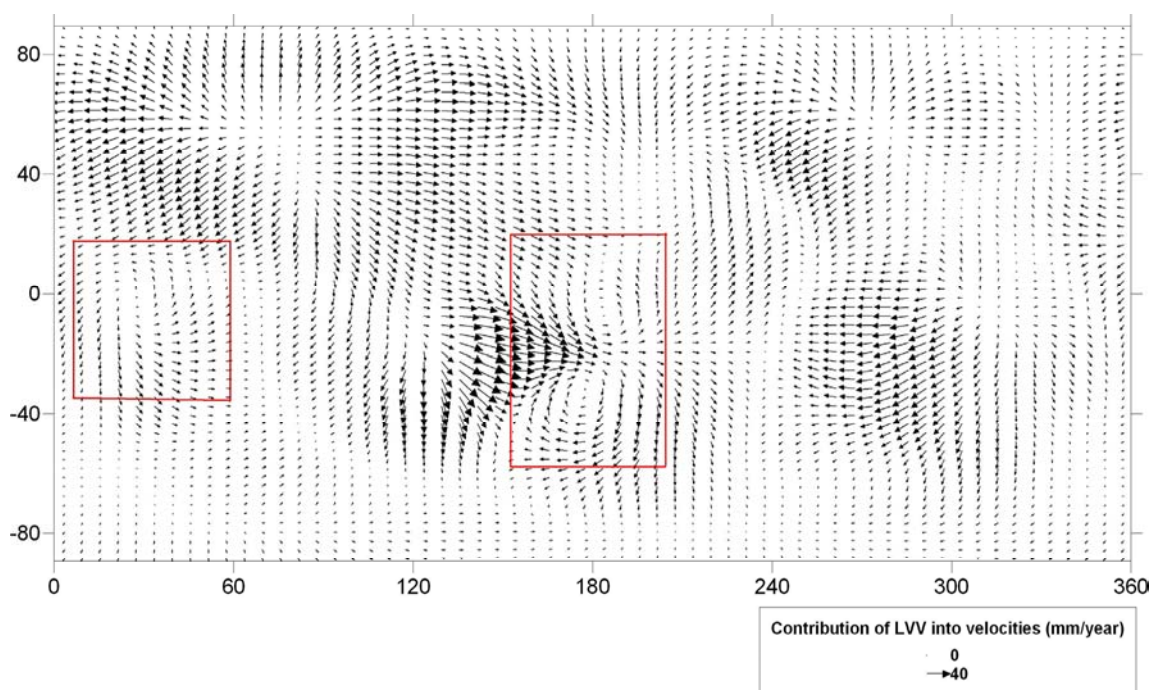


Figure (F7.8) Difference between near-surface velocities calculated with LVV and with only radial viscosity. Maximum value of resulting differences is approximately 40 mm/year. Red rectangles mark the areas with the most obvious vortical flows appearing due to LVV incorporation.

The near-surface velocities calculated at the depth 100 km are significantly affected by the LVV. A caliber of LVV impact into near-surface velocities (F7.7) becomes obvious as soon as the discrepancy between horizontal velocities obtained from the LVV model and radial viscosity model are shown (F7.8). The maximum change in velocity values due to LVV is approximately 45% of the initial velocities. Vortical flows (toroidal velocity component) appearing due to LVV are clearly seen in the Pacific Ocean and South Africa regions. The contribution of toroidal component is furthermore reflected in more details in radial vorticity (F7.9) in the form of negative and positive anomalies.

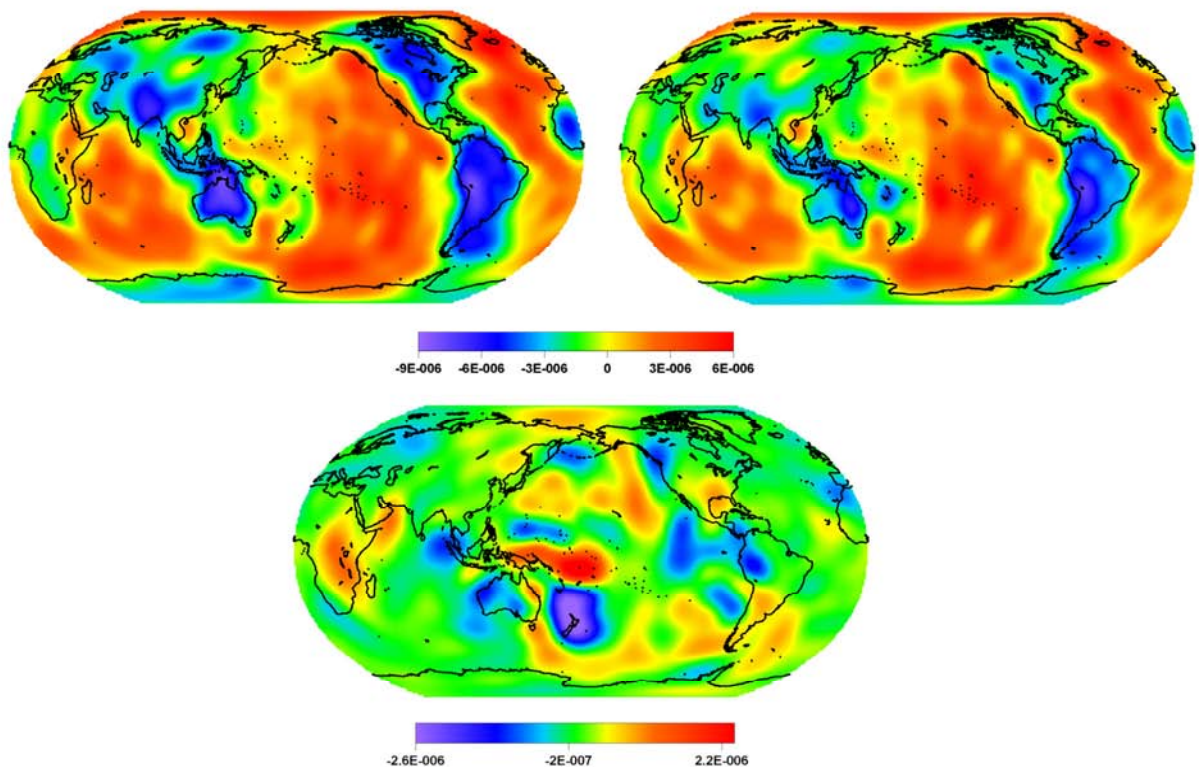


Figure (F7.9) Surface divergence and radial vorticity.

Top: Surface divergence for radial viscosity model (left) and LVV model (right).  
Bottom: Radial vorticity.

Radial vorticity represents a direct response of the surface velocities on the LVV appearance. Figure (F7.9) shows a visible fit to the published results (Moucha et al, 2007) in all main features irrespective of the different choice of the global 3-D

viscosity models. Relative proportions of surface divergence and radial vorticity are also in a good agreement with the results derived by Moucha et al, 2007 for the poloidal and toroidal surface velocities. The visible correlation between shapes of continents and negative anomalies of surface divergence is reduced by an incorporation of the LVV (F7.9) as well as in Moucha et al, 2007.

**7.3 Particular contribution of lateral viscosity variations induced in the upper and lower mantle to the geoid, dynamic topography and surface velocities.**

In this part we consider three LVV distributions: the whole-mantle LVV and two models (upper-mantle LVV and lower-mantle LVV), where LVV are restricted to the mantle above the 670 km discontinuity and below it in order to estimate the particular contribution of the LVV induced in the upper and lower mantle with respect to the effect of LVV in the whole mantle. For this purpose we use the whole-mantle LVV model of approximately 4 orders of magnitude in the lithosphere and asthenosphere and 2 orders of magnitude in the lower mantle. The 3-D viscosity models of the whole mantle (F7.10 Right), the lower mantle (F7.11 Left) and the upper mantle (F7.11 Right) are constructed based on the S-wave tomography model S20a of Ekstrom and Dziewonski (1998) as described in the Part 7.1 and on the results of joint inversion for the radial viscosity models discussed in Part 6.2 (Figure F6.2). Density anomalies are obtained from  $V_s$  using S20a tomography model

$$\delta\rho = 0.01(\%)*Sc(r)*\rho^*(r)*\frac{\delta V_s}{V_s}$$

with a scaling factor  $Sc(r)$  found from a least-squares adjustment first for radial viscosity model (F6.1), then corrected for the 3-D viscosity model (F7.12). These rescaled conversion parameters are used in both radial viscosity and LVV models in order to estimate correctly a contribution of LVV. Density distribution and its relation with the LVV distribution are shown on (F7.10).

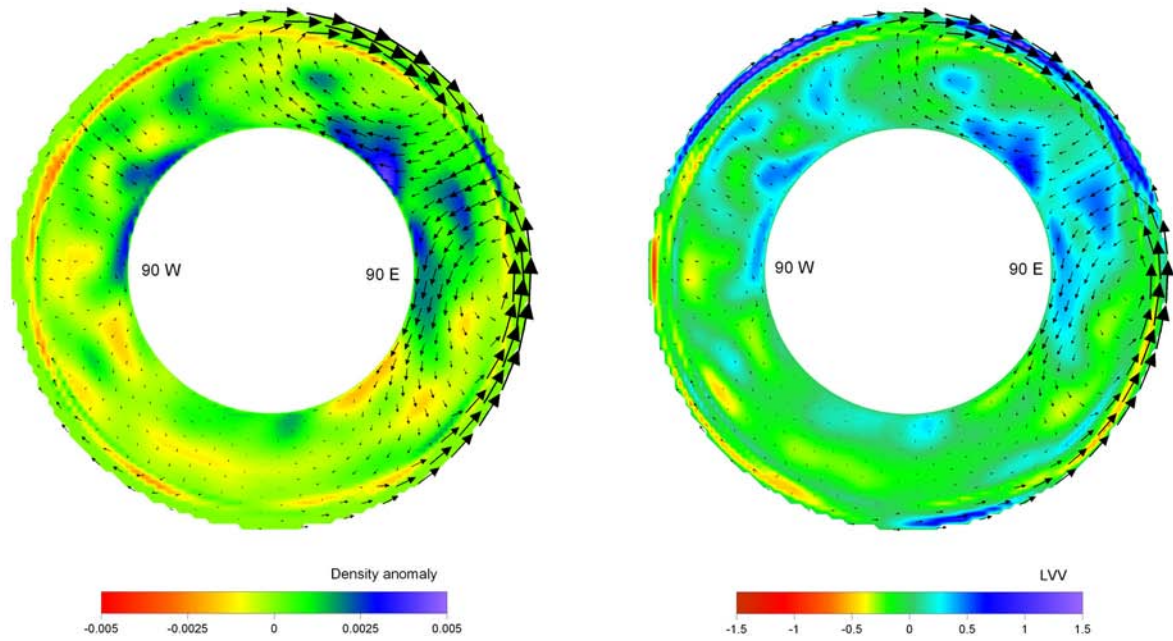


Figure (F7.10) Cross-sections showing density anomaly and LVV ( $\log_{10}$ ) in the mantle relative to the adopted vertical profile shown on (F6.2). Arrows show mantle velocities (maximal value is equal to 39.1 mm/year for the radial viscosity model (left) and 35.1 mm/year for the whole-mantle LVV model (right)) calculated with the same scaling factor shown on (F7.12 red).

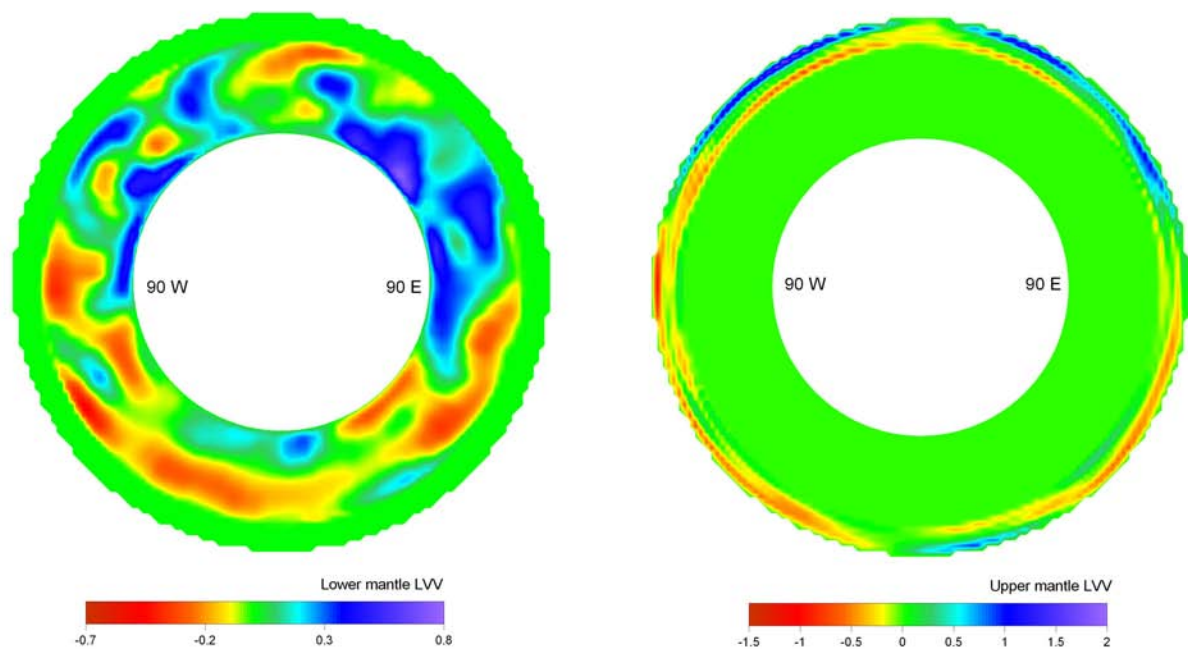


Figure (F7.11) Cross-sections showing LVV ( $\log_{10}$ ) incorporated into the lower-mantle model (left) and upper-mantle model (right) relative to the adopted vertical profile shown on (F6.2).

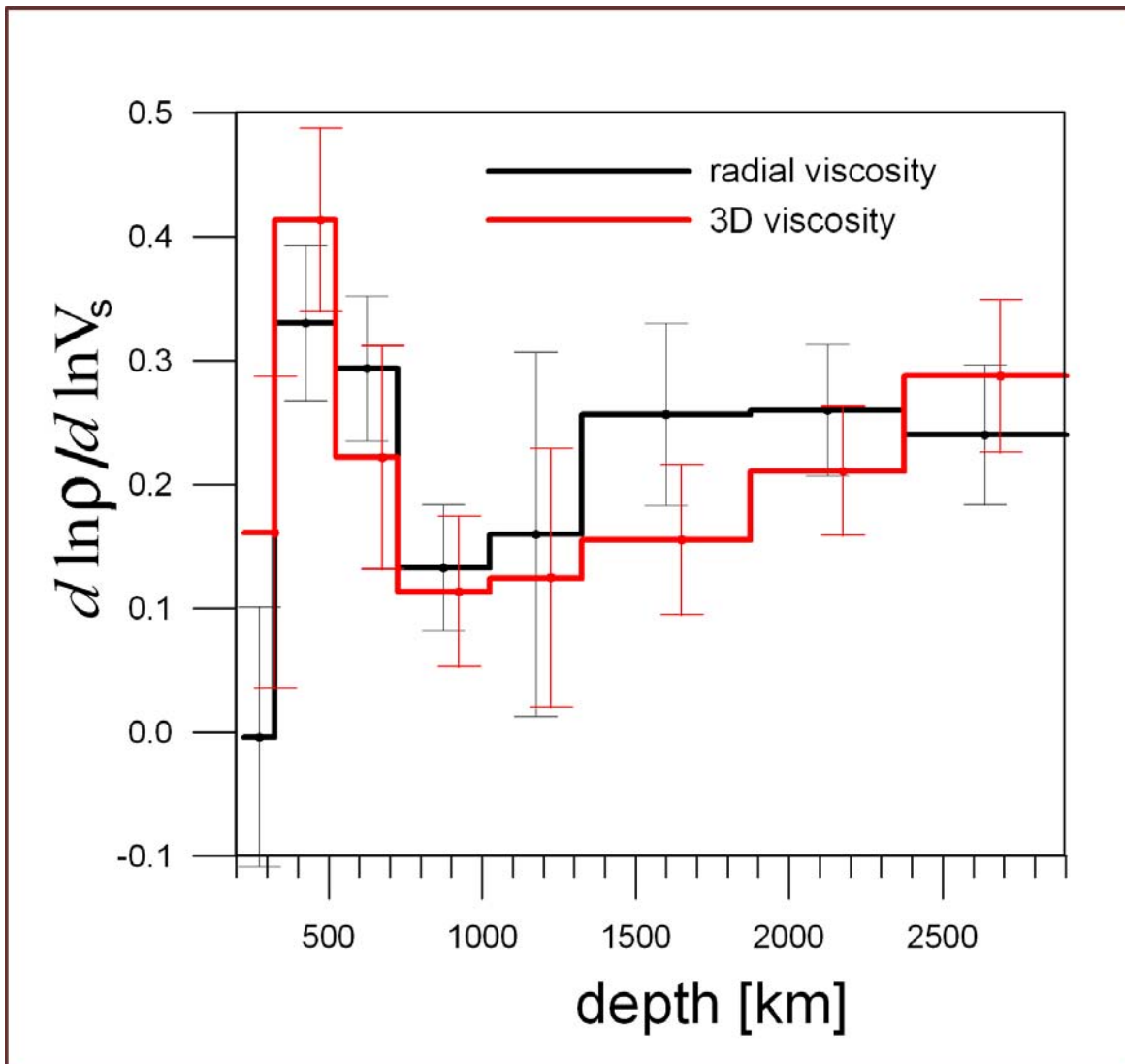


Figure (F7.12) Velocity-to-density scaling factor profile obtained from a least square adjustment to get a best fit to the observed geoid.

Black line represents scaling factor for the radially dependent viscosity model analysed in the Part 6.2 (the same as on (F6.1)).

Red line shows scaling factor for the model with the whole-mantle LVV.

Fine lines (black and red) show scaling coefficient standard deviations (E6.6).

In the lower mantle a conversion coefficient varies noticeably with a tendency to increase from approximately 0.13 to 0.27 while drawing nearer to the core-mantle boundary. In the transition zone a scaling factor exceeds 0.4 and differs significantly from the initial value (0.24). Therefore the difference with the initial scaling is quite substantial in both the lower mantle (0.11) and transition zone (0.17).

Observed Geoid (Isostatic Anomalies), no  $C_{20}$ ,  $C_{40}$

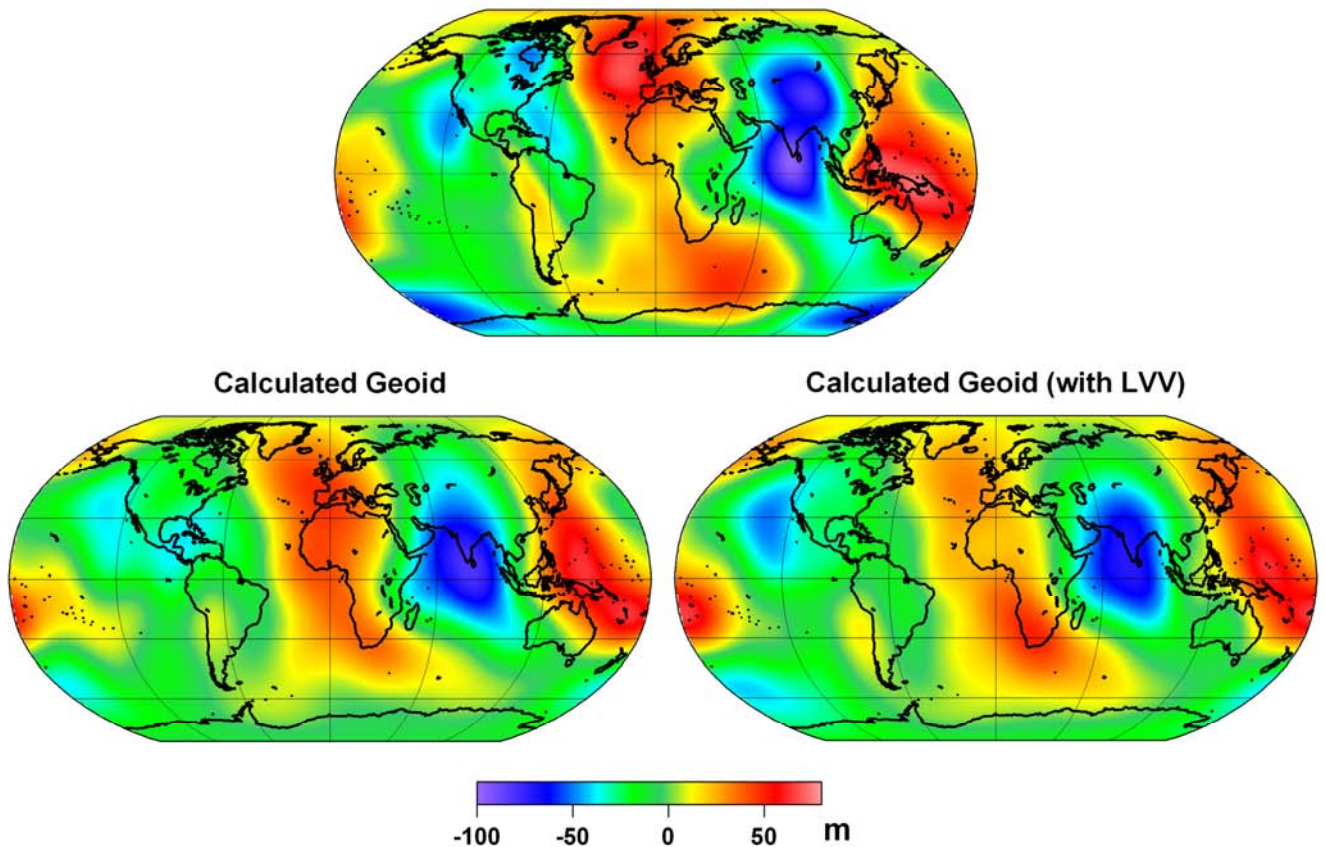


Figure (F7.13) Isostatic anomalies of geoid.

Top: Isostatic anomalies of the observed geoid (Kaban et al., 2004).

Bottom Left: Geoid undulations for the model with radially stratified viscosity.

Bottom Right: Geoid undulations for the model with LVV. Terms  $C_{20}$  and  $C_{40}$  are excluded from all fields.

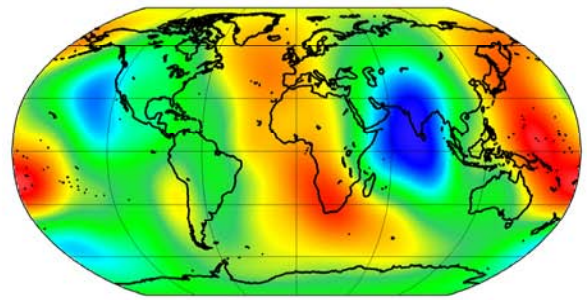
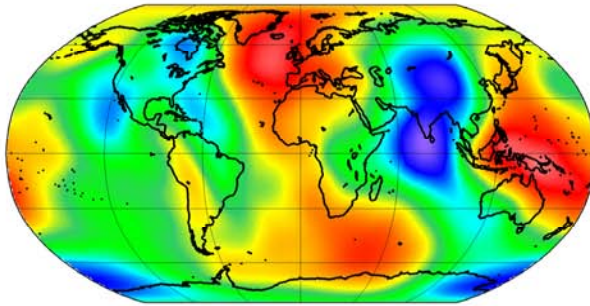
It turns out that for a seven-layer radial viscosity model it is possible to get a reasonable fit to the observed geoid. The radial viscosity model discussed in Part 6.2 explains about 80% of the observed field, being a good result especially taking into account that we have excluded the terms  $C_{20}$  and  $C_{40}$  accumulating half of the total energy of the long-wavelength non-hydrostatic geoid. The calculated geoid for the model with a radially stratified mantle is shown in (F7.13) compared to the observed non-isostatic geoid and geoid calculated taking into account whole-mantle LVV. The terms  $C_{20}$  and  $C_{40}$  are excluded from all fields as well as the impact of the isostatically compensated lithosphere is excluded from the observed geoid (F4.1). This provides a possibility to

uncover the effect of deep mantle horizons and of dynamic disturbances of the Earth's surface. The overall fit of the geoid calculated with LVV (F7.13 Bottom Right) to the observed geoid is approximately the same as for the radial viscosity model but there are several geoid features presented in the observed geoid, appearing only after introducing the LVV. The most pronounced is the negative anomaly located near the western edge of North America. The extended maxima near South America and southern part of Africa are also better presented with the LVV. The same is true for the geoid pattern in South Pacific. The slender waist of the central positive anomaly situated to the west of Africa is also better predicted by the LVV model. This preliminary analysis shows that inclusion of LVV in the whole mantle improves some mid-range features of the dynamic geoid. At the same time some features of geoid sink in precision due to inclusion of LVV in comparison with the radial viscosity model (for example Greenland and northern Australia areas). The Indian anomaly is also reduced by an introduction of the LVV, however, not that significantly.

Based on figure (F7.14) we can arrive at some general conclusion about the origin of the main geoid features whether they appear due to lower- or upper-mantle LVV. Assumptions made up on the base of this brief analysis may help to construct a combined 3-D viscosity model, which could stress special areas of low and high viscosity in the lower and upper mantle, therefore, producing a better fit to the main geoid features.

Observed Geoid (Isostatic Anomalies), no C20, C40

Calculated Geoid (Whole Mantle LVV)



Calculated Geoid (Upper Mantle LVV)

Calculated Geoid (Lower Mantle LVV)

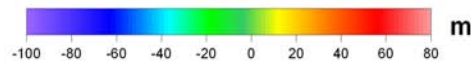
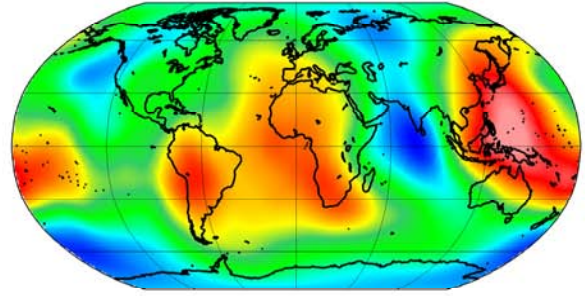
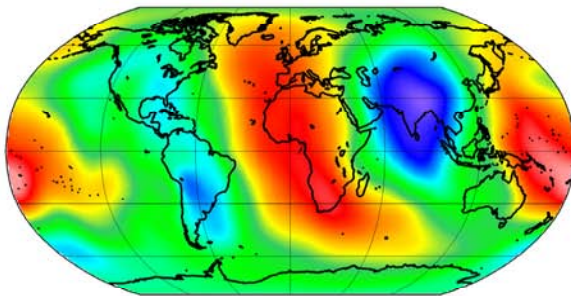


Figure (F7.14) Observed geoid and geoids calculated for various LVV models. Top Left: Isostatic anomalies of the observed geoid (Kaban et al., 2004). Top Right: Whole-mantle LVV model. Bottom Left: LVV in the upper mantle above 670 km (upper mantle LVV model). Bottom Right: LVV in the lower mantle below 670 km (lower mantle LVV model).

It is clearly seen that the strong negative anomaly in the area of Antarctica originates from the effect of lower-mantle LVV as well as the positive anomalies situated to the north of Australia and near South America. But unfortunately the latter positive anomaly shaped by the lower-mantle LVV in the area of South America is suppressed by the opposite effect of the upper-mantle LVV. The negative anomalies in the area of North America result from the combined effect of both the lower and upper mantle as well as the positive anomaly in the Pacific Ocean. Upper-mantle LVV produce a very good fit to the Indian anomaly, which is distorted by interplay between the LVV in the lower and upper mantle.

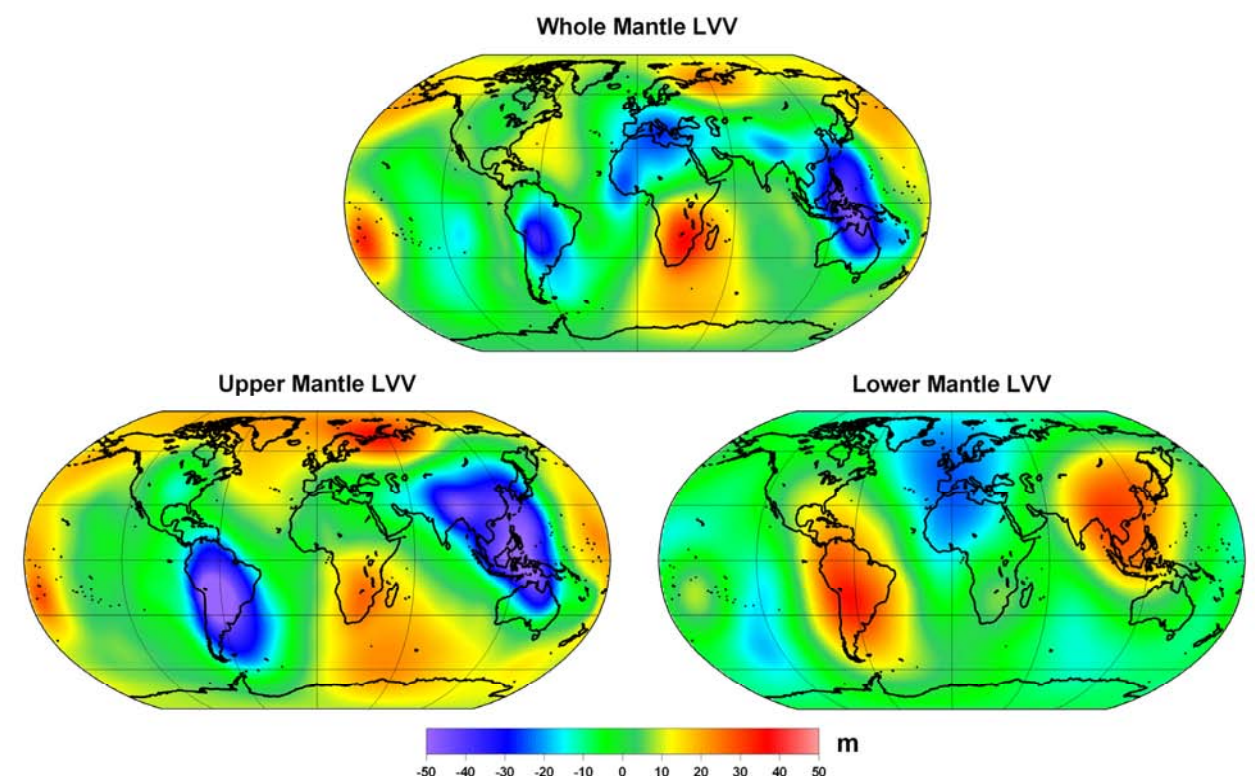


Figure (F7.15) Discrepancies between a dynamic geoid generated by the 3-D viscosity models and initial "radial" model.

Top: Whole-mantle LVV model.

Bottom Left: Upper-mantle LVV model.

Bottom Right: Lower-mantle LVV model.

Discrepancies between the dynamic geoid generated by the 3-D viscosity models and the initial "radial" model are shown in (F7.15). The difference between the initial (only radial viscosity) dynamic geoid and the geoid with implemented LVV reaches  $-47.7 - +37.1$  m for the whole mantle LVV, while the effects of the upper and lower mantle are equal to  $-68.8 - +36.3$  m and  $-24.7 - +35.9$  m correspondingly. The differences are exposed mainly at mid-range scale as it was suggested in the preliminary analysis. Noteworthy, these effects are not correlated in general, that might be of significance for future high-resolution dynamic models. In most areas the effects of the lower-mantle and upper-mantle LVV compensate each other to some extent. But anyway the strongest changes in the geoid generated by the whole-mantle LVV model are mostly produced by the upper-mantle LVV, since the effect of the upper-mantle LVV is of more significance in

comparison with the lower-mantle LVV effect. It is important that the sum of the upper and lower mantle effects is very close to the effect of the whole mantle LVV, the maximum difference is about 2 m. This provides a possibility to model lower- and upper-mantle LVV separately, e.g. using different calculation schemes, which work better in each specific case.

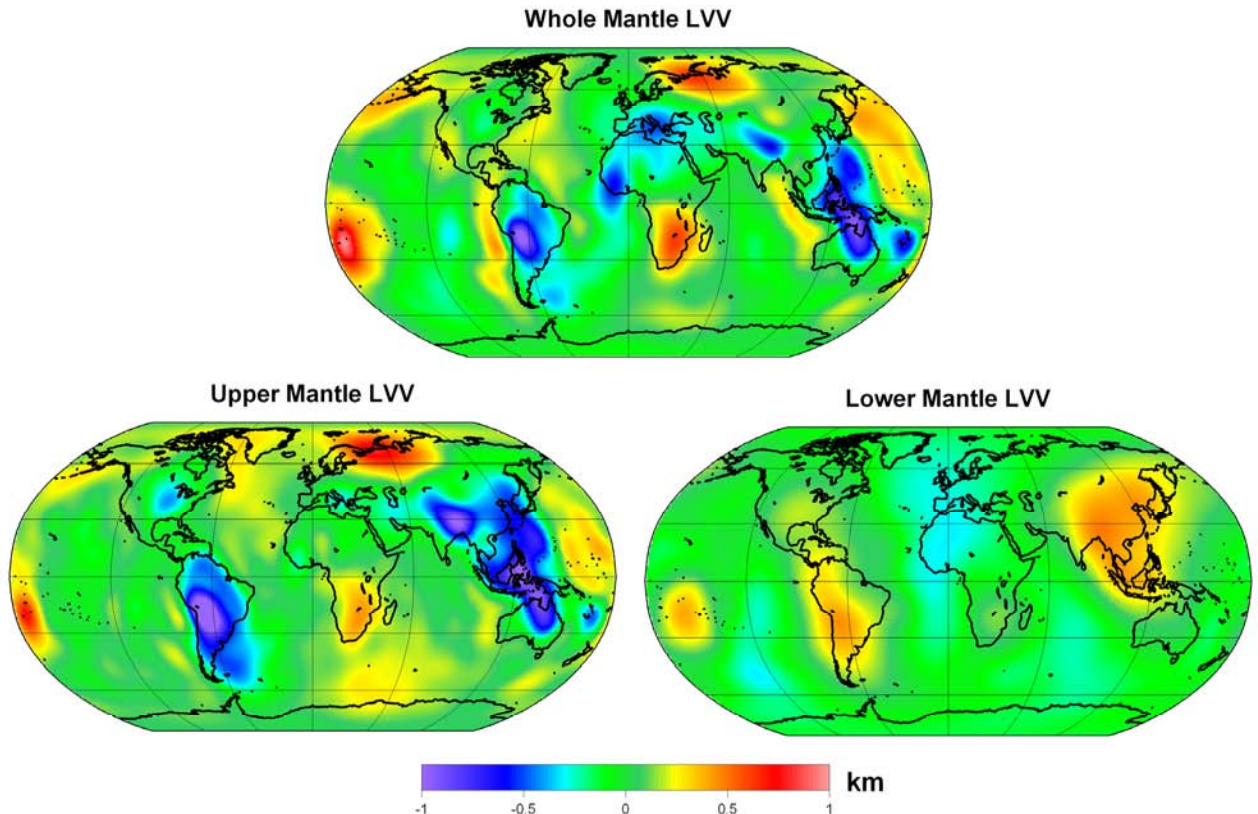


Figure (F7.16) Discrepancies between a dynamic topography generated by the 3-D viscosity models and initial "radial" model.

Top: Whole-mantle LVV model.

Bottom Left: Upper-mantle LVV model.

Bottom Right: Lower-mantle LVV model.

The modifications in the geoid shown in (F7.15) are chiefly produced by differences in surface dynamic topography since the effect of density variations remains unchanged and the effect of the core-mantle boundary is small. The dynamic topography modifications for the tested viscosity models are shown in (F7.16). They correspond qualitatively to the changes of the geoid, however, we see many small-scale details. These details,

which do not remarkably influence the geoid, are mainly due to LVV in the upper mantle (F7.16 Bottom Left). The most significant effects are produced by sharp horizontal viscosity contrast in the upper mantle, e.g. related to the ocean-continent boundaries. Therefore, a relative difference in the amplitudes of the dynamic topography variations due to upper- and lower-mantle viscosity changes is more pronounced than the difference in the dynamic geoid (F7.15). The difference between dynamic topography generated by the initial radial viscosity model and dynamic topography with implemented whole-mantle LVV reaches  $-1.06 - +0.975$  km, while the contribution of the upper- and lower-mantle LVV is equal to  $-1.48 - +0.8$  km and  $-0.31 - +0.49$  km correspondingly. In comparison with the effect on the dynamic geoid the contribution of the upper-mantle LVV into dynamic topography is even larger in amplitude with respect to the effect of the lower-mantle LVV. The higher amplitudes of the changes induced by the upper-mantle LVV are exposed in relatively small-scale details, therefore, they are more important for regional modelling.

Modifications of near-surface mantle velocities (at the depth of 100 km) caused by LVV are shown in (F7.18). These changes are remarkable and reach 21 mm/year. It is important that contrary to the dynamic geoid the effects of the upper- and lower-mantle LVV on horizontal near-surface velocities are not supplementary; generally the total change exceeds significantly the sum of the effects computed separately. The latter statement is brightly illustrated by the velocity patterns in the areas of vortical motion to the east of Australia. It is also important to note that the calculated near-surface mantle flow velocities (F7.17) and changes due to LVV (F7.18) might not completely correspond to plate velocities because our model does not imply stiff lithospheric plates, which integrate these differences over large areas. Despite individual velocity vectors could be changed due to different boundary conditions, a substantial difference between

the lower- and upper-mantle LVV effects should be still significant.

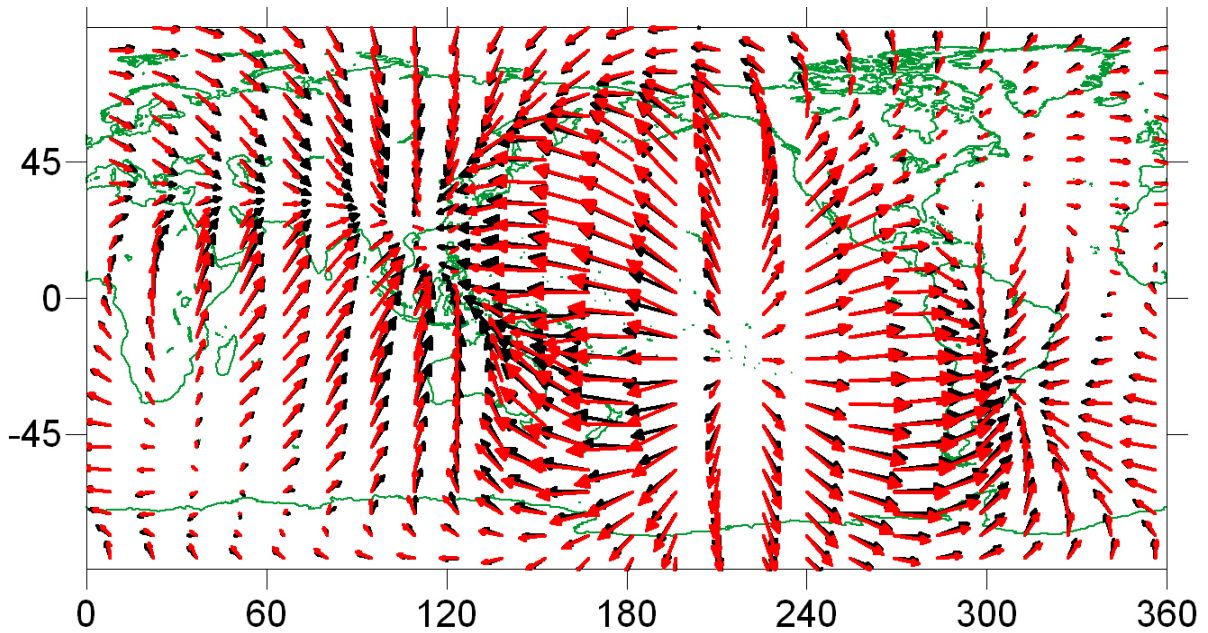


Figure (F7.17) Near-surface mantle velocities.

Black arrows: Radial viscosity model (maximum velocity value 68.7 mm/year).

Red arrows: Whole-mantle LVV model (maximum velocity value 64.5 mm/year).

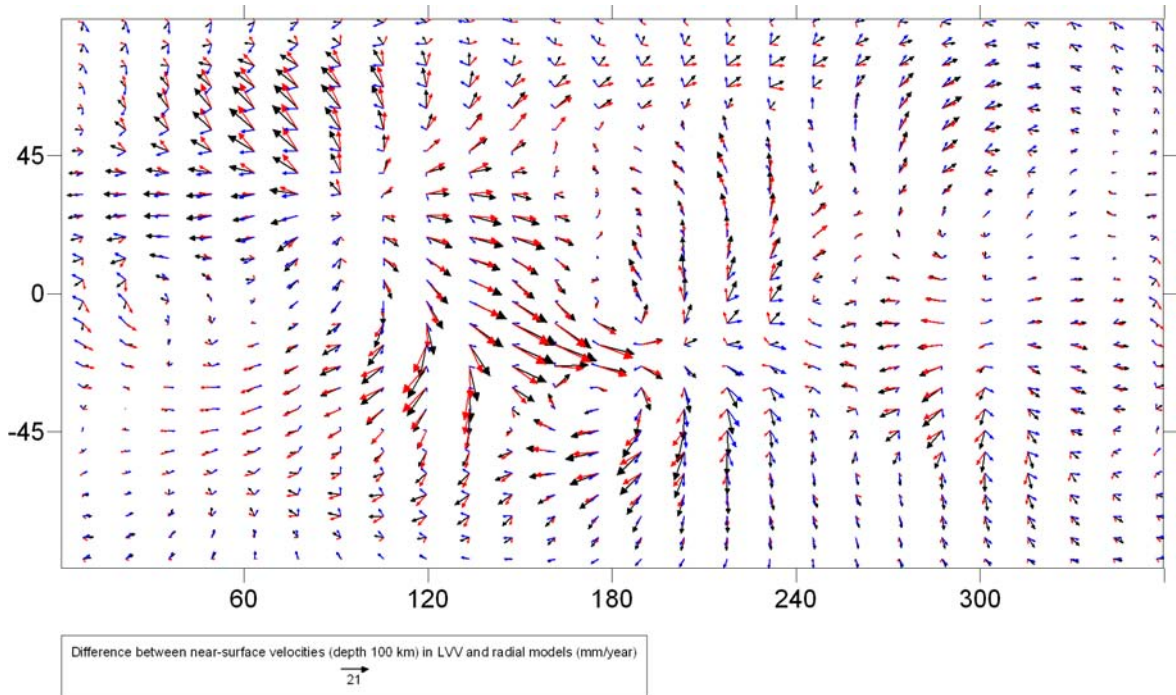


Figure (F7.18) Transformations (differences with the initial radial viscosity model) of near-surface mantle velocities caused by LVV.

Black arrows: Whole-mantle LVV model (maximum value is 20.94 mm/year).

Red arrows: Upper-mantle LVV model (maximum value is 17.79 mm/year).

Blue arrows: Lower mantle LVV model (maximum value is 8.41 mm/year).

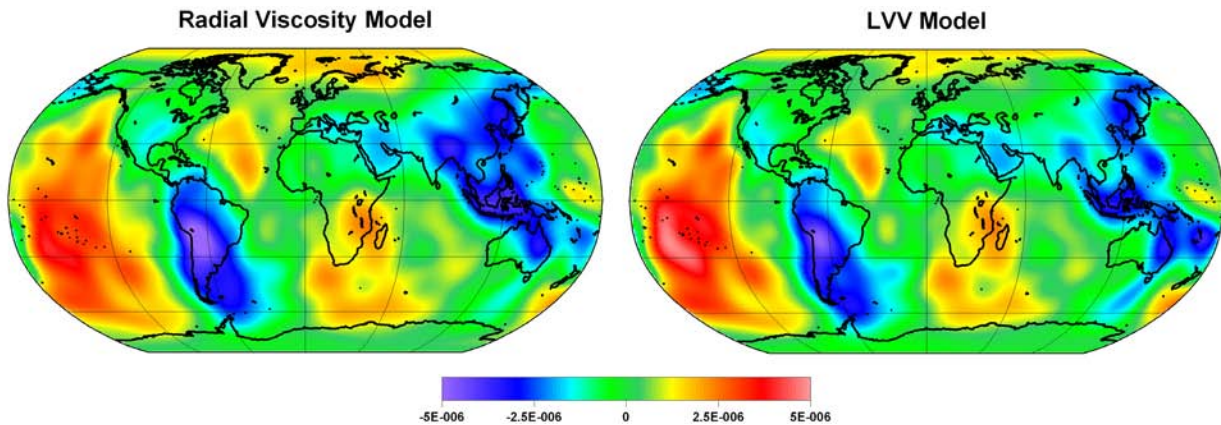


Figure (F7.19) Surface divergence calculated for the radial viscosity model (left) and for the model with whole mantle LVV (right).

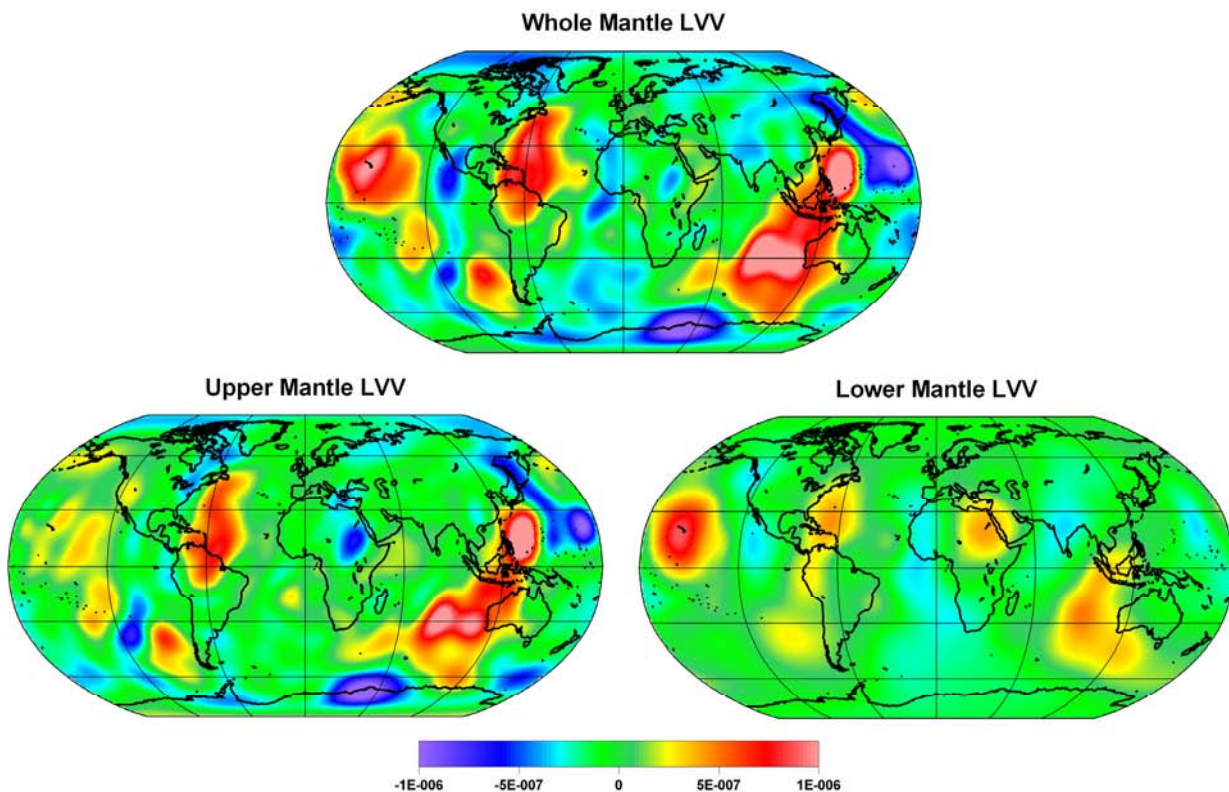


Figure (F7.20) Differences between surface divergence generated by the various LVV models and initial radial viscosity model.

Top: Whole-mantle LVV model.

Bottom Left: Upper-mantle LVV model.

Bottom Right: Lower-mantle LVV model.

As shown in Part 7.2 an obvious interrelation between deep continent roots and negative anomalies of surface divergence (F7.19 Left) is to be suppressed by the effect of LVV (F7.19

Left). Surface divergence is mostly influenced by the upper-mantle LVV (F7.20), while the effect of the lower-mantle LVV is rather minor, but still there are some surface divergence patterns appearing due to lower-mantle LVV only. In general the effect of the lower-mantle LVV tends to intensify the effect of the upper-mantle LVV on surface divergence.

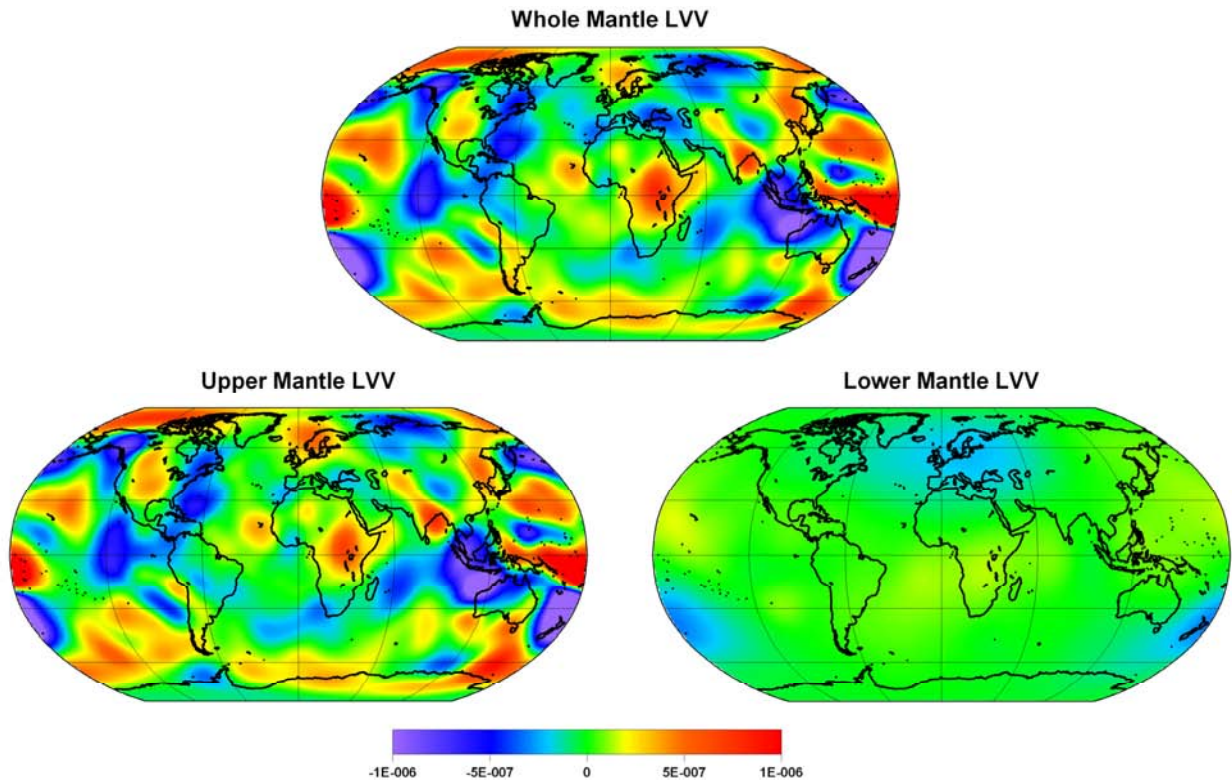


Figure (F7.21) Radial vorticity generated by various 3-D viscosity models.  
 Top: Whole-mantle LVV model.  
 Bottom Left: Upper-mantle LVV model.  
 Bottom Right: Lower-mantle LVV model.

According to (F7.21) the lower-mantle LVV do not play any significant part in forming of vortical near-surface motion. Toroidal flows observed on the surface are generated only by the upper-mantle LVV. The amplitudes of radial vorticity  $[-2.4 \cdot 10^{-6}, 2.4 \cdot 10^{-6}]$  (calculated on the base of averaged surface velocities) are almost twice as great as the amplitudes of the changes in surface divergence due to the whole-mantle LVV  $[-1.25 \cdot 10^{-6}, 1.55 \cdot 10^{-6}]$  and two times as small as the amplitudes of the

very surface divergence  $[-4.9 \cdot 10^{-6}, 4.9 \cdot 10^{-6}]$ . Therefore, an effect of LVV on the surface mantle velocities is directed at generating of the vortical motion to a great extent.

## **Chapter VIII**

### **Conclusions**

A numerical method developed in this study provides the possibility to model mantle flows together with the main convection-related observables (the dynamic geoid, topography and surface velocities), taking into account such specific effects of the Earth's mantle as lateral viscosity variations (LVV), mantle compressibility and self-gravitation. This method combines the spherical harmonic method with the direct Godunov method for the solution of systems of ordinary differential equations and the iterative method applied to incorporate the LVV effect. This combined approach is effective for overcoming all difficulties associated with the introduction of the aforementioned effects.

One of the goals of this work is to demonstrate that the effects of self-gravitation and mantle compressibility have significant influence on the dynamic geoid and mantle flow; therefore, up-to-date studies based on snap-shot models of mantle convection and convection-related observables cannot be comprehensive if these effects are ignored. These effects were analyzed using geoid kernels in a number of studies (Corrieu et al. (1995), Panasyuk et al. (1996) and some others) and found to influence the geoid rather significantly.

The particular contributions of each of these effects to both the dynamic geoid and mantle flow were estimated on the basis of synthetic and realistic models in this study. Among the existing techniques, only the spectral method is capable of taking into account both the mantle compressibility and self-gravitation effects directly. The incorporation of the aforementioned effects to spatial FE and FV methods involves a number of complications discussed in the previous chapters (e.g. Chapter I). Since both effects are found to influence very substantially the dynamic geoid, surface velocities and mantle flows, there arises the

question of whether mantle flows and the dynamic geoid can be modeled correctly by a spatial method ignoring any of these effects. Some synthetic models show that the contributions of the self-gravitation and mantle compressibility effects to the geoid figure are comparable (e.g. 26.5% and 22.5% of amplitudes respectively, see Chapter IV). In more realistic models, the contribution of the self-gravitation effect is much greater (61.5% of amplitudes), while the effect of mantle compressibility is partly opposite to the effect of self-gravitation and significantly reduces it.

This work mostly focuses on the estimation of the influence of LVV on the main observables such as the dynamic geoid, topography and near-surface velocities because the existing studies give rather contradictory conclusions on the significance of this effect. To incorporate the effect of strong LVV we developed two iterative methods (the U-transform and W-transform methods, see Chapter V) based on the concept suggested by Zhang and Christensen (1993). Both methods take into account the effect of mantle compressibility. Comparison of these methods revealed good agreement between results obtained for models with identical input data. Both methods were fully tested in order to assess their capability of taking into account strong LVV. Based on a set of synthetic models, it was shown that the U-transform iterative method could treat effectively LVV varying by about seven orders of magnitude. By contrast, the W-transform iterative method is apparently applicable only to LVV models with rather low viscosity contrasts. Moreover, it gives unreasonable results or simply does not converge if the analyzed LVV models include small-scale details. As a result, we conclude that the W-transform method is inapplicable to a model possessing a resolution higher than five or six spherical harmonics. Therefore, all global models with strong LVV analyzed in this study were calculated with the aid of the U-transform iterative method.

Following Paulson et al. (2005), we constructed a 3-D mantle viscosity model based on the global seismic tomography model of Ekstrom and Dziewonski (1998) converted to temperature variations. The LVV have been calculated according to these variations and on the basis of the assumption of a depth-dependent homologous temperature. It was found that the incorporation of LVV significantly alters the dynamic geoid and near-surface velocities. The contribution of the LVV effect to the geoid exceeds 45% of the maximum geoid undulations calculated for a radial viscosity model. The near-surface velocity distribution is strongly affected by LVV due to not only the LVV-induced toroidal component but also the change in the spheroidal velocity component. The changes in the near-surface velocities are about 30%-40% of the velocity amplitude calculated for the initial radially symmetric model. This study shows that the global flow patterns are, in general, also significantly affected by LVV. Since our 3-D viscosity model is derived from a 3-D temperature distribution, global downwellings are mainly located in areas with a predominant high viscosity, while global upwellings are mostly confined to low viscosity zones. Therefore, mantle upwellings tend to broaden and become more intense due to LVV. By contrast, mantle downwelling flows in high viscosity zones become narrower and weaker.

We also considered several special models in which strong whole-mantle LVV were intersected by small-scale high-viscosity fragments. These synthetic models were used to examine similar effects in the real Earth. We found that the small-scale high-viscosity fragments (always present in the mantle) affect global flows variously, depending mainly on the position of the fragment with respect to the global flow. If located in the way of a flow with nearly constant velocity of the global motion, a high-viscosity fragment is pulled by the surrounding material without having any significant influence on the global motion. By contrast, if a fragment is present in the zone where the motion

changes its direction and velocity values, the surrounding material moves around such a fragment and starts to swerve from a course in advance.

In this study, we specifically analyze the effects of LVV located in the major mantle layers of mantle (the upper and lower mantle) on the dynamic geoid, topography and surface velocities. Employing even a simple radial viscosity profile we are able to explain most of the observed geoid energy (see Chapter VI). Although long-wavelength features are fitted reasonably well, mid- and small-scale model features diverge with the observed fields. This is particularly evident after the removal of the terms  $C_{20}$  and  $C_{40}$  dominating in the long-wavelength nonhydrostatic geoid. We analyze the possible impact of the whole-mantle LVV based on complete resolution tomography data. LVV in the lower mantle are less contrasting than in the subcrustal layer (the maximum contrast is about two orders of magnitude), but some anomalous zones in the lower mantle are much larger than thin zones of strong LVV in the subcrustal layer. Some large viscosity anomalies extend for more than half of the lower mantle thickness. Hence, their integral effect was found to be significant for global dynamic modeling.

The difference between geoids obtained from radially stratified and whole-mantle LVV models varies from  $-47.7$  to  $+37.1$  m, and these values amount to about half of the amplitude of the observed geoid anomalies. This is a significant effect, particularly taking into account that the viscosity model used in this study is likely to represent the lower limit of possible viscosity variations in the upper mantle. Changes in the dynamic geoid modify the resulting velocity-to-density scaling factor. The differences in the scaling factors exceed 40% for the lower mantle, which can be important for mineral physics applications.

The amplitudes of geoid disturbances induced by the upper-mantle LVV ( $-68.8$  -  $+36.3$  m) are somewhat higher than those resulting

from the lower-mantle LVV effect (-24.7 - +35.9 m). However, the latter is generally found to be opposite in sign to the upper-mantle LVV effect; therefore, these effects compensate each other to a great extent. As a result, geoid disturbances induced by the whole-mantle LVV are significantly smaller than changes in the geoid figure due to solely the upper-mantle LVV effect. We also found that the effects of the upper- and lower-mantle LVV on the observed geoid are near complementary with respect to the whole-mantle LVV effect. This conclusion needs to be checked for various viscosity models. If correct, it provides the possibility of separate treatment of lower- and upper-mantle LVV, using techniques that are most effective in these mantle regions.

Although we could not remarkably improve the overall fit of the model geoid to the observed field by consideration of LVV simply incorporated into the radial viscosity model, we arrived at the conclusion that LVV play an important role in the formation of all convection-related fields and mantle flows. Apparently, the influence of LVV on the geoid is so significant that the changes induced by this effect should be adjusted by a proper variation in the radial viscosity profile in order to get a better fit to the observed fields. The inverse problem applied to the 3-D viscosity models with a variable radial viscosity can be effective for solving this problem. Moreover, the particular contributions of lower- and upper-mantle LVV to the geoid figure (see Chapter VII) might be helpful in this case because some geoid features are obviously generated by the effects of only lower- or upper-mantle LVV.

The differences in the dynamic topography induced by the upper- and lower-mantle LVV (accordingly: -1.48 - +0.8 km and -0.31 - +0.49 km for the density equal to 1 g/cm<sup>3</sup>) are qualitatively similar to the corresponding differences in the dynamic geoid. The higher amplitudes of the changes induced by the upper mantle are

exposed in relatively small-scale details therefore, they are more important for regional modelling.

The effect of LVV in the whole mantle on near-surface horizontal flow velocities is also found to be significant: the difference with the initial model reaches 21 mm/year. By contrast to geoid anomalies controlled by vertical flows, the differences of the horizontal flows induced by the lower- and upper-mantle LVV are essentially non-complementary. A joint effect of the mantle layers is normally much stronger than the separate effects of the lower- and upper-mantle LVV.

Although the 3-D viscosity models considered in this study are probably oversimplified, we find that the resulting effect of the whole-mantle LVV is significant. LVV affect substantially both the dynamic geoid and the near-surface flow velocities, the main parameters currently used to constrain dynamic models. Thus, we may conclude that the incorporation of whole-mantle LVV into the next generation global dynamic models is a task of vital significance.

## Appendix.

### Derivation of the U-transform and W-transform iterative methods.

In the following parts I keep the original notations of Zhang and Christensen (1993) (even for geopotential, which they derive separately from mantle velocities and stresses) for a better understanding of the difference between the initial formulae and recently derived formulae.

Agreed notations (N0a- N0g):

$$(a) L \equiv l(l+1)$$

$$(b) Y^\theta \equiv Y_{lm}^\theta(\theta, \varphi) = \frac{\partial Y(\theta, \varphi)}{\partial \theta}$$

$$(c) Y^\varphi \equiv Y_{lm}^\varphi(\theta, \varphi) = \frac{1}{\sin \theta} \frac{\partial Y(\theta, \varphi)}{\partial \varphi}$$

$$(d) Y^{\theta\theta} = Y_{\theta\theta} = \frac{\partial^2 Y}{\partial \theta^2} \quad (N0)$$

$$(e) Y^{\varphi\varphi} = \frac{1}{\sin^2 \theta} Y_{\varphi\varphi} = \frac{1}{\sin^2 \theta} \frac{\partial^2 Y}{\partial \varphi^2}$$

$$(f) Y^{\theta\varphi} = \frac{1}{\sin \theta} Y_{\theta\varphi} = \frac{1}{\sin \theta} \frac{\partial \left( \frac{\partial Y}{\partial \theta} \right)}{\partial \varphi}$$

$$(g) Y^{\varphi\theta} = \frac{1}{\sin \theta} Y_{\varphi\theta} = \frac{\partial \left( \frac{1}{\sin \theta} \frac{\partial Y}{\partial \varphi} \right)}{\partial \theta}$$

$$(h) c \equiv \text{ctg} \theta$$

### Part U.

In case of compressible flow the expressions for viscous stress tensor contain divergence, which may not be neglected. Shear stress is proportional only to the displacement part of the deformation but not to the total deformation, therefore the effect of triaxial compression must be included into the expression for the shear stress (Schubert et al. (2001)).

$$\begin{aligned}
\tau_{rr} &= 2\eta \left[ \frac{\partial U_r}{\partial r} - \frac{1}{3} \nabla \cdot \underline{U} \right] = 2\eta e_{rr} - \frac{2}{3} \eta (e_{rr} + e_{\theta\theta} + e_{\varphi\varphi}) \\
\tau_{r\theta} &= \tau_{\theta r} = \eta \left[ r \frac{\partial (U_\theta/r)}{\partial r} + \frac{1}{r} \frac{\partial U_r}{\partial \theta} \right] = 2\eta e_{r\theta}, \\
\tau_{r\varphi} &= \tau_{\varphi r} = \eta \left[ r \frac{\partial (U_\varphi/r)}{\partial r} + \frac{1}{(r \sin \theta)} \frac{\partial U_r}{\partial \varphi} \right] = 2\eta e_{r\varphi}, \\
\tau_{\theta\theta} &= 2\eta \left[ \frac{1}{r} \frac{\partial U_\theta}{\partial \theta} + \frac{U_r}{r} - \frac{1}{3} \nabla \cdot \underline{U} \right] = 2\eta e_{\theta\theta} - \frac{2}{3} \eta (e_{rr} + e_{\theta\theta} + e_{\varphi\varphi}), \quad (U1) \\
\tau_{\varphi\varphi} &= 2\eta \left[ \frac{1}{(r \sin \theta)} \frac{\partial U_\varphi}{\partial \varphi} + \frac{U_r}{r} + U_\theta (\text{ctg} \theta) / r - \frac{1}{3} \nabla \cdot \underline{U} \right] = 2\eta e_{\varphi\varphi} - \\
&\quad - \frac{2}{3} \eta (e_{rr} + e_{\theta\theta} + e_{\varphi\varphi}) \\
\tau_{\theta\varphi} &= \eta \left[ \frac{(\sin \theta / r)}{\partial \theta} \frac{\partial (U_\varphi / \sin \theta)}{\partial \theta} + \frac{1}{(r \sin \theta)} \frac{\partial U_\theta}{\partial \varphi} \right] = 2\eta e_{\theta\varphi},
\end{aligned}$$

Expressions for the relation between normal strains and mantle flow velocities (Landau, theory of elasticity, 1987):

$$\begin{aligned}
e_{rr} &= \frac{\partial U_r}{\partial r}, \\
e_{\theta\theta} &= \frac{1}{r} \frac{\partial U_\theta}{\partial \theta} + \frac{U_r}{r}, \\
e_{\varphi\varphi} &= \frac{1}{(r \sin \theta)} \frac{\partial U_\varphi}{\partial \varphi} + \frac{U_r}{r} + U_\theta (\text{ctg} \theta) / r \\
e_{r\theta} &= \frac{1}{2} \left[ r \frac{\partial (U_\theta/r)}{\partial r} + \frac{1}{r} \frac{\partial U_r}{\partial \theta} \right] \quad (U2) \\
e_{r\varphi} &= \frac{1}{2} \left[ r \frac{\partial (U_\varphi/r)}{\partial r} + \frac{1}{(r \sin \theta)} \frac{\partial U_r}{\partial \varphi} \right] \\
e_{\theta\varphi} &= \frac{1}{2} \left[ \frac{(\sin \theta / r)}{\partial \theta} \frac{\partial (U_\varphi / \sin \theta)}{\partial \theta} + \frac{1}{(r \sin \theta)} \frac{\partial U_\theta}{\partial \varphi} \right]
\end{aligned}$$

We can consequently represent the equation for the conservation of mass:

$$\begin{aligned}
\text{div} \underline{U} &\equiv \nabla \cdot \underline{U} = \frac{\partial U_r}{\partial r} + \frac{2}{r} U_r + \frac{1}{(r \sin \theta)} \frac{\partial (\sin \theta U_\theta)}{\partial \theta} + \frac{1}{(r \sin \theta)} \frac{\partial U_\varphi}{\partial \varphi} = \\
&= \frac{\partial U_r}{\partial r} + \frac{2}{r} U_r + \frac{1}{r} \frac{\partial U_\theta}{\partial \theta} + \frac{c}{r} U_\theta + \frac{1}{(r \sin \theta)} \frac{\partial U_\varphi}{\partial \varphi} = (e_{rr} + e_{\theta\theta} + e_{\varphi\varphi}) = \\
&= -\frac{1}{r} k U_r \quad (U3)
\end{aligned}$$

Expressions for total stress components:

$$\begin{aligned}
\sigma_{rr} &= -p + 2\eta \frac{\partial U_r}{\partial r} - \frac{2}{3} \eta \nabla \cdot \underline{U}, \\
\tau_{r\theta} &= \eta \left[ \frac{1}{r} \frac{\partial U_r}{\partial \theta} + \frac{\partial U_\theta}{\partial r} - \frac{U_\theta}{r} \right], \\
\tau_{r\varphi} &= \eta \left[ \frac{\partial U_\varphi}{\partial r} + \frac{1}{(r \sin \theta)} \frac{\partial U_r}{\partial \varphi} - \frac{U_\varphi}{r} \right], \quad (U4) \\
\sigma_{\theta\theta} &= -p + 2\eta \frac{1}{r} \left[ \frac{\partial U_\theta}{\partial \theta} + U_r \right] - \frac{2}{3} \eta \nabla \cdot \underline{U} \\
\sigma_{\varphi\varphi} &= -p + 2\eta \frac{1}{r} \left[ \frac{1}{\sin \theta} \frac{\partial U_\varphi}{\partial \varphi} + U_r + c U_\theta \right] - \frac{2}{3} \eta \nabla \cdot \underline{U} \\
\tau_{\theta\varphi} &= \eta \frac{1}{r} \left[ \frac{1}{\sin \theta} \frac{\partial U_\theta}{\partial \varphi} + \frac{\partial U_\varphi}{\partial \theta} - c U_\varphi \right]
\end{aligned}$$

Taking into account (U3)  $\nabla \cdot \underline{U} = -\frac{1}{r} k(r) U_r$

$$\begin{aligned}
\sigma_{rr} &= -p + 2\eta \frac{\partial U_r}{\partial r} + \frac{2}{3} \eta \frac{1}{r} k U_r = -p + 2\eta e_{rr} + \frac{2}{3} \eta \frac{1}{r} k U_r \\
r \tau_{r\theta} &= \eta \left[ \frac{\partial U_r}{\partial \theta} + r \frac{\partial U_\theta}{\partial r} - U_\theta \right] = 2\eta r e_{r\theta}, \\
r \tau_{r\varphi} &= \eta \left[ r \frac{\partial U_\varphi}{\partial r} + \frac{1}{\sin \theta} \frac{\partial U_r}{\partial \varphi} - U_\varphi \right] = 2\eta r e_{r\varphi}, \quad (U5)
\end{aligned}$$

$$\mathbf{r}\sigma_{\theta\theta} = -r\rho + 2\eta[\partial U_{\theta}/\partial\theta + U_r] + (2/3)\eta\mathbf{k}U_r = -r\rho + 2\eta r e_{\theta\theta} + (2/3)\eta\mathbf{k}U_r$$

$$\mathbf{r}\sigma_{\varphi\varphi} = -r\rho + 2\eta[(1/\sin\theta)\partial U_{\varphi}/\partial\varphi + U_r + cU_{\theta}] + (2/3)\eta\mathbf{k}U_r = -r\rho + 2\eta r e_{\varphi\varphi} + (2/3)\eta\mathbf{k}U_r$$

$$\mathbf{r}\tau_{\theta\varphi} = \eta[(1/\sin\theta)\partial U_{\theta}/\partial\varphi + \partial U_{\varphi}/\partial\theta - cU_{\varphi}] = 2\eta r e_{\theta\varphi},$$

Additive viscosity component is stated by means of total viscosity and radial viscosity function:  $\eta(r, \theta, \varphi)_{\text{total}} = \eta^*(r) + \eta_1(r, \theta, \varphi)$

Total stress can be expressed via the means of  $\eta^*(r)$  and  $\eta_1(r, \theta, \varphi)$ :

$$\mathbf{r}\sigma_{rr} = -r\rho + 2r\eta^*\partial U_r/\partial r + (2/3)\eta^*\mathbf{k}U_r + 2r\eta_1\mathbf{e}_{rr} + (2/3)\mathbf{k}\eta_1U_r$$

$$\mathbf{r}\tau_{r\theta} = \eta^*[\partial U_r/\partial\theta + r\partial U_{\theta}/\partial r - U_{\theta}] + 2r\eta_1\mathbf{e}_{r\theta}$$

$$\mathbf{r}\tau_{r\varphi} = \eta^*[r\partial U_{\varphi}/\partial r + (1/\sin\theta)\partial U_r/\partial\varphi - U_{\varphi}] + 2r\eta_1\mathbf{e}_{r\varphi}, \quad (\text{U6})$$

$$\mathbf{r}\sigma_{\theta\theta} = -r\rho + 2\eta^*[\partial U_{\theta}/\partial\theta + U_r] + (2/3)\eta^*\mathbf{k}U_r + 2r\eta_1\mathbf{e}_{\theta\theta} + (2/3)\mathbf{k}\eta_1U_r$$

$$\mathbf{r}\sigma_{\varphi\varphi} = -r\rho + 2\eta^*[(1/\sin\theta)\partial U_{\varphi}/\partial\varphi + U_r + cU_{\theta}] + (2/3)\eta^*\mathbf{k}U_r + 2r\eta_1\mathbf{e}_{\varphi\varphi} + (2/3)\mathbf{k}\eta_1U_r$$

$$\mathbf{r}\tau_{\theta\varphi} = \eta^*[(1/\sin\theta)\partial U_{\theta}/\partial\varphi + \partial U_{\varphi}/\partial\theta - cU_{\varphi}] + 2r\eta_1\mathbf{e}_{\theta\varphi},$$

We are looking for a solution of the Stokes equation for the mantle velocities  $\mathbf{U}$ , stresses  $\sigma_{ij}$  and geopotential  $\Phi$  in spherical harmonics:

$$\mathbf{U}_r = \sum Z_1(\mathbf{r})_{1m} Y_{1m}(\theta, \varphi)$$

$$\mathbf{U}_{\theta} = \sum [Z_2(\mathbf{r})_{1m} Y_{1m}^{\theta} + Z_5(\mathbf{r})_{1m} Y_{1m}^{\varphi}]$$

$$\mathbf{U}_{\varphi} = \sum [Z_2(\mathbf{r})_{1m} Y_{1m}^{\varphi} - Z_5(\mathbf{r})_{1m} Y_{1m}^{\theta}]$$

$$\sigma_{rr} = \sum Y_3 Y, \quad (\text{U7})$$

$$\tau_{r\theta} = \sum (y_4 Y^{\theta} + y_6 Y^{\varphi}),$$

$$\tau_{r\varphi} = \sum (y_4 Y^{\varphi} - y_6 Y^{\theta}),$$

$$\delta\rho(r, \theta, \varphi) = \sum \rho Y,$$

$$\phi(r, \theta, \varphi) = \sum \phi Y,$$

$$p(r, \theta, \varphi) = \sum p(\mathbf{r})_{1m} Y_{1m}$$

Thus, the required vector field  $\mathbf{V}$  is represented as a sum of spheroidal and toroidal fields  $\mathbf{V} = \mathbf{V}_s + \mathbf{V}_t$ :

$$\mathbf{V}_s = (Z_1 Y, Z_2 Y^{\theta}, Z_5 Y^{\varphi})$$

$$\mathbf{V}_t = (0, Z_2 Y^{\varphi}, -Z_5 Y^{\theta})$$

These vectors are mutually orthogonal in every point of the space since their scalar product is equal to zero:

$$(\mathbf{V}_s \cdot \mathbf{V}_t) = 0 + Z_2 Y^{\theta} Z_5 Y^{\varphi} - Z_2 Y^{\varphi} Z_5 Y^{\theta} = 0$$

According to Chandrasekhar, (Schubert et al. (2001)) the poloidal field must meet the requirement  $rZ_1' = -2Z_1 + LZ_2$ . Our study has revealed that under the conditions of mantle compressibility this condition is not satisfied. That's why the vector field  $V_s$  is not pure poloidal field but more comprehensive spheroidal field. The contributions of poloidal and toroidal fields are quantitatively described by the surface divergence and radial vorticity:

**Surface divergence:**

$$\nabla_H \cdot \underline{U}_i = (1/(r \sin \theta)) \partial(\sin \theta U_\theta) / \partial \theta + (1/(r \sin \theta)) \partial U_\phi / \partial \phi \quad (U8a)$$

**Radial vorticity:**

$$[\nabla \underline{U}_i] \cdot \underline{r}_k / r = (1/(r \sin \theta)) \{ \partial(U_\phi \sin \theta) / \partial \theta - \partial U_\theta / \partial \phi \} \quad (U8b)$$

$$U_\theta = \sum [Z_2(r) {}_{1m}Y_{1m}^\theta + Z_5(r) {}_{1m}Y_{1m}^\phi],$$

$$U_\phi = \sum [Z_2(r) {}_{1m}Y_{1m}^\phi - Z_5(r) {}_{1m}Y_{1m}^\theta]$$

$$r \nabla_H \cdot \underline{U}_i = (1/(\sin \theta)) \partial(\sin \theta U_\theta) / \partial \theta + (1/(\sin \theta)) \partial U_\phi / \partial \phi = \partial U_\theta / \partial \theta + c U_\theta +$$

$$+ (1/(\sin \theta)) \partial U_\phi / \partial \phi = Z_2(r) {}_{1m}Y_{1m}^{\theta\theta} + Z_5(r) {}_{1m}Y_{1m}^{\phi\theta} + c Z_2(r) {}_{1m}Y_{1m}^\theta + c Z_5(r) {}_{1m}Y_{1m}^\phi +$$

$$+ Z_2(r) {}_{1m}Y_{1m}^{\phi\phi} - Z_5(r) {}_{1m}Y_{1m}^{\theta\phi} = Z_2 \{ Y^{\theta\theta} + c Y^\theta + Y^{\phi\phi} \} + Z_5 \{ Y^{\phi\theta} + c Y^\phi - Y^{\theta\phi} \} = 0 - LZ_2 Y$$

$$[\nabla \underline{U}_i] \cdot \underline{r}_k = (1/(\sin \theta)) \{ \partial(U_\phi \sin \theta) / \partial \theta - \partial U_\theta / \partial \phi \} = \partial U_\phi / \partial \theta + c U_\phi - (1/(\sin \theta)) \partial U_\theta / \partial \phi =$$

$$= Z_2 Y^{\phi\theta} - Z_5 Y^{\theta\phi} + c \{ Z_2 Y^\phi - Z_5 Y^\theta \} - Z_2 Y^{\theta\phi} - Z_5 Y^{\phi\phi} = Z_2 \{ Y^{\phi\theta} + c Y^\phi - Y^{\theta\phi} \} - Z_5 \{ Y^{\theta\phi} + c Z_5 Y^\theta + Y^{\phi\phi} \} =$$

$$= 0 + LZ_5 Y$$

$$\nabla_H \cdot \underline{U}_i = -(L/r) Z_2 Y$$

$$[\nabla \underline{U}_i] \cdot \underline{r}_k / r = (L/r) Z_5 Y$$

Hence, velocity component  $Z_2$  is responsible for the spheroidal (poloidal in case of incompressible flow) constituent of horizontal mantle velocity, while  $Z_5$  defines the toroidal part.

Geopotential used by Zhang and Christensen (1993) is denoted  $\Phi$ , geopotential used in our study is found from E5.4g as  $Z_7$ . Relation between our notations and original notations of Zhang and Christensen (1993):

$$\Phi = Z_7 / r$$

$$\mathbf{y}_3 = (1/r) Z_3 - \rho^* \Phi \quad (N1)$$

$$\mathbf{y}_4 = (1/r) Z_4$$

$$\mathbf{y}_6 = (1/r)\mathbf{z}_6$$

This difference between notations shown in (N1) will be covered in the final deductions.

The other three components of total stress tensor  $\sigma_{rr}$ ,  $\sigma_{\theta\theta}$  and  $\sigma_{\phi\phi}$  can be found with the aid of expansions (U6) for the mantle velocities:

$$\begin{aligned} r\sigma_{\theta\theta} &= -rp + 2\eta^* [\partial U_\theta / \partial \theta + U_r] + (2/3)\eta^* k U_r + 2r\eta_1 e_{\theta\theta} + (2/3)k\eta_1 U_r \\ r\sigma_{\theta\theta} &= -r \sum p(r)_{1m} Y_{1m} + 2\eta^* \sum [Z_{21m} Y_{1m}^{\theta\theta} + Z_{51m} Y_{1m}^{\phi\theta} + Z_{11m} Y_{1m}] + (2/3)\eta^* k \sum Z_{11m} Y_{1m} + 2\eta_1 r e_{\theta\theta} + \\ &+ (2/3)k\eta_1 U_r \end{aligned} \quad (U9a)$$

$$\begin{aligned} r\sigma_{\phi\phi} &= -rp + 2\eta^* [(1/\sin\theta)\partial U_\phi / \partial \phi + U_r + cU_\theta] + (2/3)\eta^* k U_r + 2r\eta_1 e_{\phi\phi} + (2/3)k\eta_1 U_r \\ r\sigma_{\phi\phi} &= -r \sum p Y + 2\eta^* \sum [Z_1 Y + Z_2 (Y^{\phi\phi} + cY^\theta) + Z_5 (-Y^{\theta\phi} + cY^\phi)] + (2/3)\eta^* k \sum Z_1 Y + 2r\eta_1 e_{\phi\phi} + \\ &+ (2/3)k\eta_1 U_r \end{aligned} \quad (U9b)$$

$$\begin{aligned} r\tau_{\theta\phi} &= \eta^* [(1/\sin\theta)\partial U_\theta / \partial \phi + \partial U_\phi / \partial \theta - cU_\phi] + 2\eta_1 r e_{\theta\phi}, \\ r\tau_{\theta\phi} &= \eta^* \sum [(Z_2 Y^{\theta\phi} + Z_5 Y^{\phi\phi}) + (Z_2 Y^{\phi\theta} - Z_5 Y^{\theta\theta}) - c(Z_2 Y^\phi - Z_5 Y^\theta)] + 2\eta_1 r e_{\theta\phi}, \\ r\tau_{\theta\phi} &= \eta^* \sum [Z_2 (Y^{\theta\phi} + Y^{\phi\theta} - cY^\phi) + Z_5 (Y^{\phi\phi} - Y^{\theta\theta} + cY^\theta)] + 2\eta_1 r e_{\theta\phi}, \\ r\tau_{\theta\phi} &= \eta^* \sum [2Z_2 (Y^{\theta\phi} - cY^\phi) - Z_5 (LY + Y^{\theta\theta})] + 2r\eta_1 e_{\theta\phi}, \end{aligned} \quad (U9c)$$

where the coefficients  $p(r)_{lm}$  depend only on  $r$ , spherical functions  $\eta_1 e_{\theta\theta}$  and  $\eta_1 U_r$  are obtained from the previous iterative step.

### Derivation of the ODE system for the spherical harmonic coefficients

$Z_{11m}(r)$ ,  $Z_{21m}(r)$ ,  $Z_{51m}(r)$ ,  $Y_{31m}(r)$ ,  $Y_{41m}(r)$ ,  $Y_{61m}(r)$  and  $p_{1m}(r)$ :

1) Mass conservation:

$$\begin{aligned} 2U_r/r + \partial U_r / \partial r + (1/r) [\partial U_\theta / \partial \theta + cU_\theta + (1/\sin\theta)\partial U_\phi / \partial \phi] &= -(1/r)k(r)U_r \\ 2\sum (Z_1/r)Y + \sum Y Z_1' + \sum (Z_2/r) [Y^{\theta\theta} + cY^\theta + Y^{\phi\phi}] + \sum (Z_5/r) [Y^{\phi\theta} + cY^\phi - Y^{\theta\phi}] &= -(1/r)k \sum Z_1 Y \\ 2\sum (Z_1/r)Y + \sum Z_1' Y - \sum (Z_2/r)LY &= -(1/r)k \sum Z_1 Y \\ 2\sum Z_1 Y + r \sum Z_1' Y - \sum Z_2 LY &= -k \sum Z_1 Y \\ rZ_1' &= -(2+k)Z_1 + LZ_2 \quad \Rightarrow A_{1m} = 0 \end{aligned}$$

$$r \frac{dZ_1^{lm}}{dr} = -(2+k)Z_1^{lm} + LZ_2^{lm} \quad (U10)$$

2) Relation between  $\sigma_{rr}$  and mantle velocities:

$$r\sigma_{rr} = -rp + 2r\eta^* \partial U_r / \partial r + (2/3)\eta^* k U_r + 2r\eta_1 e_{rr} + (2/3)\eta_1 k U_r$$

Viscous terms can be represented via the means of spherical functions:

$$\begin{aligned}\eta_1 \mathbf{e}_{rr} &= \sum (\eta_1 \mathbf{e}_{rr})_{1m} Y_{1m}(\theta, \varphi) \\ \eta_1 \mathbf{U}_r &= \sum (\eta_1 \mathbf{U}_r)_{1m} Y_{1m}(\theta, \varphi)\end{aligned}\tag{U11}$$

$$(\eta_1 \mathbf{e}_{rr})_{1m} = (1/s_{m0}) \iint \eta_1 U_r Y_{1m} d\varphi \sin\theta d\theta,$$

$$(\eta_1 \mathbf{U}_r)_{1m} = (1/s_{m0}) \iint \eta_1 e_{rr} Y_{1m} d\varphi \sin\theta d\theta$$

$$r \sum Y_3 Y = -r \sum p + 2r \eta^* \sum Z_1' Y + (2/3) \eta^* k \sum Z_1 Y + 2r \sum (\eta_1 \mathbf{e}_{rr})_{1m} Y_{1m}(\theta, \varphi) + (2/3) k \sum (\eta_1 \mathbf{U}_r) Y$$

$$r p_{1m} = 2\eta^* r Z_1' - r y_3 + (2/3) \eta^* k Z_1 + 2r (\eta_1 \mathbf{e}_{rr})_{1m} + (2/3) k (\eta_1 \mathbf{U}_r)_{1m}$$

Using the derived relation (U10)  $r Z_1' = -(2+k) Z_1 + L Z_2$ :

$$r p = -2\eta^* (2+k) Z_1 + 2\eta^* L Z_2 - r y_3 + (2/3) \eta^* k Z_1 + 2r (\eta_1 \mathbf{e}_{rr}) + (2/3) k (\eta_1 \mathbf{U}_r)$$

Hence, the spherical pressure function can be obtained from the following expression:

$$\begin{aligned}r p(r, \theta, \varphi) &= \sum \{ -2\eta^* (2+k) Z_{11m}(r) + 2\eta^* L Z_2(r) - r y_3(r) + (2/3) \eta^* k Z_1(r) \}_{1m} Y_{1m} + \\ &+ \sum [ 2r (\eta_1 \mathbf{e}_{rr})_{1m} + (2/3) k (\eta_1 \mathbf{U}_r)_{1m} ] Y_{1m}\end{aligned}$$

Switching to the notations of Zhang and Christensen (1993):

$$\begin{aligned}r p(r, \theta, \varphi) &= \sum \{ -2\eta^* (2+k) Z_{11m}(r) + 2\eta^* L Z_2(r) - Z_3(r) + (2/3) \eta^* k Z_1(r) + r \rho_0 \Phi \}_{1m} Y_{1m} + \\ &+ \sum [ (2/3) k (\eta_1 \mathbf{U}_r)_{1m} + 2r (\eta_1 \mathbf{e}_{rr})_{1m} ] Y_{1m}\end{aligned}\tag{U12}$$

4) Relation between  $\tau_{r\theta}$  and mantle velocities:

$$r \tau_{r\theta} = \eta^* [ \partial U_r / \partial \theta + r \partial U_\theta / \partial r - U_\theta ] + 2r \eta_1 \mathbf{e}_{r\theta}$$

$$\sum r y_4 Y^\theta + \sum r y_6 Y^\varphi = \eta^* \sum Z_1 Y^\theta + \eta^* r \sum [ Z_2' Y^\theta + Z_5' Y^\varphi ] - \eta^* \sum [ Z_2 Y^\theta + Z_5 Y^\varphi ] + 2r \eta_1 \mathbf{e}_{r\theta}$$

$$Z_4 Y^\theta + Z_6 Y^\varphi = \eta^* Z_1 Y^\theta + \eta^* r [ Z_2' Y^\theta + Z_5' Y^\varphi ] - \eta^* [ Z_2 Y^\theta + Z_5 Y^\varphi ] + 2r \eta_1 \mathbf{e}_{r\theta}$$

$$\sum [ r Z_2' - Z_4 / \eta^* + Z_1 - Z_2 ] Y^\theta + \sum [ r Z_5' - Z_6 / \eta^* - Z_5 ] Y^\varphi + (2r / \eta^*) \eta_1 \mathbf{e}_{r\theta} = 0$$

Viscous terms corresponding to  $\tau_{r\theta}$  and  $\tau_{r\varphi}$  must be represented as a sum of spheroidal and toroidal fields as well as the components of viscous stress tensor  $\tau_{r\theta}$  and  $\tau_{r\varphi}$  themselves:

$$\eta_1 \mathbf{e}_{r\theta} = F_1(r, \theta, \varphi) = \sum f_a(r)_{1m} Y_{1m}^\theta + f_b(r)_{1m} Y_{1m}^\varphi \Rightarrow\tag{U13a}$$

$$\begin{aligned}\sum [ r Z_2' - Z_4 / \eta^* + Z_1 - Z_2 + (2r / \eta^*) f_a(r) ] Y^\theta + [ r Z_5' - Z_6 / \eta^* - Z_5 + \\ + (2r / \eta^*) f_b(r) ] Y^\varphi = 0\end{aligned}\tag{U13b}$$

5) Relation between  $\tau_{r\varphi}$  and mantle velocities:

$$r \tau_{r\varphi} = \eta^* [ r \partial U_\varphi / \partial r + (1/\sin\theta) \partial U_r / \partial \varphi - U_\varphi ] + 2r \eta_1 \mathbf{e}_{r\varphi},$$

$$r y_4 Y^\theta - r y_6 Y^\varphi = \eta^* [ r Z_2' Y^\theta - r Z_5' Y^\varphi + Z_1 (1/\sin\theta) \partial Y / \partial \varphi - Z_2 Y^\theta + Z_5 Y^\varphi ] + 2r \eta_1 \mathbf{e}_{r\varphi}.$$

$$Z_4 Y^\varphi - Z_6 Y^0 = \eta^* [r Z'_2 Y^\varphi - r Z'_5 Y^0 + Z_1 \partial Y^\varphi - Z_2 Y^\varphi + Z_5 Y^0] + 2r \eta_1 \mathbf{e}_{r\varphi}.$$

$$[-Z_4 + \eta^* r Z'_2 + \eta^* Z_1 - \eta^* Z_2] Y^\varphi + [Z_6 - \eta^* r Z'_5 + \eta^* Z_5] Y^0 + 2r \eta_1 \mathbf{e}_{r\varphi} = 0$$

$$\Sigma [r Z'_2 - Z_4 / \eta^* + Z_1 - Z_2] Y^\varphi - \Sigma [r Z'_5 - Z_6 / \eta^* - Z_5] Y^0 + (2r / \eta^*) \eta_1 \mathbf{e}_{r\varphi} = 0$$

In a similar manner as in (U13a) we represent the viscous term  $\eta_1 \mathbf{e}_{r\varphi}$  as a sum of spheroidal and toroidal fields:

$$\eta_1 \mathbf{e}_{r\varphi} = F_2(r, \theta, \varphi) = \Sigma f_a(r)_{1m} Y_{1m}^\varphi - f_b(r)_{1m} Y_{1m}^0 \quad (\text{U14a})$$

$$\Sigma [r Z'_2 - Z_4 \eta^* + Z_1 - Z_2 + 2(r / \eta^*) f_a] Y^\varphi - \Sigma [r Z'_5 - Z_6 / \eta^* - Z_5 + 2(r / \eta^*) f_b] Y^0 = 0 \quad (\text{U14b})$$

Coefficients  $f_a(r)_{1m}$  and  $f_b(r)_{1m}$  are the same for (U13b) and (U14b). The equations (U13b) and (U14b) can be represented in common form as:

$$\Sigma A Y^0 + \Sigma B Y^\varphi = 0, \quad | * Y(\theta', \varphi')^0$$

$$\Sigma A Y^\varphi - \Sigma B Y^0 = 0 \quad | * Y(\theta', \varphi')^\varphi$$

The first and the second equations multiplied by  $Y(\theta', \varphi')^0$  and  $Y(\theta', \varphi')^\varphi$  correspondently are integrated and summed up:

$$\Sigma A \int \{ Y^0 Y^0 + Y^\varphi Y^\varphi \} \sin \theta' d\theta' d\varphi' + \Sigma B \int \{ Y^\varphi Y^0 - Y^0 Y^\varphi \} \sin \theta' d\theta' d\varphi' = A$$

In much the same way the first and the second equations are multiplied conversely by  $Y(\theta', \varphi')^\varphi$  and  $Y(\theta', \varphi')^0$  correspondently, integrated and subtracted one from another:

$$\Sigma A \int \{ Y^0 Y^\varphi - Y^\varphi Y^0 \} \sin \theta' d\theta' d\varphi' + \Sigma B \int \{ Y^\varphi Y^\varphi + Y^0 Y^0 \} \sin \theta' d\theta' d\varphi' = 0 + B = B$$

Both expressions must be equal to zero  $\Rightarrow A = B = 0$ .

Therefore we can avoid unnecessary calculations and obtain the solution from (U13b) without considering (U14b), which gives the same result.

$$f_a = (1 / s_{m1}) \int_0^{2\pi} d\varphi \int_0^\pi \{ F_1 Y_{1m}^\theta + F_2 Y_{1m}^\varphi \} \sin \theta d\theta.$$

$$\mathbf{f}_a = (1 / s_{m1}) \int_0^{2\pi} d\varphi \int_0^\pi \eta^* [\eta_1 \mathbf{e}_{r\theta}] Y_{1m}^\theta + [\eta_1 \mathbf{e}_{r\varphi}] Y_{1m}^\varphi \sin \theta d\theta,$$

$$f_b = (1 / s_{m1}) \int_0^{2\pi} d\varphi \int_0^\pi \{ F_1 Y_{1m}^\varphi - F_2 Y_{1m}^\theta \} \sin \theta d\theta.$$

$$\mathbf{f}_b = (1 / s_{m1}) \int_0^{2\pi} d\varphi \int_0^\pi [\eta^* \{ [\eta_1 \mathbf{e}_{r\theta}] Y_{1m}^\varphi - [\eta_1 \mathbf{e}_{r\varphi}] Y_{1m}^\theta \}] \sin \theta d\theta$$

$$r Z'_2 = -Z_1 + Z_2 + Z_4 / \eta^* - (2r / \eta^*) \mathbf{f}_a,$$

$$r Z'_2 = -Z_1 + Z_2 + Z_4 / \eta^* + B,$$

$$\mathbf{f}_a = (1 / s_{1m}) \iint \eta_1 \{ \mathbf{e}_{r\theta} Y^\theta + \mathbf{e}_{r\varphi} Y^\varphi \} d\varphi \sin \theta d\theta,$$

$$\mathbf{B}^{1m} = -2(r / \eta^*) \mathbf{f}_a$$

$$r \frac{dZ_2^{lm}}{dr} = -Z_1^{lm} + Z_2^{lm} + \frac{1}{\eta^*} Z_4^{lm} - \frac{2r}{s_{lm} \eta^*} \int_0^{2\pi} d\varphi \int_0^\pi \tilde{\eta} (e_{r\theta} Y_{lm}^\theta + e_{r\varphi} Y_{lm}^\varphi) \sin \theta d\theta \quad (U15)$$

$$\mathbf{rZ}'_5 = \mathbf{Z}_5 + \mathbf{Z}_6 / \eta^* - 2(\mathbf{r} / \eta^*) \mathbf{f}_b,$$

$$\mathbf{rZ}'_5 = \mathbf{Z}_5 + \mathbf{Z}_6 / \eta^* + \mathbf{E}^{1m},$$

$$\mathbf{E}^{1m} = -2(\mathbf{r} / \eta^*) \mathbf{f}_b,$$

$$\mathbf{f}_b = (1 / (s_{1m})) \iint \eta_1 \{ \mathbf{e}_{r\theta} \mathbf{Y}^\varphi - \mathbf{e}_{r\varphi} \mathbf{Y}^\theta \} d\varphi \sin \theta d\theta$$

$$r \frac{dZ_5^{lm}}{dr} = Z_5^{lm} + \frac{1}{\eta^*} Z_6^{lm} - \frac{2r}{s_{lm} \eta^*} \int_0^{2\pi} d\varphi \int_0^\pi \tilde{\eta} (e_{r\theta} Y_{lm}^\varphi - e_{r\varphi} Y_{lm}^\theta) \sin \theta d\theta \quad (U16)$$

As it is easy to see, the expressions for the viscous terms appearing in the equations E5.4b and E5.4e (spheroidal and toroidal mantle velocities) differ from those stated by Zhang and Christensen (1993) not only by sign but also by coefficient 2.

6) Stokes equation along the axis  $\mathbf{e}_r$ :

$$\partial \sigma_{rr} / \partial r + (1/r) \partial \tau_{r\theta} / \partial \theta + (1/r \sin \theta) \partial \tau_{r\varphi} / \partial \varphi + (1/r) [2\sigma_{rr} - \sigma_{\theta\theta} - \sigma_{\varphi\varphi} + c\tau_{r\theta}] - \delta \rho g_0 + \rho_0 \partial \Phi / \partial r = 0$$

$$r^2 \partial \sigma_{rr} / \partial r + r \partial \tau_{r\theta} / \partial \theta + (r / \sin \theta) \partial \tau_{r\varphi} / \partial \varphi + r [2\sigma_{rr} - \sigma_{\theta\theta} - \sigma_{\varphi\varphi} + c\tau_{r\theta}] - r^2 \delta \rho g_0 + r^2 \rho_0 \partial \Phi / \partial r = 0.$$

Expressions for the stress tensor components in spherical harmonics are substituted into the considered equation:

$$\sigma_{rr} = \sum Y_3 Y,$$

$$\tau_{r\theta} = \sum Y_4 Y^\theta + y_6 Y^\varphi,$$

$$\tau_{r\varphi} = \sum Y_4 Y^\varphi - y_6 Y^\theta,$$

$$r\sigma_{\theta\theta} = -rp + 2\eta^* [\partial U_\theta / \partial \theta + U_r] + (2/3)\eta^* k U_r + 2r\eta_1 e_{\theta\theta} + (2/3)k\eta_1 U_r$$

$$r\sigma_{\varphi\varphi} = -rp + 2\eta^* [(1/\sin \theta) \partial U_\varphi / \partial \varphi + U_r + cU_\theta] + (2/3)\eta^* k U_r + 2r\eta_1 e_{\varphi\varphi} + (2/3)k\eta_1 U_r$$

$$r^2 \mathbf{y}'_3 \mathbf{Y} + r y_4 Y^{\theta\theta} + r y_6 Y^{\varphi\varphi} + r y_4 Y^{\varphi\theta} - r y_6 Y^{\theta\varphi} + 2r y_3 Y + \{ rp - 2\eta^* [Z_2 Y^{\theta\theta} + Z_5 Y^{\varphi\varphi} + Z_1 Y] -$$

$$-(2/3)\eta * k Z_1 Y - 2r\eta_1 e_{\theta\theta} - (2/3)k\eta_1 U_r + \{rp - 2\eta * [Z_1 Y + Z_2 (Y^{\theta\theta} + cY^\theta) + Z_5 (-Y^{\theta\theta} + cY^\theta)] - (2/3)\eta * k Z_1 Y - 2r\eta_1 e_{\phi\phi} - (2/3)k\eta_1 U_r\} + c(rY_4 Y^\theta + rY_6 Y^\phi) - r^2 \delta\rho g_0 Y + r^2 \rho_0 \partial\Phi / \partial r Y = 0.$$

$$r^2 \sum Y'_{3Y} + r \sum Y_4 [Y^{\theta\theta} + Y^{\phi\phi} + cY^\theta] + r \sum Y_6 [Y^{\theta\theta} - Y^{\phi\phi} + cY^\theta] + 2r \sum Y_3 Y + 2rp + 2\eta * \sum [-Z_2 Y^{\theta\theta} - Z_5 Y^{\phi\phi} - Z_1 Y] + 2\eta * \sum [-Z_2 (Y^{\phi\phi} + cY^\theta) + Z_5 (Y^{\theta\theta} - cY^\theta) - Z_1 Y] - (4/3)\eta * k \sum Z_1 Y - 2r\eta_1 e_{\theta\theta} - 2r\eta_1 e_{\phi\phi} - (4/3)k\eta_1 U_r - r^2 \sum \delta\rho g_0 Y + r^2 \rho_0 \sum \partial\Phi / \partial r Y = 0.$$

Taking into account properties of spherical functions' derivatives E3.7a and E3.7b  $\underline{Y^{\theta\theta} + Y^{\phi\phi} + cY^\theta = -LY}$ ,  $\underline{Y^{\theta\theta} + cY^\theta - Y^{\phi\phi} = 0}$  to the derived equation we simplify derived equation:

$$r^2 \sum Y'_{3Y} - Lr \sum Y_4 Y + 2r \sum Y_3 Y + 2rp + 2\eta * \sum [-Z_2 (Y^{\theta\theta} + Y^{\phi\phi} + cY^\theta) + Z_5 (-Y^{\theta\theta} + Y^{\phi\phi} - cY^\theta) - Z_1 Y] - 2r\eta_1 e_{\theta\theta} - 2r\eta_1 e_{\phi\phi} - (4/3)k\eta_1 U_r - (4/3)\eta * k \sum Z_1 Y - r^2 g_0 \sum \delta\rho Y + r^2 \rho_0 \sum \partial\Phi / \partial r Y = 0.$$

$$r^2 \sum Y'_{3Y} - Lr \sum Y_4 Y + 2r \sum Y_3 Y + 2rp + 2\eta * \sum [LZ_2 Y - 2Z_1 Y] - 2r\eta_1 e_{\theta\theta} - 2r\eta_1 e_{\phi\phi} - (4/3)k\eta_1 U_r - (4/3)\eta * k \sum Z_1 Y - r^2 g_0 \sum \delta\rho Y + r^2 \rho_0 \sum \partial\Phi / \partial r Y = 0.$$

Now it is time to substitute the expression for the dynamic pressure (U12) into considered equation:

$$rp(r, \theta, \phi) = \sum \{-2\eta * (2+k) Z_{11m}(r) + 2\eta * LZ_2(r) - Z_3(r) + (2/3)\eta * k Z_1(r) + r\rho_0 \Phi\}_{1m} Y_{1m} + \sum [(2/3)k(\eta_1 U_r) + 2r(\eta_1 e_{rr})] Y_{1m}$$

$$r^2 \sum Y'_{3Y} - Lr \sum Y_4 Y + 2r \sum Y_3 Y + \sum \{-4\eta * (2+k) Z_1(r) + 4\eta * LZ_2(r) - 2Z_3(r) + (4/3)\eta * k Z_1(r) + 2r\rho_0 \Phi\}_{1m} Y_{1m} + \sum [(4/3)k(\eta_1 U_r) + 4r(\eta_1 e_{rr})] Y_{1m} + 2\eta * \sum [LZ_2 Y - 2Z_1 Y] - 2r\eta_1 e_{\theta\theta} - 2r\eta_1 e_{\phi\phi} - (4/3)k\eta_1 U_r - (4/3)\eta * k \sum Z_1 Y - r^2 g_0 \sum \delta\rho Y + r^2 \rho_0 \sum \partial\Phi / \partial r Y = 0.$$

$$Y_3 = (1/r) Z_3 - \rho_0 \Phi,$$

$$r^2 \sum Y'_{3Y} - Lr \sum Y_4 Y - 2r\rho_0 \Phi + \sum \{-4\eta * (2+k) Z_1 + 2r\rho_0 \Phi\}_{1m} Y_{1m} + \sum [(4/3)k(\eta_1 U_r) + 4r(\eta_1 e_{rr})] Y_{1m} + 6\eta * LZ_2 Y - 4\eta * Z_1 Y - 2r\eta_1 e_{\theta\theta} - 2r\eta_1 e_{\phi\phi} - (4/3)k\eta_1 U_r - r^2 g_0 \sum \delta\rho Y + r^2 \rho_0 \sum \partial\Phi / \partial r Y = 0.$$

$$r^2 \sum Y'_{3Y} - Lr \sum Y_4 Y + 6\eta * \sum Z_2 LY - 4\eta * (3+k) \sum Z_1 Y + \sum [(4/3)k(\eta_1 U_r) + 4r(\eta_1 e_{rr})] Y_{1m} - 2r\eta_1 (e_{\theta\theta} + e_{\phi\phi}) - (4/3)k\eta_1 U_r - r^2 g_0 \sum \delta\rho Y + r^2 \rho_0 \sum \partial\Phi / \partial r Y = 0.$$

Expression for divergence (U3):

$$(e_{rr} + e_{\theta\theta} + e_{\phi\phi}) = -(1/r)kU_r,$$

$$(e_{\theta\theta} + e_{\phi\phi}) = -e_{rr} - (1/r)kU_r,$$

$$-2r\eta_1 (e_{\theta\theta} + e_{\phi\phi}) = 2\eta_1 (re_{rr} + kU_r) = 2r\eta_1 e_{rr} + 2k\eta_1 U_r,$$

Taking into account that functions  $\eta_1 \mathbf{e}_r$  and  $\eta_1 \mathbf{U}_r$  are expanded into spherical harmonics (U11):

$$\mathbf{r}^2 \sum \mathbf{y}'_3 \mathbf{Y} - L \mathbf{r} \sum \mathbf{y}_4 \mathbf{Y} + 6\eta^* \sum \mathbf{z}_2 L \mathbf{Y} - 4\eta^* (3+k) \sum \mathbf{z}_1 \mathbf{Y} + \sum [ (4/3) \mathbf{k} (\eta_1 \mathbf{U}_r) + 4\mathbf{r} (\eta_1 \mathbf{e}_{rr}) ] \mathbf{Y}_{1m} + \sum [ 2\mathbf{r} (\eta_1 \mathbf{e}_{rr}) - (2/3) \mathbf{k} (\eta_1 \mathbf{U}_r) ] \mathbf{Y}_{1m} - r^2 g_0 \sum \delta \rho \mathbf{Y} + r^2 \rho_0 \sum \partial \Phi / \partial r \mathbf{Y} = 0.$$

Switching to the notations of Zhang and Christensen (1993):

$$\mathbf{r} \mathbf{z}'_3 - \mathbf{z}_3 - r^2 \rho'_0 \Phi - r^2 \rho_0 \Phi' = 4\eta^* (3+k) \mathbf{z}_1 \mathbf{Y} - 6\eta^* \mathbf{z}_2 L \mathbf{Y} + L \mathbf{z}_4 - \sum [ (4/3) \mathbf{k} (\eta_1 \mathbf{U}_r) + 4\mathbf{r} (\eta_1 \mathbf{e}_{rr}) ] \mathbf{Y} + r^2 \delta \rho g_0 - r^2 \rho_0 \partial \Phi / \partial r - \sum [ 2\mathbf{r} (\eta_1 \mathbf{e}_{rr}) + (2/3) \mathbf{k} (\eta_1 \mathbf{U}_r) ] \mathbf{Y}_{1m}$$

$$\sum \{ \mathbf{r} \mathbf{z}'_3 - \mathbf{z}_3 - r^2 \rho'_0 \Phi_{1m} \} \mathbf{Y} = \{ 4\eta^* (3+k) \mathbf{z}_1 \mathbf{Y} - 6\eta^* \mathbf{z}_2 L \mathbf{Y} + L \mathbf{z}_4 + r^2 g_0 \delta \rho_{1m} \} \mathbf{Y} - \sum [ 6\mathbf{r} (\eta_1 \mathbf{e}_{rr}) - 2\mathbf{k} (\eta_1 \mathbf{U}_r) ] \mathbf{Y}_{1m}$$

$$\mathbf{r} \sum \mathbf{z}'_3 = 4\eta^* (3+k) \sum \mathbf{z}_1 \mathbf{Y} - 6\eta^* \sum \mathbf{z}_2 L \mathbf{Y} + \sum \mathbf{z}_3 + L \sum \mathbf{z}_4 + r \rho'_0 \sum \Phi + r^2 \sum \delta \rho g_0 - \sum [ 6\mathbf{r} (\eta_1 \mathbf{e}_{rr}) - 2\mathbf{k} (\eta_1 \mathbf{U}_r) ] \mathbf{Y}_{1m}$$

$$\mathbf{r} \mathbf{z}'_{31m} = \eta^* (12+4k) \mathbf{z}_{11m} - 6\eta^* L \mathbf{z}_{21m} + \mathbf{z}_{31m} + L \mathbf{z}_{41m} + r k \rho_0 \Phi_{1m} + r^2 \delta \rho_{1m} g_0 + \mathbf{C}_{1m}$$

$$\mathbf{C}_{1m} = -6\mathbf{r} (\eta_1 \mathbf{e}_{rr})_{1m} - 2\mathbf{k} (\eta_1 \mathbf{U}_r)_{1m}$$

$$r \frac{dZ_3^{lm}}{dr} = (12+4k) \eta^* Z_1^{lm} - 6L \eta^* Z_2^{lm} + Z_3^{lm} + L Z_4^{lm} - k \rho^* Z_5^{lm} + \frac{\delta \rho g r^2}{\eta_0} - \frac{6r}{s_{m0}} \int_0^{2\pi} d\varphi \int_0^\pi \tilde{\eta} \left( e_{rr} + \frac{k(r)}{3} u_r \right) Y_{lm} \sin \theta d\theta \quad (\text{U17})$$

Viscous term appearing in the equation E5.4c (radial stress) again differs from the term stated by Zhang and Christensen (1993). The nature of the distinction is the same as in (U16). The additional member  $-2\mathbf{k} (\eta_1 \mathbf{U}_r)_{1m}$  in the viscous term appears due to the effect of mantle compressibility.

7) Stokes equation along the axis  $\mathbf{e}_\theta$ :

$$0 = \mathbf{r}^2 \partial \tau_{r\theta} / \partial r + r \partial \sigma_{\theta\theta} / \partial \theta + (\mathbf{r} / \sin \theta) \partial \tau_{\theta\varphi} / \partial \varphi + r (c \sigma_{\theta\theta} - c \sigma_{\varphi\varphi} + 3 \tau_{r\theta}) + r \rho_0 \partial \Phi / \partial \theta$$

$$\tau_{r\theta} = \sum Y_4^\theta Y^\varphi + Y_6^\theta Y^\varphi.$$

$$\mathbf{r} \mathbf{y}_4 = \mathbf{z}_4,$$

$$\mathbf{r}^2 \mathbf{y}'_4 = \mathbf{r} \mathbf{z}'_4 - \mathbf{z}_4,$$

$$r^2 \partial \tau_{r\varphi} / \partial r = \sum [ \mathbf{r} \mathbf{z}'_4(\mathbf{r})_{1m} Y_{1m}^\theta + \mathbf{r} \mathbf{z}'_6(\mathbf{r})_{1m} Y_{1m}^\varphi ] - \sum [ \mathbf{z}_4(\mathbf{r})_{1m} Y_{1m}^\theta + \mathbf{z}_6(\mathbf{r})_{1m} Y_{1m}^\varphi ]$$

$$\mathbf{r} \sigma_{\theta\theta} = -\mathbf{r} p + 2\eta^* [ \partial U_\theta / \partial \theta + U_r ] + (2/3) \eta^* k U_r + 2\mathbf{r} \eta_1 \mathbf{e}_{\theta\theta} + (2/3) \mathbf{k} \eta_1 \mathbf{U}_r$$

$$\mathbf{r} \sigma_{\varphi\varphi} = -\mathbf{r} p + 2\eta^* [ (1/\sin \theta) \partial U_\varphi / \partial \varphi + U_r + c U_\theta ] + (2/3) \eta^* k U_r + 2\mathbf{r} \eta_1 \mathbf{e}_{\varphi\varphi} + (2/3) \mathbf{k} \eta_1 \mathbf{U}_r$$

$$\mathbf{r} \tau_{\theta\varphi} = \eta^* [ (1/\sin \theta) \partial U_\theta / \partial \varphi + \partial U_\varphi / \partial \theta - c U_\varphi ] + 2\mathbf{r} \eta_1 \mathbf{e}_{\theta\varphi},$$

$$\begin{aligned}
r\sigma_{\theta\theta} &= -r\sum p(r)_{1m}Y_{1m} + 2\eta^* \sum [Z_2 Y^{\theta\theta} + Z_5 Y^{\varphi\theta} + Z_1 Y] + (2/3)\eta^* k \sum Z_1 Y + 2r\eta_1 e_{\theta\theta} + (2/3)k\eta_1 U_r \\
r\sigma_{\varphi\varphi} &= -r\sum pY + 2\eta^* \sum [Z_1 Y + Z_2 (Y^{\varphi\varphi} + cY^\theta) + Z_5 (-Y^{\theta\varphi} + cY^\varphi)] + (2/3)\eta^* k \sum Z_1 Y + 2r\eta_1 e_{\varphi\varphi} + \\
&+ (2/3)k\eta_1 U_r \\
r\tau_{\theta\varphi} &= \eta^* \sum [(Z_2 Y^{\theta\varphi} + Z_5 Y^{\varphi\varphi}) + (Z_2 Y^{\varphi\theta} - Z_5 Y^{\theta\theta}) - c(Z_2 Y^\varphi - Z_5 Y^\theta)] + 2r\eta_1 e_{\theta\varphi}, \\
rp(r, \theta, \varphi) &= \sum \{-2\eta^* (2+k)Z_{11m}(r) + 2\eta^* LZ_2(r) - Z_3(r) + (2/3)\eta^* kZ_1(r) + r\rho_0 \Phi\}_{1m} Y_{1m} + \\
&+ \sum [(2/3)k(\eta_1 U_r) + 2r(\eta_1 e_{rr})] Y_{1m} \\
r\sigma_{\theta\theta} - r\sigma_{\varphi\varphi} &= -r\sum p(r)_{1m}Y_{1m} + 2\eta^* \sum [Z_2 Y^{\theta\theta} + Z_5 Y^{\varphi\theta} + Z_1 Y] + (2/3)\eta^* k \sum Z_1 Y + 2r\eta_1 e_{\theta\theta} + \\
&+ (2/3)k\eta_1 U_r + r\sum pY - 2\eta^* \sum [Z_1 Y + Z_2 (Y^{\varphi\varphi} + cY^\theta) + Z_5 (-Y^{\theta\varphi} + cY^\varphi)] - (2/3)\eta^* k \sum Z_1 Y - \\
&- 2r\eta_1 e_{\varphi\varphi} - (2/3)k\eta_1 U_r \\
r\sigma_{\theta\theta} - r\sigma_{\varphi\varphi} &= 2\eta^* \sum [Z_2 Y^{\theta\theta} + Z_5 Y^{\varphi\theta} + Z_1 Y] - 2\eta^* \sum [Z_1 Y + Z_2 (Y^{\varphi\varphi} + cY^\theta) + Z_5 (-Y^{\theta\varphi} + cY^\varphi)] + \\
&+ 2r(\eta_1 e_{\theta\theta} - \eta_1 e_{\varphi\varphi}) \\
0 &= r^2 \partial \tau_{r\theta} / \partial r + r \partial \sigma_{\theta\theta} / \partial \theta + (r / \sin \theta) \partial \tau_{\theta\varphi} / \partial \varphi + r(c\sigma_{\theta\theta} - c\sigma_{\varphi\varphi} + 3\tau_{r\theta}) + r\rho_0 \partial \Phi / \partial \theta \\
0 &= r \sum Z'_4 Y^0 + r \sum Z'_6 Y^\varphi - \sum Z_4 Y^\theta - \sum Z_6 Y^\varphi - r \sum p(r)_{1m} Y_{1m}^0 + 2\eta^* \sum [Z_2 Y^{\theta\theta} + Z_5 Y^{\varphi\theta} + Z_1 Y^0] + \\
&+ (2/3)\eta^* k \sum Z_1 Y^0 + [2r\eta_1 e_{\theta\theta} + (2/3)k\eta_1 U_r]_\theta + \eta^* \sum [2Z_2 (Y^{\theta\varphi\varphi} - cY^{\varphi\varphi}) - Z_5 [LY^\varphi + Y^{\theta\theta\varphi}]] + \\
&+ (1/\sin \theta) 2[\eta_1 e_{\theta\varphi}]_\varphi + c2\eta^* \sum [Z_2 Y^{\theta\theta} + Z_5 Y^{\varphi\theta} + Z_1 Y] - c2\eta^* \sum [Z_1 Y + Z_2 (Y^{\varphi\varphi} + cY^\theta) + \\
&+ Z_5 (-Y^{\theta\varphi} + cY^\varphi)] + 2cr(\eta_1 e_{\theta\theta} - \eta_1 e_{\varphi\varphi}) + 3\sum Z_4 Y^0 + 3Z_6 Y^\varphi + r\rho_0 \sum \Phi Y^0 \\
0 &= r \sum Z'_4 Y^0 + r \sum Z'_6 Y^\varphi - \sum Z_4 Y^\theta - \sum Z_6 Y^\varphi + \sum \{2\eta^* (2+k)Z_{11m}(r) - 2\eta^* LZ_2(r) + Z_3(r) - \\
&- (2/3)\eta^* kZ_1(r) - r\rho_0 \Phi\}_{1m} Y_{1m}^0 - \sum \{[(2/3)k(\eta_1 U_r) + 2r(\eta_1 e_{rr})] Y_{1m}^0 + \\
&+ 2\eta^* \sum [Z_2 Y^{\theta\theta} + Z_5 Y^{\varphi\theta} + Z_1 Y^0] + (2/3)\eta^* k \sum Z_1 Y^0 + [2r\eta_1 e_{\theta\theta} + (2/3)k\eta_1 U_r]_\theta + \\
&+ \eta^* \sum [2Z_2 (Y^{\theta\varphi\varphi} - cY^{\varphi\varphi}) - Z_5 [LY^\varphi + Y^{\theta\theta\varphi}]] + (1/\sin \theta) 2[\eta_1 e_{\theta\varphi}]_\varphi + c2\eta^* \sum [Z_2 Y^{\theta\theta} + Z_5 Y^{\varphi\theta} + \\
&+ Z_1 Y] - c2\eta^* \sum [Z_1 Y + Z_2 (Y^{\varphi\varphi} + cY^\theta) + Z_5 (-Y^{\theta\varphi} + cY^\varphi)] + 2cr(\eta_1 e_{\theta\theta} - \eta_1 e_{\varphi\varphi}) + 3\sum Z_4 Y^0 + 3Z_6 Y^\varphi + \\
&+ r\rho_0 \sum \Phi Y^0 \\
0 &= r \sum Z'_4 Y^0 + r \sum Z'_6 Y^\varphi + \dots - \sum [(2/3)k(\eta_1 U_r) + 2r(\eta_1 e_{rr})] Y_{1m}^0 + \\
&+ [2r\eta_1 e_{\theta\theta} + (2/3)k\eta_1 U_r]_\theta + (1/\sin \theta) 2[\eta_1 e_{\theta\varphi}]_\varphi + 2cr(\eta_1 e_{\theta\theta} - \eta_1 e_{\varphi\varphi}) \\
0 &= r \sum Z'_4 Y^0 + r \sum Z'_6 Y^\varphi + \dots - \sum [(2/3)k(\eta_1 U_r) + 2r(\eta_1 e_{rr})] Y_{1m}^0 + 2r^2 \underline{c} \quad (U18)
\end{aligned}$$

where  $\underline{c} = \{[r\eta_1 e_{\theta\theta} + (1/3)k\eta_1 U_r]_\theta + (r/\sin \theta) [\eta_1 e_{\theta\varphi}]_\varphi + cr(\eta_1 e_{\theta\theta} - \eta_1 e_{\varphi\varphi})\} / r^2$

8) Stokes equation along the axis  $\underline{e}_\varphi$ :

$$0 = r^2 \partial \tau_{r\varphi} / \partial r + r \partial \tau_{\theta\varphi} / \partial \theta + (r / \sin \theta) \partial \sigma_{\varphi\varphi} / \partial \varphi + (3r\tau_{r\varphi} + 2cr\tau_{\theta\varphi}) + [(r\rho_0) / (\sin \theta)] \partial \Phi / \partial \varphi,$$

$$r\tau_{r\varphi} = \sum [Z_4(r)_{1m} Y_{1m}^\varphi - Z_6(r)_{1m} Y_{1m}^\theta],$$

$$r\mathbf{y}_4 = Z_4,$$

$$r^2 \mathbf{y}'_4 = rZ'_4 - Z_4$$

$$\begin{aligned}
\tau_{r\varphi} &= (1/r) \sum [Z_4(r)_{1m} Y_{1m}^\varphi - Z_6(r)_{1m} Y_{1m}^\theta], \\
\partial \tau_{r\varphi} / \partial r &= (1/r) \sum [Z'_4(r)_{1m} Y_{1m}^\varphi - Z'_6(r)_{1m} Y_{1m}^\theta] - (1/r^2) \sum [Z_4(r)_{1m} Y_{1m}^\varphi - Z_6(r)_{1m} Y_{1m}^\theta] \\
r^2 \partial \tau_{r\varphi} / \partial r &= \sum [r Z'_4(r)_{1m} Y_{1m}^\varphi - r Z'_6(r)_{1m} Y_{1m}^\theta] - \sum [Z_4(r)_{1m} Y_{1m}^\varphi - Z_6(r)_{1m} Y_{1m}^\theta] \\
\tau_{r\theta} &= \sum Y_4 Y^\theta + Y_6 Y^\varphi. \\
r \sigma_{\varphi\varphi} &= -r \sum p Y + 2\eta^* \sum [Z_1 Y + Z_2 (Y^{\varphi\varphi} + c Y^\theta) + Z_5 (-Y^{\theta\theta} + c Y^\varphi)] + (2/3) \eta^* k \sum Z_1 Y + 2r \eta_1 e_{\varphi\varphi} + \\
&+ (2/3) k \eta_1 U_r \\
r \tau_{\theta\varphi} &= \eta^* \sum [2Z_2 Y^{\varphi\theta}] - Z_5 [LY + Y^{\theta\theta}] + (2/3) \eta^* k \sum V_r Y + 2r \eta_1 e_{\theta\varphi} \\
r p(r, \theta, \varphi) &= \sum \{-2\eta^* (2+k) Z_{11m}(r) + 2\eta^* LZ_2(r) - Z_3(r) + (2/3) \eta^* k Z_1(r) + r \rho_0 \Phi\}_{1m} Y_{1m} + \\
&+ \sum [(2/3) k (\eta_1 U_r) + 2r (\eta_1 e_{rr})] Y_{1m} \\
0 &= r^2 \partial \tau_{r\varphi} / \partial r + r \partial \tau_{\theta\varphi} / \partial \theta + (r / \sin \theta) \partial \sigma_{\varphi\varphi} / \partial \varphi + (3r \tau_{r\varphi} + 2cr \tau_{\theta\varphi}) + [(r \rho_0) / (\sin \theta)] \partial \Phi / \partial \varphi, \\
0 &= \sum r Z'_4(r)_{1m} Y_{1m}^\varphi - r Z'_6(r)_{1m} Y_{1m}^\theta - \sum [Z_4(r)_{1m} Y_{1m}^\varphi - Z_6(r)_{1m} Y_{1m}^\theta] + \eta^* \sum [2Z_2 Y^{\varphi\theta\theta}] - \\
&- Z_5 [LY^\theta + Y^{\theta\theta\theta}] + (2/3) \eta^* k \sum V_r Y^\theta + 2r [\eta_1 e_{\theta\varphi}]_\theta - r \sum p Y^\varphi + 2\eta^* \sum [Z_1 Y^\varphi + Z_2 (Y^{\varphi\varphi\varphi} + c Y^{\theta\varphi}) + \\
&+ Z_5 (-Y^{\theta\varphi\varphi} + c Y^{\varphi\varphi})] + (2/3) \eta^* k \sum Z_1 Y^\varphi + (1/\sin \theta) [2r \eta_1 e_{\varphi\varphi} + (2/3) k \eta_1 U_r]_\varphi + \\
&+ 3 \sum [Z_4(r)_{1m} Y_{1m}^\varphi - Z_6(r)_{1m} Y_{1m}^\theta] + 2c \eta^* \sum [2Z_2 Y^{\varphi\theta}] - Z_5 [LY + Y^{\theta\theta}] + (4c/3) \eta^* k \sum V_r Y + \\
&+ 4cr \eta_1 e_{\theta\varphi} + [(r \rho_0) / (\sin \theta)] \partial \Phi / \partial \varphi, \\
0 &= \sum r Z'_4(r)_{1m} Y_{1m}^\varphi - r Z'_6(r)_{1m} Y_{1m}^\theta - \sum [Z_4(r)_{1m} Y_{1m}^\varphi - Z_6(r)_{1m} Y_{1m}^\theta] + \eta^* \sum [2Z_2 Y^{\varphi\theta\theta}] - \\
&- Z_5 [LY^\theta + Y^{\theta\theta\theta}] + (2/3) \eta^* k \sum V_r Y^\theta + 2r [\eta_1 e_{\theta\varphi}]_\theta + \sum \{2\eta^* (2+k) Z_{11m}(r) - 2\eta^* LZ_2(r) + \\
&+ Z_3(r) - (2/3) \eta^* k Z_1(r) - r \rho_0 \Phi\}_{1m} Y_{1m}^\varphi - \sum \{[(2/3) k (\eta_1 U_r) + 2r (\eta_1 e_{rr})] Y_{1m}^\varphi + \\
&+ 2\eta^* \sum [Z_1 Y^\varphi + Z_2 (Y^{\varphi\varphi\varphi} + c Y^{\theta\varphi}) + Z_5 (-Y^{\theta\varphi\varphi} + c Y^{\varphi\varphi})] + (2/3) \eta^* k \sum Z_1 Y^\varphi + (1/\sin \theta) [2r \eta_1 e_{\varphi\varphi} + \\
&+ (2/3) k \eta_1 U_r]_\varphi + 3 \sum [Z_4(r)_{1m} Y_{1m}^\varphi - Z_6(r)_{1m} Y_{1m}^\theta] + 2c \eta^* \sum [2Z_2 Y^{\varphi\theta}] - Z_5 [LY + Y^{\theta\theta}] + \\
&+ (4c/3) \eta^* k \sum V_r Y + 4cr \eta_1 e_{\theta\varphi} + [(r \rho_0) / (\sin \theta)] \partial \Phi / \partial \varphi, \\
0 &= \sum r Z'_4(r)_{1m} Y_{1m}^\varphi - r Z'_6(r)_{1m} Y_{1m}^\theta + \dots - \sum \{[(2/3) k (\eta_1 U_r) + 2r (\eta_1 e_{rr})] Y_{1m}^\varphi + \\
&+ 2r [\eta_1 e_{\theta\varphi}]_\theta + (1/\sin \theta) [2r \eta_1 e_{\varphi\varphi} + (2/3) k \eta_1 U_r]_\varphi + 4cr \eta_1 e_{\theta\varphi} \\
0 &= \sum r Z'_4(r)_{1m} Y_{1m}^\varphi - r Z'_6(r)_{1m} Y_{1m}^\theta + \dots - \sum \{[(2/3) k (\eta_1 U_r) + 2r (\eta_1 e_{rr})] Y_{1m}^\varphi + \\
&+ 2r^2 \underline{D} \tag{U19}
\end{aligned}$$

where  $\underline{D} = \{r [\eta_1 e_{\theta\varphi}]_\theta + (1/\sin \theta) [r \eta_1 e_{\varphi\varphi} + (1/3) k \eta_1 U_r]_\varphi + 2cr \eta_1 e_{\theta\varphi}\} / r^2$

Hence, we have arrived at the following equation system:

$$\begin{aligned}
0 &= r \sum Z'_4 Y^\theta + r \sum Z'_6 Y^\varphi + \dots - \sum [(2/3) k (\eta_1 U_r) + 2r (\eta_1 e_{rr})] Y_{1m}^\theta + 2r^2 \underline{C} \\
\underline{C} &= \{[r \eta_1 e_{\theta\theta} + (1/3) k \eta_1 U_r]_\theta + (r / \sin \theta) [\eta_1 e_{\theta\varphi}]_\varphi + cr (\eta_1 e_{\theta\theta} - \eta_1 e_{\varphi\varphi})\} / r^2 \\
0 &= \sum r Z'_4(r)_{1m} Y_{1m}^\varphi - r Z'_6(r)_{1m} Y_{1m}^\theta + \dots - \sum \{[(2/3) k (\eta_1 U_r) + 2r (\eta_1 e_{rr})] Y_{1m}^\varphi + 2r^2 \underline{D} \\
\underline{D} &= \{r [\eta_1 e_{\theta\varphi}]_\theta + (1/\sin \theta) [r \eta_1 e_{\varphi\varphi} + (1/3) k \eta_1 U_r]_\varphi + 2cr \eta_1 e_{\theta\varphi}\} / r^2
\end{aligned}$$

$$\begin{aligned}
\underline{\mathbf{C}} &= \sum g_a(r) {}_{1m}Y_{1m}^\theta + g_b(r) {}_{1m}Y_{1m}^\varphi \\
\underline{\mathbf{D}} &= \sum g_a(r) {}_{1m}Y_{1m}^\varphi - g_b(r) {}_{1m}Y_{1m}^\theta \\
g_a &= \mathbf{D} = (\mathbf{r}^2 / \mathbf{s}_{m1}) \int_0^{2\pi} d\varphi \int_0^\pi [\underline{\mathbf{C}}\mathbf{Y}_{1m}^\theta + \underline{\mathbf{D}}\mathbf{Y}_{1m}^\varphi] \sin\theta d\theta \\
g_b &= \mathbf{F} = (\mathbf{r}^2 / \mathbf{s}_{m1}) \int_0^{2\pi} d\varphi \int_0^\pi [\underline{\mathbf{C}}\mathbf{Y}_{1m}^\varphi - \underline{\mathbf{D}}\mathbf{Y}_{1m}^\theta] \sin\theta d\theta \\
\mathbf{0} &= r \sum Z'_{4} Y^\theta + r \sum Z'_{6} Y^\varphi + \dots - \sum [ (2/3)k(\eta_1 \mathbf{U}_r) + 2r(\eta_1 \mathbf{e}_{rr}) ] Y_{1m}^\theta + 2 \sum g_a(r) {}_{1m}Y_{1m}^\theta + \\
&+ 2 \sum g_b(r) {}_{1m}Y_{1m}^\varphi \\
\underline{\mathbf{C}} &= \{ [r\eta_1 \mathbf{e}_{\theta\theta} + (1/3)k\eta_1 \mathbf{U}_r]_{\theta} + (r/\sin\theta) [\eta_1 \mathbf{e}_{\theta\varphi}]_{\varphi} + cr(\eta_1 \mathbf{e}_{\theta\theta} - \eta_1 \mathbf{e}_{\varphi\varphi}) \} / r^2 \\
\mathbf{0} &= \sum r Z'_{4}(r) {}_{1m}Y_{1m}^\varphi - r Z'_{6}(r) {}_{1m}Y_{1m}^\theta + \dots - \sum [ (2/3)k(\eta_1 \mathbf{U}_r) + 2r(\eta_1 \mathbf{e}_{rr}) ] Y_{1m}^\varphi + \\
&+ 2 \sum g_a(r) {}_{1m}Y_{1m}^\varphi - 2 \sum g_b(r) {}_{1m}Y_{1m}^\theta \\
\underline{\mathbf{D}} &= \{ r[\eta_1 \mathbf{e}_{\theta\varphi}]_{\theta} + (1/\sin\theta) [r\eta_1 \mathbf{e}_{\varphi\varphi} + (1/3)k\eta_1 \mathbf{U}_r]_{\varphi} + 2cr\eta_1 \mathbf{e}_{\theta\varphi} \} / r^2 \\
\mathbf{0} &= r \sum Z'_{4} Y^\theta + r \sum Z'_{6} Y^\varphi + \dots + 2 \sum g_a^*(r) {}_{1m}Y_{1m}^\theta + 2 \sum g_b(r) {}_{1m}Y_{1m}^\varphi \\
\underline{\mathbf{C}} &= \{ [r\eta_1 \mathbf{e}_{\theta\theta} + (1/3)k\eta_1 \mathbf{U}_r]_{\theta} + (r/\sin\theta) [\eta_1 \mathbf{e}_{\theta\varphi}]_{\varphi} + cr(\eta_1 \mathbf{e}_{\theta\theta} - \eta_1 \mathbf{e}_{\varphi\varphi}) \} / r^2 \\
\mathbf{0} &= \sum r Z'_{4}(r) {}_{1m}Y_{1m}^\varphi - r Z'_{6}(r) {}_{1m}Y_{1m}^\theta + \dots + 2 \sum g_a^*(r) {}_{1m}Y_{1m}^\varphi - 2 \sum g_b(r) {}_{1m}Y_{1m}^\theta \\
\underline{\mathbf{D}} &= \{ r[\eta_1 \mathbf{e}_{\theta\varphi}]_{\theta} + (1/\sin\theta) [r\eta_1 \mathbf{e}_{\varphi\varphi} + (1/3)k\eta_1 \mathbf{U}_r]_{\varphi} + 2cr\eta_1 \mathbf{e}_{\theta\varphi} \} / r^2 \\
g_a^*(r) &= g_a(r) - [ (1/3)k(\eta_1 \mathbf{U}_r) + r(\eta_1 \mathbf{e}_{rr}) ] \\
r Z'_{4} &= \dots - 2g_{a1m} + [ (2/3)k(\eta_1 \mathbf{U}_r) + 2r(\eta_1 \mathbf{e}_{rr}) ]_{1m} = -2g^* \\
r Z'_{6} &= \dots - 2g_{b1m} \\
g_a &= (\mathbf{r}^2 / \mathbf{s}_{m1}) \int_0^{2\pi} d\varphi \int_0^\pi [\underline{\mathbf{C}}\mathbf{Y}_{1m}^\theta + \underline{\mathbf{D}}\mathbf{Y}_{1m}^\varphi] \sin\theta d\theta \tag{U20} \\
g_b &= (\mathbf{r}^2 / \mathbf{s}_{m1}) \int_0^{2\pi} d\varphi \int_0^\pi [\underline{\mathbf{C}}\mathbf{Y}_{1m}^\varphi - \underline{\mathbf{D}}\mathbf{Y}_{1m}^\theta] \sin\theta d\theta \\
\eta_1 \mathbf{U}_r &= (1/\mathbf{s}_{m0}) \iint \eta_1 \mathbf{U}_r Y_{1m} d\varphi \sin\theta d\theta, \\
\eta_1 \mathbf{e}_{rr} &= (1/\mathbf{s}_{m0}) \iint \eta_1 \mathbf{e}_{rr} Y_{1m} d\varphi \sin\theta d\theta \\
g_a^* &= g_a(r) - [ (1/3)k(\eta_1 \mathbf{U}_r) + r(\eta_1 \mathbf{e}_{rr}) ] = (\mathbf{r}^2 / \mathbf{s}_{m1}) \int_0^{2\pi} d\varphi \int_0^\pi [\underline{\mathbf{C}}\mathbf{Y}_{1m}^\theta + \underline{\mathbf{D}}\mathbf{Y}_{1m}^\varphi] \sin\theta d\theta - \\
&- (1/\mathbf{s}_{m0}) \int_0^{2\pi} d\varphi \int_0^\pi [ (1/3)k(\eta_1 \mathbf{U}_r) + r(\eta_1 \mathbf{e}_{rr}) ] Y_{1m} \sin\theta d\theta \\
\mathbf{D}_{1m} &= -2g_{a1m}^* = -2(\mathbf{r}^2 / \mathbf{s}_{m1}) \int_0^{2\pi} d\varphi \int_0^\pi [\underline{\mathbf{C}}\mathbf{Y}_{1m}^\theta + \underline{\mathbf{D}}\mathbf{Y}_{1m}^\varphi] \sin\theta d\theta + \\
&+ 2(1/\mathbf{s}_{m0}) \int_0^{2\pi} d\varphi \int_0^\pi [ (1/3)k(\eta_1 \mathbf{U}_r) + r(\eta_1 \mathbf{e}_{rr}) ] Y_{1m} \sin\theta d\theta \\
r \frac{dZ_4^{lm}}{dr} &= -(6 + 2k)\eta^* Z_1^{lm} - 2(2L - 1)\eta^* Z_2^{lm} - Z_3^{lm} - 2Z_4^{lm} - \\
&- \frac{2r^2}{s_{lm}} \int_0^{2\pi} d\varphi \int_0^\pi (\underline{\mathbf{C}}Y_{lm}^\theta + \underline{\mathbf{D}}Y_{lm}^\varphi) \sin\theta d\theta + \frac{2r}{s_{m0}} \int_0^{2\pi} d\varphi \int_0^\pi \tilde{\eta} \left( e_{rr} + \frac{k(r)}{3} u_r \right) Y_{lm} \sin\theta d\theta \tag{U21} \\
\mathbf{F}_{1m} &= -2g_{b1m} = -2(\mathbf{r}^2 / \mathbf{s}_{m1}) \int_0^{2\pi} d\varphi \int_0^\pi [\underline{\mathbf{C}}\mathbf{Y}_{1m}^\varphi - \underline{\mathbf{D}}\mathbf{Y}_{1m}^\theta] \sin\theta d\theta
\end{aligned}$$

$$r \frac{dZ_6^{lm}}{dr} = (L-2)\eta^* Z_5^{lm} - 2Z_6^{lm} - \frac{2r^2}{s_{lm}} \int_0^{2\pi} d\varphi \int_0^\pi [CY_{lm}^\varphi - DY_{lm}^\theta] \sin\theta d\theta \quad (\text{U22})$$

$$\underline{C} = \frac{1}{r^2} \left[ \frac{\partial \left( r\tilde{\eta}e_{\theta\theta} + \frac{k(r)}{3}\tilde{\eta}u_r \right)}{\partial\theta} + \frac{r}{\sin\theta} \frac{\partial(\tilde{\eta}e_{\theta\varphi})}{\partial\varphi} + r \text{ctg}\theta \tilde{\eta}(e_{\theta\theta} - e_{\varphi\varphi}) \right] \quad (\text{U23})$$

$$\underline{D} = \frac{1}{r^2} \left[ r \frac{\partial(\tilde{\eta}e_{\theta\varphi})}{\partial\theta} + \frac{1}{\sin\theta} \frac{\partial \left( r\tilde{\eta}e_{\varphi\varphi} + \frac{k(r)}{3}\tilde{\eta}u_r \right)}{\partial\varphi} + 2r \text{ctg}\theta \tilde{\eta}e_{\theta\varphi} \right]$$

$$\underline{C} = \{ [r\eta_1 e_{\theta\theta} + (1/3)k\eta_1 U_r]_\theta + (r/\sin\theta) [\eta_1 e_{\theta\varphi}]_\varphi + cr(\eta_1 e_{\theta\theta} - \eta_1 e_{\varphi\varphi}) \} / r^2$$

$$\underline{D} = \{ r[\eta_1 e_{\theta\varphi}]_\theta + (1/\sin\theta) [r\eta_1 e_{\varphi\varphi} + (1/3)k\eta_1 U_r]_\varphi + 2cr\eta_1 e_{\theta\varphi} \} / r^2$$

Again the same distinction in sign and coefficient... The additional members due to the effect of mantle compressibility appeared once more in both viscous terms. Expressions for the viscous terms themselves are obviously different from those derived by Zhang and Christensen (1993), they differ at least in the member  $2(1/s_{m0}) \int_0^{2\pi} d\varphi \int_0^\pi [(1/3)k(\eta_1 U_r) + r(\eta_1 e_{rr})] Y_{1m} \sin\theta d\theta$ , which is absent in Zhang and Christensen (1993). It is clearly seen that the former viscous terms are comprised by only coefficients for spherical functions' derivatives  $Y_{lm}^\theta(\theta, \varphi)$  and  $Y_{lm}^\varphi(\theta, \varphi)$ , while the new formulae for  $\underline{D}_{1m}$  and  $\underline{F}_{1m}$  include the coefficients for spherical functions  $Y_{lm}(\theta, \varphi)$  as well.

### Part W.

The process of derivation of the viscous terms for the W-transform method is rather similar to the calculations done for the U-transform method in the previous part.

Relation between viscous stress tensor and mantle velocities:

$$\tau_{rr} = 2\eta [\partial U_r / \partial r - (1/3)\nabla \cdot \underline{U}_i] ,$$

$$\begin{aligned}
\tau_{r\theta} &= \eta [r \partial(U_\theta/r) / \partial r + (1/r) \partial U_r / \partial \theta], \\
\tau_{r\varphi} &= \eta [r \partial(U_\varphi/r) / \partial r + (1/(r \sin \theta)) \partial U_r / \partial \varphi], \quad (W1) \\
\tau_{\theta\theta} &= 2\eta [(1/r) \partial U_\theta / \partial \theta + U_r/r - (1/3) \nabla \cdot \underline{U}], \\
\tau_{\varphi\varphi} &= 2\eta [(1/(r \sin \theta)) \partial U_\varphi / \partial \varphi + U_r/r + U_\theta (\text{ctg} \theta) / r - (1/3) \nabla \cdot \underline{U}], \\
\tau_{\theta\varphi} &= \eta [(\sin \theta / r) \partial(U_\varphi / \sin \theta) / \partial \theta + 1 / r \sin \theta \partial U_\theta / \partial \varphi],
\end{aligned}$$

As it is seen from above an application of total stress instead of viscous shear stress to the Stokes equations simplifies the deductions:

$$\begin{aligned}
\sigma_{rr} &= -p + \tau_{rr}, \\
\sigma_{\theta\theta} &= -p + \tau_{\theta\theta}, \\
\sigma_{\varphi\varphi} &= -p + \tau_{\varphi\varphi},
\end{aligned}$$

Mass conservation:

$$\begin{aligned}
\nabla \cdot (\rho_0 \underline{U}) &= (1/r^2) \partial / \partial r (r^2 \rho_0 U_r) + (1/(r \sin \theta)) \partial / \partial \theta (\sin \theta \rho_0 U_\theta) + \\
&+ (1/(r \sin \theta)) \partial \rho_0 U_\varphi / \partial \varphi = 0 \\
\nabla \cdot \underline{U} &= 2U_r/r + \partial U_r / \partial r + (1/r) [\partial U_\theta / \partial \theta + c U_\theta + (1/\sin \theta) \partial U_\varphi / \partial \varphi] = -(1/r) k(r) U_r \quad (W2)
\end{aligned}$$

Stokes equation along the axis  $\mathbf{e}_r$ :

$$\begin{aligned}
0 &= \partial \sigma_{rr} / \partial r + (1/r) \partial \tau_{r\theta} / \partial \theta + (1/(r \sin \theta)) \partial \tau_{r\varphi} / \partial \varphi + (1/r) (2\tau_{rr} - \tau_{\theta\theta} - \tau_{\varphi\varphi} + \tau_{r\theta} \text{ctg} \theta) - \\
&- \delta \rho g_0 + \rho_0 \partial \Phi / \partial r \\
0 &= r^2 \partial \sigma_{rr} / \partial r + r \partial \tau_{r\theta} / \partial \theta + (r/\sin \theta) \partial \tau_{r\varphi} / \partial \varphi + r (2\tau_{rr} - \tau_{\theta\theta} - \tau_{\varphi\varphi} + \tau_{r\theta} \text{ctg} \theta) - r^2 \delta \rho g_0 + \\
&+ r^2 \rho_0 \partial \Phi / \partial r \quad (W3)
\end{aligned}$$

Stokes equation along the axis  $\mathbf{e}_\theta$ :

$$\begin{aligned}
0 &= \partial \tau_{r\theta} / \partial r + (1/r) \partial \sigma_{\theta\theta} / \partial \theta + (1/(r \sin \theta)) \partial \tau_{\theta\varphi} / \partial \varphi + (1/r) (c \sigma_{\theta\theta} - c \sigma_{\varphi\varphi} + 3\tau_{r\theta}) + \\
&+ (\rho_0 / r) \partial \Phi / \partial \theta, \\
0 &= r^2 \partial \tau_{r\theta} / \partial r + r \partial \sigma_{\theta\theta} / \partial \theta + (r/\sin \theta) \partial \tau_{\theta\varphi} / \partial \varphi + r (c \sigma_{\theta\theta} - c \sigma_{\varphi\varphi} + 3\tau_{r\theta}) + r \rho_0 \partial \Phi / \partial \theta, \quad (W4)
\end{aligned}$$

Stokes equation along the axis  $\mathbf{e}_\varphi$ :

$$\begin{aligned}
0 &= \partial \tau_{r\varphi} / \partial r + (1/r) \partial \tau_{\theta\varphi} / \partial \theta + (1/r \sin \theta) \partial \sigma_{\varphi\varphi} / \partial \varphi + (1/r) (3\tau_{r\varphi} + \\
&+ 2c \tau_{\theta\varphi}) + [\rho_0 / (r \sin \theta)] \partial \Phi / \partial \varphi, \\
0 &= r^2 \partial \tau_{r\varphi} / \partial r + r \partial \tau_{\theta\varphi} / \partial \theta + (r/\sin \theta) \partial \sigma_{\varphi\varphi} / \partial \varphi + r (3\tau_{r\varphi} + 2c \tau_{\theta\varphi}) + [r \rho_0 / (\sin \theta)] \partial \Phi / \partial \varphi, \quad (W5)
\end{aligned}$$

Relation between total stress and mantle velocities:

$$\begin{aligned}
\sigma_{rr} &= -p + 2\eta \partial U_r / \partial r - (2/3) \eta \nabla \cdot \underline{U} \\
r \tau_{r\theta} &= \eta [\partial U_r / \partial \theta + r \partial U_\theta / \partial r - U_\theta],
\end{aligned}$$

$$\begin{aligned}
\mathbf{r}\tau_{r\varphi} &= \eta [r\partial U_\varphi / \partial r + (1/\sin\theta)\partial U_r / \partial \varphi - U_\varphi], \\
\mathbf{r}\sigma_{\theta\theta} &= -rp + 2\eta [\partial U_\theta / \partial \theta + U_r] - (2/3)r\eta \nabla \cdot \mathbf{U}_\perp \\
\mathbf{r}\sigma_{\varphi\varphi} &= -rp + 2\eta [(1/\sin\theta)\partial U_\varphi / \partial \varphi + U_r + cU_\theta] - (2/3)r\eta \nabla \cdot \mathbf{U}_\perp
\end{aligned} \tag{W6}$$

$$\mathbf{r}\tau_{\theta\varphi} = \eta [(1/\sin\theta)\partial U_\theta / \partial \varphi + \partial U_\varphi / \partial \theta - cU_\varphi],$$

Change of variables applied to mantle velocities:

$$\eta(r, \theta, \varphi) = \eta^*(r) \cdot T(r, \theta, \varphi)$$

$$V_r(r, \theta, \varphi) = T(r, \theta, \varphi) U_r,$$

$$U_i = V_i / T, \tag{W7}$$

$$V_\theta(r, \theta, \varphi) = T(r, \theta, \varphi) U_\theta,$$

$$V_\varphi(r, \theta, \varphi) = T(r, \theta, \varphi) U_\varphi.$$

In the general form:

$$U_i = V_i / T,$$

$$\partial U_i / \partial \xi_k = (1/T) [\partial V_i / \partial \xi_k - V_i \partial \ln T / \partial \xi_k] = (1/T) [\partial V_i / \partial \xi_k - V_i T^\xi] \tag{W8}$$

$$\text{where } T^\xi \equiv \partial \ln T / \partial \xi_k = (1/T) \partial T / \partial \xi_k$$

In spherical coordinates:

$$\mathbf{rV}\nabla \ln T = V_r T^r + V_\theta T^\theta + (1/\sin\theta) V_\varphi T^\varphi$$

$$\mathbf{r}\partial \ln T / \partial r = T^r,$$

$$\partial \ln T / \partial \theta = T^\theta, \tag{W9}$$

$$(1/\sin\theta) \partial \ln T / \partial \varphi = T^\varphi$$

$$\mathbf{rV}\nabla \ln T = V_r T^r + V_\theta T^\theta + V_\varphi T^\varphi$$

Applying this change of variables to the continuity equation:

$$\nabla \cdot \mathbf{U}_\perp = 2U_r / r + \partial U_r / \partial r + (1/r) [\partial U_\theta / \partial \theta + cU_\theta + (1/\sin\theta) \partial U_\varphi / \partial \varphi] = -(1/r) k(r) U_r,$$

$$(1/T) [2V_r / r + \partial V_r / \partial r + (1/r) [\partial V_\theta / \partial \theta + cV_\theta + (1/\sin\theta) \partial V_\varphi / \partial \varphi] - (1/T) [V_r T^r +$$

$$+ (1/r) V_\theta T^\theta + (1/r \sin\theta) V_\varphi T^\varphi] = -(1/r) k(r) (1/T) V_r,$$

$$2V_r / r + \partial V_r / \partial r + (1/r) [\partial V_\theta / \partial \theta + cV_\theta + (1/\sin\theta) \partial V_\varphi / \partial \varphi] = -(1/r) k(r) V_r + \mathbf{rV}\nabla \ln T$$

$$\text{where } \mathbf{rV}\nabla \ln T = V_r T^r + (1/r) V_\theta T^\theta + (1/r \sin\theta) V_\varphi T^\varphi$$

$$2V_r + \mathbf{r}\partial V_r / \partial r + [\partial V_\theta / \partial \theta + cV_\theta + (1/\sin\theta) \partial V_\varphi / \partial \varphi] = -k(r) V_r + \mathbf{rV}\nabla \ln T$$

$$\text{where } \mathbf{rV}\nabla \ln T = V_r T^r + V_\theta T^\theta + V_\varphi T^\varphi \quad (\nabla \cdot \mathbf{v}_\perp = -k(r) V_r + \mathbf{rV}\nabla \ln T)$$

Applying change of variable to the expressions for the relation between non-hydrstatic normal stress and mantle velocities:

$$\sigma_{rr} = -p + 2\eta \partial U_r / \partial r - (2/3)\eta \nabla \cdot \underline{U} = -p + 2\eta * T [ (1/T) \partial V_r / \partial r - (1/T^2) V_r \partial T / \partial r ] + (2/3)\eta * (1/r) k(r) V_r$$

$$\sigma_{rr} = -p + 2\eta * T [ (1/T) \partial V_r / \partial r - (1/T^2) V_r \partial T / \partial r ] + (2/3)\eta * (1/r) k(r) V_r$$

$$\sigma_{rr} = -p + 2\eta * \partial V_r / \partial r - 2\eta * V_r \partial \ln T / \partial r + (2/3)\eta * (1/r) k(r) V_r$$

$$\mathbf{r} \sigma_{rr} = -r p + 2r \eta * \partial V_r / \partial r - 2\eta * T^r V_r + (2/3)\eta * k(r) V_r \quad (W10a)$$

$$\tau_{r\theta} = \eta [ (1/r) \partial U_r / \partial \theta + \partial U_\theta / \partial r - U_\theta / r ]$$

$$\tau_{r\theta} = \eta * [ (1/r) \partial V_r / \partial \theta + \partial V_\theta / \partial r - V_\theta / r ] - \eta * [ (1/r) V_r T^\theta + V_\theta T^r ]$$

$$\mathbf{r} \tau_{r\theta} = \eta * [ \partial V_r / \partial \theta + r \partial V_\theta / \partial r - V_\theta ] - \eta * [ V_r T^\theta + V_\theta T^r ] \quad (W10b)$$

$$\tau_{r\phi} = \eta [ \partial U_\phi / \partial r + (1/r \sin \theta) \partial U_r / \partial \phi - U_\phi / r ]$$

$$\tau_{r\phi} = \eta * [ \partial V_\phi / \partial r + (1/r \sin \theta) \partial V_r / \partial \phi - V_\phi / r ] - \eta * [ V_\phi T^r + (1/r \sin \theta) V_r T^\phi ]$$

$$\mathbf{r} \tau_{r\phi} = \eta * [ r \partial V_\phi / \partial r + (1/\sin \theta) \partial V_r / \partial \phi - V_\phi ] - \eta * [ V_\phi T^r + V_r T^\phi ] \quad (W10c)$$

$$\sigma_{\theta\theta} = -p + 2\eta [ (1/r) \partial U_\theta / \partial \theta + U_r / r ] - (2/3)\eta \nabla \cdot \underline{U}$$

$$\sigma_{\theta\theta} = -p + 2\eta * [ (1/r) \partial V_\theta / \partial \theta + V_r / r ] - 2\eta * [ (1/r) V_\theta T^\theta ] + (2/3)\eta * (1/r) k(r) V_r,$$

$$\mathbf{r} \sigma_{\theta\theta} = -r p + 2\eta * [ \partial V_\theta / \partial \theta + V_r ] - 2\eta * [ V_\theta T^\theta ] + (2/3)\eta * k V_r \quad (W10d)$$

$$\tau_{\theta\phi} = \eta [ (1/r \sin \theta) \partial U_\theta / \partial \phi + (1/r) \partial U_\phi / \partial \theta - U_\phi / r ]$$

$$\tau_{\theta\phi} = \eta * [ (1/r \sin \theta) \partial V_\theta / \partial \phi + (1/r) \partial V_\phi / \partial \theta - V_\phi / r ] - \eta * [ (1/r \sin \theta) V_\theta T^\phi + (1/r) V_\phi T^\theta ],$$

$$\mathbf{r} \tau_{\theta\phi} = \eta * [ (1/\sin \theta) \partial V_\theta / \partial \phi + \partial V_\phi / \partial \theta - V_\phi ] - \eta * [ V_\theta T^\phi + V_\phi T^\theta ], \quad (W10e)$$

Spherical functions for mantle velocities, stresses, dynamic pressure, density and geopotential are represented in spherical harmonics:

$$V_r(r, \theta, \phi) = T(r, \theta, \phi) U_r = \sum Z_1(r) {}_{1m} Y_{1m}(\theta, \phi)$$

$$V_\theta(r, \theta, \phi) = T(r, \theta, \phi) U_\theta = \sum [ Z_2(r) {}_{1m} Y_{1m}^\theta + Z_5(r) {}_{1m} Y_{1m}^\phi ]$$

$$V_\phi(r, \theta, \phi) = T(r, \theta, \phi) U_\phi = \sum [ Z_2(r) {}_{1m} Y_{1m}^\phi - Z_5(r) {}_{1m} Y_{1m}^\theta ]$$

$$\sigma_{rr} = \sum Y_3 Y,$$

$$\tau_{r\theta} = \sum (y_4 Y^\theta + y_6 Y^\phi),$$

(W11)

$$\tau_{r\phi} = \sum (y_4 Y^\phi - y_6 Y^\theta),$$

$$\delta \rho(r, \theta, \phi) = \sum \rho Y,$$

$$\phi(r, \theta, \phi) = \sum \phi Y,$$

$$p(r, \theta, \phi) = \sum p(r) {}_{1m} Y_{1m}$$

$$r \sigma_{\theta\theta} = -r p + 2\eta * [ \partial V_\theta / \partial \theta + V_r ] - 2\eta * [ (V_\theta T^\theta) ] + (2/3)\eta * k V_r,$$

$$\mathbf{r} \sigma_{\theta\theta} = -r \sum p(r) {}_{1m} Y_{1m} + 2\eta * \sum [ Z_{21m} Y_{1m}^{\theta\theta} + Z_{51m} Y_{1m}^{\phi\theta} + Z_{11m} Y_{1m} ] + (2/3)\eta * k \sum Z_{11m} Y_{1m} -$$

$$-2\eta^*[(V_\theta T^\theta)], \quad (W12a)$$

$$r\sigma_{\phi\phi} = -r\rho + 2\eta^*[(1/\sin\theta)\partial V_\phi/\partial\phi + V_r + cV_\theta] - 2\eta^*[(1/\sin\theta)V_\phi T^\phi] + (2/3)\eta^*kV_r -$$

$$-2\eta^*[V_\phi T^\phi]$$

$$r\sigma_{\phi\phi} = -r\rho + 2\eta^*[(1/\sin\theta)\partial V_\phi/\partial\phi + V_r + cV_\theta] = -r\rho + 2\eta^*\sum[(Z_2 Y^{\phi\phi} - Z_5 Y^{\theta\phi}) + Z_1 Y +$$

$$+ (Z_2 Y^\theta + Z_5 Y^\phi)c] + (2/3)\eta^*k\sum Z_1 Y - 2\eta^*[V_\phi T^\phi]$$

$$r\sigma_{\phi\phi} = -r\rho + 2\eta^*\sum[(Z_2 Y^{\phi\phi} - Z_5 Y^{\theta\phi}) + Z_1 Y + c(Z_2 Y^\theta + Z_5 Y^\phi)] + (2/3)\eta^*k\sum Z_1 Y -$$

$$-2\eta^*[(1/\sin\theta)V_\phi T^\phi]$$

$$r\sigma_{\phi\phi} = -r\rho + 2\eta^*\sum[Z_1 Y + Z_2(Y^{\phi\phi} + cY^\theta) + Z_5(-Y^{\theta\phi} + cY^\phi)] + (2/3)\eta^*k\sum Z_1 Y -$$

$$-2\eta^*[V_\phi T^\phi] \quad (W12b)$$

$$r\tau_{\theta\phi} = \eta^*[(1/\sin\theta)\partial V_\theta/\partial\phi + \partial V_\phi/\partial\theta - cV_\phi] - \eta^*[(1/\sin\theta)V_\theta T^\theta + V_\phi T^\phi],$$

$$r\tau_{\theta\phi} = \eta^*\sum[(Z_2 Y^{\theta\phi} + Z_5 Y^{\phi\phi}) + (Z_2 Y^{\theta\theta} - Z_5 Y^{\phi\phi}) - c(Z_2 Y^\phi - Z_5 Y^\theta)] - \eta^*[V_\theta T^\theta + V_\phi T^\phi]$$

$$r\tau_{\theta\phi} = \eta^*\sum[Z_2(Y^{\theta\phi} + Y^{\phi\phi} - cY^\phi) + Z_5(Y^{\phi\phi} - Y^{\theta\theta} + cY^\theta)] - \eta^*[V_\theta T^\theta + V_\phi T^\phi]$$

$$r\tau_{\theta\phi} = \eta^*\sum[2Z_2(Y^{\theta\phi} - cY^\phi) - Z_5(LY + Y^{\theta\theta})] - \eta^*[V_\theta T^\theta + V_\phi T^\phi] \quad (W12c)$$

Relation between notations used in this study and original notations of Zhang and Christensen (1993):

$$\sigma_{rr} = \sigma_{rr} + \rho_0(r)\phi(r, \theta, \phi) = -p + \tau_{rr} + \rho_0(r)\phi(r, \theta, \phi) = (1/r)\sum Z_3(r)_{1m} Y_{1m}(\theta, \phi)$$

$$\sigma_{rr} = (1/r)\sum Z_3 Y - \rho_0\phi$$

$$\tau_{r\theta} = (1/r)\sum[Z_4(r)_{1m} Y_{1m}^\theta + Z_6(r)_{1m} Y_{1m}^\phi]$$

$$\tau_{r\phi} = (1/r)\sum[Z_4(r)_{1m} Y_{1m}^\phi - Z_6(r)_{1m} Y_{1m}^\theta] \quad (W13)$$

$$y_3 = (1/r)Z_3 - \rho_0\phi$$

$$y_4 = (1/r)Z_4$$

$$y_6 = (1/r)Z_6$$

$$\phi = Z_7/r$$

### Derivation of the ODE system for the spherical harmonic coefficients

$Z_{11m}(r), Z_{21m}(r), Z_{51m}(r), Y_{31m}(r), Y_{41m}(r), Y_{61m}(r)$  and  $p_{1m}(r)$ :

1) Mass conservation:

$$2V_r/r + \partial V_r/\partial r + (1/r)[\partial V_\theta/\partial\theta + cV_\theta + (1/\sin\theta)\partial V_\phi/\partial\phi] = -(1/r)k(r)V_r + v\nabla \ln T$$

$$2\sum(Z_1/r)Y + \sum Y Z_1' + \sum(Z_2/r)[Y^{\theta\theta} + cY^\theta + Y^{\phi\phi}] + \sum(Z_5/r)[Y^{\phi\phi} + cY^\phi - Y^{\theta\phi}] =$$

$$= -(1/r)k\sum Z_1 Y + v\nabla \ln T$$

$$2\sum(Z_1/r)Y + \sum Z_1' Y - \sum(Z_2/r)LY = -(1/r)k\sum Z_1 Y + v\nabla \ln T$$

$$2\sum Z_1 Y + r\sum Z_1' Y - \sum Z_2 LY = -k\sum Z_1 Y + r v\nabla \ln T$$

$$r\mathbf{V}\nabla\ln\mathbf{T}=\sum A(r)_{1m}Y_{1m}(\theta,\varphi)$$

$$rZ_1' = -(2+k)Z_1 + LZ_2 + A_{1m}$$

$$\text{where } A_{1m} = (1/s_{m0}) \iint (r\mathbf{V}\nabla\ln\mathbf{T})Y_{1m}d\varphi\sin\theta d\theta$$

$$r \frac{dZ_1^{lm}}{dr} = -(2+k)Z_1^{lm} + LZ_2^{lm} + \frac{r}{s_{m0}} \int_0^{2\pi} d\varphi \int_0^\pi \mathbf{V}\nabla\ln\mathbf{T}Y_{lm}(\theta,\varphi)\sin\theta d\theta \quad (\text{W14})$$

2) Relation between stress  $\sigma_{rr}$  and mantle velocities:

$$\sigma_{rr} = -p + 2\eta^* \partial V_r / \partial r - 2\eta^* V_r \partial \ln T / \partial r + (2/3r)\eta^* k V_r,$$

$$\mathbf{T}^r = \partial \ln T / \partial r$$

$$\mathbf{T}^r \mathbf{V}_r = \sum (\mathbf{T}^r \mathbf{V}_r)_{1m} Y_{1m}(\theta, \varphi) = (1/r) \sum R_{1m} Y_{1m}(\theta, \varphi)$$

$$R_{1m} = (r \mathbf{T}^r \mathbf{V}_r)_{1m} = (1/s_{m0}) \iint (r \mathbf{T}^r \mathbf{V}_r) Y_{1m} d\varphi \sin\theta d\theta, \quad (\text{W15})$$

$$\sum Y_3 Y = -\sum p + 2\eta^* \sum Z_1' Y - 2\eta^* (1/r) \sum R Y + (2/3r)\eta^* k \sum Z_1 Y,$$

$$p_{1m} = 2\eta^* Z_1' - y_3 - 2\eta^* (1/r) R_{1m} + (2/3r)\eta^* k Z_1$$

$$r p_{1m} = 2\eta^* r Z_1' - r y_3 - 2\eta^* R_{1m} + (2/3)\eta^* k Z_1$$

Using (5.1) we arrive at the expression for dynamic pressure:

$$r Z_1' = -(2+k)Z_1 + LZ_2 + A_{1m}$$

$$r p = -2\eta^* (2+k)Z_1 + 2\eta^* LZ_2 + 2\eta^* A_{1m} - r y_3 - 2\eta^* R + (2/3)\eta^* k Z_1$$

$$r p_{1m} = -2\eta^* (2+k)Z_{11m} + 2\eta^* LZ_{21m} - r y_{31m} + (2/3)\eta^* k Z_{11m} + 2\eta^* (A_{1m} - R_{1m}) \quad (\text{W16})$$

$$\text{where } A_{1m}(r) = (1/s_{m0}) \iint (r\mathbf{V}\nabla\ln\mathbf{T})Y_{1m}d\varphi\sin\theta d\theta$$

$$R_{1m}(r) = (1/s_{m0}) \iint (\mathbf{T}^r \mathbf{V}_r) Y_{1m} d\varphi \sin\theta d\theta \quad (\text{W17})$$

Spherical function for dynamic pressure can be found from:

$$r p(r, \theta, \varphi) = \sum \{ -2\eta^* (2+k)Z_{11m}(r) + 2\eta^* LZ_2(r) - r y_3(r) + (2/3)\eta^* k Z_1(r) \}_{1m} Y_{1m} + 2\eta^* \sum \{ A_{1m}(r) - R_{1m}(r) \} Y_{1m}$$

Reverting to the notations of Zhang and Christensen (1993):

$$r y_3 = Z_3 - r \rho_0 \Phi,$$

$$r p(r, \theta, \varphi) = \sum \{ -2\eta^* (2+k)Z_{11m}(r) + 2\eta^* LZ_2(r) - Z_3(r) + (2/3)\eta^* k Z_1(r) + r \rho_0 \Phi \}_{1m} Y_{1m} + 2\eta^* \sum \{ A_{1m}(r) - R_{1m}(r) \} Y_{1m} \quad (\text{W18})$$

3) Relation between stress  $\tau_{r\theta}$  and mantle velocities:

$$r \tau_{r\theta} = \eta^* [ \partial V_r / \partial \theta + \partial V_\theta / \partial r - V_\theta / r ] - \eta^* [ V_r T^\theta + r V_\theta T^r ]$$

$$\begin{aligned}
& \Sigma r_Y Y^\theta + \Sigma r_Y Y^\phi = \eta^* \Sigma Z_1 Y^\theta + \eta^* r \Sigma [Z'_2 Y^\theta + Z'_5 Y^\phi] - \eta^* \Sigma [Z_2 Y^\theta + Z_5 Y^\phi] - \eta^* \Sigma [V_r T^\theta + r V_\theta T^r] \\
& Z_4 Y^\theta + Z_6 Y^\phi = \eta^* Z_1 Y^\theta + \eta^* r [Z'_2 Y^\theta + Z'_5 Y^\phi] - \eta^* [Z_2 Y^\theta + Z_5 Y^\phi] - \eta^* [V_r T^\theta + r V_\theta T^r] \\
& [Z_4 - \eta^* Z_1 - \eta^* r Z'_2 + \eta^* Z_2] Y^\theta + [Z_6 - \eta^* r Z'_5 + \eta^* Z_5] Y^\phi + \eta^* [V_r T^\theta + r V_\theta T^r] = 0 \\
& [Z_4 \eta^* - Z_1 - r Z'_2 + Z_2] Y^\theta + [Z_6 / \eta^* - r Z'_5 + Z_5] Y^\phi + [V_r T^\theta + r V_\theta T^r] = 0 \\
& \Sigma [r Z'_2 - Z_4 \eta^* + Z_1 - Z_2] Y^\theta + \Sigma [r Z'_5 - Z_6 / \eta^* - Z_5] Y^\phi - [V_r T^\theta + r V_\theta T^r] = 0 \\
& [V_r T^\theta + r V_\theta T^r] = F_1(r, \theta, \varphi) = \Sigma f_a(r)_{1m} Y_{1m}^\theta + f_b(r)_{1m} Y_{1m}^\phi \\
& \Sigma [r Z'_2 - Z_4 \eta^* + Z_1 - Z_2 - f_a(r)] Y^\theta + \Sigma [r Z'_5 - Z_6 / \eta^* - Z_5 - f_b(r)] Y^\phi = 0 \tag{W19}
\end{aligned}$$

4) Relation between stress  $\tau_{r\varphi}$  and mantle velocities:

$$\begin{aligned}
& r \tau_{r\varphi} = \eta^* [r \partial V_\varphi / \partial r + (1/\sin\theta) \partial V_r / \partial \varphi - V_\varphi] - \eta^* [r V_\varphi T^r + (1/\sin\theta) V_r T^\theta] \\
& r Y_4 Y^\theta - r Y_6 Y^\phi = \eta^* [r Z'_2 Y^\theta - r Z'_5 Y^\phi + Z_1 (1/\sin\theta) \partial Y / \partial \varphi - Z_2 Y^\theta + Z_5 Y^\phi] - \eta^* [r V_\varphi T^r + \\
& + (1/\sin\theta) V_r T^\theta]. \\
& Z_4 Y^\theta - Z_6 Y^\phi = \eta^* [r Z'_2 Y^\theta - r Z'_5 Y^\phi + Z_1 \partial Y^\theta / \partial \varphi - Z_2 Y^\theta + Z_5 Y^\phi] - \eta^* [r V_\varphi T^r + (1/\sin\theta) V_r T^\theta]. \\
& [Z_4 - \eta^* r Z'_2 - \eta^* Z_1 + \eta^* Z_2] Y^\theta + [-Z_6 + \eta^* r Z'_5 - \eta^* Z_5] Y^\phi + \eta^* [r V_\varphi T^r + (1/\sin\theta) V_r T^\theta] = 0 \\
& [Z_4 / \eta^* - r Z'_2 - Z_1 + Z_2] Y^\theta - [Z_6 / \eta^* - r Z'_5 + Z_5] Y^\phi + [r V_\varphi T^r + (1/\sin\theta) V_r T^\theta] = 0 \\
& \Sigma [r Z'_2 - Z_4 \eta^* + Z_1 - Z_2] Y^\theta - \Sigma [r Z'_5 - Z_6 / \eta^* - Z_5] Y^\phi - [V_\varphi T^r + V_r T^\theta] = 0 \\
& [r V_\varphi T^r + (1/\sin\theta) V_r T^\theta] = F_2(r, \theta, \varphi) = \Sigma f_a(r)_{1m} Y_{1m}^\theta - f_b(r)_{1m} Y_{1m}^\phi \\
& \Sigma [r Z'_2 - Z_4 \eta^* + Z_1 - Z_2 - f_a] Y^\theta - \Sigma [r Z'_5 - Z_6 / \eta^* - Z_5 - f_b] Y^\phi = 0 \tag{W20}
\end{aligned}$$

Taking into account (W19) and (W20) we arrive at the equations for the spheroidal and toroidal components of the mantle velocity:

$$r Z'_2 = -Z_1 + Z_2 + Z_4 / \eta^* + f_{a1m}$$

$$r Z'_5 = Z_5 + Z_6 / \eta^* + f_{b1m}$$

$$f_a = (1/s_{m1}) \int_0^{2\pi} d\varphi \int_0^\pi \{F_1 Y_{1m}^\theta + F_2 Y_{1m}^\phi\} \sin\theta d\theta.$$

$$f_a = (1/s_{m1}) \int_0^{2\pi} d\varphi \int_0^\pi \eta^* [r V_r T^\theta + V_\theta T^r] Y_{1m}^\theta + [r V_\varphi T^r + (1/\sin\theta) V_r T^\theta] Y_{1m}^\phi \sin\theta d\theta,$$

$$f_b = (1/s_{m1}) \int_0^{2\pi} d\varphi \int_0^\pi \{F_1 Y_{1m}^\theta - F_2 Y_{1m}^\phi\} \sin\theta d\theta.$$

$$f_b = (1/s_{m1}) \int_0^{2\pi} d\varphi \int_0^\pi [\eta^* \{ [V_r T^\theta + r V_\theta T^r] Y_{1m}^\theta - [r V_\varphi T^r + (1/\sin\theta) V_r T^\theta] Y_{1m}^\phi \}] \sin\theta d\theta$$

The final formulae for the equations E5.4b and E5.4e:

$$r Z'_2 = -Z_1 + Z_2 + Z_4 / \eta^* + f_a$$

$$f_a = (1/s_{1m}) \iint \{ [V_\theta T^r + V_r T^\theta] Y^\theta + [V_\varphi T^r + V_r T^\theta] Y^\phi \} d\varphi \sin\theta d\theta = B^{1m}$$

$$r \frac{dZ_2^{lm}}{dr} = -Z_1^{lm} + Z_2^{lm} + \frac{1}{\eta^*} Z_4^{lm} + \frac{1}{s_{lm}} \int_0^{2\pi} d\varphi \int_0^\pi [(T_r V_\theta + T_\theta V_r) Y_{lm}^\theta + (T_r V_\varphi + T_\varphi V_r) Y_{lm}^\varphi] \sin \theta d\theta \quad (W21)$$

$$r Z'_5 = Z_5 + Z_6 / \eta^* + f_b,$$

$$f_b = (1/s_{1m}) \iint \{ [V_\theta T^r + V_r T^\theta] Y^\varphi - [V_\varphi T^r + V_r T^\varphi] Y^\theta \} d\varphi \sin \theta d\theta = E^{1m}$$

$$r \frac{dZ_5^{lm}}{dr} = Z_5^{lm} + \frac{1}{\eta^*} Z_6^{lm} + \frac{1}{s_{lm}} \int_0^{2\pi} d\varphi \int_0^\pi [(T_r V_\theta + T_\theta V_r) Y_{lm}^\varphi - (T_r V_\varphi + T_\varphi V_r) Y_{lm}^\theta] \sin \theta d\theta \quad (W22)$$

5) Stokes equation along the axis  $\underline{e}_r$ :

$$\partial \sigma_{rr} / \partial r + (1/r) \partial \tau_{r\theta} / \partial \theta + (1/r \sin \theta) \partial \tau_{r\varphi} / \partial \varphi + (1/r) [2\sigma_{rr} - \sigma_{\theta\theta} - \sigma_{\varphi\varphi} + c\tau_{r\theta}] - \delta \rho g_0 + \rho_0 \partial \Phi / \partial r = 0.$$

$$r^2 \partial \sigma_{rr} / \partial r + r \partial \tau_{r\theta} / \partial \theta + (r / \sin \theta) \partial \tau_{r\varphi} / \partial \varphi + r [2\sigma_{rr} - \sigma_{\theta\theta} - \sigma_{\varphi\varphi} + c\tau_{r\theta}] - r^2 \delta \rho g_0 + r^2 \rho_0 \partial \Phi / \partial r = 0.$$

Substituting the expansions for stress tensor components:

$$\sigma_{rr} = \sum Y_3 Y,$$

$$\tau_{r\theta} = \sum Y_4 Y^\theta + Y_6 Y^\varphi,$$

$$\tau_{r\varphi} = \sum Y_4 Y^\varphi - Y_6 Y^\theta,$$

$$r \sigma_{\theta\theta} = -r \sum p(r)_{1m} Y_{1m} + 2\eta^* \sum [z_2 Y^{\theta\theta} + z_5 Y^{\varphi\theta} + z_1 Y] + (2/3) \eta^* k \sum z_1 Y - 2\eta^* [V_\theta T^\theta]$$

$$r \sigma_{\varphi\varphi} = -r \sum p_{1m} Y_{1m} + 2\eta^* \sum [z_1 Y + z_2 (Y^{\varphi\varphi} + cY^\theta) + z_5 (-Y^{\theta\varphi} + cY^\varphi)] + (2/3) \eta^* k \sum z_1 Y - 2\eta^* [V_\varphi T^\varphi]$$

$$r^2 Y'_3 Y + r Y_4 Y^{\theta\theta} + r Y_6 Y^{\varphi\theta} + r Y_4 Y^{\varphi\varphi} - r Y_6 Y^{\theta\varphi} + [2r Y_3 Y + r p - 2\eta^* [z_2 Y^{\theta\theta} + z_5 Y^{\varphi\theta} + z_1 Y] -$$

$$- (2/3) \eta^* k z_1 Y + 2\eta^* [V_\theta T_\theta] + r p - 2\eta^* [z_1 Y + z_2 (Y^{\varphi\varphi} + cY^\theta) + z_5 (-Y^{\theta\varphi} + cY^\varphi)] -$$

$$- (2/3) \eta^* k z_1 Y + 2\eta^* [V_\varphi T^\varphi] + c(r Y_4 Y^\theta + r Y_6 Y^\varphi) - r^2 \delta \rho g_0 Y + r^2 \rho_0 \partial \Phi / \partial r Y = 0.$$

$$r^2 \sum Y'_3 Y + r \sum Y_4 [Y^{\theta\theta} + Y^{\varphi\varphi} + cY^\theta] + r \sum Y_6 [Y^{\varphi\theta} - Y^{\theta\varphi} + cY^\varphi] + 2r \sum Y_3 Y + 2r p + 2\eta^* \sum [-z_2 Y^{\theta\theta} -$$

$$-z_5 Y^{\varphi\theta} - z_1 Y] + 2\eta^* \sum [-z_2 (Y^{\varphi\varphi} + cY^\theta) + z_5 (Y^{\theta\varphi} - cY^\varphi) - z_1 Y] - (4/3) \eta^* k \sum z_1 Y +$$

$$+ 2\eta^* [V_\theta T_\theta] + 2\eta^* [V_\varphi T^\varphi] - r^2 \sum \delta \rho g_0 Y + r^2 \rho_0 \sum \partial \Phi / \partial r Y = 0.$$

Using properties of the spherical functions' derivatives E3.7a and

$$E3.7b \quad \underline{Y^{\theta\theta} + Y^{\varphi\varphi} + cY^\theta = -LY}, \quad \underline{Y^{\varphi\theta} + cY^\varphi - Y^{\theta\varphi} = 0}:$$

$$r^2 \sum Y'_{3Y} - Lr \sum Y_4 Y + 2r \sum Y_3 Y + 2rp + 2\eta * \sum [-Z_2 (Y^{\theta\theta} + Y^{\phi\phi} + cY^\theta) + Z_5 (-Y^{\theta\theta} + Y^{\phi\phi} - cY^\phi) - 2Z_1 Y] + 2\eta * [V_\theta T^\theta] + 2\eta * [V_\phi T^\phi] - (4/3) \eta * k \sum Z_1 Y - r^2 g_0 \sum \delta \rho Y + r^2 \rho_0 \sum \partial \Phi / \partial r Y = 0.$$

$$r^2 \sum Y'_{3Y} - Lr \sum Y_4 Y + 2r \sum Y_3 Y + 2rp + 2\eta * \sum [LZ_2 Y - 2Z_1 Y] + 2\eta * [V_\theta T^\theta] + 2\eta * [V_\phi T^\phi] - (4/3) \eta * k \sum Z_1 Y - r^2 g_0 \sum \delta \rho Y + r^2 \rho_0 \sum \partial \Phi / \partial r Y = 0.$$

Derived expression for dynamic pressure (W16) is substituted into equation:

$$rp(r, \theta, \phi) = \sum \{-2\eta * (2+k) Z_{11m}(r) + 2\eta * LZ_2(r) - Z_3(r) + (2/3) \eta * k Z_1(r) + r\rho_0 \phi\}_{1m} Y_{1m} + 2\eta * \sum \{A_{1m}(r) - R_{1m}(r)\} Y_{1m}$$

$$r^2 \sum Y'_{3Y} - Lr \sum Y_4 Y + 2r \sum Y_3 Y - 4\eta * \sum Z_1 Y + 2\eta * \sum Z_2 LY + \sum \{-4\eta * (2+k) Z_1 Y + 4\eta * LZ_2 Y - 2ry_3 Y + (4/3) \eta * k Z_1 Y + 4\eta * \sum [A_{1m}(r) - R_{1m}(r)]\} Y_{1m} + 2\eta * [V_\theta T^\theta] + 2\eta * [V_\phi T^\phi] - (4/3) \eta * k \sum Z_1 Y - r^2 g_0 \sum \delta \rho Y + r^2 \rho_0 \sum \partial \Phi / \partial r Y = 0.$$

$$r^2 \sum Y'_{3Y} - Lr \sum Y_4 Y + 6\eta * \sum Z_2 LY - 4\eta * (3+k) \sum Z_1 Y + 4\eta * \sum [A_{1m} - R_{1m}] Y_{1m} + 2\eta * [V_\theta T^\theta + V_\phi T^\phi] - r^2 g_0 \sum \delta \rho Y + r^2 \rho_0 \sum \partial \Phi / \partial r Y = 0.$$

$$r^2 \sum Y'_{3Y} Y_{1m} = 4\eta * (3+k) \sum Z_1 Y - 6\eta * \sum Z_2 LY + Lr \sum Y_4 - 4\eta * \sum [A_{1m} - R_{1m}] Y + r^2 g_0 \sum \delta \rho Y - r^2 \rho_0 \sum \partial \Phi / \partial r Y_{1m} - 2\eta * [V_\theta T^\theta + V_\phi T^\phi]$$

Reverting to the notations of Zhang and Christensen (1993):

$$rZ'_{3Y} - Z_3 - r^2 \rho'_{0\phi} - r^2 \rho_0 \phi' = 4\eta * (3+k) Z_1 Y - 6\eta * Z_2 LY + Lry_4 - 4\eta * \sum [A_{1m} - R_{1m}] Y + r^2 \delta \rho g_0 - r^2 \rho_0 \partial \Phi / \partial r - 2\eta * [V_\theta T^\theta + V_\phi T^\phi]$$

$$\sum \{rZ'_{3Y} - Z_3 - r^2 \rho'_{0\phi}\}_{1m} Y = \{4\eta * (3+k) Z_1 Y - 6\eta * Z_2 LY + Lry_4 - 4\eta * \sum [A_{1m} - R_{1m}] Y + r^2 g_0 \delta \rho_{1m}\} Y - 2\eta * [V_\theta T^\theta + V_\phi T^\phi]$$

$$r \sum Z'_{3Y} = 4\eta * (3+k) \sum Z_1 Y - 6\eta * \sum Z_2 LY + \sum Z_3 + Lr \sum Y_4 + r\rho_0 \sum \phi + r^2 \sum \delta \rho g_0 - 4\eta * \sum [A_{1m} - R_{1m}] Y - 2\eta * [V_\theta T^\theta + V_\phi T^\phi]$$

$$[V_\theta T^\theta + (1/\sin\theta) V_\phi T^\phi] = \sum s_{1m} Y_{1m},$$

where  $s_{1m} = (1/s_{m0}) \iint [V_\theta T^\theta + (1/\sin\theta) V_\phi T^\phi] Y_{1m} d\phi \sin\theta d\theta$

$$\sum rZ'_{3Y} Y_{1m} = \sum \{4\eta * (3+k) Z_1 - 6\eta * Z_2 L + Z_3 + Lry_4 + r\rho_0 \phi + r^2 \delta \rho g_0 - 4\eta * [A_{1m}(r) - R_{1m}(r)] - 2\eta * s_{1m}\} Y_{1m}$$

$$rZ'_{31m} = \eta * (12+4k) Z_{11m} - 6\eta * LZ_{21m} + Z_{31m} + LZ_{41m} + rk\rho_0 \phi_{1m} + r^2 \delta \rho_{1m} g_0 + C_{1m},$$

where  $C_{1m} = 6\eta * r [V_r T^r - V \nabla \ln T]_{1m} = 6\eta * (R_{1m} - A_{1m})$

$$R_{1m}(r) = (1/s_{m0}) \iint (T^r V_r) Y_{1m} d\phi \sin\theta d\theta$$

$$A_{1m} = (r/s_{m0}) \iint (V \nabla \ln T) Y_{1m} d\phi \sin\theta d\theta$$

$$A_{1m} - R_{1m} = -[1/(6\eta *)] C_{1m} = -(1/s_{m0}) \iint (T^r V_r - V \nabla \ln T) Y_{1m} d\phi \sin\theta d\theta$$

$$r \frac{dZ_3^{lm}}{dr} = (12 + 4k)\eta^* Z_1^{lm} - 6L\eta^* Z_2^{lm} + Z_3^{lm} + LZ_4^{lm} - k\rho^* Z_5^{lm} + \frac{\delta\rho g r^2}{\eta_0} -$$

$$- \frac{6\eta^* r}{S_{m0}} \int_0^{2\pi} d\varphi \int_0^\pi (T_\theta V_\theta + T_\varphi V_\varphi) Y_{lm} \sin\theta d\theta \quad (W23)$$

6) Stokes equation along the axis  $\underline{e}_\theta$

$$0 = \partial\tau_{r\theta}/\partial r + (1/r)\partial\sigma_{\theta\theta}/\partial\theta + (1/r\sin\theta)\partial\tau_{\theta\varphi}/\partial\varphi + (1/r)(c\sigma_{\theta\theta} - c\sigma_{\varphi\varphi} + 3\tau_{r\theta}) + (\rho_0/r)\partial\Phi/\partial\theta$$

$$0 = r^2\partial\tau_{r\theta}/\partial r + r\partial\sigma_{\theta\theta}/\partial\theta + (r/\sin\theta)\partial\tau_{\theta\varphi}/\partial\varphi + r(c\sigma_{\theta\theta} - c\sigma_{\varphi\varphi} + 3\tau_{r\theta}) + r\rho_0\partial\Phi/\partial\theta$$

$$\tau_{r\theta} = \sum Y_4 Y^\theta + Y_6 Y^\varphi.$$

$$r\mathbf{y}_4 = \mathbf{z}_4,$$

$$r^2\mathbf{y}'_4 = r\mathbf{z}'_4 - \mathbf{z}_4,$$

$$r^2\partial\tau_{r\theta}/\partial r = \sum [r\mathbf{z}'_4(r)_{1m} Y_{1m}^\theta + r\mathbf{z}'_6(r)_{1m} Y_{1m}^\varphi] - \sum [z_4(r)_{1m} Y_{1m}^\theta + z_6(r)_{1m} Y_{1m}^\varphi]$$

$$r\sigma_{\theta\theta} = -r\sum p(r)_{1m} Y_{1m} + 2\eta^* \sum [z_2 Y^{\theta\theta} + z_5 Y^{\varphi\varphi} + z_1 Y] + (2/3)\eta^* k \sum z_1 Y - 2\eta^* [V_\theta T^\theta],$$

$$r\sigma_{\varphi\varphi} = -r\sum p Y + 2\eta^* \sum [z_1 Y + z_2 (Y^{\varphi\varphi} + cY^\theta) + z_5 (-Y^{\theta\varphi} + cY^\varphi)] + (2/3)\eta^* k \sum z_1 Y - 2\eta^* [V_\varphi T^\varphi]$$

$$r\tau_{\theta\varphi} = \eta^* \sum [(z_2 Y^{\theta\varphi} + z_5 Y^{\varphi\theta}) + (z_2 Y^{\varphi\theta} - z_5 Y^{\theta\theta}) - c(z_2 Y^\varphi - z_5 Y^\theta)] - \eta^* [V_\theta T^\varphi + V_\varphi T^\theta]$$

$$r\tau_{\theta\varphi} = \eta^* \sum [2z_2 (Y^{\theta\varphi} - cY^\varphi) - z_5 (LY + Y^{\theta\theta})] - \eta^* [V_\theta T^\varphi + V_\varphi T^\theta]$$

$$rp(r, \theta, \varphi) = \sum \{-2\eta^* (2+k) Z_{11m}(r) + 2\eta^* LZ_2(r) - Z_3(r) + (2/3)\eta^* k Z_1(r) + r\rho_0\Phi_{1m} + 2\eta^* (A-R)\}_{1m} Y_{1m}$$

$$r\sigma_{\theta\theta} - r\sigma_{\varphi\varphi} = -r\sum p(r)_{1m} Y_{1m} + 2\eta^* \sum [z_2 Y^{\theta\theta} + z_5 Y^{\varphi\varphi} + z_1 Y] + (2/3)\eta^* k \sum z_1 Y - 2\eta^* [(V_\theta T^\theta) + r\sum p Y - 2\eta^* \sum [z_1 Y + z_2 (Y^{\varphi\varphi} + cY^\theta) + z_5 (-Y^{\theta\varphi} + cY^\varphi)] - (2/3)\eta^* k \sum z_1 Y + 2\eta^* [V_\varphi T^\varphi]$$

$$r\sigma_{\theta\theta} - r\sigma_{\varphi\varphi} = 2\eta^* \sum [z_2 Y^{\theta\theta} + z_5 Y^{\varphi\varphi} + z_1 Y] - 2\eta^* [(V_\theta T^\theta) - 2\eta^* \sum [z_1 Y + z_2 (Y^{\varphi\varphi} + cY^\theta) + z_5 (-Y^{\theta\varphi} + cY^\varphi)] + 2\eta^* [V_\varphi T^\varphi]$$

$$0 = r^2\partial\tau_{r\theta}/\partial r + r\partial\sigma_{\theta\theta}/\partial\theta + (r/\sin\theta)\partial\tau_{\theta\varphi}/\partial\varphi + r(c\sigma_{\theta\theta} - c\sigma_{\varphi\varphi} + 3\tau_{r\theta}) + r\rho_0\partial\Phi/\partial\theta$$

$$0 = r\sum z'_4 Y^\theta + r\sum z'_6 Y^\varphi - \sum z_4 Y^\theta - \sum z_6 Y^\varphi - r\sum p(r)_{1m} Y_{1m}^\theta + 2\eta^* \sum [z_2 Y^{\theta\theta} + z_5 Y^{\varphi\varphi} + z_1 Y^\theta] +$$

$$+ (2/3)\eta^* k \sum z_1 Y^\theta - 2\eta^* [(V_\theta T^\theta)_\theta + \eta^* \sum [2z_2 (Y^{\theta\varphi} - cY^{\varphi\varphi}) - z_5 (LY^\varphi + Y^{\theta\theta})] -$$

$$-\eta^* (1/\sin\theta) [V_\theta T^\varphi + V_\varphi T^\theta]_\varphi + c2\eta^* \sum [z_2 Y^{\theta\theta} + z_5 Y^{\varphi\varphi} + z_1 Y] - c2\eta^* [V_\theta T^\theta] - c2\eta^* \sum [z_1 Y +$$

$$+ z_2 (Y^{\varphi\varphi} + cY^\theta) + z_5 (-Y^{\theta\varphi} + cY^\varphi)] + c2\eta^* [V_\varphi T^\varphi] + 3\sum [z_4 Y^\theta + z_6 Y^\varphi] + r\rho_0\sum\Phi Y^\theta$$

$$0 = r\sum z'_4 Y^\theta + r\sum z'_6 Y^\varphi - \sum z_4 Y^\theta - \sum z_6 Y^\varphi + \sum \{2\eta^* (2+k) Z_{11m}(r) - 2\eta^* LZ_2(r) + Z_3(r) -$$

$$- (2/3)\eta^* k Z_1(r) - r\rho_0\Phi - 2\eta^* (A-R)\}_{1m} Y_{1m}^\theta + 2\eta^* \sum [z_2 Y^{\theta\theta} + z_5 Y^{\varphi\varphi} + z_1 Y^\theta] +$$

$$+ (2/3)\eta^* k \sum z_1 Y^\theta - 2\eta^* [(V_\theta T^\theta)_\theta + \eta^* \sum [2z_2 (Y^{\theta\varphi} - cY^{\varphi\varphi}) - z_5 (LY^\varphi + Y^{\theta\theta})] -$$

$$-\eta^* (1/\sin\theta) [V_\theta T^\varphi + V_\varphi T^\theta]_\varphi + c2\eta^* \sum [z_2 Y^{\theta\theta} + z_5 Y^{\varphi\varphi} + z_1 Y] - c2\eta^* [V_\theta T^\theta] -$$

$$- c2\eta^* \sum [z_1 Y + z_2 (Y^{\varphi\varphi} + cY^\theta) + z_5 (-Y^{\theta\varphi} + cY^\varphi)] + c2\eta^* [V_\varphi T^\varphi] + 3\sum z_4 Y^\theta + z_6 Y^\varphi + r\rho_0\sum\Phi_{1m} Y^\theta$$

This equation can be represented in common form as:

$$0 = \sum(rZ'_{41m} + \dots) Y^\theta + \sum(rZ'_{61m} + \dots) Y^\varphi - \sum 2\eta^* (A-R) Y^\theta_{1m} - \eta^* \underline{C}_2$$

$$0 = \sum(rZ'_{41m} + \dots) Y^\theta + \sum(rZ'_{61m} + \dots) Y^\varphi - \eta^* \underline{C}_1 - \eta^* \underline{C}_2$$

$$\underline{C}_1 = 2 \sum (A-R)_{1m} Y^\theta_{1m}$$

$$\begin{aligned} G = & rZ'_{4-} Z_4 + \{ 2\eta^* (2+k) Z_{11m}(r) - 2\eta^* LZ_2(r) + Z_3(r) - (2/3)\eta^* kZ_1(r) - r\rho_0 \Phi - \\ & - 2\eta^* (A-R) \} + (2/3)\eta^* kZ_1 + 3Z_4^\theta + Z_6^\varphi + r\rho_0 \Phi_{1m} + \eta^* \{ 2Z_2 Y^{\theta\theta\theta} + 2Z_5 Y^{\varphi\theta\theta} + Z_1 Y^\theta + 2Z_2 (Y^{\theta\varphi\varphi} - \\ & - cY^{\varphi\varphi}) - Z_5 [LY^\varphi + Y^{\theta\theta\varphi}] + c2 [Z_2 Y^{\theta\theta} + Z_5 Y^{\varphi\theta} + Z_1 Y] - 2cZ_1 Y - 2cZ_2 (Y^{\varphi\varphi} + cY^\theta) + \\ & + 2cZ_5 (Y^{\theta\varphi} - cY^\varphi) \} \end{aligned}$$

$$\begin{aligned} G = & rZ'_{4-} Z_4 + \{ 2\eta^* (2+k) Z_{11m}(r) - 2\eta^* LZ_2(r) + Z_3(r) - (2/3)\eta^* kZ_1(r) - r\rho_0 \Phi - \\ & - 2\eta^* (A-R) \} + (2/3)\eta^* kZ_1 + 3Z_4^\theta + Z_6^\varphi + r\rho_0 \Phi_{1m} + 2\eta^* \{ Z_2 Y^{\theta\theta\theta} + Z_5 Y^{\varphi\theta\theta} + Z_1 Y^\theta + Z_2 (Y^{\theta\varphi\varphi} - \\ & - cY^{\varphi\varphi}) - (1/2)Z_5 [LY^\varphi + Y^{\theta\theta\varphi}] + c [Z_2 Y^{\theta\theta} + Z_5 Y^{\varphi\theta} + Z_1 Y] - cZ_1 Y - cZ_2 (Y^{\varphi\varphi} + cY^\theta) + cZ_5 (Y^{\theta\varphi} - \\ & - cY^\varphi) \} \end{aligned}$$

$$\begin{aligned} G = & r \sum Z'_{4+} \{ 2\eta^* (2+k) Z_{11m}(r) - 2\eta^* LZ_2(r) + Z_3(r) - (2/3)\eta^* kZ_1(r) - r\rho_0 \Phi - \\ & - 2\eta^* (A-R) \} + (2/3)\eta^* kZ_1 + 3Z_4^\theta + Z_6^\varphi + r\rho_0 \Phi_{1m} + 2\eta^* \{ Z_2 Y^{\theta\theta\theta} + Z_5 Y^{\varphi\theta\theta} + Z_1 Y^\theta + Z_2 (Y^{\theta\varphi\varphi} - \\ & - cY^{\varphi\varphi}) - (1/2)Z_5 [LY^\varphi + Y^{\theta\theta\varphi}] + c [Z_2 Y^{\theta\theta} + Z_5 Y^{\varphi\theta}] - cZ_2 (Y^{\varphi\varphi} + cY^\theta) + cZ_5 (Y^{\theta\varphi} - cY^\varphi) \} \end{aligned}$$

$$\begin{aligned} G = & r \sum Z'_{4+} \{ 2\eta^* (2+k) Z_{11m}(r) - 2\eta^* LZ_2(r) + Z_3(r) - (2/3)\eta^* kZ_1(r) - r\rho_0 \Phi - \\ & - 2\eta^* (A-R) \} + (2/3)\eta^* kZ_1 + 3Z_4^\theta + Z_6^\varphi + r\rho_0 \Phi_{1m} + 2\eta^* Z_1 + 2\eta^* \{ Z_2 Y^{\theta\theta\theta} + Z_5 Y^{\varphi\theta\theta} + Z_2 (Y^{\theta\varphi\varphi} - \\ & - cY^{\varphi\varphi}) - (1/2)Z_5 [LY^\varphi + Y^{\theta\theta\varphi}] + c [Z_2 Y^{\theta\theta} + Z_5 Y^{\varphi\theta}] - cZ_2 (Y^{\varphi\varphi} + cY^\theta) + cZ_5 (Y^{\theta\varphi} - cY^\varphi) \} \end{aligned}$$

$$\begin{aligned} \underline{C}_2(v, T) = \underline{C}_2(r, \theta, \varphi) = & 2\eta^* [(v_\theta T^\theta]_\theta + \eta^* (1/\sin\theta) [(1/\sin\theta)v_\theta T^\varphi + v_\varphi T^\theta]_\varphi + \\ & + c2\eta^* [(v_\theta T^\theta] - 2c\eta^* [(1/\sin\theta)v_\varphi T^\varphi] \end{aligned}$$

$$\underline{C}_2 = 2[(v_\theta T^\theta]_\theta + 2c[(v_\theta T^\theta - v_\varphi T^\varphi] + (1/\sin\theta)[v_\theta T^\varphi + v_\varphi T^\theta]_\varphi \quad (W24)$$

$$\underline{C}_1 = 2 \sum (A-R)_{1m} Y^\theta_{1m}$$

7) Stokes equation along the axis  $\underline{e}_\varphi$ :

$$0 = r^2 \partial \tau_{r\varphi} / \partial r + r \partial \tau_{\theta\varphi} / \partial \theta + (r / \sin\theta) \partial \sigma_{\varphi\varphi} / \partial \varphi + (3r \tau_{r\varphi} + 2cr \tau_{\theta\varphi}) + [(r\rho_0) / \sin\theta] \partial \Phi / \partial \varphi,$$

$$r \tau_{r\varphi} = \sum [Z_4(r)_{1m} Y_{1m}^\varphi - Z_6(r)_{1m} Y_{1m}^\theta],$$

$$r y_4 = Z_4,$$

$$r^2 y'_{4-} = rZ'_{4-} Z_4$$

$$\tau_{r\varphi} = (1/r) \sum [Z_4(r)_{1m} Y_{1m}^\varphi - Z_6(r)_{1m} Y_{1m}^\theta],$$

$$\partial \tau_{r\varphi} / \partial r = (1/r) \sum [Z'_{4-}(r)_{1m} Y_{1m}^\varphi - Z'_{6-}(r)_{1m} Y_{1m}^\theta] - (1/r^2) \sum [Z_4(r)_{1m} Y_{1m}^\varphi - Z_6(r)_{1m} Y_{1m}^\theta]$$

$$r^2 \partial \tau_{r\varphi} / \partial r = \sum [rZ'_{4-}(r)_{1m} Y_{1m}^\varphi - rZ'_{6-}(r)_{1m} Y_{1m}^\theta] - \sum [Z_4(r)_{1m} Y_{1m}^\varphi - Z_6(r)_{1m} Y_{1m}^\theta]$$

$$r \sigma_{\varphi\varphi} = -r \sum p Y + 2\eta^* \sum [Z_1 Y + Z_2 (Y^{\varphi\varphi} + cY^\theta) + Z_5 (-Y^{\theta\varphi} + cY^\varphi)] + (2/3)\eta^* k \sum Z_1 Y - 2\eta^* [v_\varphi T^\varphi]$$

Properties of spherical functions' derivatives E3.7a and 3.7b =>

$$r\tau_{\theta\varphi} = \eta^* \sum [2Z_2(Y^{\theta\varphi} - cY^\varphi) - Z_5(LY + Y^{\theta\theta})] + (2/3)\eta^* k \sum V_r Y - \eta^* [V_\theta T^\varphi + V_\varphi T^\theta]$$

$$r\tau_{\theta\varphi} = \eta^* \sum [2Z_2 Y^{\theta\theta}] - Z_5(LY + Y^{\theta\theta}) + (2/3)\eta^* k \sum V_r Y - \eta^* [V_\theta T^\varphi + V_\varphi T^\theta]$$

$$rp(r, \theta, \varphi) = \sum \{-2\eta^*(2+k)Z_{1m}(r) + 2\eta^* LZ_2(r) - Z_3(r) + (2/3)\eta^* k Z_1(r) + r\rho_0 \Phi_{1m} + 2\eta^*(A-R)\}_{1m} Y_{1m}$$

$$0 = \sum rZ'_4(r)_{1m} Y_{1m}^\varphi - rZ'_6(r)_{1m} Y_{1m}^\theta - \sum [Z_4(r)_{1m} Y_{1m}^\varphi - Z_6(r)_{1m} Y_{1m}^\theta] + \eta^* \sum [2Z_2 Y^{\varphi\theta\theta}] - Z_5(LY^\theta + Y^{\theta\theta}) + (2/3)\eta^* k \sum V_r Y^\theta - \eta^* [V_\theta T^\varphi + V_\varphi T^\theta]_\theta - r \sum p Y^\varphi + 2\eta^* \sum [Z_1 Y^\varphi + Z_2(Y^{\varphi\varphi\varphi} + cY^{\theta\varphi}) + Z_5(-Y^{\theta\varphi\varphi} + cY^{\varphi\varphi})] + (2/3)\eta^* k \sum Z_1 Y^\varphi - 2\eta^*(1/\sin\theta)[V_\varphi T^\varphi]_\varphi + 3\sum [Z_4(r)_{1m} Y_{1m}^\varphi - Z_6(r)_{1m} Y_{1m}^\theta] + 2c\eta^* \sum [2Z_2 Y^{\theta\theta}] - Z_5(LY + Y^{\theta\theta}) + (4c/3)\eta^* k \sum V_r Y - c\eta^* [V_\theta T^\varphi + V_\varphi T^\theta] + [(r\rho_0)/\sin\theta] \partial\Phi/\partial\varphi,$$

$$0 = \sum rZ'_4(r)_{1m} Y_{1m}^\varphi - rZ'_6(r)_{1m} Y_{1m}^\theta - \sum [Z_4(r)_{1m} Y_{1m}^\varphi - Z_6(r)_{1m} Y_{1m}^\theta] + \eta^* \sum [2Z_2 Y^{\theta\theta}] - Z_5(LY^\theta + Y^{\theta\theta}) + (2/3)\eta^* k \sum V_r Y^\theta - \eta^* [V_\theta T^\varphi + V_\varphi T^\theta]_\theta - \sum \{-2\eta^*(2+k)Z_{11m}(r) + 2\eta^* LZ_2(r) - Z_3(r) + (2/3)\eta^* k Z_1(r) + r\rho_0 \Phi_{1m} + 2\eta^*(A-R)\}_{1m} Y^\varphi + 2\eta^* \sum [Z_1 Y^\varphi + Z_2(Y^{\varphi\varphi\varphi} + cY^{\theta\varphi}) + Z_5(-Y^{\theta\varphi\varphi} + cY^{\varphi\varphi})] + (2/3)\eta^* k \sum Z_1 Y^\varphi - 2\eta^*(1/\sin\theta)[V_\varphi T^\varphi]_\varphi + 3\sum [Z_4(r)_{1m} Y_{1m}^\varphi - Z_6(r)_{1m} Y_{1m}^\theta] + 2c\eta^* \sum [2Z_2 Y^{\theta\theta}] - Z_5(LY + Y^{\theta\theta}) + (4c/3)\eta^* k \sum V_r Y - 2c\eta^* [V_\theta T^\varphi + V_\varphi T^\theta] + [(r\rho_0)/\sin\theta] \partial\Phi/\partial\varphi$$

This equation can be rewritten in common form:

$$0 = \sum (rZ'_{41m} + \dots) Y^\varphi - \sum (Z'_{61m} + \dots) Y^\theta - 2\eta^*(A_{1m} - R_{1m}) Y^\varphi_{1m} - \eta^* \underline{D}_2$$

$$0 = \sum (rZ'_{41m} + \dots) Y^\varphi - \sum (Z'_{61m} + \dots) Y^\theta - \eta^* \underline{D}_1 - \eta^* \underline{D}_2$$

$$\underline{D}_2 = [V_\theta T^\varphi + V_\varphi T^\theta]_\theta + 2\eta^*(1/\sin\theta)[V_\varphi T^\varphi]_\varphi + 2c\eta^*[V_\theta T^\varphi + V_\varphi T^\theta] \quad (W25)$$

$$\underline{D}_1 = \sum 2(A-R)_{1m} Y^\varphi_{1m}$$

Therefore we arrive at the final equation system:

$$0 = \sum (rZ'_{41m} + \dots) Y^\varphi + \sum (rZ'_{61m} + \dots) Y^\theta - \eta^* \underline{C}_1 - \eta^* \underline{C}_2$$

$$\text{where } \underline{C}_1 = 2\sum (A-R)_{1m} Y^\theta_{1m}$$

$$\underline{C}_2 = 2\eta^* [(V_\theta T^\theta]_\theta + 2c\eta^* [(V_\theta T^\theta - V_\varphi T^\varphi] + \eta^*(1/\sin\theta)[V_\theta T^\varphi + V_\varphi T^\theta]_\varphi$$

$$0 = \sum (rZ'_{41m} + \dots) Y^\varphi - \sum (Z'_{61m} + \dots) Y^\theta - \eta^* \underline{D}_1 - \eta^* \underline{D}_2$$

$$\text{where } \underline{D}_1 = 2(A_{1m} - R_{1m}) Y^\varphi_{1m}$$

$$\underline{D}_2 = \eta^* [V_\theta T^\varphi + V_\varphi T^\theta]_\theta + 2\eta^*(1/\sin\theta)[V_\varphi T^\varphi]_\varphi + 2c\eta^*[V_\theta T^\varphi + V_\varphi T^\theta]$$

Using the same technique as for the U-transform method:

$$\underline{C}_2 = \sum f_a(r)_{1m} Y_{1m}^\theta + f_b(r)_{1m} Y_{1m}^\varphi$$

$$\underline{D}_2 = \sum f_a(r)_{1m} Y_{1m}^\varphi - f_b(r)_{1m} Y_{1m}^\theta$$

$$f_a = (1/s_{m1}) \int_0^{2\pi} d\varphi \int_0^{\pi} [\underline{C}_2 Y_{1m}^\theta + \underline{D}_2 Y_{1m}^\varphi] \sin\theta d\theta$$

$$f_b = (1/s_{m1}) \int_0^{2\pi} d\varphi \int_0^{\pi} [\underline{C}_2 Y_{1m}^\varphi - \underline{D}_2 Y_{1m}^\theta] \sin\theta d\theta$$

$$\underline{C}_1 = 2 \sum (A_{1m} - R_{1m}) Y_{1m}^\theta$$

$$\underline{D}_1 = \sum 2(A - R)_{1m} Y_{1m}^\varphi$$

$$\underline{C}_1 = \sum g_a(r)_{1m} Y_{1m}^\theta + g_b(r)_{1m} Y_{1m}^\varphi$$

$$\underline{D}_1 = \sum g_a(r)_{1m} Y_{1m}^\varphi - g_b(r)_{1m} Y_{1m}^\theta$$

$$g_{a1} = (1/s_{m1}) \int_0^{2\pi} d\varphi \int_0^{\pi} [\underline{C}_1 Y_{1m}^\theta + \underline{D}_1 Y_{1m}^\varphi] \sin\theta d\theta =$$

$$= (1/s_{m1}) \int_0^{2\pi} d\varphi \int_0^{\pi} [2 \sum (A_{1m} - R_{1m}) Y_{1,m}^\theta Y_{1m}^\theta + 2(A_{1,m'} - R_{1,m'}) Y_{1m}^\varphi Y_{1m}^\varphi] \sin\theta d\theta =$$

$$= (1/s_{m1}) 2 \sum (A_{1m} - R_{1m}) \int_0^{2\pi} d\varphi \int_0^{\pi} [Y_{1,m}^\theta Y_{1m}^\theta + Y_{1m}^\varphi Y_{1m}^\varphi] \sin\theta d\theta =$$

$$= (1/s_{m1}) 2 \sum (A_{1m} - R_{1m}) s_{m1} = 2 \sum (A_{1m} - R_{1m})$$

$$g_{b1} = (1/s_{m1}) \int_0^{2\pi} d\varphi \int_0^{\pi} [\underline{C}_1 Y_{1m}^\varphi - \underline{D}_1 Y_{1m}^\theta] \sin\theta d\theta =$$

$$= 2 \sum (A_{1,m'} - R_{1,m'}) (1/s_{m1}) \int_0^{2\pi} d\varphi \int_0^{\pi} [Y_{1,m'}^\theta Y_{1m}^\varphi - Y_{1,m'}^\varphi Y_{1m}^\theta] \sin\theta d\theta = 0$$

$$\Rightarrow g_{a1} = 2 \sum (A_{1m} - R_{1m}) = -2\eta * [(1/s_{m0}) \iint (T^r V_r - v \nabla \ln T) Y_{1m} d\varphi \sin\theta d\theta]$$

$$g_{b1} = 0$$

$$0 = \sum (r Z'_{41m} + \dots) Y^\theta + \sum (r Z'_{61m} + \dots) Y^\varphi - \eta * [2 \sum (A_{1m} - R_{1m}) Y_{1m}^\theta] - \eta * [\sum f_a(r)_{1m} Y_{1m}^\theta + f_b(r)_{1m} Y_{1m}^\varphi]$$

$$0 = \sum (r Z'_{41m} + \dots) Y^\varphi - \sum (Z'_{61m} + \dots) Y^\theta - \eta * [\sum 2(A - R)_{1m} Y_{1m}^\varphi] - \eta * [\sum f_a(r)_{1m} Y_{1m}^\varphi - f_b(r)_{1m} Y_{1m}^\theta]$$

$$D_{1m} = \eta * 2(A_{1m} - R_{1m}) + \eta * f_a(r)_{1m}$$

$$F_{1m} = \eta * f_b(r)_{1m}$$

$$f_a = (1/s_{m1}) \int_0^{2\pi} d\varphi \int_0^{\pi} [\underline{C}_2 Y_{1m}^\theta + \underline{D}_2 Y_{1m}^\varphi] \sin\theta d\theta$$

$$f_b = (1/s_{m1}) \int_0^{2\pi} d\varphi \int_0^{\pi} [\underline{C}_2 Y_{1m}^\varphi - \underline{D}_2 Y_{1m}^\theta] \sin\theta d\theta$$

$$\underline{C}_2 = 2[(V_\theta T^\theta]_\theta + 2c[(V_\theta T^\theta - V_\varphi T^\varphi] + (1/\sin\theta)[V_\theta T^\varphi + V_\varphi T^\theta]_\varphi$$

$$\underline{D}_2 = [V_\theta T^\varphi + V_\varphi T^\theta]_\theta + (2/\sin\theta)[V_\varphi T^\varphi]_\varphi + 2c[V_\theta T^\varphi + V_\varphi T^\theta]$$

$$D_{1m} = f_a = (\eta^*/s_{m1}) \int_0^{2\pi} d\varphi \int_0^{\pi} [\underline{C}_2 Y_{1m}^\theta + \underline{D}_2 Y_{1m}^\varphi] \sin\theta d\theta - 2\eta^* [(1/s_{m0}) \iint (T^r V_r - v \nabla \ln T) Y_{1m} d\varphi \sin\theta d\theta]$$

$$r \frac{dZ_4^{lm}}{dr} = -(6 + 2k)\eta^* Z_1^{lm} - 2(2L - 1)\eta^* Z_2^{lm} - Z_3^{lm} - 2Z_4^{lm} +$$

$$+ \frac{\eta^*}{s_{lm}} \int_0^{2\pi} d\varphi \int_0^{\pi} [\underline{C}_2 Y_{lm}^\theta + \underline{D}_2 Y_{lm}^\varphi] \sin\theta d\theta + \frac{2\eta^* r}{s_{m0}} \int_0^{2\pi} d\varphi \int_0^{\pi} (T_\theta V_\theta + T_\varphi V_\varphi) Y_{lm} \sin\theta d\theta \quad (W26)$$

$$F_{1m} = (\eta^*/s_{m1}) \int_0^{2\pi} d\varphi \int_0^{\pi} [\underline{C}_2 Y_{1m}^\varphi - \underline{D}_2 Y_{1m}^\theta] \sin\theta d\theta$$

$$r \frac{dZ_6^{lm}}{dr} = (L-2)\eta^* Z_5^{lm} - 2Z_6^{lm} + \frac{\eta^*}{s_{lm}} \int_0^{2\pi} d\varphi \int_0^\pi [C_2 Y_{lm}^\varphi - D_2 Y_{lm}^\theta] \sin \theta d\theta \quad (\text{W27})$$

$$\begin{aligned} \underline{C}_2 &= 2 \frac{\partial(V_\theta T_\theta)}{\partial \theta} + 2ctg\theta(V_\theta T_\theta - V_\varphi T_\varphi) + \frac{1}{\sin \theta} \frac{\partial(V_\theta T_\varphi + V_\varphi T_\theta)}{\partial \theta} \\ \underline{D}_2 &= \frac{\partial(V_\theta T_\varphi + V_\varphi T_\theta)}{\partial \theta} + 2ctg\theta(V_\theta T_\varphi + V_\varphi T_\theta) + \frac{2}{\sin \theta} \frac{\partial(V_\varphi T_\varphi)}{\partial \theta} \end{aligned} \quad (\text{W28})$$

Viscous terms (W26) and (W27) in the equations for spheroidal and toroidal stress differ from those stated by Zhang and Christensen (1993) in the same manner as (U21) and (U22) derived for the U-transform method. The reason of this distinction is also the same: incorrect understanding of the particular role of dynamic pressure.

## *List of abbreviations*

- FD - finite difference
- FE - finite element
- FV - finite volume
- LVV - lateral viscosity variations
- ODE - ordinary differential equations
- ZC - indicator for the formulae stated by Zhang and Christensen (1993)

### Model abbreviations:

- No-effect model: no compressibility, no self-gravitation and no radial gravity change
- All-effect model: all three effects are included
- No-compressibility model: all effects are included except for mantle compressibility.
- No-self-gravitation model: all effects are included except for self-gravitation.
- No-radial-gravity model: all effects are included except for depth-dependent gravity.

## **List of notations**

### *Chapter II. Part 2.1*

$p$  - fluid pressure

$g_i$  - acceleration of gravity

$\tau_{ij}$  - deviator stress tensor

$e_{ij}$  - strain rate tensor

$\delta_{ij}$  - Kronecker delta

$\eta$  - dynamic viscosity

$\lambda$  - second viscosity

$k_B$  - bulk viscosity

$V$  - gravitational potential

$\rho$  - density distribution in the mantle

$\bar{\rho}$  - radial density profile

$\delta\rho$  - density anomaly

$G$  - universal gravitational constant

$k$  - thermal conductivity

$s$  - entropy per unit mass

$H$  - rate of internal heat production per mass unit

$T$  - temperature.

$\alpha$  - coefficient of thermal expansion of material

$v$  - specific volume

$(*)_p$  ( $(*)_v$ ) - the pressure (volume) is held fixed

$c_p$  ( $c_v$ ) - specific heat at constant pressure (volume)

$\Phi = \tau_{ij} \frac{\partial u_i}{\partial x_j}$  - viscous dissipation function.

### *Chapter II. Part 2.2*

$R_c$  - radius of the core

$R_e$  - radius of the Earth

$\bar{g}$  - radial gravity

$u$  - mantle flow velocity

$\sigma_{ij}$  - total stress tensor

### *Chapter III. Part 3.1*

$Y_{lm}(\theta, \varphi)$  - spherical functions

$l$  - spherical harmonic degree

$m$  - spherical harmonic order

$P_l^m(\cos\theta)$  - associated Legendre functions

$P_l(\cos\theta)$  - Legendre polynomials

$N_{lm}$  - normalization coefficients for associated Legendre functions

$Y_{lm}^\theta(\theta, \varphi)$  and  $Y_{lm}^\varphi(\theta, \varphi)$  - spherical functions' derivatives

$s_{m0}$  and  $s_{ml}$  - orthonormalization coefficients for spherical functions and their derivatives

#### Chapter III. Part 3.2

$\eta_0$  - mean mantle viscosity

$r$  - relative radius

$\eta^*(r)$  - dimensionless radial viscosity function

$\rho_0$  - mean mantle density

$g_0$  - acceleration of gravity on the Earth surface

$\rho^*(r)$  - dimensionless radial density

$g^*(r)$  - dimensionless acceleration of gravity

$k(r)$  - mantle compressibility

$r_e$  and  $r_c$  - relative values of radius of the Earth's surface and the core boundary

#### Chapter III. Part 3.3

$l_{\max}$  - maximum spherical harmonic degree

#### Chapter IV. Part 4.1

$\delta r$  - departure of the geoid from a sphere

$\delta V$  - angular-dependent component of the gravitational field

$\delta N$  - geoid undulations (departure of the geoid from an ellipsoid)

$C_{20}$  and  $C_{40}$  - zonal spherical harmonic coefficients with order  $l=2$  and  $l=4$

#### Chapter IV. Part 4.2

$(*)_s$  ( $(*)_p$ ) - isentropic (isobaric) variations - reversible process

without heat transfer (process with constant pressure)

#### Chapter VI. Part 6.1

$V_s$  - seismic velocity distribution

$Sc(r)$  - scaling factor

$a_j^0$  - initial scaling factor

$a_j$  - unknown scaling factors

$N_{obs}^{l,m}$  - spherical harmonic coefficients of the observed geoid

$N_j^{l,m}$  - geoid variations induced by a layer j

$\beta_j$  - damping factors introduced to stabilize a solution

$Sc_j$  - density-velocity scaling coefficient standard deviations

*Chapter VII. Part 7.1*

$T_m(r)$  - solidus temperature

$\bar{\eta}_0(r)$  - initial coefficients

$\gamma(r)$  - activation parameters

$E^*$  - activation energy of the subsolidus creep deformation

h - depth

$h_c$  - depth of the core-mantle boundary

*Appendix.*

$c \equiv ctg\theta$

$$Y^{\theta\theta} = Y_{\theta\theta} = \frac{\partial^2 Y}{\partial \theta^2}$$

$$Y^{\varphi\varphi} = \frac{1}{\sin^2 \theta} Y_{\varphi\varphi} = \frac{1}{\sin^2 \theta} \frac{\partial^2 Y}{\partial \varphi^2}$$

$$Y^{\theta\varphi} = \frac{1}{\sin \theta} Y_{\theta\varphi} = \frac{1}{\sin \theta} \frac{\partial \left( \frac{\partial Y}{\partial \theta} \right)}{\partial \varphi}$$

$$Y^{\varphi\theta} = \frac{1}{\sin \theta} Y_{\varphi\theta} = \frac{\partial \left( \frac{1}{\sin \theta} \frac{\partial Y}{\partial \varphi} \right)}{\partial \theta}$$

$\nabla_H \cdot \mathbf{U}_i$  - surface divergence

$[\nabla \mathbf{U}_i] \cdot \mathbf{r}_k / r$  - radial vorticity

## *List of Figures*

### *Chapter IV.*

(F4.1) Isostatic reduction of the geoid _____	44
(F4.2) Radial density distribution according to PREM _____	46
(F4.3) Mantle compressibility _____	47
(ES4.1) Removal of mantle compressibility and partial self-gravitation effects from the equation system _____	48

### *Artificial model:*

(F4.4) Density anomalies: cross-section through the longitude 30; view from the surface _____	50
(F4.5) Velocities near surface and core _____	51
(F4.6) Profiles for lateral velocity components at the surface and near the core _____	52
(F4.7) Velocity distribution for the model without effects of self-gravitation, mantle compressibility and radial gravity ____	53
(F4.8) Velocity components and differences between models with various effect combinations (cross-section through the longitude 60) _____	54
(F4.9) Velocity components and differences between models with various effect combinations (cross-section through the longitude 90) _____	55
(F4.10) Geoids obtained from the models without effects and with all effects. Difference between calculated geoids _____	56
(F4.11) Impact of self-gravitation, mantle compressibility and radial gravity into geoid _____	57

### *Realistic model:*

(F4.12) Radial viscosity profile _____	59
(F4.13) Density anomalies (cross-section through the longitude 30) ____	59
(F4.14) Velocity distribution in the model without effects _____	60
(F4.15) Profiles for horizontal velocities $u_\theta$ and $u_\phi$ with and without effects _____	61
(F4.16) Velocities near surface and core calculated with and without effects _____	62
(F4.17) Difference between horizontal velocities calculated for the models with and without effects _____	63
(F4.18) Geoids obtained from the models without effects and with all	

effects. Difference between calculated geoids _____	64
(F4.19) Impact of each effect into geoid figure _____	65
<i>Chapter V.</i>	
(VT5.1) Misprints in U-transform method by Zhang and Christensen (1993) and Zhang (1993) _____	75
(NC5.1) Misprints in normalization coefficients in U-transform method by Zhang and Christensen (1993) and Zhang (1993) _____	75
(VT5.2) Misprints in W-transform method by Zhang and Christensen (1993) and Zhang (1993) _____	79
(NC5.2) Misprints in normalization coefficients in W-transform method by Zhang and Christensen (1993) and Zhang (1993) _____	79
<i>Model 5.4a:</i>	
(F5.1) Density anomalies and LVV _____	82
(F5.2) Comparison of velocity flows calculated by U-transform and W-transform iterative methods _____	83
(F5.3) Comparison of vertical profiles of mantle velocities _____	84
(F5.4) Dynamic geoid calculated for the constant viscosity model _____	85
(F5.5) Difference between geoid calculated with effect of LVV by U-transform method and geoid calculated with the constant viscosity model _____	85
(F5.6) Difference between geoids calculated with effect of LVV by U-transform and W-transform iterative methods _____	86
<i>Model 5.4b:</i>	
(F5.7) LVV and velocity distributions calculated by iterative methods with the formulae stated by Zhang and Christensen (1993) _____	87
<i>Model 5.4c:</i>	
(F5.8) Convergence of U-transform method applied to the strong LVV models (3.5, 4.2, 6 and 7 orders of magnitude) _____	88
(F5.9) Response of mantle flow on LVV in the area with low viscosity _____	89
(F5.10) Convergence of W-transform method _____	90
<i>Model 5.4d:</i>	
(F5.11) Radial viscosity profile _____	92
(F5.12) Small-scale high-viscous fragments located inside the low viscosity area _____	92
(F5.13) Zoomed small-scale high-viscous fragment situated on the way of descending flow _____	93

(F5.14) Zoomed small-scale high-viscous fragment in the area where the motion changes its direction and velocity _____	94
--	----

*Model 5.4e:*

(F5.15) Density anomalies and LVV in cross-section through the longitude 90 _____	96
(F5.16) Geoid calculated by the new realization of the U-transform method and geoid stated by Zhang (1993) _____	97
(F5.17) Surface divergence calculated for the constant viscosity model and with LVV by new realizations of the U- and W-transform. Surface divergence stated by Zhang (1993) _____	98
(F5.18) Radial vorticity calculated by U- and W-transform with new formulae. Radial vorticity stated by Zhang (1993) _____	99

*Chapter VI.*

(F6.1) Scaling factors (from joint inversion) and scaling coefficient standard deviations, which correspond to the radial viscosity profile in (F6.2) _____	104
(F6.2) Radial viscosity profile, which corresponds to the model with the best fit to both the observed geoid (78.2%) and initial scaling factors in the lower mantle. Search area _____	105
(F6.3) Residual geoid versus perturbations to the initial scaling factor in different radial viscosity models (model cluster for viscosity value in asthenosphere) _____	106
(F6.4) Residual geoid versus perturbations to the initial scaling factor in different radial viscosity models (model cluster for viscosity value in the upper part of the transition zone (above 670 km)) _____	107
(F6.5) Isostatic anomalies of the observed geoid and geoid calculated with radial viscosity _____	108

*Chapter VII.*

(F7.1) Temperature profiles _____	112
(F7.2) Relative radial viscosity _____	114
(F7.3) Density anomaly distribution. Velocities calculated for radial viscosity model _____	115
(F7.4) LVV and velocity redistribution due to LVV _____	115
(F7.5) Zoomed area with low viscosity _____	116
(F7.6) Zoomed area with high viscosity _____	117
(F7.7) Near-surface velocities at the depth 100 km _____	118
(F7.8) Difference between near-surface velocities calculated with LVV	

and with only radial viscosity _____	118
(F7.9) Surface divergence and radial vorticity _____	119
(F7.10) Cross-sections showing density anomaly and LVV in the mantle relative to the adopted vertical profile _____	121
(F7.11) Cross-sections showing LVV incorporated into the lower-mantle model (left) and upper-mantle model (right) relative to the adopted vertical profile _____	121
(F7.12) Velocity-to-density scaling factor profile obtained from a least square adjustment to get a best fit to the observed geoid _____	122
(F7.13) Isostatic anomalies of geoid calculated with radial viscosity and LVV. Observed geoid _____	123
(F7.14) Observed geoid and geoids calculated for various LVV models _	125
(F7.15) Discrepancies between a dynamic geoid generated by the 3-D viscosity models and initial "radial" model _____	126
(F7.16) Discrepancies between a dynamic topography generated by the 3-D viscosity models and initial "radial" model _____	127
(F7.17) Near-surface mantle velocities _____	129
(F7.18) Transformations (differences with the initial radial viscosity model) of near-surface mantle velocities caused by LVV _____	129
(F7.19) Surface divergence calculated for the radial viscosity model and for the model with whole mantle LVV _____	130
(F7.20) Differences between surface divergence generated by the various LVV models and initial radial viscosity model _____	130
(F7.21) Radial vorticity generated by various 3-D viscosity models __	131

## References

- Anderson D. L., 1989. Theory of the Earth. Blackwell Scientific Publications.
- Bachelor G. K., 1967. Fluid Mechanics. Cambridge University Press, Cambridge.
- Baranov A., Trubitsyn V., Kaban M. K., Rogozhina I., 2007. Effect of strong lateral viscosity variations on the global mantle flow. EGU.
- Bunge H. P., Richards M. A., Baumgardner J. R., 1996. Effect of depth-dependent viscosity on the planform of mantle convection. Nature. 379, 436-438.
- Bunge H. P., Richards M. A., Baumgardner J. R., 1997. A sensitivity study of three-dimensional spherical mantle convection at  $10^8$  Rayleigh number: Effects of depth-dependent viscosity, heating mode, and an endothermic phase change. J. Geophys. Res. 102, 11991-12008.
- Čadek O., Fleitout L., 1999. A global geoid model with imposed plate velocities and partial layering. J. Geophys. Res. 104(12), 29055-29075
- Čadek O., Fleitout L., 2003. Effect of lateral viscosity variations in the top 300 km on the geoid and dynamic topography. Geophys. J. Int. 152(3), 566-580.
- Čadek, O., Fleitout, L., 2006. Effect of lateral viscosity variations in the core-mantle boundary region on predictions of the long-wavelength geoid. Stud. Geophys. Geod., 50, 217-232.
- Čadek O., Ricard Y., 1992. Toroidal/poloidal energy partitioning and global lithospheric rotation during Cenozoic time. Earth planet. Sci. Lett., 109, 621-632.
- Čadek O., Ricard Y., Martinec Z., Matyska C., 1993. Comparison between Newtonian and non-Newtonian flow driven by internal loads. Geophys. J. Int., 112, 103-114.
- Chandrasekhar S., 1961. Hydrodynamic and hydromagnetic stability. Clarendon Press, Oxford.
- Christensen U. R., 1984. Convection with pressure and temperature dependent non-Newtonian rheology. Geophys. J. R. astr. Soc., 77, 343-384.
- Christensen U. R., Harder H., 1991. 3-D convection with variable viscosity. Geophys. J. Int., 104, 213-226.

- Clayton R. W., Comer R. P., 1983. A tomographic analysis of mantle heterogeneities from body wave travel time. *EOS Trans. Am. Geophys. Un.*, 62, 776.
- Colin P., 1993. *Geoid global, topographie associee et structure de la convection dans le manteau terrestre: Modelisation et observation*. Ph. D. Thesis, Ecole normale superieure, Paris, France.
- Corrieu V., Ricard Y., Froidevaux C., 1994. Converting mantle tomography into mass anomalies to predict the Earth's radial viscosity. *Physics of the Earth and Planetary Interiors*. 84(1-4), 3-13.
- Corrieu, V., Thoraval, C., Ricard, Y., 1995, Mantle dynamics and geoid Green functions. *Geophysical-Journal-International*. 120(2), 516-523
- Dziewonski A., D. L. Anderson, 1981. Preliminary reference Earth model (PREM). *Phys. Earth Planet. Inter.* 25, 297-356.
- Ekstrom G., Dziewonski A. M., 1998. The unique anisotropy of the Pacific upper mantle. *Nature (London)*. 394, 6689, 168-172.
- Flechtner F., Schmidt R., Meyer U., Neumayer K.H., König, R., Rothacher M., Kusche J., 2007. The new EIGEN-GRACE05S (RL04) Gravity Field Time Series. EGU.
- Förste Ch., Flechtner F., Schmidt R., Biancale R., Lemoine J.-M., Stubenvoll R., Neumayer H., Loyer S., Rothacher M., Kusche J., 2007. THE EIGEN TEAM EIGEN-05C - A new global mean Gravity Field Model from Combination of Satellite Mission and Altimetry/Gravimetry Surface data. EGU.
- Forte A. M., 2000. Seismic-geodynamic constraints on mantle flow: Implications for layered convection, mantle viscosity, and seismic anisotropy in the deep mantle. *In Earth's Deep Interior: Mineral Physics From the Atomic to the Global Scale*, Geophys. Monogr. Ser. 117, edited by S. Karato et al., AGU, Washington, DC, pp. 3-36.
- Forte A. M., Mitrovica J. X., 2001. Deep-mantle high-viscosity flow and thermochemical structure inferred from seismic and geodynamic data. *Nature*. 410, 1049-1056.
- Forte A. M., Mitrovica J. X., 2004. Deep-mantle high-viscosity flow and thermochemical structure inferred from seismic and geodynamic data. *Nature*, 410, 1049-1056.
- Forte, A. M., Peltier, W. R., 1987. Plate tectonics and aspherical Earth structure: the importance of poloidal-toroidal coupling. *Journal of Geophysical Research*. 92(B5), 3645-3679

- Forte A. M., Peltier W. R., 1991. Viscous flow models of global geophysical observables: 1. Forward problems. *J. geophys. Un.*, 73, 200.
- Forte A. M., Peltier W. R., 1994. The kinematics and dynamics of poloidal-toroidal coupling in mantle flow: the importance of surface plates and lateral viscosity variations. *Adv. Geophys.*, 36, 1-119.
- Forte A. M., Woodward R. L. and Dziewonski A. M., 1994. Joint inversions of seismic and geodynamical data for models of three-dimensional mantle heterogeneity. *J. Geophys. Res.*, 99. 21857-21877.
- Forte A. M., Mitrovica J. X., Espeset A., 2002. Geodynamic and seismic constraints on the thermochemical structure and dynamics of convection in the deep mantle, *Philos. Trans. R. Soc. London*, 360 (1800), 2521-2543.
- Gable C. W., O'Connell R. J., Travis B. J., 1991. Convection in three dimensions with surface plates: generation of toroidal flow. *J. Geophys. Res.* 96, 8391-8405.
- Gasperini P., Sabadini R., 1989. Lateral heterogeneities in mantle viscosity and postglacial rebound, *Geophys. J.*, 98, 413-428.
- Gasperini, P., and R. Sabadini, 1990. Finite element modeling of lateral viscosity heterogeneities and post-glacial rebound. *Tectonophysics*. 179, 141-149.
- Gasperini P., Sabadini. R., Yuen D. A., 1991. Deep continental roots: the effect of lateral variations of viscosity on post-glacial rebound. In *Glacial Isostasy, Sea-Level and Mantle Rheology*, pp. 21-32, eds Sabadini R. et al., Kluwer, Dordrecht.
- Grand S. P., van der Hilst R.D., Widiyantoro S., 1997. Global seismic tomography: a snapshot of convection in the Earth. *GSA Today*. 7(4), 1-7.
- Godunov S. K., 1961. "O chislennom reshenii kraevykh zadach dlya sistem lineynykh obyknovennykh differentsial'nykh uravneniy", *Journal "Uspehi matematicheskikh nauk"*.
- Gurnis, M., Wysession, M., Knittle, E., and Buffett, B. , 1998. *The Core Mantle Boundary Region, Geodynamics Series, Volume 28*, AGU, Washington, D.C.
- Gurnis M., Davis G. F., 1986. Numerical study of high Rayleigh number convection in a medium with depth-dependent viscosity. *Geophys, J. R. astr. Soc.* 85, 523-542.

- Hager B. H., 1984. Subducted slabs and the geoid: constraints on mantle rheology and flow. *J. Geophys. Res.* 89, 6003-6015.
- Hager B. H., Clayton R. W., Richards M. A., Comer R. P., Dziewonski A. M., 1985. Lower mantle heterogeneity, dynamic topography, and the geoid. *Nature*. 313, 541-545.
- Hager B. H., Clayton R. W., 1989. Constraints on the structure of the mantle convection using seismic observations, flow models, and the geoid. *Mantle Convection*, pp.657-764.
- Hager B. H., O'Connell R. J., 1978. Subduction zone dip angles and flow driven by plate motion, *Tectonophysics*, 50, 111-133.
- Hager B. H., O'Connell R. J., 1981. A simple global model of plate dynamics and mantle convection. *J. Geophys. Res.* 86, 4843-4867.
- Heiskanen W. A., Moritz H., 1967. *Physical Geodesy*. W.H. Freeman and Company. San Francisco and London.
- Kaban M. K., Rogozhina I., 2007. Global modeling of the dynamic geoid: an integrative approach. EGU.
- Kaban M. K., Rogozhina I., Trubitsyn V., 2007. Importance of lateral viscosity variations in the whole mantle for modelling of the dynamic geoid and surface velocities, *Journal of Geodynamics*, 43, 262-273.
- Kaban M. K., Schwintzer P., Tikhotsky S. A., 1999. A global isostatic gravity model of the Earth. *Geophys. J. Int.* 136 (3), 519-536.
- Kaban M. K., Schwintzer P., 2001. Oceanic upper mantle structure from experimental scaling of  $V_s$  and density at different depths. *Geophysical Journal International*. 147, 1, 199-214.
- Kaban M. K., Schwintzer P., Reigber Ch., 2004. A new isostatic model of the lithosphere and gravity field. *Journal-of-Geodesy*. 78(6), 368-385
- Karato S., Wu P., 1993. Rheology of the upper mantle: A synthesis. *Science*. 260, 771-778.
- Karato S., 1993. Importance of anelasticity in the interpretation of seismic tomography. *Geophys. Res. Lett.* 20, 1623-1626.
- Karpychev M., Fleitout L., 1996. Simple consideration of forces driving plate motion and on the plate-tectonic contribution to the long-wavelength geoid. *Geophys. J. Int.*, 127, 268-282.
- Karpychev M., Fleitout L., 2000. Long-wavelength geoid: the effect of continental roots and lithosphere thickness variations. *Gephys. J. Int.* 143, 945-963.
- Kaufmann G., Wu P., 1998. Upper mantle lateral viscosity variations and postglacial rebound: application to the Barents Sea. In "Dynamics of

- the Ice Age Earth: A Modern Perspective" edited by P.Wu, Trans Tech Publ., Switzerland, p.583-602.
- Kaufmann G., Wu P., 1998. Lateral asthenospheric viscosity variations and postglacial rebound: a case study for the Barents Sea. *Geophys. Res Lett.* 25, 1963-1966.
- Kaufmann G., Wu P., 1998. Upper mantle lateral viscosity variations and postglacial rebound: application to the Barents Sea, *Ann. Geophys.* Vol. 16, pp. C53.
- Kaufmann G., Wu P., 2002. Glacial isostatic adjustment in Fennoscandia with a three dimensional viscosity structure as an inverse problem, *Earth and Planetary Science Letters*, 197, 1-10.
- Kaufmann G., Wu P., Ivins E. R., 2005. Lateral viscosity variations beneath Antarctica and their implications on regional rebound motions and seismotectonics, *J. Geodyn.* 39, 165-181
- Kido M., Čadek O., 1997. Inferences of viscosity from oceanic geoid: Indication of a low viscosity zone below the 660-km discontinuity. *Earth Planet. Sci. Lett.*, 151, 125-138.
- King S. D., 1995. Radial models of mantle viscosity: Results from a genetic algorithm. *Geophys. J. Int.*, 122, 725-734.
- King S. D., Hager, B. H., 1994. Subducted slabs and the geoid: 1) numerical calculations with temperature-dependent viscosity. *J. Geophys. Res.*, 99, 19843-19852.
- King S. D., Masters G., 1992. An inversion for radial viscosity structure using seismic tomography. *Geophys. Res. Lett.* 19(15), 1551-1554.
- Kious W. J., Tilling R. I., 1996. This dynamic earth: the story of plate tectonics: U.S. Geological Survey General Information Product, 77.
- Koch D. M., Ribe N. M., 1989. The effect of lateral viscosity variations on surface observables. *Geophys. Res. Lett.* 16(6), 535-538.
- Landau L. D., Lifshitz E. M., 1987. *Theory of elasticity.* Oxford, Pergamon Press.
- Latychev K., Mitrovica J. X., Tamisiea J., Tromp J., Christara C., Moucha R., 2005. GIA-induced secular variations in the Earth's long wavelength gravity field: Influence of 3-D viscosity variations. *Earth. Planet. Science Lett.* 240, 322-327.
- Latychev K., Mitrovica J. X., Tromp J., Tamisiea J., Komatitisch D., Christara C., 2005. Glacial isostatic adjustment on 3-D earth models: A finite-element formulation. *161(2)*, 421-444.

- Marquart G., Schmeling H., 1989. Topography and geoid undulations caused by small scale convection beneath continental lithosphere of variable elastic thickness. *J. Geophys.* 97, 511-527.
- Martinec Z., Matyska C., Čadek O., Hrdina P., 1993. The Stokes problem with 3-D Newtonian rheology in a spherical shell. *Comput. Phys. Commun.* 76, 63-79.
- Mitrovica J. X., Forte A. M., 2004. A new inference of mantle viscosity based upon joint inversion of convection and glacial isostatic adjustment data. *Earth planet. Sci. Lett.* 225, 177-189.
- Moresi L. N., Solomatov V. S., 1995. Numerical investigation of 2-D convection with extremely large viscosity variations. *Phys. Fluids.* 7, 2154-2162.
- Moresi L., Zhong S. J., Gurnis M., 1996. The accuracy of finite element solutions of Stokes' flow with strongly varying viscosity. *Phys. Earth Planet. Inter.* 97, 83-94.
- Mound J. E., Mitrovica J. X., Forte A. M., 2003. The equilibrium form of a rotating earth with an elastic shell. *Geophys. J. Int.* 152, 237-241.
- Moucha R., Forte A. M., Mitrovica J. X., Daradich A., 2007. Lateral variations in mantle rheology: implications for convection-related surface observables and inferred viscosity models. *Geophys. J. Int.*, 169, 113-135.
- Nakiboglu S. M., 1982. Hydrostatic theory of the Earth and its mechanical implications. *Physics-of-the-Earth-and-Planetary-Interiors.* 28(4), 302-311.
- Niehuus K., Schmeling H., 2003. Geoid, its Temporal Variation and Dynamic Topography as Constraints in Global Geodynamics. AGU.
- Niehuus K., Schmeling H., 2004. Geodynamic interpretation of temporal geoid variations. EGU.
- Niehuus K., Schmeling H., 2005. Models of Laterally Variable Viscous Flow in the Earth's Mantle With Constraints From Mineral Physics and Surface Observations. AGU.
- O'Connell R. J., Gable C. W., Hager B. H., 1991. Toroidal-poloidal partitioning of lithospheric plate motion. In *Glacial Isostasy, Sea-Level and Mantle Rheology*, pp. 545-551, Eds. Sabadini R., Lambeck K., Boshci E., Kluwer, Dordrecht.
- Olson P., Bercovici D., 1991. On the equipartitioning of kinetic energy in plate tectonics, *Geophys. Res. Lett.* 18, 1751-1754.

- Panasjuk S. V., Hager B. H., Forte A. M., 1996. Understanding the effects of mantle compressibility on geoid kernels. *Geophysical Journal International*. 124, 1, 121-133.
- Paulson A., Zhong S., Wahr J., 2005. Modeling post-glacial rebound with lateral viscosity variations. *GJI*. 163, 357-371.
- Reigber C., Schmidt R., Flechtner F., Koenig R., Meyer U., Neumayer K.-H., Schwintzer P., Zhu S. Y., 2005. An Earth gravity field model complete to degree and order 150 from GRACE: EIGEN-GRACE02S, *Journal of Geodynamics*, 39, 1-10.
- Ribe N. M., 1992. The dynamics of thin shells with variable viscosity and the origin of toroidal flow in the mantle. *Geophys. J. Int.* 110, 537-552.
- Ricard Y., Bai W., 1991. Inferring viscosity and the 3-D density structure of the mantle from geoid, topography and plate velocities. *Geophys. J. Int.*, 105, 561-572.
- Ricard Y., Fleitout L., Froidevaux C., 1984. Geoid heights and lithospheric stresses for a dynamic Earth. *Ann. Geophys.* 2, 267-286.
- Ricard Y., Froidevaux C., Fleitout L., 1988. Global plate motion and the geoid: a physical model. *Geophys. J.* 93, 477-484.
- Ricard Y., Vigny C., 1989. mantle dynamics with induced plate tectonics. *J. Geophys. Res.* 94, 17543-17559.
- Richards M. A., Hager B. H., 1984. Geoid anomalies in a dynamic earth, *J. Geophys. Res.* 89(B7), 5987-6002.
- Richards M. A., Hager B. H., 1989. Effects of lateral viscosity variations on long-wavelength geoid anomalies and topography. *Journal of Geophysical Research*. 94(B8), 10299-10313.
- Richards M. A., Yang W. S., Baumgardner J. R., Bunge H. P., 2001. Role of a low-viscosity zone in stabilizing plate tectonics: Implications for comparative terrestrial planetology, *Geochem. Geophys. Geosyst.*, vol. 2, 2000GC000115.
- Ritzert M., Jacoby W. R., 1992. Geoid effects in a convecting system with lateral viscosity variations, *Geophys. Res. Lett.*, 19, 1547-1550.
- Rogozhina I., Kaban M. K., Trubitsyn V., Schwintzer P., 2005. Modeling of dynamic geoid with lateral viscosity variations, *EGU*.
- Rogozhina I., Kaban M. K., Trubitsyn V., Rothacher M., 2006. Importance of lateral viscosity variations for a modeling of geoid and dynamic topography. *EGU*.

- Rogozhina I., Kaban M. K., Trubitsyn V., 2007. Perturbation method for modeling of lateral viscosity variations of 7 orders of magnitude, EGU.
- Rykov V. V., Trubitsyn V., 1996. Numerical technique for calculation of three-dimensional mantle convection and tectonics of continental plates. In *Computational Seismology and Geodynamics*; ed. by D. K. Chowdhury. Am. Geophys. Un., Washington D.C. 3, 17-22.
- Schmeling H., 1989. Numerical models of Rayleigh-Taylor instabilities superimposed upon convection. *Bulletin of the Geological Institutions of the University of Uppsala*, 14.
- Schmeling H., 1989. Compressible convection with constant and variable viscosity: the effect on geoid, topography, and slab formation, *J. Geophys. Res.* 94, 12463-12481.
- Schmeling H., Jacoby W. R., 1981. On modelling the lithosphere in mantle convection. *J. Geophys.* 50, 89-100.
- Schmeling, H., 1991. Variable viscosity convection in a compressible upper mantle and the thickness of continental lithosphere. In: *Glacial Isostasy, Sea-Level and Mantle Rheology*. Ed.: R. Sabadini, K. Lambeck, E. Boschi, Kluwer, Dordrecht, 607-636.
- Schubert G., Turcotte D. L., Olson P., 2001. *Mantle convection in the Earth and planets*. Cambridge Univ. Press, Cambridge, UK, p. 940.
- Steffen H., Kaufmann G., Wu P., 2006. Three-dimensional finite-element modelling of glacial isostatic adjustment in Fennoscandia. *Earth and Planet. Sci. Lett.* 250(1-2), 358-375.
- Steinberger B., Calderwood A., 2006. Models of large-scale viscous flow in the earth's mantle with constraints from mineral physics and surface observations. *Geophys. J. Int.* 167, 1461-1481.
- Steinberger B., O'Connell R. J., 1998. Advection of plumes in mantle flow: Implication for hotspot motion, mantle viscosity and plume distribution. *Geophys. J. Int.*, 132, 412-434.
- Stemmer K., Harder H., Hansen U., 2006. A new method to simulate convection with strongly temperature- and pressure-dependent viscosity in a spherical shell: application to the Earth's mantle. *Physics of the Earth and Planetary Interiors.* 157(3-4), 223-249.
- Su W., Dziewonski A. M., 1997. Simultaneous inversion for 3-D variations in shear and bulk velocity in the mantle. *Phys. Earth planet. Inter.* 100, 135-156.

- Tackley P., 2000. Three-dimensional simulations of mantle convection with a thermochemical basal boundary layer: D"? In: M. Gurnis, M. E. Wysession, E. Knittle and B. A. Buffett (Eds), *The Core-Mantle Boundary Region*, Geophysics series, 28, AGU, Washington, D. C., 231-253.
- Tan E., Thoutireddy P., Choi E., Gurnis M., Aivazis M., 2000. GeoFramework Part1: Coupling models of mantle convection with Python framework. *Geochemistry, Geophysics, Geosystems*.
- Thoroval C., Machel P. and Cazanave A., 1995. Locally layered convection inferred from dynamic models of the Earth's mantle. *Nature*, 375, 777-780.
- Trubitsyn V., Kaban M. K., Rothacher M., 2007. Evolution of global mantle convection: mechanical and thermal effects of floating continents. EGU.
- Trubitsyn V., Rykov V. V., 1995. A 3-D numerical model of the Wilson cycle. *J. Geodynamics*. 20, 63-75.
- Trubitsyn V., Rykov V. V., 1999. 3-D spherical models of mantle convection, continental drift and the formation and disintegration of supercontinents. *Russian J. Earth's Sciences*. 1, no 2, <http://rjes.agu.org>.
- Trubitsyn V., Rykov V. V., 2000. 3-D spherical models of mantle convection with floating continents. U.S. Geological Survey Open File Report 00-218. 2-44.
- Trubitsyn V., Rykov V. V., 2001. A numerical evolution model of interacting continents floating on a spherical Earth. *Russian J. Earth's Sciences*. 2, no 6, <http://rjes.agu.org>.
- Wang H. S., Wu P., 2006. Effects of lateral variations in lithospheric thickness and mantle viscosity on glacially induced surface motion on a spherical, self-gravitating Maxwell Earth. *Earth and Planetary Science Letters*. 244, 576-589.
- Wen L., Anderson D. L., 1997. Present-day plate motion constraint on mantle rheology and convection. *J. Geophys. Res.*, 102, 24639-24653.
- Wu P., 2002. Mode coupling in a viscoelastic self-gravitating spherical earth induced by axisymmetric loads and lateral viscosity variations. *Earth and Planetary Science Lett.*, 202, 49-60.
- Wu P., 2005. Effects of lateral variations in lithospheric thickness and mantle viscosity on glacially induced surface motion in Laurentia. *Earth and Planetary Science Lett.* 235, 549-563.

- Wu P., 2006. Sensitivity of relative sea levels and crustal velocities in Laurentide to radial and lateral viscosity variations in the mantle, *Geophys. J. Int.*, 165, 401-413.
- Wu P., Wang H. S., 2006. Effects of Mode Coupling and Location of Rotational Axis on Glacial Induced Rotational Deformation in a Laterally Heterogeneous Viscoelastic Earth. *Geophys. J. Int.* 167, 853-859.
- Wu P., Wang H. S., Schotman H., 2005. Postglacial Induced Surface Motions, Sea-levels & Geoid Rates on a Spherical, Self-gravitating Laterally Heterogeneous Earth. *J. Geodyn.* 39(2), 127-142.
- Yang W. S., Baumgardner J. R., 2000. Matrix-dependent transfer multigrid method for strongly variable viscosity infinite Prandtl number thermal convection. *Geophys. and Astrophys. Fluid Dyn.* 92, 151-195.
- Yamazaki, D., Karato, S. I., 2001. Some mineral physics constraints on the rheology and geothermal structure of Earth's lower mantle. *American Mineralogist.* 86(4), 385-391.
- Yoshida M., 2004. Possible effects of lateral viscosity variations induced by plate-tectonic mechanism on geoid inferred from numerical models of mantle convection. *Physics of the Earth and Planet. Inter.* 147(1), 67-85.
- Zhang S., 1993. 3-D modelling of present mantle structure, constrained by plate subduction, geoid and mantle tomography: flow in a spherical shell with lateral viscosity variations. Dissertation, Johannes Gutenberg-Universitaet in Mainz.
- Zhang S., Christensen U., 1993. Some effects of lateral viscosity variations on geoid and surface velocities induced by density anomalies in the mantle. *Geophys. J. Int.* 114, 551-547.
- Zhong S., 2001. Role of ocean-continent contrast and continental keels on plate motion, net rotation of lithosphere, and the geoid. *J. Geophys. Res.*, 106, 703-712.
- Zhong S., Davis G. F., 1999. Effects of plate and slab viscosities on the geoid. *Earth Planet Sci. Lett.*, 170, 487-496.
- Zhong S., Gurnis M., 1994. Role of plates and temperature-dependent viscosity in phase change dynamics, *J. Geophys. Res.*, 99, 15903-15917.
- Zhong S., Zuber M. T., Moresi L. N., Gurnis M., 2000. The role of temperature dependent viscosity and surface plates in spherical shell models of mantle convection. *J. Geophys. Res.* 105, 11063-11082.

Zhu T., Feng R., 2005. The patterns of high-degree thermal free convection and its features in a spherical shell. *Acta Seismologica Sinica*. 18(1), 12-26.

